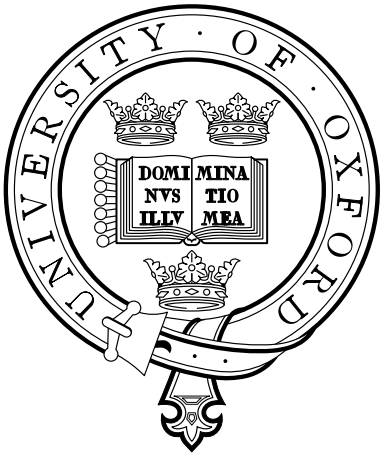
Deterministic Quantum Feedback Control in Probabilistic Atom-Photon Entanglement

OLIVER STEPHEN BARTER

A thesis submitted in partial fulfilment of
the requirements for the degree of
Doctor of Philosophy at the University of Oxford



St Peter's College
University of Oxford
2016

Deterministic Quantum Feedback Control in Probabilistic Atom-Photon Entanglement

Oliver Stephen Barter, St Peter's College.
(Departments of Physics)

Thesis submitted for the degree of Doctor of Philosophy
at the University of Oxford, Hilary 2016.

Abstract

The prospect of a universal quantum computer is alluring, yet formidable. Smaller scale quantum information processing, however, has been demonstrated. Quantum networks, interlinking flying and stationary qubits, and linear optical quantum computing (LOQC) are both good candidates for scaling up such computations. A strongly coupled atom-cavity system is a promising approach for applications in these fields, both as a node in a quantum network, and as a source of photons for LOQC. This thesis demonstrates the versatile capabilities of an atom-cavity system comprising a single ^{87}Rb atom within a macroscopic high-finesse Fabry-Pérot cavity. It operates intermittently for periods of up to 100 μs, with single-photon repetition rates of 1 MHz and an intra-cavity production efficiency of up to 85%. Exploiting the long coherence time of around 500 ns, the photons are subdivided into d time bins, with arbitrary amplitudes and phases, thus encoding arbitrary qudits. High fidelity quantum logic is shown, operating a controlled-NOT gate integrated into a photonic chip with a classical fidelity of $95.9^{+1.4}_{-1.7}$%. Additionally, the generation of entanglement is verified and non-classical correlations between events separated by periods exceeding the travel time across the chip by three orders of magnitude are observed. Photonic quantum simulation is performed, using temporally encoded qudits to mimic the correlation statistics of both fermions and anyons, in addition to bosons. Finally measurement-based quantum feedback is demonstrated and used to actively control the routing of temporal qubits.

Statement of Originality

This thesis is entirely my own work. I contributed to the experiments in Chapter 3 in my first year, and provided the subsequent data analysis, which are published in [110]. The experiments in Chapters 4 and 5 were carried out in collaboration with J. C. F. Matthews et al, the contributors are named in the authorship list of [122].

Acknowledgements

Firstly, I would like to express my sincere gratitude to Dr. Axel Kuhn for his support and guidance over the past four and a half years. His knowledge about and enthusiasm for the field have made the lab always interesting and enjoyable. I could not have wished for a more friendly supervisor.

I must thank Peter Nisbet-Jones and Jerome Dilley for providing me with a remarkably complex and capable experimental apparatus with which to work; and Annemarie Holleczek for doggedly assisting in operating it.

To Dustin, a fount of knowledge, for making Room 301 an entertaining and stimulating place to work and for all his assistance in lab, your help has been invaluable. To the younger members of the group, Tom for invigorating discussions and adept assistance in the lab. And to all, including Naomi and Marwan for kindly proofreading sections of this thesis.

I would also like to thank my colleagues from Bristol, Dr Jonathan Matthews, Dr Kostas Poulios, and Allison Rubenok, without whose knowledge and determination much of this thesis would not exist, it was a pleasure collaborating with you. Thanks again to Kostas for the raki and taking us to Enagron, I will return.

I would like to thank the amazing Alex Lucas for keeping me company and keeping me going.

And finally my family, for their love and support.

Contents

1 Introduction **1**

2 Physical Approach **10**
2.1 Controlling an Atom 10
2.1.1 Atom-Cavity Interaction 11
2.1.2 STIRAP – Controlling the Photon 22
2.2 Hong-Ou-Mandel Interference 29
2.2.1 Time-Resolved HOM 32
2.3 Experimental Setup 40
2.3.1 Cavity 41
2.3.2 MOT and Atomic Fountain 43
2.3.3 Lasers 46
2.3.4 Experimental Timing and Control 48
2.3.5 Detection and Data Recording 52

3 Temporally Encoded Qudits **59**
3.1 Introduction 59
3.2 Time-Resolved Two-Photon Interference 61
3.3 Qudit Preparation 65
3.4 Results - Qubits 69
3.5 Data Analysis 73
3.5.1 Identifying Correlations 74
3.5.2 Sliding Histogram 76
3.5.3 Background Correction 76
3.5.4 Normalisation 83
3.5.5 Errors 86
3.5.6 Discretised Time Bins 88
3.6 Results - Qutrits & Ququads 89
3.7 Conclusions 94

3.7.1 Fidelity of the Qudit Preparation 95

4 Operation of a Linear-optical CNOT Gate 97
4.1 Introduction 97
4.1.1 Photonic Circuit 99
4.1.2 Circuit Based Source Characterisation 101
4.2 LOQC Model 104
4.3 Results 110
4.3.1 Time Resolved Similarity 118
4.3.2 Maximum Likelihood Estimation 119
4.4 Entanglement Verification 126
4.4.1 Generating entanglement 128
4.4.2 Verifying entanglement 130
4.4.3 Results 134
4.4.4 Backfiring 137
4.5 Conclusions 138

5 CNOT with Temporal Qubits 141
5.1 Introduction 141
5.2 Time-Bin LOQC Model 145
5.3 Results 148
5.3.1 Finer Phase Resolution 152
5.4 Conclusions 158

6 Quantum Feedback 159
6.1 Introduction 159
6.1.1 Feedback Plan 162
6.2 Implementation 164
6.2.1 Time Budget 165
6.2.2 EOM 169
6.2.3 Fast Electronics 173
6.3 Results 177
6.4 Discussion 182

7 Outlook 185
7.1 Source Improvements 186
7.2 Future Work 192

A Feedback Controller Circuit Design 195
A.1 Introduction 195
A.2 Logical Processing 197

A.3 Output Stage 202
A.4 Conclusions 205

Acronyms

AOM Acousto-Optic Modulator

AWG Arbitrary Waveform Generator

CDF Cumulative Distribution Function

CNOT Controlled-NOT

DAQ Data Acquisition

EOM Electro-Optic Modulator

FSR Free Spectral Range

FWHM Full Width Half Maximum

HBT Hanbury Brown and Twiss

HOM Hong-Ou-Mandel

LIAD Light Induced Atomic Desorption

LO Local Oscillator

LOQC Linear Optical Quantum Computing

MOT Magneto-Optical Trap

PBS Polarising Beam Splitter

PCB Printed Circuit Board

PDF Probability Distribution Function

PDH Pound-Drever-Hall

PID Proportional-Integral-Derivative

QIP Quantum Information Processing

QKD Quantum Key Distribution

RF Radio Frequency

SPAD Single-Photon Avalanche Diode

SPCM Single Photon Counting Modules

SPDC Spontaneous Parametric Down Conversion

STIRAP Stimulated Raman Adiabatic Passage

TDC Time-to-Digital Converter

TEM Transverse Electromagnetic

TTL Transistor-Transistor Logic

UHV Ultra High Vacuum

List of Figures

1.1 Overview 8

2.1 Fabry-Pérot resonator 11
2.2 Fabry-Pérot transmission 13
2.3 Cavity mode structure 18
2.4 STIRAP level diagram 23
2.5 STIRAP pulse shapes 28
2.6 Outcomes for a 50:50 beam splitter 29
2.7 Two photon interference 30
2.8 Hom dip 32
2.9 Time-resolved correlations as a function of polarisation 37
2.10 Time-resolved correlations as a function of frequency and time difference 38
2.11 Effect of frequency jitter on time-resolved correlations 39
2.12 Effect of emission time jitter on time-resolved correlations . . 40
2.13 Hyperfine energy level structure of the ^{87}Rb D_2 line. 47
2.14 Schematic of the laser setup 48
2.15 Photon pistol control sequence 50
2.16 SPCM errors 51
2.17 Optical delay line 52
2.18 Histograms of t_{STIRAP} 57
2.19 Histogram of t_{MOT} 58
2.20 Hanbury Brown – Twiss $g^{(2)}$ 58

3.1 Time-binned HOM 63
3.2 Theoretical HOM interference patterns for double-hump photons with a phase shift 65
3.3 Qubit photon generation waveform 68
3.4 Measured HOM interference patterns for double-hump photons with a phase shift 70
3.5 Phase dependence of coincidence probability 73
3.6 Dual-rail equivalent circuit for qubits 74
3.7 HOM background estimation 79
3.8 HOM background correction 81
3.9 Overview of background estimation and correction 82
3.10 HOM zero parameter theory comparison 86
3.11 HOM error bounds 88
3.12 Time-binned HOM 89
3.13 Time-binned HOM results 90
3.14 Qutrit photon shape 91
3.15 Qutrit HOM interference 92
3.16 Dual-rail equivalent circuit for qutrits 93
3.17 Ququad HOM interference 94

4.1 CNOT and CNOT4 photonic circuit diagrams 100
4.2 Photonic chip imperfections 101
4.3 On-chip $g^{(2)}$ 102
4.4 On-chip HOM 103
4.5 Beam splitters vs directional couplers 106
4.6 CNOT4 chip operation 109
4.7 Equivalent looped chip layout 110
4.8 Measured CNOT truth table - raw counts 112
4.9 Measured CNOT truth table - simple background subtraction 113
4.10 Measured CNOT truth table - MLE 114
4.11 Measured perpendicular CNOT truth table - MLE 115
4.12 Full correlation matrix 117
4.13 Time-resolved similarity 120
4.14 Likelihood distributions 124

4.15 Normalised likelihood distributions . . . 125
4.16 Similarity distribution . . . 126
4.17 Operation of directional coupler . . . 128
4.18 Generating entanglement . . . 129
4.19 Pauli observables circuit diagrams . . . 133
4.20 Control and target loop truth tables . . . 134
4.21 Bell state correlation measurements . . . 135
4.22 Time-resolved fidelity of entanglement . . . 136
4.23 SPCM photo-emission . . . 139

5.1 Qubit photon envelope . . . 142
5.2 On-chip double-hump HOM . . . 144
5.3 Equivalent virtual circuit . . . 145
5.4 CNOT truth table as a function of particle class . . . 147
5.5 CNOT4 chip operation with phase difference . . . 147
5.6 Measured $\phi = \pi$ truth table . . . 150
5.7 CNOT C_1T_0 row as a function of phase . . . 152
5.8 Experimental quantum simulation . . . 153
5.9 Complete phase behaviour of CNOT gate . . . 155
5.10 Complete unique phase behaviour of CNOT gate . . . 157

6.1 Feedback control setup . . . 167
6.2 Feedback error analysis . . . 169
6.3 Unstable interferometric phase voltage characterisation of EOM 171
6.4 EOM phase voltage relationship . . . 172
6.5 EOM timing calibration . . . 174
6.6 Control logical circuit . . . 175
6.7 Control circuit response . . . 177
6.8 Verification of control circuit functionality . . . 178
6.9 Time-resolved HOM interference under feedback control . . . 180
6.10 Time-binned HOM interference under feedback control . . . 181
6.11 Time-binned HOM . . . 183

7.1 Cavity efficiencies . . . 189
7.2 Time-resolved chirped HOM . . . 193

A.1 Photo of controller circuit 196
A.2 Complete controller circuit diagram 198
A.3 Logic circuit diagram 199
A.4 Impedance matching at the DET input. 201
A.5 PHASE rise times 202
A.6 Pull-up resistor choice 204

List of Tables

2.1 Properties of the high-finesse cavity 42

3.1 Photon emission delay arm branching 84

4.1 Similarities 116
4.2 Reference similarities 116
4.3 Correlation matrix similarities 118
4.4 Basis vectors 127

6.1 Feedback latency breakdown 170
6.2 Control circuit latency breakdown 176

7.1 Photon source efficiency breakdown 187

Chapter 1

Introduction

Information is entering a quantum age. The unintuitive laws of quantum mechanics hold the keys to solving currently intractable computational problems and providing unconditionally secure communication.

Quantum mechanics is a branch of physics established in the 1920s, which arose out of Max Planck's assumption at the dawn of the 20th century that electromagnetic energy could be emitted only in quantised form, where the energy of the quanta are proportional to their frequency [1]. This resolved many notable problems in physics at the time, including the black-body radiation problem, later known as the ultraviolet catastrophe [2]. The concept was later extended by Einstein, who in 1905 suggested that electromagnetic waves could only exist as discrete wave-packets to explain the photoelectric effect [3]. These discrete light quanta later came to be called *photons* [4].

Quantum mechanics describes many phenomena unknown to classical physics, the most famous of which include: the concept of wave-particle

duality, arising from the 1924 assertion of de Broglie that just as light has both wave-like and particle-like properties, all particles also have wave-like properties [5]; the uncertainty principle, introduced in 1927 by Heisenberg which details a fundamental limit to the precision with which certain pairs of physical properties of a particle can simultaneously be known [6]; superposition, fundamental to quantum information processing, which states that any two or more quantum states can be added together ("superposed") and the result will be another valid quantum state; and entanglement, whereby for some pairs or groups of particles the quantum state of each particle cannot be described independently and instead, the quantum state must be described for the system as a whole. Entanglement seemed to be so at odds with physical reality that the famous 1935 EPR (Einstein-Podolsky-Rosen) paradox suggested quantum mechanics was incomplete, and that there must exist some "hidden variables" [7]. Bell's theorem of 1964 gave a means to test the veracity of quantum mechanics, stating: "No physical theory of local hidden variables can ever reproduce all of the predictions of quantum mechanics." [8]. It was with photons that Bell's theorem was first tested, and local hidden variables ruled out, showing that indeed the phenomena of quantum mechanics go beyond our classical intuition [9]. Until recently most experimental tests of Bell's theorem were subject to caveats, known as loopholes, however recently loophole-free tests of Bell's theorem have been performed [10, 11].

Alongside testing the foundations of quantum mechanics, people started to examine the possibilities of exploiting the unusual behaviours of quantum mechanics for practical purposes. The unusual properties of entangled states, at the heart of the EPR paradox, led to the development of the field of

quantum cryptography[1], which details information-theoretically secure communications protocols [12–14]. Richard Feynman argued that the ability of quantum systems to exist in a superposition of many different states simultaneously fundamentally limits the efficiency of their simulation on classical computers [15], however in the same conference talk he suggested that a quantum computer might be more efficient. It has since been shown that it is possible for a quantum computer to solve certain computational problems exponentially more efficiently than a classical computer [16, 17]. The most famous demonstrations of this are Shor's algorithm [18] for efficiently finding the prime factors of an integer, which would break the widely used RSA cryptosystem; and Grover's algorithm [19, 20], applicable to a wide range of problems including efficiently searching a database. These algorithms manipulate quantum information, the fundamental unit of which is the qubit (quantum-bit), generally represented as the superposition of two states, $|\psi\rangle = \alpha|0\rangle + \beta|1\rangle$, where $|0\rangle$ and $|1\rangle$ are the states of a two-level quantum system and α and β are probability amplitudes whose squares sum to one.

Any two-level quantum system can be thought of as a qubit, however to be useful as a qubit for quantum information processing (QIP) [21] the physical system must satisfy 5+2 conditions, known as DiVincenzo's criteria [22]. Succinctly these require: that the system be scalable; initialiseable; have long coherence time; allow "universal" computations; and allow qubit-specific measurements. Additionally for quantum communication the system must also be able to interconvert stationary and flying qubits and faithfully transmit flying qubits between specified locations. The fundamental step in quantum computing is a quantum logic gate operating on one or more

[1] Although the very first quantum cryptographic protocol (BB84) does not involve entanglement.

qubits, it has been shown that "universal" computations can be carried out with only single and two-qubit gates [23]. Many physical systems are capable of satisfying these requirements including quantum dots [24], diamond colour centres [25], Rydberg atoms [26], superconducting circuits [27], single electron spins in semiconductors [28], two-dimensional quasiparticles [29], photons [30], atoms [31], and perhaps most auspiciously trapped ions [32]. A general review comparing different systems can be found at [33].

Central to many quantum computation and quantum cryptography systems is the concept of a quantum network, which allows for the transportation of quantum information between physically separated quantum systems [34]. This can not only be used for the quantum cryptographic task of quantum key distribution (QKD), which then allows secure communication between classical computing environments, but also for distributed quantum information processing where each node in the network can store or process quantum information. A quantum network consists of stationary quantum nodes connected by quantum channels for flying information carriers. Although many of the quantum systems mentioned above are suitable for stationary qubits, only one stands out as a suitable candidate for flying qubits: photons [35]. Optical photons, ideally in the infrared, are able to transmit quantum information over large distances using mature existing telecommunication fibre technology [36]. However, the weak interaction of photons with the environment, which allows them to carry quantum information over such great distances, makes it difficult to interact with them at the stationary nodes. Therefore a number of the most promising proposals for quantum networks exploit the principles of cavity quantum electrodynamics to enhance the light-matter interaction using high finesse optical cavities [37]. The most promising network nodes are based upon either trapped ions [38] or atoms [31]. Since

the first experimental demonstration of deterministic single photon emission from an atom-cavity system in 2002 [39], the quantum state of a single atom has been mapped onto a photon [40] and an elementary quantum network implemented [41].

Realistic long distance quantum networking is going to be subject to to both signal propagation loss and decoherence. The *no-cloning theorem* forbids the copying of arbitrary unknown quantum states [42, 43], therefore standard amplification of the signal cannot be performed. Quantum networks will therefore likely include quantum repeaters [44], which make use of quantum teleportation [45] to create long-distance entanglement from shorter-distance entanglement via entanglement swapping [46, 47]. Many repeater designs incorporate quantum memories to temporarily store the quantum states [48], often in atomic ensembles [49]; storage has also been achieved in doped optical fibre [50], and even single atoms in a repeater design based upon the atom-cavity systems that might comprise the computational nodes of a network [51].

The no cloning theorem also prohibits classical error correction techniques, as it is not possible to create backup copies (required for majority vote correction) of a quantum state. quantum error correction codes, provide the vital ability to correct errors during quantum computation, whilst circumventing the no cloning theorem [52, 53].

It should not be surprising that photons feature so heavily in quantum technologies, given light exhibits quantum features at room temperature. It was as early as the 1950s that the field of quantum optics began to emerge with the work of Hanbury Brown and Twiss on correlations between coherent beams of light [54]. The advent of the laser in the 1960s accelerated the field and the first quantum states of light were described in 1963 [55] and observed

for the first time in 1977 with the demonstration of photon *anti-bunching* [56]. Since the violations of Bell's inequality in the early 1980s [9] the field of QO has played an increasingly large role in quantum information processing and other quantum-enhanced technologies [57].

In 2001, it was shown that all-optical scalable quantum computing is possible with just single-photon sources, linear optical elements, and single-photon detectors [58]. This was first demonstrated experimentally in 2002 with a parity check of two qubits [59] and a general CNOT gate followed in 2003 [60]; both in bulk optics requiring apparatus covering on the order around square metre. A number of improvements on the original scheme have since been proposed [30, 61], which combined with the relatively recent ability to integrate optical elements into a centimetre scale "photonic chip" [62], including reconfigurable active elements [63], makes linear optical quantum computing (LOQC) a very attractive platform for QIP. The integrated environment is essential for scalability as it allows the implementation of sophisticated interferometers with the sub-wavelength stability required for reliable operation. Integrated demonstrations include Shor's quantum factoring algorithm [64], on-chip photonic teleportation [65], and boson sampling [66]. Not only does LOQC provide a platform for computing in its own right, but also the ability to process the quantum information travelling between the nodes of a quantum network.

Aside from the linear optical elements, LOQC obviously demands high efficiency single photon detectors [67], which recently have exceeded 90% detection efficiency at telecom wavelengths [68], and a bright source of indistinguishable single photons; see [69] for a recent review of both. There are a great many physical systems which have been used as single photon sources, which are generally divided into two fundamental classes: determin-

istic, where single photons are emitted 'at the push of a button' with some finite efficiency; and probabilistic, where photon pairs are generated randomly and one is used to herald the other. The workhorse of experiments requiring single photons is currently spontaneous parametric down-conversion (SPDC) whereby pairs of photons are generated by passing a strong pump laser beam through a non-linear crystal. These sources are intrinsically hampered by the need to keep the average pair production levels much less than one to avoid producing more-than-one photon states [70], and also by the finite heralding efficiency. However these issues can be mitigated somewhat with the use of quantum memories [71]. Recently a chip-based array of near-identical, heralded single photon sources has been demonstrated based on spontaneous four-wave mixing [72], another parametric nonlinear process.

Deterministic sources do not suffer the same scalability issues. The most promising systems are quantum dots [73], colour centres in diamond [74, 75], and single atoms in optical cavities [76]. Recently both quantum dots and diamond colour centres have started to be integrated into photonic crystal cavities, which analogously to optical cavities for atoms, enhance the emission probability and provide a known emission mode [77, 78]. However, the unique structure of each individual quantum dot produces slightly different emission properties, tuning is therefore required to provide indistinguishable photons [79]; diamond colour centres also suffer from similar indistinguishability problems. Single atoms have no such issues and additionally produce very narrow bandwidth photons, providing the good indistinguishability essential for high fidelity LOQC [80], and therefore are an excellent source of photons for QIP [81].

The promising prospects for atom-cavity systems as both the nodes in a quantum network and for efficient sources of indistinguishable single pho-

tons for QIP motivate the following work. This thesis demonstrates several unique features of an atom-cavity source. The source is based on a single ^{87}Rb atom loaded into a high-finesse optical cavity by an atomic fountain from a magneto-optical-trap (MOT). The temporally long, narrowband in the frequency domain, photons emitted are used for high fidelity LOQC and can be used to temporally encode qubits and higher dimensional superpositions, in addition quantum feedback can be introduced into the photon generation process.

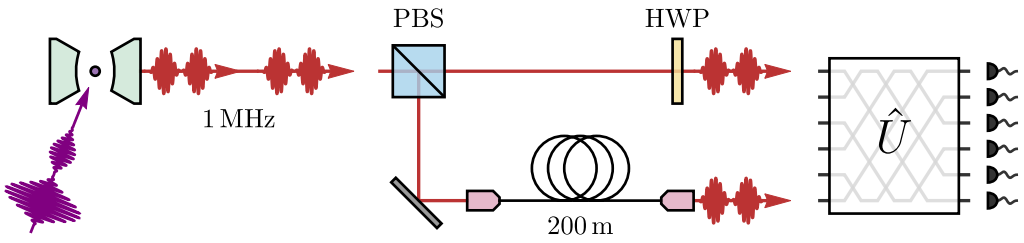


Figure 1.1: Overview: The cartoon outlines the key features of the experimental set-up. With an atom coupled to our cavity, a shaped driving pulse (purple) is used to generate shaped single photons (shown above as "double-hump photons") at a repetition rate of 1 MHz. This stream of sequential randomly polarised single photons is then demultiplexed using a polarising beam splitter (PBS) with 200 m of fibre providing a 1 μs delay in one of the two output ports. A half-wave plate (HWP) provides control over the polarisation of the photons. The resulting pairs of single photons are then input into a photonic network — this could be a simple beam splitter or a more complicated integrated photonic chip — before arriving at a bank of detectors.

The physical details of the atom-cavity source are detailed in Chapter 2. The theoretical foundations of the atom-cavity system, as well as the photon generation process are presented, followed by some details of the experimental setup. Chapter 3 demonstrates the versatility of the source by subdividing the deterministically emitted photons, which are of the order of 500 ns long, into d time bins of various amplitudes and phases, which are used for encoding arbitrary qu-d-its. The chapter also elucidates the data processing behind the atom-cavity system and the time-resolved HOM interference of photons.

In Chapter 4 quantum logic is demonstrated using the narrow linewidth photons within an integrated photonic chip. A high fidelity controlled-NOT gate is implemented and used to entangle the photons. We consequently observe non-classical correlations between events separated by periods exceeding the travel time across the chip by three orders of magnitude. Chapter 5 extends the work with the integrated photonic chip by using temporally encoded qubits to probe the sensitivity of the CNOT gate design to phase errors. Additionally the complex interference of classes of particles other than bosons is experimentally simulated. In Chapter 6 measurement-based quantum feedback is implemented to achieve active control over the routing of temporally encoded qubits in long photons. This requires conditionally changing the state of a photon halfway through its generation process. Finally in Chapter 7 the tantalising future of atom-cavity systems in QIP is contemplated.

Chapter 2

Physical Approach

This chapter first presents the theory behind the atom-cavity photon source (Section 2.1), followed by the theoretical framework of the time-resolved interference of two photons (Section 2.2), and concludes with the experimental details of the source (Section 2.3).

2.1 Controlling an Atom

We are able to generate single photons from a single atom with an unprecedented level of control via a coherent Raman process, known as stimulated Raman adiabatic passage (STIRAP). However an atom does not natively interact very strongly with the electromagnetic field and therefore a high-finesse optical cavity is used to enhance this interaction. An overview of the key facets of the theory describing atom-cavity interactions, cavity quantum electrodynamics (cQED), is first presented in Section 2.1.1 followed by the theory behind STIRAP in Section 2.1.2.

2.1.1 Atom-Cavity Interaction

This section focuses on the origin of the three key parameters which describe an atom-cavity system, namely the cavity field decay rate, κ, the atom cavity interaction rate, g, and the atomic decay rate, γ. The structure of the electromagnetic field inside the cavity is also considered along with the requirement for a stable cavity. There are number of good references describing the interaction of atoms and cavities, including [82, 83], and more recently [84] provides an excellent overview with many references to works performed.

Cavity Field Decay Rate

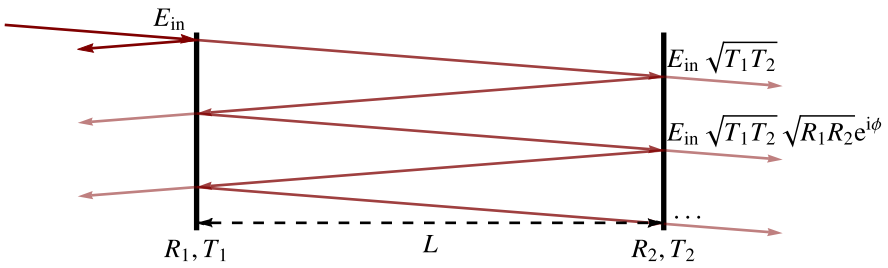


Figure 2.1: Fabry-Pérot resonator: An incident electromagnetic wave makes multiple passes between the two opposing flat mirrors. The total transmitted amplitude E_{T} is the sum of all the partial transmissions.

Let us first consider the properties of the empty cavity, without an atom present. The cavity acts as a simple Fabry-Pérot resonator of two mirrors with reflectivities R_1, R_2 and transmissions T_1, T_2 (Figure 2.1). We can write down the transmitted field as the sum of the all the amplitudes after the second mirror:

$$E_{\text{T}} = E_{\text{in}}(T + TRe^{i\phi} + TR^2e^{2i\phi} + ...) = E_{\text{in}}\frac{T}{1 - Re^{i\phi}}\,, \tag{2.1}$$

where $R = \sqrt{R_1R_2}$, $T = \sqrt{T_1T_2}$, and $\phi = 2Lk$ is the round trip phase in the

length L cavity for a field with wavevector k. The transmitted intensity will be the square of this field:

$$I_{\mathrm{T}} = |E_{\mathrm{T}}|^2 = E_{\mathrm{in}}^2 |\frac{T}{1 - R\mathrm{e}^{\mathrm{i}\phi}}|^2 = E_{\mathrm{in}}^2 \frac{T^2}{(1-R)^2} \frac{1}{1 + \frac{4R}{(1-R)^2} \sin(\frac{\phi}{2})^2} \,. \tag{2.2}$$

The transmitted intensity thus varies as a function of the round trip phase ϕ. It can be seen that maximal transmission occurs when ϕ is a multiple of 2π, the resonance frequencies, ω_{res}, are therefore given by:

$$\begin{aligned} \phi = 2Lk = 2L\frac{\omega}{c} = 2\pi q \\ \therefore \omega_{\mathrm{res}} = \frac{\pi c}{L} q, \quad q = 1, 2, ... \end{aligned} \tag{2.3}$$

The distance between two consecutive resonances is known as the free spectral range (FSR), therefore

$$\Delta\omega_{\mathrm{FSR}} = \frac{\pi c}{L} \,. \tag{2.4}$$

The linewidth (FWHM) of these resonance peaks can be found by solving for the frequencies ω where the transmitted intensity drops to one half its maximum value. Doing so yields

$$\Delta\omega_{\mathrm{FWHM}} \approx \Delta\omega_{\mathrm{FSR}} \frac{1-R}{\pi\sqrt{R}} = \frac{\Delta\omega_{\mathrm{FSR}}}{\mathcal{F}} \,. \tag{2.5}$$

Where we have defined

$$\mathcal{F} = \frac{\pi\sqrt{R}}{1-R} \tag{2.6}$$

which is known as the cavity finesse. This quantifies how many round trips within the cavity a photon will on average make before leaking out.

The field inside the cavity will be a standing wave, with the field strength varying as a function of axial position. At an anti-node constructive inter-

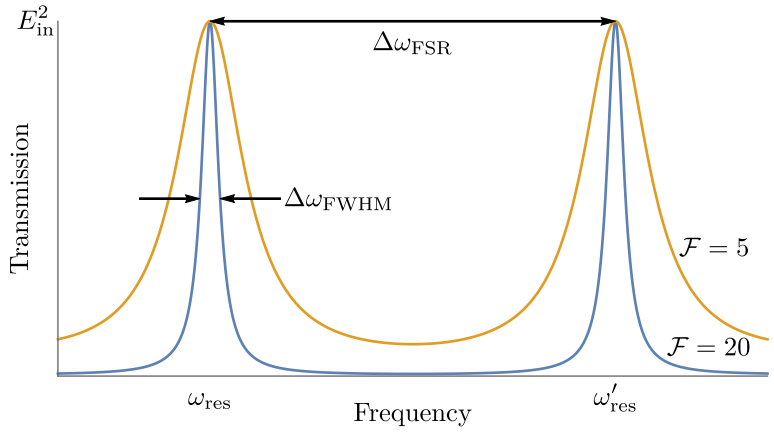


Figure 2.2: Fabry-Pérot transmission: The transmission varies strongly as a function of the frequency of the incident light. The free spectral range, $\Delta\omega_{\text{FSR}}$, remains unchanged but the linewidth, $\Delta\omega_{\text{FWHM}}$, narrows for increasing cavity finesse, $\mathcal{F}$. Real optical cavities achieve finesses into the 100 000s.

ference gives a maximum strength of

$$E_0 = E_{\text{in}}\sqrt{T_1}\left(1+\sqrt{R_2}\right)\left(1+R+R^2+...\right) = E_{\text{in}}\frac{\sqrt{T_1}\left(1+\sqrt{R_2}\right)}{1-R}\,. \quad (2.7)$$

For a near symmetric, high reflectivity cavity neglecting losses, this results in

$$I_0 = I_{\text{in}}\frac{1}{1-R} \approx 4\frac{\mathcal{F}}{\pi}I_{\text{in}}\,. \quad (2.8)$$

Thus it can be seen that the finesse of the cavity also describes the enhancement provided by the cavity. Real optical cavities can achieve finesses into the 100 000s. The capacity to enhance the interaction of the atom with an electromagnetic field by many orders of magnitude makes cavities a powerful tool for atom-optical applications.

Let us now consider a photon inside the cavity. Due to the finite reflectivity of the mirrors the photon will slowly decay out of the cavity. The loss

on one round trip cycle is:

$$I(t) - I(t + t_{\text{trip}}) = I(t)(1 - R^2)\,. \tag{2.9}$$

For a high finesse cavity the loss per trip will be small. As the cavity is traversed at the speed of light t_{trip} will also be very small. We may therefore write the rate of change of photon intensity as

$$\begin{aligned} \frac{\mathrm{d}I}{\mathrm{d}t} &= \frac{I(t) - I(t + t_{\text{trip}})}{t_{\text{trip}}} = \frac{I(t)(1 - R_1 R_2)}{2L/c} \\ &= \frac{I(t)(1 - R^2)c}{2L} = \frac{I(t)(1 - R^2)\Delta\omega_{\text{FSR}}}{2\pi} \\ &= I(t)\frac{\sqrt{R}(1 + R)}{2}\Delta\omega_{\text{FWHM}} \approx I(t)\Delta\omega_{\text{FWHM}}\,, \end{aligned} \tag{2.10}$$

which describes an exponential decay of the cavity intensity:

$$I(t) = \mathrm{e}^{-\Delta\omega_{\text{FWHM}}t}\,. \tag{2.11}$$

The cavity field is given by the square root of the intensity and therefore decays at half the rate, thus we define the *cavity field decay rate*, κ, as

$$\kappa = \frac{\Delta\omega_{\text{FWHM}}}{2}\,. \tag{2.12}$$

A note of caution to the reader, whilst some references follow the definition of κ as the cavity *field* decay rate as given here, others use κ to refer to the cavity *intensity* decay rate, this can lead to confusion over factors of 2 if overlooked.

Atom-Cavity Coupling Rate

Now we have a description of the cavity let us consider the interaction of a simple two-level atom with this cavity. The combined atom-cavity system is described by a Hamiltonian of three parts:

$$\widehat{H} = \widehat{H}_{\text{cav}} + \widehat{H}_{\text{atom}} + \widehat{H}_{\text{int}} \,. \tag{2.13}$$

The first details quantised excitations of the cavity field at frequency ω_{c} using the standard photon creation and annihilation operators $\hat{a}^\dagger$ and $\hat{a}$. The second describes a two-level atom with ground state $|g\rangle$ and excited state $|x\rangle$, with energies $\hbar\omega_g$ and $\hbar\omega_x$ respectively and atomic raising and lowering operators $\hat{\sigma}^\dagger = |x\rangle\langle g|$ and $\hat{\sigma} = |g\rangle\langle x|$. The final term is the Jaynes-Cummings interaction Hamiltonian which, having made the rotating wave approximation, describes the exchange of quanta between the cavity mode and atom via the electric dipole interaction [85, 86]. Explicitly

$$\widehat{H}_{\text{cav}} = \hbar\omega_{\text{c}} \left(\hat{a}^\dagger \hat{a} + \frac{1}{2} \right) \tag{2.14}$$

$$\widehat{H}_{\text{atom}} = \hbar\omega_{xg} \hat{\sigma}^\dagger \hat{\sigma} \tag{2.15}$$

$$\widehat{H}_{\text{int}} = \hbar g \left(\hat{a}^\dagger \hat{\sigma} + \hat{\sigma}^\dagger \hat{a} \right) \,. \tag{2.16}$$

The parameter g describes the atom-cavity coupling rate and is given by

$$g = \frac{\boldsymbol{\mu}_{xg} \cdot \boldsymbol{E}}{\hbar} \tag{2.17}$$

where $\boldsymbol{\mu}_{xg}$ is the transition dipole moment and $\boldsymbol{E}$ the electric field of the cavity mode[1]. We are mostly concerned with the interaction of an atom with

[1] Often in reality, transitions between multiple atomic sub-levels with differing transition dipole moments are driven simultaneously and a weighted average μ is considered.

an otherwise empty cavity (no laser field), therefore the electric field E of interest is the magnitude of the vacuum electric field. Its value can be found by equating the zero point energy of $\frac{1}{2}\hbar\omega_c$ per mode to the electromagnetic energy within a mode volume V. We can make use of the fact that the time-averaged energy contributions of the electric and magnetic fields are identical to write

$$U = 2\int \frac{1}{2}\epsilon_0 |E(\mathbf{r})|^2 \mathrm{d}^3\mathbf{r} = \frac{1}{2}\hbar\omega_c \,. \tag{2.18}$$

It is useful to pull a factor of $|E_0|^2$, the maximum field strength squared, out of the integral as it allows a definition of the mode volume with dimensions only concerning length. Solving we therefore find

$$\begin{aligned} \epsilon_0 |E_0|^2 \frac{\int |E(\mathbf{r})|^2 \mathrm{d}^3\mathbf{r}}{|E_0|^2} &= \frac{1}{2}\hbar\omega_c \\ E_0 &= \sqrt{\frac{\hbar\omega_c}{2\epsilon_0 V_{\text{eff}}}} \,, \end{aligned} \tag{2.19}$$

where the effective mode volume of the cavity, V_{eff} is defined as

$$V_{\text{eff}} = \frac{\int |E(\mathbf{r})|^2 \mathrm{d}^3\mathbf{r}}{|E_0|^2} \tag{2.20}$$

and $|E_0|^2 = \max\left[|E(\mathbf{r})|^2\right]$. The full form of the maximum value of the atom-cavity coupling strength as found at an antinode is therefore

$$g_0 = \sqrt{\frac{\mu_{xg}^2 \omega_c}{2\epsilon_0 \hbar V_{\text{eff}}}} \,. \tag{2.21}$$

The coupling strength, g, experienced by an atom will vary within the cavity from 0 to g_0 with the same positional dependence as the electric field.

Cavity Field Structure

The profile of the electric field inside the cavity can be found solving Maxwell's equations with the boundary conditions imposed by the mirror surfaces. The solutions are standing waves which can be described in the paraxial approximation using the set of Ince-Gaussian polynomials[2] [87]. The fundamental TEM_{00} mode is the mode which we wish to use and has a simple Gaussian form:

$$E_{00}(\mathbf{r}) = E_0 \frac{w_0}{w(z)} \exp\left(-\frac{r^2}{w^2(z)} + \mathrm{i}\frac{kr^2}{2R(z)} - \mathrm{i}\psi_{\mathrm{GS}} - \mathrm{i}k\left(z - \frac{L}{2}\right)\right), \quad (2.22)$$

where $w(z)$ describes the beam width at axial position z, $R(z)$ is the radius of curvature of the phase front, and ψ_{GS} is the Gouy phase shift:

$$w(z) = w_0\sqrt{1 + \left(\frac{z}{z_{\mathrm{R}}}\right)^2} \quad (2.23)$$

$$R(z) = z + \frac{z_{\mathrm{R}}^2}{z} \quad (2.24)$$

$$\psi_{\mathrm{GS}}(z) = \arctan\left(\frac{z}{z_{\mathrm{R}}}\right). \quad (2.25)$$

The central waist w_0, and the Rayleigh range z_R — the distance from where $w(z) = w_0$ to where the mode has expanded to $w(z) = \sqrt{2}w_0$ — are in turn given by

$$w_0^2 = \frac{\lambda}{\pi}\sqrt{\frac{L}{2}\left(R_{\mathrm{c}} - \frac{L}{2}\right)} \quad (2.26)$$

$$z_{\mathrm{R}} = \frac{\pi}{\lambda}w_0^2, \quad (2.27)$$

[2]These modes are derived for elliptical symmetry and reach the Hermite- or Laguerre-Gaussian polynomials as limiting cases.

where R_c is the radius of curvature of the mirror surfaces. The Gouy phase shift lifts the degeneracy of the transverse modes (as can be seen by repeating the etalon analysis with a round trip phase including the Gouy shift) which results in successive modes transverse being separated by

$$\Delta\omega_{\text{trans}} = \frac{1}{\pi}\Delta\omega_{\text{FSR}} \arccos\left(1 - \frac{L}{R_c}\right) = \frac{c}{L}\arccos\left(1 - \frac{L}{R_c}\right). \tag{2.28}$$

For the TEM_{00} Gaussian mode, the effective mode volume (Equation (2.20)) simplifies to

$$V_{\text{eff}} = \frac{\pi w_0^2 L}{4}. \tag{2.29}$$

No approximations are made to reach this result, thus it is therefore valid even for strongly non-cylindrical cavity modes near the concentric limit [88, p. 422].

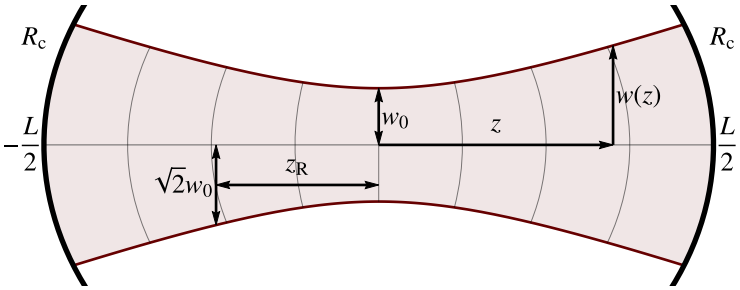


Figure 2.3: Cavity mode structure: The schematic shows the envelope of the fundamental Gaussian mode inside an optical cavity. The beam waist, $w(z)$ is the radius at which the field amplitude falls to $1/e$ of their axial values. The Rayleigh range z_R is the distance from the beam waist $w(z) = w_0$ to where the mode has expanded by $\sqrt{2}$.

Vacuum Rabi Oscillations

The form of the Jaynes-Cummings interaction Hamiltonian (Equation (2.16)) describes coupling between the atom-cavity states $|g, n\rangle$ and $|x, n-1\rangle$, corresponding respectively to an atom in the ground state with n quanta in the

cavity, and the atom now excited with one fewer cavity quanta. Therefore for each photon number n, there are two non-degenerate dressed states split by some frequency, known as the effective Rabi frequency, $\Omega_{\text{eff},n}$; the resulting ladder of doublets is known as the Jaynes-Cummings ladder. The eigenfrequencies of the total atom-cavity Hamiltonian (Equation (2.13)) can easily be found in the rotating wave approximation, they are given by

$$\omega_n^{\pm} = \omega_{\text{c}} \left(n + \frac{1}{2} \right) + \frac{1}{2} \left(\Delta_{\text{c}} \pm \sqrt{4ng_0^2 + \Delta_{\text{c}}^2} \right) \tag{2.30}$$

where $\Delta_{\text{c}} = \omega_{xg} - \omega_{\text{c}}$ is the detuning between the atom and the cavity. Therefore within each manifold the two states are split by

$$\Omega_{\text{eff},n} = \sqrt{4ng_0^2 + \Delta_{\text{c}}^2}\,. \tag{2.31}$$

Therefore, for an excited atom in an empty cavity, the system oscillates between excited atom, empty cavity, $|x, 0\rangle$ and de-excited atom, single photon in the cavity, $|g, 1\rangle$ at the frequency $\sqrt{4g_0^2 + \Delta_{\text{c}}^2}$. On resonance $\Delta_{\text{c}} = 0$ and the oscillations proceed at $2g_0$, known as the vacuum Rabi frequency. Such shifting of the atom-cavity system resonance frequency can be used to register the presence of an atom in the cavity.

Atomic Decay Rate

Finally, when we wish to consider the effect of the cavity on the enhancement of the emission properties of the atom we must consider the other decay mechanisms available to an excited atom in the cavity. For a single atom the only process available is radiative decay to non-resonant photon modes, i.e. spontaneous emission; there are no population-conserving scattering processes at work. The population decay rate, Γ, can be found using

Fermi's golden rule and is described by the Einstein A coefficient

$$\Gamma = A_{21} = \frac{1}{\tau} \tag{2.32}$$

where τ is the excited state lifetime. In our consideration of the cavity decay rate and atom-coupling rate we have used the convention of describing rates for the field and therefore our atomic polarisation field decay rate, γ is

$$\gamma = \frac{\Gamma}{2}\,. \tag{2.33}$$

Cooperativity and Strong-Coupling

The behaviour of any atom-cavity system is thus described by the three parameters, g_0, κ, and γ. Typically two different regimes prevail, that of interest is known as the strong-coupling regime, in which the atom-cavity coupling dominates over the other two decay rates, $g_0 \gg \{\kappa, \gamma\}$, and is required for the STIRAP photon generation process described in the next section. This is more formally defined with respect to the dimensionless atom-cavity cooperativity [89]

$$C = \frac{g_0^2}{2\kappa\gamma}\,, \tag{2.34}$$

where the strong-coupling regime is defined by $C > 1$. The cooperativity is equal to half the Purcell factor, F_P, which directly describes the enhancement to the emission properties of the atom provided by the cavity, defined as the ratio of the cavity and free space emission rates [90]:

$$F_\mathrm{P} = \frac{W^\mathrm{cav}}{W^\mathrm{free}} = \frac{3Q\lambda^3}{4\pi^2 V}\,. \tag{2.35}$$

The parameter Q is the quality factor of the cavity, defined as $Q = \omega_{\rm res}/\Delta\omega_{\rm FWHM}$, and related to the finesse by $Q = 2\mathcal{F}L/\lambda^3$. We can therefore find the fraction of the total number of photons which are emitted into the cavity mode, thus defining the maximum possible production efficiency for an atom-cavity system, $\eta_{\rm cav}$:

$$\eta_{\rm cav} = \frac{W^{\rm cav}}{W^{\rm cav} + W^{\rm free}} = \frac{F_{\rm P}}{F_{\rm P} + 1} = \frac{2C}{2C + 1}\,. \tag{2.36}$$

In practice this maximum is only reached in the limit of very long photons. For realistic photon pulses a lower, pulse shape dependent efficiency limit $\eta_{\rm max}$ is reached, as discussed in the next section.

The final figure of merit for a cavity is how efficiently can a photon in the cavity be extracted. We can only usefully collect emission from one side of our cavity which motivates the choice of asymmetric mirror reflectivities (see Section 2.3.1). Considering now the finite losses, L_1 and L_2, associated with real mirrors, the probability the photon will leak out via the desired mirror (mirror 2) is

$$\eta_{\rm extract} = \frac{T_2}{T_1 + T_2 + L_1 + L_2}\,. \tag{2.37}$$

In Chapter 7 these efficiencies are considered in more detail and it is shown that for very high finesse cavities, a greater overall photon generation and extraction efficiency can be obtained by lowering the reflectivity of the out-coupler mirror in order to increase $\eta_{\rm extract}$, even to the detriment of $\eta_{\rm cav}$.

Cavity Stability

In a planar cavity the two mirrors must be very close to parallel with one another otherwise the intracavity beam will spill out of the cavity due to

[3]The finesse can be considered as the number of mirror bounces light makes in the cavity before escaping, whilst the quality factor is the number of oscillations of the field before decay. Thus for wavelength scale cavities the two become equivalent.

walkoff. To circumvent this problem it is common to use curved mirrors to form a more stable cavity. However, not all values of mirror curvature, $R_{c,1}$, $R_{c,2}$, and cavity length, L, form stable cavities. Methods such as ray transfer matrix analysis allow the derivation of a stability criterion:

$$0 \leqslant g_1 g_2 \leqslant 1 \tag{2.38}$$

where

$$g_1 = \left(1 - \frac{L}{R_{c,1}}\right) \qquad g_2 = \left(1 - \frac{L}{R_{c,2}}\right). \tag{2.39}$$

Two notable regimes are when $g_1 = g_2 = 0$ ($R_{c,1} = R_{c,2} = L$), known as a confocal cavity, for which the restoration of displaced beams is maximised, and $g_1 = g_2 = -1$ ($R_{c,1} = R_{c,2} = L/2$), known as a concentric cavity, which produces a diffraction limited beam waist at the cavity centre.

2.1.2 STIRAP – Controlling the Photon

We now extend the two-level Jaynes-Cummings model to a three level Λ-type atom, by introducing a second ground state, $|e\rangle$, with transition frequency ω_{xe} to the excited state (Figure 2.4). If the cavity mode still couples the previous $|g\rangle \leftrightarrow |x\rangle$ transition, and a laser field with Rabi frequency Ω is introduced on the $|e\rangle \leftrightarrow |x\rangle$ transition then the interaction Hamiltonian is

$$\widehat{H}_{\text{int}} = \hbar \left(\Delta_L |e\rangle\langle e| + \Delta_c |g\rangle\langle g| - \frac{\Omega}{2} \left(|x\rangle\langle e| + |e\rangle\langle x| \right) - g_0 \left(|x\rangle\langle g| \hat{a} + \hat{a}^\dagger |g\rangle\langle x| \right) \right), \tag{2.40}$$

where Δ_L is the detuning $\omega_{xe} - \omega_L$, $\Delta_c = \omega_{xg} - \omega_c$ and we have assumed that our atom is coupled to an antinode of the cavity, $g = g_0$. For a Raman-

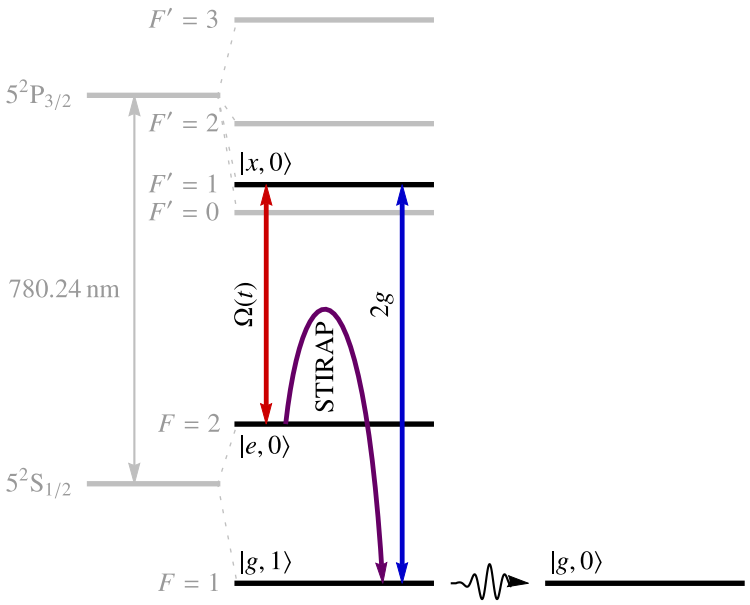


Figure 2.4: STIRAP level diagram: The levels in the hyperfine structure of the ^{87}Rb D_2 used in the STIRAP photon generation process. The time dependent Rabi driving pulse $\Omega(t)$ and the cavity vacuum mode $2g$ each couple a ground state to the same excited state, thus driving a coherent Raman process.

resonant interaction $\Delta_L = \Delta_c$ and the eigenfrequencies of the system are given by

$$\begin{aligned} \omega_n^0 &= \omega_c \left(n + \frac{1}{2}\right) \\ \omega_n^\pm &= \omega_c \left(n + \frac{1}{2}\right) + \frac{1}{2}\left(\Delta \pm \sqrt{4ng_0^2 + \Omega^2 + \Delta^2}\right) \end{aligned} \tag{2.41}$$

where n is once again the excitation number of the cavity mode. The previous Jaynes-Cummings ladder of doublets is now replaced by a ladder of triplets with the eigenstates given by

$$\begin{aligned} |\phi_n^0\rangle &= \cos\Theta|e, n-1\rangle - \sin\Theta|g, n\rangle \\ |\phi_n^+\rangle &= \cos\Phi\sin\Theta|e, n-1\rangle - \sin\Phi|x, n-1\rangle + \cos\Phi\cos\Theta|g, n\rangle \\ |\phi_n^-\rangle &= \sin\Phi\sin\Theta|e, n-1\rangle + \cos\Phi|x, n-1\rangle + \sin\Phi\cos\Theta|g, n\rangle \end{aligned} \tag{2.42}$$

where the mixing angles Θ and Φ are given by

$$\tan\Theta = \frac{\Omega}{2g_0\sqrt{n}}, \qquad \tan\Phi = \frac{\sqrt{4ng_0^2+\Omega^2}}{\sqrt{4ng_0^2+\Omega^2+\Delta^2}-\Delta}\,. \tag{2.43}$$

This system of energy levels exhibits several important properties. Firstly we note that the state $|\phi_n^0\rangle$ contains no component of the excited atomic state $|x, n-1\rangle$ and is therefore a 'dark state', impervious to spontaneous emission. With no driving laser, $\Omega = 0$, the eigenstates $|\phi_n^\pm\rangle$ collapse to the original Jaynes-Cummings doublets (Equation (2.30)), and the dark $|\phi_n^0\rangle$ state reduces to the $|e, n-1\rangle$ state. Non-zero Rabi frequency Ω leaves $|\phi_n^0\rangle$ in a mixture of $|e, n-1\rangle$ and $|g, n\rangle$ which reaches pure $|g, n\rangle$ in limit $\Omega \gg 2g_0\sqrt{n}$. In summary:

$$\begin{aligned}
&\Omega = 0 && |\phi_n^0\rangle = |e, n-1\rangle \\
&\Omega > 0 && |\phi_n^0\rangle = \cos\Theta|e, n-1\rangle - \sin\Theta|g, n\rangle \\
&\Omega \gg 2g_0\sqrt{n} && |\phi_n^0\rangle \approx |g, n\rangle\,.
\end{aligned}$$

Therefore we might expect that with some judicious application of a time dependent Rabi frequency the state of the atom will be transferred from one ground state $|e, n-1\rangle$, to the other $|g, n\rangle$, thus generating a single photon, without populating the atomic excited state $|x, n-1\rangle$. This process, known as stimulated Raman adiabatic passage (STIRAP)[4], must be performed adiabatically, which demands that the eigenstates change slowly with respect to the eigenfrequency difference [76, 91, 92].

We can find the required form of the time-dependent Rabi frequency by starting with the Schrödinger equation describing the atom-photon system.

[4] Also referred to as V-STIRAP when one of the two arms of the Raman process is fulfilled by a vacuum mode, as is the case here.

We consider just the $n = 1$ triplet of states $\{|e,0\rangle, |x,0\rangle, |g,1\rangle\}$ and their corresponding probability amplitudes $[c_e(t), c_x(t), c_g(t)]^T = \boldsymbol{c}(t)$. We must include the two known loss mechanisms, namely atomic polarisation decay at rate γ and cavity decay at κ, which results in the non-Hermitian Hamiltonian

$$\widehat{H}'_{\text{int}} = \widehat{H}_{\text{int}} - \mathrm{i}\hbar\kappa\hat{a}^\dagger\hat{a} - \mathrm{i}\hbar\gamma|x\rangle\langle x| \tag{2.44}$$

where $\widehat{H}_{\text{int}}$ is given by Equation (2.40). Thus the Schrödinger equation

$$\mathrm{i}\hbar\frac{\mathrm{d}}{\mathrm{d}t}\boldsymbol{c}(t) = \widehat{H}'_{\text{int}}\boldsymbol{c}(t) \tag{2.45}$$

can be expanded as

$$\mathrm{i}\hbar\frac{\mathrm{d}}{\mathrm{d}t}\boldsymbol{c}(t) = -\frac{\hbar}{2}\begin{pmatrix} 0 & \Omega(t) & 0 \\ \Omega(t) & 2\mathrm{i}\gamma & 2g \\ 0 & 2g & 2\mathrm{i}\kappa \end{pmatrix}\boldsymbol{c}(t). \tag{2.46}$$

which yields the set of coupled equations:

$$\mathrm{i}\dot{c_e}(t) = \frac{1}{2}\Omega(t)c_x(t) \tag{2.47}$$

$$\mathrm{i}\dot{c_x}(t) = \frac{1}{2}\Omega(t)c_e(t) + \mathrm{i}\gamma c_x(t) + gc_g(t) \tag{2.48}$$

$$\mathrm{i}\dot{c_g}(t) = gc_x(t) + \mathrm{i}\kappa c_g(t)\,. \tag{2.49}$$

We are no longer assuming that the atom is coupled to a cavity antinode. Although we know the coupling g varies as a function of position within the cavity, the atom can be considered stationary on the timescales of interest and therefore g is not a function of time. Rearranging Equation (2.47) gives

an expression for the Rabi frequency

$$\Omega(t) = -2\mathrm{i}\frac{\dot{c_e}(t)}{c_x(t)} \tag{2.50}$$

and Equation (2.49) gives

$$c_x(t) = -\frac{\mathrm{i}}{g}\left(\dot{c_g}(t) + \kappa c_g(t)\right) . \tag{2.51}$$

Due to the non-zero cavity decay rate κ, the state $|g,1\rangle$ will decay to $|g,0\rangle$ as the photon leaks out of the cavity. The timescale for this, κ^{-1}, is much shorter than the photon temporal length and therefore $|g,0\rangle$ and hence also the field amplitude of the generated photon ψ_{ph} will exactly follow the probability amplitude of the state $|g,1\rangle$. Therefore

$$c_g(t) = \sqrt{\frac{\eta}{2\kappa}}\psi_0(t) \tag{2.52}$$

where $\psi_0(t) = \psi_{\mathrm{ph}}/\sqrt{\eta}$ is the normalised photon wavefunction and η denotes the total probability for a single-photon generation within the cavity. This emission efficiency η is limited by the η_{cav} introduced in Equation (2.36). However for a finite length photon the ground state population of the atom, $c_e(t)$, will at some time be fully depleted by the driving Rabi pulse, $\Omega(t)$, calculated for some $\eta = \eta_{\mathrm{max}} < \eta_{\mathrm{cav}}$, thus imposing a lower maximum generation efficiency. The value of η_{max} for a given photon shape can be calculated by finding the minima of the population $c_e(t)$ and solving for the value of η which sets any one of the minima to zero. For the sinusoidal photons used throughout this thesis the difference between η_{max} and η_{cav} is less than 1% and can be neglected.

We now have relations to reduce to denominator of our expression for $\Omega(t)$

(Equation (2.50)) to expressions just involving our desired photon shape, $\psi_0(t)$, but not yet the numerator. We can use the continuity of the system to obtain another expression relating the amplitudes of the states. The population in the system must always equal unity, provided we account for that lost by our decay processes. The populations of the states are given by $c_i c_i^*$, therefore we have

$$|c_e(t)|^2 = 1 - |c_x(t)|^2 - |c_g(t)|^2 - \int_0^t \mathrm{d}t \left(2\gamma|c_x(t)|^2 + 2\kappa|c_g(t)|^2\right) . \quad (2.53)$$

Due to the lack of any detunings in the Hamiltonian, if we assume ψ_{ph} is real, one can verify that $c_x(t)$ is purely imaginary, whilst $c_e(t)$ and $c_g(t)$ are both real. Substituting back into Equation (2.50) yields the desired analytical expression for the Rabi frequency:

$$\Omega(t) = \frac{2\left(\mathrm{i}\dot{c_x}(t) + \mathrm{i}\gamma c_x(t) - g c_g(t)\right)}{\sqrt{1 - |c_x(t)|^2 - |c_g(t)|^2 - \int_0^t \mathrm{d}t \left(2\gamma|c_x(t)|^2 + 2\kappa|c_g(t)|^2\right)}} , \quad (2.54)$$

with $c_x(t)$ and $c_g(t)$ both functions of only $\psi_0(t)$ as given by Equations (2.51) and (2.52) above.

Figure 2.5 shows some plots of the shape of the Rabi pulse required to generate a photon of desired shape. There are two points of interest here. The first is that stronger driving is required to counterbalance the depletion of atom-cavity system towards the end of the pulse. The second is that stronger driving overall is required to generate a photon with greater efficiency, and that if one attempts to calculate a pulse shape for an efficiency greater than the limit given by Equation (2.36)), the resulting shape is divergent [93].

This section has outlined the theory behind the interaction of an atom with an optical cavity. We have shown there exists dark eigenstates of the

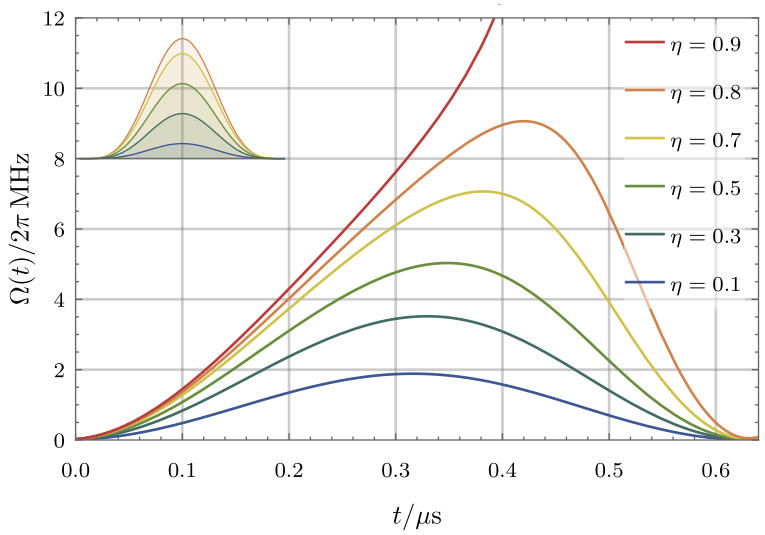


Figure 2.5: STIRAP pulse shapes: The traces shows the required Rabi frequencies $\Omega(t)$ to generate symmetric photons with a $\sin^2$ amplitude envelope. The pulses generated for increasing efficiency η produce photons more efficiently — increased area under the photon in the inset. However if η exceeds $\eta_{\max} \approx \eta_{\text{cav}} = 2C/(2C+1)$ the required pulse is divergent; for the above $\{g, \kappa, \gamma\} = 2\pi\,\{15, 12, 3\}$ which give $\eta_{\text{cav}} = 0.86$.

atom-cavity system, which facilitate adiabatic transfer of the atomic population between ground states, coherently generating single photons. Furthermore we have derived an analytical expression for the Rabi driving pulse required to generate a photon of desired temporal envelope. The experimental details of the implementation of these methods are presented later in this chapter in Section 2.3. The toy atoms we have considered have been idealised, comprising only two or three energy levels. In reality atoms often have many different states of similar energy contributing to transitions. For the the D_2 line in ^{87}Rb it has been shown the effects of the other levels is negligible [94].

2.2 Hong-Ou-Mandel Interference

The quantum interference of two indistinguishable photons is an essential ingredient in many quantum devices and protocols. If we consider two photons entering separate input ports of a 50:50 beam splitter there are four possible outcomes as illustrated in Figure 2.6. Of these four possibilities only the middle two are observed for identical photons, that is they always leave via the same random output port as each other. The effect was first observed by Hong, Ou, and Mandel in 1987 with photons from a SPDC source and the effect now commonly bears their name, the HOM-effect [95]. The phenomenon is often used to demonstrate, and indeed quantify, the indistinguishability of photons from a source [96]. It is also able to reveal further details about the properties of the photons such as their relative frequency or phase. To that end the HOM-effect is used extensively in the work presented in this thesis and therefore time is given to the theory here.

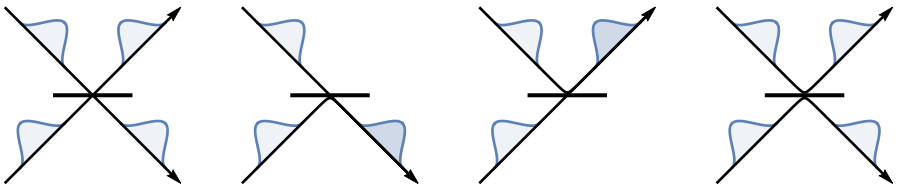


Figure 2.6: Outcomes for a 50:50 beam splitter: When two photons meet at a 50:50 beam splitter, there are four different possible outcomes, arising from the combinations of each photon either being transmitted or reflected at the interface. If the photons are distinguishable each outcome is equally likely. However for identical photons only the middle two outcomes are observed. This is known as the Hong-Ou-Mandel effect.

To understand the origin of the phenomenon we must consider a quantum mechanical formulation of the beam splitter. We can assign to each port of the beam splitter creation operators, $\hat{a}_k^\dagger$, for a single photon in that mode, Figure 2.7 details the labelling of the modes. The output operators

can be expressed in terms of the input operators by the following unitary transformations:

$$\hat{a}_A^\dagger = \frac{1}{\sqrt{2}}(\hat{a}_C^\dagger + \hat{a}_D^\dagger) \qquad \hat{a}_C^\dagger = \frac{1}{\sqrt{2}}(\hat{a}_A^\dagger + \hat{a}_B^\dagger)$$
$$\hat{a}_B^\dagger = \frac{1}{\sqrt{2}}(\hat{a}_C^\dagger - \hat{a}_D^\dagger) \qquad \hat{a}_D^\dagger = \frac{1}{\sqrt{2}}(\hat{a}_A^\dagger - \hat{a}_B^\dagger)\,.$$

These can be more compactly written as

$$\begin{pmatrix} \hat{a}_A^\dagger \\ \hat{a}_B^\dagger \end{pmatrix} = \frac{1}{\sqrt{2}} \begin{pmatrix} 1 & 1 \\ 1 & -1 \end{pmatrix} \begin{pmatrix} \hat{a}_C^\dagger \\ \hat{a}_D^\dagger \end{pmatrix} . \tag{2.55}$$

The origin of these relations is discussed in more detail when describing the transformations for directional couplers in Section 4.2.

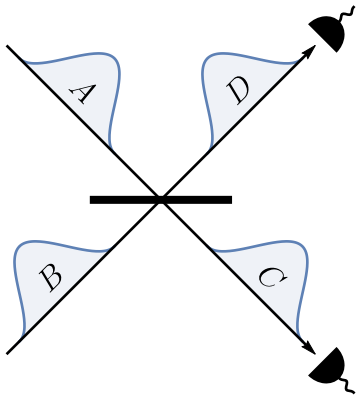


Figure 2.7: Two photon interference: Photons arriving in input port A or B will leave via one of the output ports C or D.

Two photons simultaneously incident on the beam splitter can therefore be described in the Fock-state picture by applying the corresponding operators to the vacuum state $|1_A 1_B\rangle = \hat{a}_A^\dagger \hat{a}_B^\dagger |0\rangle$. Using the relations in

Equation (2.55) we can expand this:

$$\begin{aligned}\hat{a}_A^\dagger \hat{a}_B^\dagger |0\rangle &= \frac{1}{2}\left(\hat{a}_C^\dagger + \hat{a}_D^\dagger\right)\left(\hat{a}_C^\dagger - \hat{a}_D^\dagger\right)|0\rangle \\ &= \frac{1}{2}\left(\hat{a}_C^\dagger \hat{a}_C^\dagger - \hat{a}_C^\dagger \hat{a}_D^\dagger + \hat{a}_D^\dagger \hat{a}_C^\dagger - \hat{a}_D^\dagger \hat{a}_D^\dagger\right)|0\rangle \\ &= \frac{1}{2}\left(\hat{a}_C^\dagger \hat{a}_C^\dagger - \hat{a}_D^\dagger \hat{a}_D^\dagger\right)|0\rangle \\ &= \frac{1}{2}\left(|2_C 0_D\rangle - |0_C 2_D\rangle\right)\end{aligned} \tag{2.56}$$

where we have made use of the fact that orthogonal modes commute and therefore $\hat{a}_C^\dagger \hat{a}_D^\dagger = \hat{a}_D^\dagger \hat{a}_C^\dagger$. Thus the photons bunch and with equal probability will leave via either output port C or D together. Number resolving detectors are not commonplace, therefore when experimentally studying HOM interference one does not aim to detect directly the two photon Fock states $|2_C 0_D\rangle$ or $|0_C 2_D\rangle$. Instead one infers the bunching by the absence of the correlated detections of one photon on each detector at outputs C and D that would occur if the term $|1_C 1_D\rangle$ was still present.

Photons are not point particles, they have some finite spatio-temporal extent as alluded to in the figures so far. If the temporal overlap of these wavefunctions at the beam splitter is not perfect then there is a finite probability that they will not interact and a coincident detection will occur. Furthermore, even when perfectly overlapped, if there is some other distinguishability between the photons, for example they have different polarisations or frequencies, there is a chance they may not interact. This indistinguishability is probed by delaying the arrival of one of the two photons with respect to the other and monitoring the coincidence rate as a function of this delay. When perfectly overlapped the coincidence rate will reach a minimum, which will only be zero if the two photons are completely indistinguishable; such a reduction is known as a HOM dip, shown in Figure 2.8.

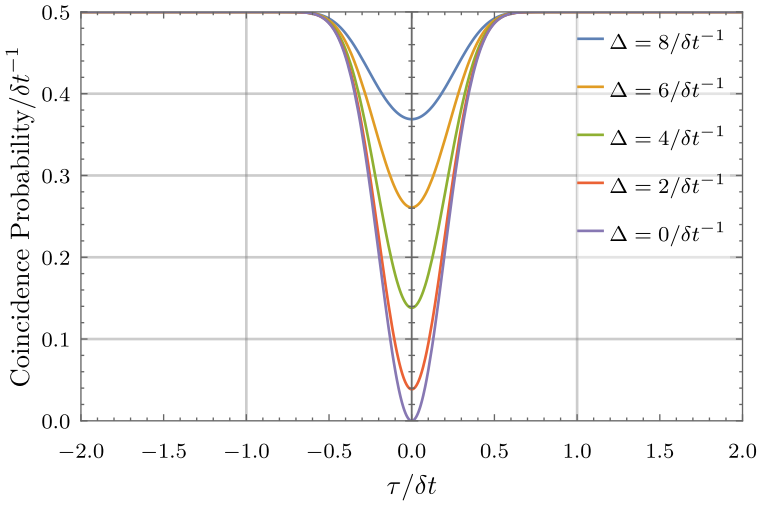


Figure 2.8: Hom dip: When pairs of photons are incident on a beam splitter, with the arrival time of one of the photons varied, the number of correlation between detectors at the output ports is seen to vary as a function of the arrival time delay. A minima in the correlation probability is observed when the two photons are exactly coincident, the value of which details the indistinguishability of the photons. The behaviour is shown for photons with frequency difference, Δ in normalised units of the inverse of the photon length.

So far we have assumed that the photons under consideration are shorter than the time resolution of the detectors, and that therefore if the two photons do not interfere, and leave via separate output ports, the two detectors fire simultaneously, as best we can determine. This is indeed true for many photon sources. For example SPDC photons are typically up to 500 fs long, whilst the timing resolution for SPCMs is typically around 300 ps. However the photons used in the following chapters are up to and in some cases more than 500 ns long. It is therefore possible for two perfectly temporally overlapped photons to lead to two detections, discernibly separated in time.

2.2.1 Time-Resolved HOM

To investigate what might be observed with such 'long' photons we must provide a description of the single photon wavepackets in the space-time domain.

We note that the above analysis placed no restrictions on the creation operators and we are therefore free to define them in such a way that they create photons in our new modes. The following presentation closely follows that developed in [76, 97]. We now describe our modes by the one-dimensional spatio-temporal mode function

$$\zeta_k(t) = \epsilon_k(t)\mathrm{e}^{-\mathrm{i}\phi_k(t)} \tag{2.57}$$

where k labels the mode, $\phi_k(t)$ details the phase evolution, and $\epsilon_k(t)$ is the amplitude envelope, assumed to be normalised such that $\int \mathrm{d}t|\epsilon_k(t)|^2 = 1$. If we assume that the Hilbert space is spanned by an orthonormal set of modes $\zeta_k(t)$, then the electric field operators are

$$\hat{E}^+(t) = \sum_k \zeta_k(t)\hat{a}_k \qquad \text{and} \qquad \hat{E}^-(t) = \sum_k \zeta_k^*(t)\hat{a}_k^\dagger\,. \tag{2.58}$$

We can see that provided a photon is present in mode i, the probability to measure it at time t is

$$P_i(t) = \langle 1_i|\hat{E}^-(t)\hat{E}^+(t)|1_i\rangle = \zeta_i^*(t)\zeta_i(t)\langle 1_i|\hat{a}_i^\dagger\hat{a}_i|1_i\rangle = |\epsilon_i(t)|^2\,, \tag{2.59}$$

which is solely defined by the amplitude envelope of the photon as we would expect.

The beam splitter provides entirely analogous transformations for these field operators as for the original creation operators given in Equation (2.55). We hope to acquire an intuitive understanding of these phenomena by taking a stepwise approach, considering the detection of one photon, followed by the detection of the second photon conditioned upon the first. Let us therefore consider the probability to make the first detection in output port C at time

t_0, given our standard input $|1_A 1_B\rangle$. The probability is

$$\begin{aligned} P_C^{(1)}(t_0) &= \langle 1_A 1_B | \hat{E}_C^-(t_0) \hat{E}_C^+(t_0) | 1_A 1_B \rangle \\ &= \frac{1}{2} \langle 1_A 1_B | (\hat{E}_A^-(t_0) + \hat{E}_B^-(t_0))(\hat{E}_A^+(t_0) + \hat{E}_B^+(t_0)) | 1_A 1_B \rangle \\ &= \frac{1}{2} \left(|\epsilon_A(t)|^2 + |\epsilon_B(t)|^2 \right) . \end{aligned} \tag{2.60}$$

Repeating the analysis one will find the exact same expression for $P_D^{(1)}(t_0)$. After this detection in port C, D the remaining state is given by

$$\begin{aligned} \hat{E}_{C,D}^+(t_0)|1_A 1_B\rangle = \; & \zeta_A(t_0)|0_A 1_B\rangle \pm \zeta_B(t_0)|1_A 0_B\rangle \\ & \xrightarrow{\text{norm}} \frac{\zeta_A(t_0)|0_A 1_B\rangle \pm \zeta_B(t_0)|1_A 0_B\rangle}{\sqrt{|\epsilon_A(t)|^2 + |\epsilon_B(t)|^2}} = |\Psi_{\text{cond } C,D}\rangle . \end{aligned} \tag{2.61}$$

From this we can see interference; the amplitudes of states $|0_A 1_B\rangle$ and $|1_A 0_B\rangle$ evolve according to the phases in $\zeta_A(t)$ and $\zeta_B(t)$. The probability of detecting the second photon at time $t_0 + \tau$ in output D, given the first detection in output C is

$$\begin{aligned} P_{D|C}^{(2)}(t_0 + \tau) &= \langle \Psi_{\text{cond } C} | \hat{E}_D^-(t_0 + \tau) \hat{E}_D^+(t_0 + \tau) | \Psi_{\text{cond } C} \rangle \\ &= \frac{|\zeta_A(t_0 + \tau)\zeta_B(t_0) - \zeta_B(t_0 + \tau)\zeta_A(t_0)|^2}{2(|\epsilon_A(t)|^2 + |\epsilon_B(t)|^2)} . \end{aligned} \tag{2.62}$$

Again, the same result is obtained for $P_{C|D}^{(2)}(t_0 + \tau)$. Therefore the joint probability for the two detections is given by

$$\begin{aligned} P_{\text{joint}}(t_0, \tau) &= P_C^{(1)}(t_0) P_{D|C}^{(2)}(t_0 + \tau) = P_D^{(1)}(t_0) P_{C|D}^{(2)}(t_0 + \tau) \\ &= \frac{1}{4} |\zeta_A(t_0 + \tau)\zeta_B(t_0) - \zeta_B(t_0 + \tau)\zeta_A(t_0)|^2 . \end{aligned} \tag{2.63}$$

This result illustrates several important things. Firstly we can see that

no matter how different the mode functions of the two incoming photons, the joint probability is zero for $\tau = 0$. Also, for all time differences τ, $P_{\text{joint}}(t_0, \tau) = 0$ if the two photons are identical, $\zeta_A = \zeta_B$. For completeness, note that the probability for two detections on the same detector is given by the same equation but with a sign change. The majority of the time one is not actually interested in the exact timings of the two detections but merely the time difference between them, τ, we therefore integrate over t_0 to obtain

$$P_{\text{joint}}(\tau) = \int_{-\infty}^{\infty} P_{\text{joint}}(t_0, \tau) \mathrm{d}t_0 \,. \tag{2.64}$$

With careful construction of $\zeta_k(t)$, most if not all, facets of two photon interference can be analysed with the above. A simple method to incorporate the effect of polarisation is found by noting that Equation (2.63) can be expanded out as the sum of two terms:

$$P_{\text{joint}}(t_0, \tau) \equiv G^{(2)}_{\text{HH}}(t_0, t_0 + \tau) = G^{(2)}_{\text{HV}}(t_0, t_0 + \tau) - F(t_0, t_0 + \tau) \,, \tag{2.65}$$

where $G^{(2)}_{\text{HH}}$ ($G^{(2)}_{\text{HV}}$) is the correlation function for parallel (perpendicular) polarised photons, and F describes the interference between parallel polarised photons, governed by their relative phase. $G^{(2)}_{\text{HV}}(t_0, t_0 + \tau)$ and $F(t_0, t_0 + \tau)$ are given by

$$G^{(2)}_{\text{HV}}(t_0, t_0 + \tau) = \frac{1}{4}(|\epsilon_A(t_0)\epsilon_B(t_0 + \tau)|^2 + |\epsilon_A(t_0 + \tau)\epsilon_B(t)|^2) \tag{2.66}$$

$$F(t_0, t_0 + \tau) = \frac{1}{2}\epsilon_A(t_0)\epsilon_B(t_0 + \tau)\epsilon_A(t_0 + \tau)\epsilon_B(t_0)\times \cos(\phi_A(t_0) - \phi_A(t_0 + \tau) + \phi_B(t_0 + \tau) - \phi_B(t_0)) \,. \tag{2.67}$$

It is straightforward to see that the expected correlation function for the perpendicular case, $G^{(2)}_{\text{HV}}(\tau)$, is simply the convolution of the two intensity

envelopes:

$$\begin{aligned}\int_{-\infty}^{\infty} G^{(2)}_{\mathrm{HV}}(t_0, t_0+\tau)\mathrm{d}t_0 &= \frac{1}{4}\left(\int_{-\infty}^{\infty} |\epsilon_A(t_0)|^2 |\epsilon_B(t_0+\tau)|^2 \mathrm{d}t_0 + \right. \\ &\qquad \left. \int_{-\infty}^{\infty} |\epsilon_A(t_0+\tau)|^2 |\epsilon_B(t)|^2 \mathrm{d}t_0 \right) \\ &= \frac{1}{2}\left(|\epsilon_A|^2 * |\epsilon_B|^2\right)(\tau)\,. \end{aligned} \tag{2.68}$$

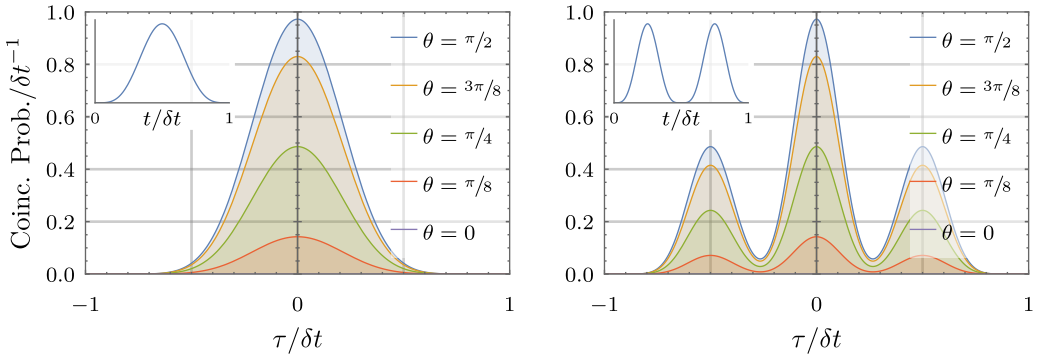
For two photons of arbitrary polarisation with a relative angle θ the correlation function is therefore given by

$$G^{(2)}_{\psi}(t_0, t_0+\tau) = G^{(2)}_{\mathrm{HV}}(t_0, t_0+\tau) - \sin^2(\theta) F(t_0, t_0+\tau)\,. \tag{2.69}$$

This is plotted for photons with an amplitude envelope $\epsilon(t) \propto \sin^2(t)$ in Figure 2.9. One can see that if the polarisations are not perfectly parallel then correlations are introduced at all time differences, proportional to the autocorrelation convolution envelope limit. This increase in area is analogous to the reduction in HOM dip observed in Figure 2.8; the area is in fact equal to the value of the HOM dip at $\delta\tau = 0$.

Decoherence

Unfortunately the photons emitted from our atom-cavity source will not always have exactly the desired frequency or emission time characteristics. Variations in the value of g_{eff} experienced by the atom, laser noise, uncontrolled magnetic perturbations to the atomic energy levels, and jitter in the timing of the driving pulse will all contribute to an uncontrollable random variation in the frequency and timing of the emitted photons. This will introduce some distinguishability between the photons which will impact the



(a) Single Hump **(b)** Double Hump

Figure 2.9: Time-resolved correlations as a function of polarisation: The expected time-resolved dependence of the number of correlations on detection time difference is shown for both single hump (a) and double hump (b) photons with a $\sin^2$ intensity envelope as shown inset. No correlations are observed at any time difference for perfectly identical photons, with parallel polarisation, $\theta = 0$. As their indistinguishability is reduced by increasing the angle θ between their polarisation vectors the number of correlations increases to a maximum for perpendicularly polarised photons, $\theta = \pi/2$.

HOM interference. We can probe the effect of this by considering two photons with frequency difference $\Delta = \omega_B - \omega_A$, emitted with a time difference $\delta\tau$. The corresponding mode functions for such photons with $\epsilon(t) \propto \sin^2(t)$ are

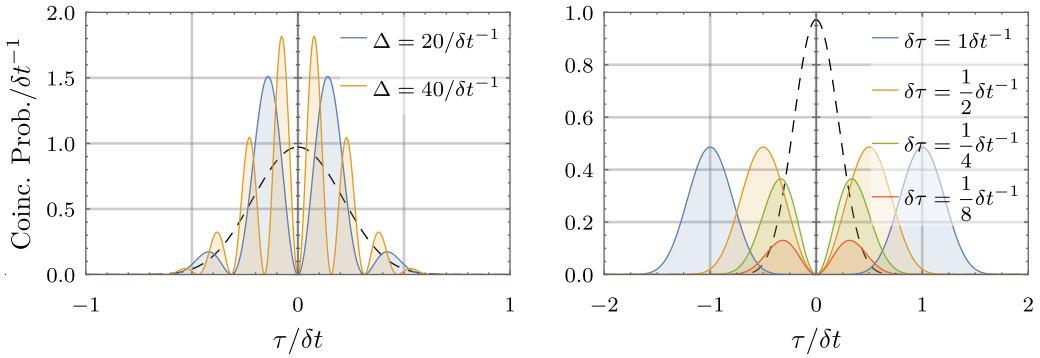
$$\begin{aligned} \zeta_A(t) &= \sqrt{\frac{8}{3}} \sin^2\left(\pi\left(t - \frac{\delta t}{2}\right)\right) \mathrm{e}^{-\mathrm{i}t\left(\omega - \frac{\Delta}{2}\right)} \\ \zeta_B(t) &= \sqrt{\frac{8}{3}} \sin^2\left(\pi\left(t + \frac{\delta t}{2}\right)\right) \mathrm{e}^{-\mathrm{i}t\left(\omega + \frac{\Delta}{2}\right)}, \end{aligned} \tag{2.70}$$

defined on the interval $0 < t \pm \frac{\delta t}{2} < 1$ for $\zeta_{A,B}$, with $\omega = \frac{1}{2}(\omega_A + \omega_B)$. For simplicity all times are in units of δt and all frequencies in units of $1/\delta t$, where δt is the photon temporal length. Constructing $P_{\text{joint}}(t_0, \tau)$ according to Equation (2.63) and integrating over t_0 produces an equation for $P'_{\text{joint}}(\tau, \delta\tau, \Delta)$, detailing the correlation function as a function of detection time difference, emission time difference and frequency difference. For two photons with a

well defined frequency difference Δ, the relative phase between them will increase linearly as a function of the time after the first detection — the corollary of this is that the relative phase is always zero at $\tau = 0$, this is an important point. It is little surprise therefore that

$$P'_{\text{joint}}(\tau, 0, \Delta) = (1 - \cos(\Delta\tau))G^{(2)}_{\text{HV}}(\tau)\,. \tag{2.71}$$

This is plotted in Figure 2.10 along with the complementary $P'_{\text{joint}}(\tau, \delta\tau, 0)$, where imperfect overlap between the photons leads to an increase in correlations.



(a) Different frequency **(b)** Different time

Figure 2.10: Time-resolved correlations as a function of frequency and time difference: Two photons with a frequency difference Δ show a quantum-beat signal in their interference pattern (a). This both enhances and suppresses the correlation probability at different detection time differences; the reference profile for non-interfering photons is shown dashed. The interference of photons with different emission times is merely a product of their overlap (b).

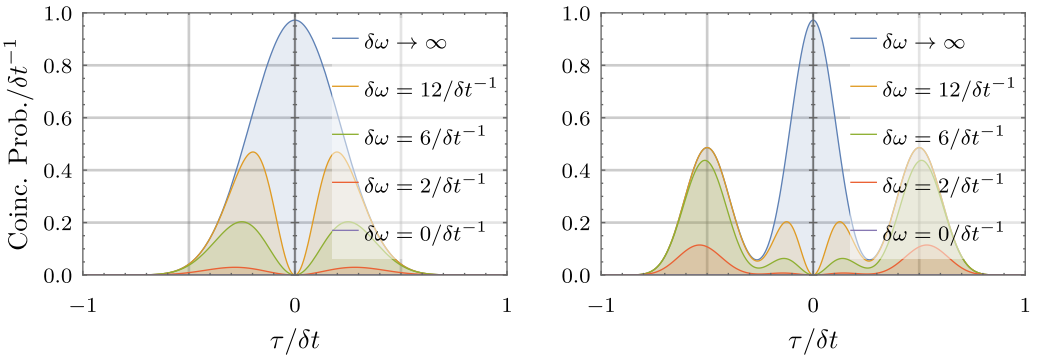
We can now examine the effect of a random variation in the emission frequency by assuming a Gaussian distribution of frequencies with bandwidth $\delta\omega$,

$$f_{\delta\omega}(\Delta) = \frac{1}{\delta\omega\sqrt{\pi}} \mathrm{e}^{-\left(\frac{\Delta}{\delta\omega}\right)^2}\,, \tag{2.72}$$

and integrating to obtain

$$P_{\text{inh}}(\tau, \delta\omega) = \int_{-\infty}^{\infty} f_{\delta\omega}(\Delta) P'_{\text{joint}}(\tau, 0, \Delta) \mathrm{d}\Delta$$
$$= \left(1 - \mathrm{e}^{-\frac{1}{4}\delta\omega^2\tau^2}\right) G^{(2)}_{\text{HV}}(\tau)\,, \tag{2.73}$$

which is plotted for both single and double hump photons in Figure 2.11. It should now not be surprising to see the correlation function drop to zero



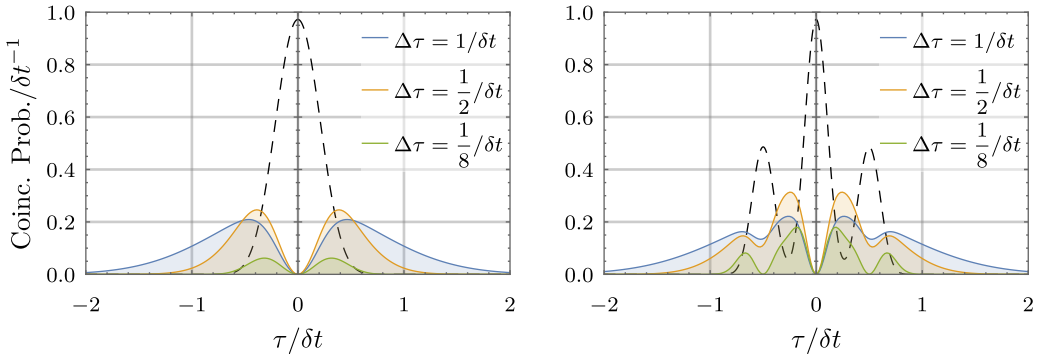
(a) Single Hump **(b)** Double Hump

Figure 2.11: Effect of frequency jitter on time-resolved correlations: If two photons frequencies differ by a random and changing amount, then the probability of observing a correlation increases towards later detection time differences (notwithstanding the photons convolution envelope). $\delta\omega$ parameterises the width of the distribution of frequency differences.

at $\tau = 0$ as we know the relative phase is not defined until the first detection. The effect of the jitter in the frequency is therefore to increase the distinguishability of the photons the further apart in time they are detected, known as decoherence. The different manifestations of decoherence (Figure 2.11) and imperfect polarisation (Figure 2.9) in the HOM usefully allow one to determine from an experimentally measured HOM, to what extent each source of imperfection is present.

A similar analysis can be carried out with a Gaussian distribution of emission times. The predominant effect is the introduction of correlations

outside of the envelope prescribed by $G^{(2)}_{\mathrm{HV}}(\tau)$; experimentally such contributions to the HOM are not observed, thereby suggesting emission time jitter is negligable compared to other sources of decoherence.



(a) Single Hump **(b)** Double Hump

Figure 2.12: Effect of emission time jitter on time-resolved correlations: The distribution of correlations for pairs of photons emitted with a random time difference, where $\Delta\tau$ parameterises the width of the distribution of emission time difference. Again no correlations are observed at zero detection time difference.

2.3 Experimental Setup

The heart of the experimental apparatus is simply a single atom sitting between two mirrors. With this we are able to generate a menagerie of photons with different properties and perform high fidelity quantum logic and feedback. Our cavity is formed of two carefully positioned highly reflective dielectric mirrors and we place individual cold ^{87}Rb atoms within. A significant experimental setup is required to achieve this ultimately simple goal. Initial construction of the source was carried out by Peter Nisbet-Jones and Jerome Dilley, whose theses provide detailed discussions of the apparatus [94, 98].

This section presents a shorter overview of this achievement, starting with the construction and stabilisation of the cavity (Section 2.3.1) followed by the cooling and loading of the atoms (Section 2.3.2). A broader look at the setup of the laser system is presented in Section 2.3.3, and the control and careful timing of the "Photon Pistol" as a whole is presented in Section 2.3.4.

2.3.1 Cavity

Cavity design is a nuanced topic as a cavity is described by a number of properties dependent on many parameters. There is a key requirement that our atom-photon interactions must take place in the strong-coupling regime ($g_0 \gg \{\kappa, \gamma\}$) if the evolution of the system is to remain coherent. This demands mirrors of the highest possible reflectivity. However in practice, one of the two mirrors must have a significantly larger transmission than the other if the photon is to be extracted from the cavity into a known mode. Details of the characterisation of the cavity can be found in [94]. Improved cavity designs, yielding potentially a three-fold increase in co-operativity and above 90% overall efficiency are discussed in Chapter 7.

The mirrors, manufactured by Research-Electro-Optics Inc in Boulder, Colorado, are made from a BK7 glass substrate with one face polished to a spherically concave surface with a 5 cm radius of curvature and a surface roughness of $\lambda/20$. The front surfaces are coated with a reflective dielectric layer, giving transmissions of 2 ppm and 40 ppm for the two mirrors, and the flat rear surface of the out-coupling mirror has an anti-reflection coating. From an original diameter of 7.75 mm the front faces were coned down to 1 mm by Hellma Optics GmbH which allows a shorter cavity length and also reduces the scattering of the nearby MOT beams. The mirrors are held

in ceramic mounts (MACOR) which in turn are glued to shear piezos thus providing means to scan and stabilise the cavity. One of the piezos developed an electrical short during the vacuum system bakeout, however the remaining actuator can still provide a stable lock in isolation. The key parameters of the cavity, reproduced from [94], are listed in Table 2.1. The cavity finesse, $\mathcal{F}$, was measured to be significantly higher, around 160 000, during cavity alignment before being inserted into the vacuum chamber. It is thought that during activation of the rubidium source the coating of the mirrors was damaged increasing their losses from 2 ppm to 18 ppm.

Name	Symbol	Value	Unit
Cavity Length	L	74	μm
Radius of Curvature	R_c	5	cm
Mirror Diameter	$\varnothing$	1	mm
Mode Waist	w_0	18.4	μm
Mode size at mirror	w	18.4	μm
Mode Volume	V_{eff}	2×10^4	μm^3
Linewidth	$\Delta\omega_{\text{FWHM}}$	23.7	$2\pi\cdot$MHz
Free Spectral Range	$\Delta\omega_{\text{FSR}}$	2.0	$2\pi\cdot$THz
TEM Splitting	$\Delta\omega_{\text{trans}}$	35	$2\pi\cdot$GHz
Finesse	$\mathcal{F}$	85 000	-
Atom-Cavity Coupling	g_0	15	$2\pi\cdot$MHz
Cavity Decay	κ	12	$2\pi\cdot$MHz
Atomic Decay	γ	3	$2\pi\cdot$MHz
Co-operativity	C	3	-
Photon Generation Efficiency	η_{cav}	0.86	-
Photon Extraction Efficiency	η_{extract}	0.52	-

Table 2.1: Properties of the high-finesse cavity: Reproduced mostly unchanged from [94]. Where necessary, values for the properties of ^{87}Rb were obtained from [99].

The cavity linewidth given in Table 2.1 corresponds to a shift in the cavity length of only 4.5 pm, and to ensure the cavity and STIRAP laser are always Raman-resonant we would like length variations to be a small fraction of this. Stability to within 100 fm is achieved with active locking. The PDH technique

[100, 101] is used to generate, from the intensity of the light back reflected from the cavity, an error signal proportional to the deviation of the cavity from the desired resonance; a PID controller then moderates the correcting feedback. The resonance frequency is prescribed by the central frequency of the locking laser which also contains 20 MHz sidebands, against which the carrier frequency is beaten after reflection from the cavity. These sidebands are also used for locking the laser to an atomic reference. A symmetric, lossless Fabry-Pérot cavity will induce a π phase shift in the reflected beam, the extreme asymmetry present (and necessary) in our cavity limits this phase change to only $\pi/250$. Great care is therefore taken to remove noise from the error signal electrically, optically and mechanically: the locking electronics are powered by batteries to remove 50 Hz mains noise, APC fibres are used to minimise intra-fibre etalons, and all optics are mounted on 1" steel posts with minimised beam distances.

During the period of time for which we hope to interact an atom with the cavity there can be no light within the cavity, we therefore interrupt the locking beam for this 25 ms period and rely on the passive stability of the cavity — which fortunately is sufficient to remain on resonance. A sample and hold is used to pause the error signal during this time such that the PID is capable of reliable re-locking the cavity after each interruption.

2.3.2 MOT and Atomic Fountain

At room temperature rubidium atoms will move with a thermal velocity of nearly 300 ms^{-1}, thus crossing the approximately 20 μm cavity mode in under 100 ns — far too quickly for photon production. We therefore laser cool our atoms to a few tens of microkelvin in a magneto optical trap (MOT), as used

in so many atomic physics experiments. At this temperature it would be possible to trap the atoms within the cavity mode, however running a trap within the cavity adds a great deal of complication and at 100 μK the cavity crossing time is greater than 100 μs which is plenty long enough for photon production. We therefore do not trap the atoms but position the MOT as close to the cavity as possible and then launch the diffuse cloud of atoms through the cavity in an atomic fountain.

The MOT must be run in a vacuum chamber as collisions with background gas at atmospheric pressure would inhibit cooling. We use an octagonal cross section, non-magnetic stainless steel chamber with 10 glass viewports providing optical access. After multiple bakeout phases (outlined in detail in [102]) a UHV pressure of less than 10^{-9} mbar is maintained with a single ion getter pump. The chamber is surrounded by three orthogonal pairs of magnetic field coils to compensate for the Earth's magnetic field, and a further pair of water cooled coils to provide the field gradient for the MOT. Rubidium atoms are injected into the vacuum from an Alvatec metal vapour dispenser[5]. The MOT loading rate is substantially enhanced by twelve 390 nm 20 mW UV LEDs[6] promoting light-induced atom desorption (LIAD) from the chamber walls [103, 104]. This not only improves the loading rate but also results in a reduction of the background pressure when the LEDs are switched off, allowing access to temperatures of down to 10 μK [105].

Once loaded, typically for around 300 ms, the MOT field coils are turned off and the upper and lower cooling beams are detuned with respect to one another, thus cooling the atoms into a moving rest frame with an upward

[5] Alvasource AS-5-Rb-160-S
[6] BIVAR UV5TZ-390-30

velocity of

$$v = \sqrt{2}\lambda\Delta f\,, \tag{2.74}$$

where λ is the laser wavelength and Δf the frequency difference between the upper and lower beams. A true moving rest frame requires the frequency of the centre MOT cooling beam to be half way between the frequencies of the upper and lower beams. However in our setup the centre beam is derived from the lower cooling beams and therefore we cannot meet this condition. This results in some unwanted heating in the plane perpendicular to the centre beams. The MOT sits around 10 mm below the cavity and should therefore be launched with a velocity of around $0.44\,\mathrm{ms}^{-1}$ to position the turning point of its trajectory within the cavity mode (this would give the longest interaction times). Unfortunately such a trajectory takes around 40 ms to reach the cavity, during which time the expansion of the cloud due to the atoms thermal velocity results in negligible atom flux delivered to the cavity. Therefore a faster launch of around $1\,\mathrm{ms}^{-1}$ is used, requiring a frequency difference of $\Delta f = 1\,\mathrm{MHz}$, which delivers suitable atom flux to the cavity with each atom still interacting for up to $100\,\mu$s.

The atomic fountain is very sensitive to the alignment, power, and frequencies of all six of the MOT beams. As such, small changes in the launch parameters can drastically affect the alignment of the fountain. Absorption imaging is used on a daily basis to check both the temperature of the atoms and the alignment of the fountain. Unfortunately the transition from MOT to moving molasses results in a slight heating of the atoms, typically from around $20\,\mu$K to around $100\,\mu$K in the fountain. The launch is normally conducted by shifting the frequency of just one of the upper of lower MOT beam pairs by using an AOM. Detuning both pairs (which might seem preferential as it reduces the overall detuning from the MOT phase) results in

greater heating and atom loss. This is likely due to the nonlinear response of the AOMs, which although measured and minimised, still persists. For similar reasons the frequency shift is conducted as a step change rather than a smoother transition.

During this detuned launch phase, the atoms quickly leave the region of optimal overlap between the MOT beams (one potential cause of the slight heating observed), if the lasers are not switched off before atoms more too far then the MOT is fragmented into two velocity classes with opposing non-zero lateral velocity — these two lobes consequently both miss the cavity. Therefore the launch phase typically only lasts a few milliseconds.

2.3.3 Lasers

A number of different laser frequencies are required for the complete operation of the photon pistol, resonant on the transitions shown in Figure 2.13. These are derived from two external cavity diode lasers[7], one for transitions on the $F = 1 \rightarrow F'$ manifold, the other for $F = 2 \rightarrow F'$. Both are locked to crossover lines in the saturated Doppler-free absorption spectrum using the PDH technique [100, 101] — 20 MHz sidebands for this purpose are generated by rapid modulation of the laser current. The frequency shifts required for the individual beams are then applied using AOMs, in most cases in the double pass configuration to eliminate the beam displacement. All of the derived laser beams are fibre (de)coupled after beam preparation before their alignment into the chamber (Figure 2.14). This facilitates the stable alignment necessary for the fountain and, more critically, the locking and driving of the 20 μm cavity mode.

[7] Toptica DL-100

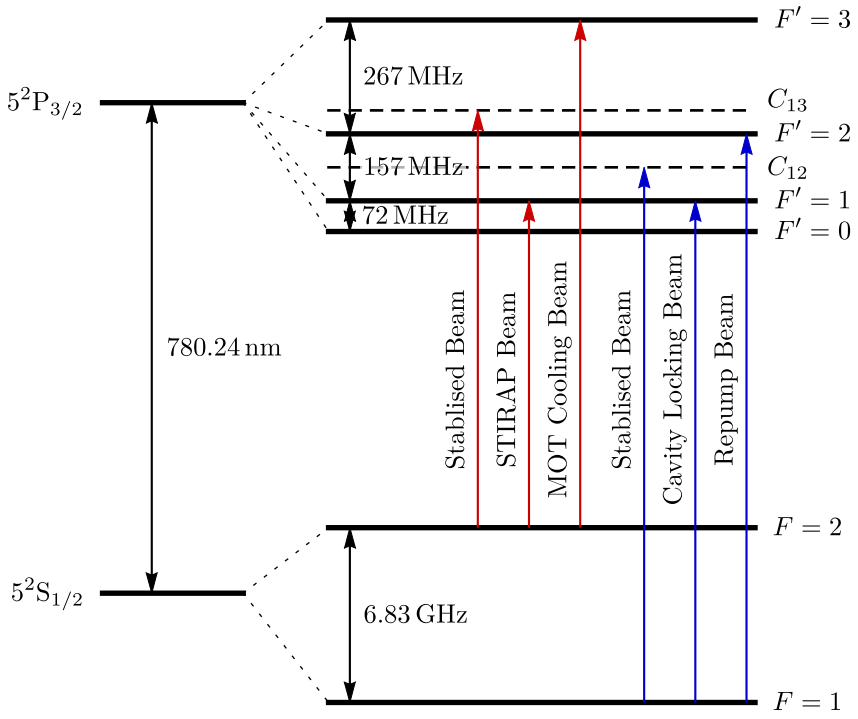


Figure 2.13: Hyperfine energy level structure of the ^{87}Rb D_2 line: The $F = 1 \rightarrow F'$ and $F = 2 \rightarrow F'$ transitions are accessed with separate lasers, both locked to crossover lines. The stabilised beams are then shifted by AOMs to the required frequencies indicated.

The RF frequencies for the majority of the AOMs are generated with in-house electronics. The AOM modulating the shape and frequency of the STIRAP laser beam is controlled by an arbitrary waveform generator[8] running at 1.25 Gs/s. Compensating for the intrinsic nonlinear intensity response of the AOM to applied RF voltage is even more important for this beam. We therefore map the response of the AOM across its voltage range at the desired frequency(s) and invert it, thus producing a normalisation that is applied to the computer generated STIRAP waveform.

After the STIRAP photon generation process the atom is left in the $F = 1$ state, however the STIRAP process requires the atom to start in the $F = 2$

[8] Agilent N6031A, 1.25 Gs/s

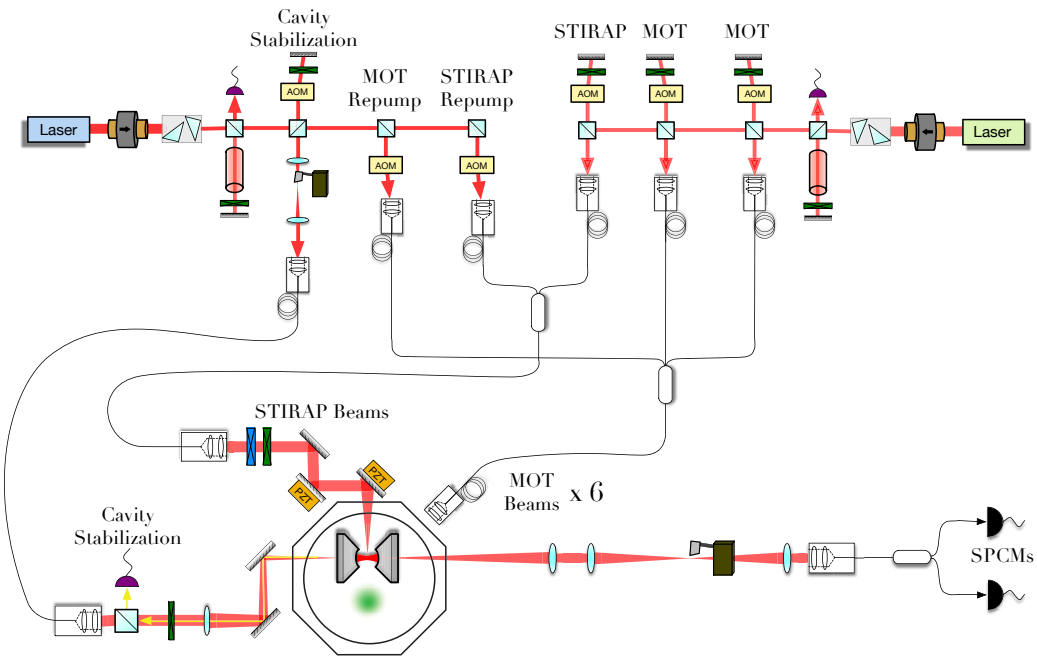


Figure 2.14: Schematic of the laser setup: Two lasers are used, one for each $F \rightarrow F'$ manifold, and are locked using the PDH technique on the saturated Doppler-free absorption spectrum from Rb vapour cells. Individual beams are then shifted to the correct frequency and switched using AOMs. The MOT and cavity are isolated from the lasers using optical fibres. Reproduced with permission from [94].

state, this can be seen in Figure 2.4. Therefore the "Repump Beam" in Figure 2.14 is used not only to repump atoms back onto the cooling transition during the MOT but also a short pulse is used after every STIRAP generation process to reset the atom into the $F = 1$ state.

2.3.4 Experimental Timing and Control

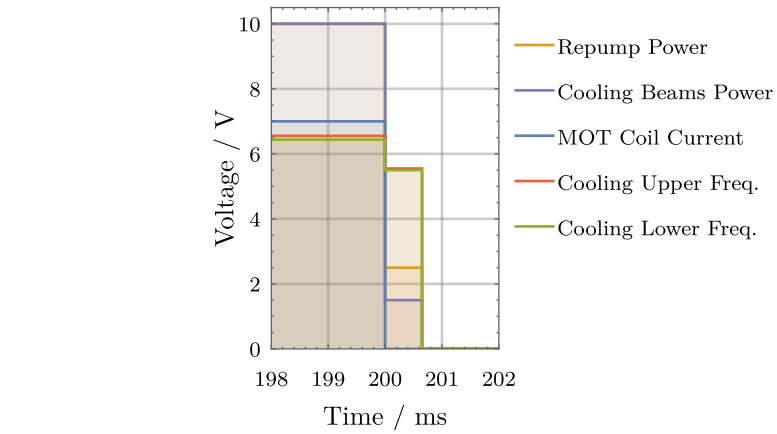
Successful operation of the source requires careful timing of not only the frequency and power of many of the beams passing through AOMs, but also the current in the magnetic field coils, various shutters used to temporarily occlude beams, and the photon detectors. This is all achieved with com-

puter control from a LabVIEW VI[9] interfacing via two synchronised DAQ cards[10] providing 12-bit precision, 10 V outputs, on 8 analogue channels each, updated at up to 100 kHz.

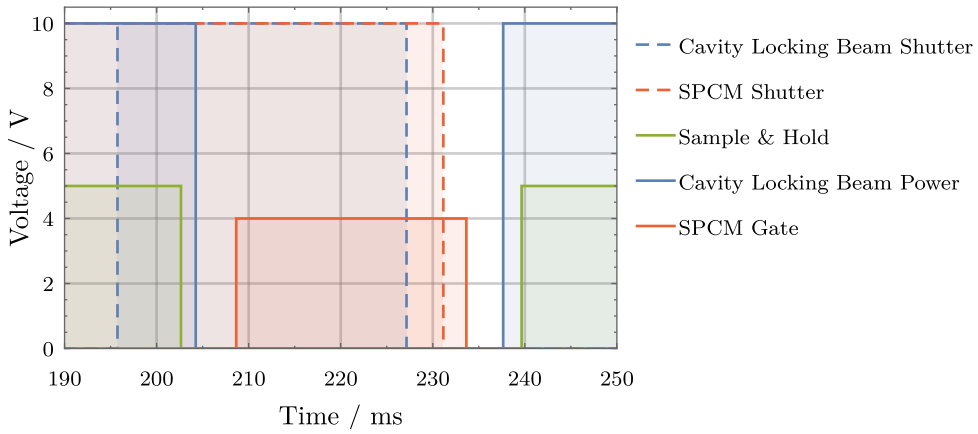
An overview of the sequence of operation is shown in Figure 2.15. Typically the MOT is loaded for ~ 200 ms before the sequence begins; the first 200 ms of the sequence is also a steady state MOT loading period but without the LIAD LEDs active. After this 200 ms there is a brief (typically < 2 ms) 'launch phase' to kick the atoms towards the cavity Figure 2.15a. The final stages of the sequence are to pause the cavity lock and enable the SPCMs Figure 2.15b, which at the same time triggers the generation of STIRAP laser pulses under control from the AWG. The AWG is pre-programmed to generate 25 000 $\sim 1\,\mu$s sequences of STIRAP driving and repump pulses in the following 25 ms, and for each of these triggers a time-to-digital converter which records the counts from the SPCMs. The shutters may appear to be operated too early, however they exhibit significant lags of a few milliseconds which are measured using fast photodiodes and then compensated for as shown.

The total repetition rate of the source is therefore approximately 2 Hz (during which photons are generated at 1 MHz for 25 ms). Curiously, when using SPCMs manufactured by Perkin-Elmer[11] we must avoid repetition periods around 1.1 s as when gated at this rate the detectors do not register any counts approximately during every other gated-open window. The fraction of windows in which the detector fails to operate appears to be strongly dependent on the repetition period as shown in Figure 2.16, fortunately away from this 1-1.2 s region they function normally.

[9] National Instruments software
[10] ADLINK DAQ-2502
[11] Now Excelitas, the problem persists.

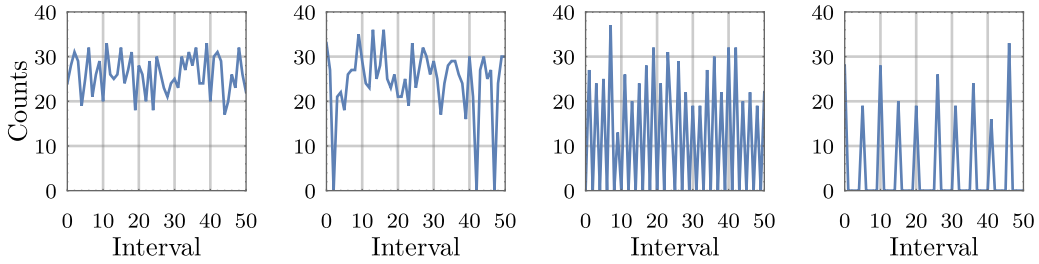


(a) Launch



(b) Photon Generation and Detection

Figure 2.15: Photon pistol control sequence: To launch the cloud of cooled atoms towards the cavity in an atomic fountain a number of laser beam powers and frequencies are switched from a steady state MOT loading phase to launch settings simultaneously (a). This launch phase is short, in the above < 1 ms so to minimise the disturbance to the atom cloud. Both before and after the launch other electronics are switched to: pause the cavity lock, fully block the cavity locking beam, ready the photon counters (b). The shutters exhibit such lag that their control signals are sent 5-10 ms earlier than required.



(a) 1028 ms **(b)** 1078 ms **(c)** 1128 ms **(d)** 1178 ms

Figure 2.16: SPCM errors: The SPCMS are de(activated) using their gate input such that they only report photon detections during the 25 ms interval for which photons are generated. However, when the period between the active windows are times around 1.1 s the modules supplied by Perkin-Elmer do not re-activate for some intervals, resulting in strictly zero count rates. At 1128 ms the modules miss every other interval, at 1178 ms they miss most. We have observed this behaviour between 1000-1300 ms with all Perkin-Elmer SPCMS.

Optical Delay Line

When there is an atom in the cavity, the train of STIRAP pulses described above produces a train of single photons separated by roughly 1 μs. We would like a source of pairs of photons, therefore we need to delay every other photon by 1 μs. This is achieved with a PBS which divides the stream into two paths, one of which contains a spool of 200 m of optical fibre which takes the photon 1 μs to traverse, as shown in Figure 2.17. Polarisation optics are placed at the output of each arm to provide control of the (in)distinguishability of the pair. Thus our atom-cavity system produces pairs of identical single photons.

The photon stream from the cavity is randomly polarised and therefore the splitting into the two paths is random. Consequently every sequential pair of emitted photons have only a $\frac{1}{4}$ chance of routing to form a simultaneous pair. Methods to improve this routing efficiency are discussed in Chapter 7.

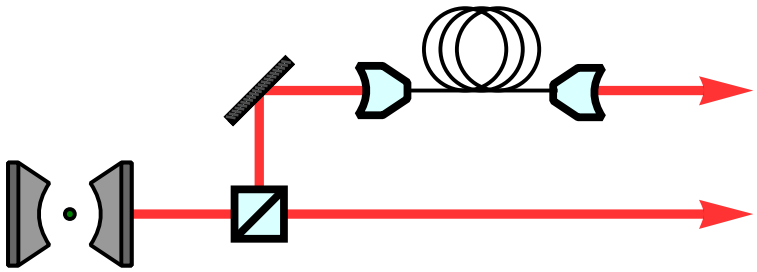


Figure 2.17: Optical delay line: A PBS is used to randomly split the stream of photons emitted from the cavity between two paths. One of these contains 200 m of optical fibre which delays the photons by the photon repetition period, 1 μs. Thus simultaneous pairs of photons are produced with an efficiency of 25% (for every emitted pair).

2.3.5 Detection and Data Recording

Detection

The final aspect to the experimental apparatus is the detection of the generated photons and the recording of the data. Detection is carried out by an array of single photon counting modules (SPCMs) which register the impact of a single photon with a typical efficiency of 60-65% [12]. Silicon-based SPCMs provide good detection efficiency around 780 nm at reasonable cost, they do however have some limitations and some undesirable features whose origins can be better understood when considering their principle of operation. The SPCMs are a combination of a single-photon avalanche diode (SPAD) with an active quenching circuit. The SPAD is a p-n junction operated with a reverse bias well above the breakdown voltage (known as Geiger mode). In this mode a single charge carrier injected into the depletion layer (by e.g. a photon) can trigger a self sustaining avalanche, the rising edge of this cur-

[12] We use modules from three different manufacturers, all with similar performance: Laser Components COUNT, Excelitas SPCM-AQRH-780-14-FC, Perkin-Elmer SPCM QC6-14

rent signals the arrival of a photon. The quenching circuit must detect this edge, then quickly lower the bias voltage to below the breakdown voltage, thus allowing the avalanche to relax and free charge carriers to recombine. Finally the bias must be raised once again to prime the photodiode ready for the next detection.

The SPCMs therefore present with the following limitations: they are not number resolving; there is a delay between photon impact and TTL pulse out, typically 30-50 ns; there is a finite chance that a free charge carrier may still be present in the depletion layer when the bias field is reintroduced, this results in an instant cascade thus signalling another detection event, known as an *afterpulse*; to reduce the probability of an afterpulse, there is a pause before the bias field is reintroduced which constitutes a period of time during which no detections will be registered, termed *dead time*; in addition to photons, thermally-generated carriers can also trigger the avalanche process, thus leading a background rate of false detections even in the absence of any light known as *dark count*, this is typically 10-100 Hz for SPCMS; the modules generally have a time resolution no better than 300 ps, which dominates over that of the TDC (80 ps); the efficiency is limited to at best 70% at 780 nm; the modules will begin to saturate at count rates around 3 MHz or more, which precludes measurement of even nW beams; being able to do so would simplify many alignment procedures.

There are many other technologies for photon detection, all with their own benefits and drawbacks [67], and the field is one under active development. One particularly promising recent technology is that of superconducting nanowire detectors which, although requiring cryogenic temperatures, can achieve in excess of 90% detection efficiency with under 1 Hz dark count [68].

Recording

The SPCMs above signal a detection by outputting a voltage pulse. We use a time-to-digital converter (TDC) to record the timing of these detection pulses with respect to the photon generation process. We record every detection event from our SPCMs, instead of just correlations identified at a hardware level. Recording all events allows us to derive a great deal of understanding about how the source is performing and calculate parameters such as the time for which an atom interacts with the cavity. Furthermore it is in fact essential to record all detections if we are to normalise our data as our source works in a fundamentally different way to those used in most other correlation experiments — we do not herald our photon pairs so must use other means to calculate the number of pairs contributing to an experiment.

The AWG controls the timing of the photon generation process and as such it also sends a trigger to provide that timing information to the TDC. Four parameters are recorded for each detection event:

1. The channel of the TDC on which the detection was recorded, Ch_{TDC}.
2. The time since the beginning of the most recent STIRAP pulse, t_{STIRAP}.
3. The time since the beginning of the 25 ms STIRAP pulse train, t_{MOT}.
4. The number of the pulse in the pulse train, n_{pulse}.

There is in the above a redundancy in that the final three values are related by the equation $t_{\mathrm{MOT}} = T_{\mathrm{STIRAP}}(n_{\mathrm{pulse}} - 1) + t_{\mathrm{STIRAP}}$, where T_{STIRAP} is the length of an individual pulse (992 ns). However the value t_{MOT} is useful diagnostically at runtime and is therefore calculated and recorded on the fly.

Preliminary Data Analysis

Hopefully a brief look at some sample detection data from source will help clarify its operation. Let us look at some of the basic diagnostic information derived from the data. A more in depth discussion of the processing of the data is saved for the next chapter where the identification of correlations, the compensation of background effects, and normalisation of the data are discussed. Further details of the data acquisition hardware and the synchronisation of timings surrounding the control of the data acquisition side of the apparatus can be found in Chapter 6 where they are pertinent to the discussion of the feedback control implemented.

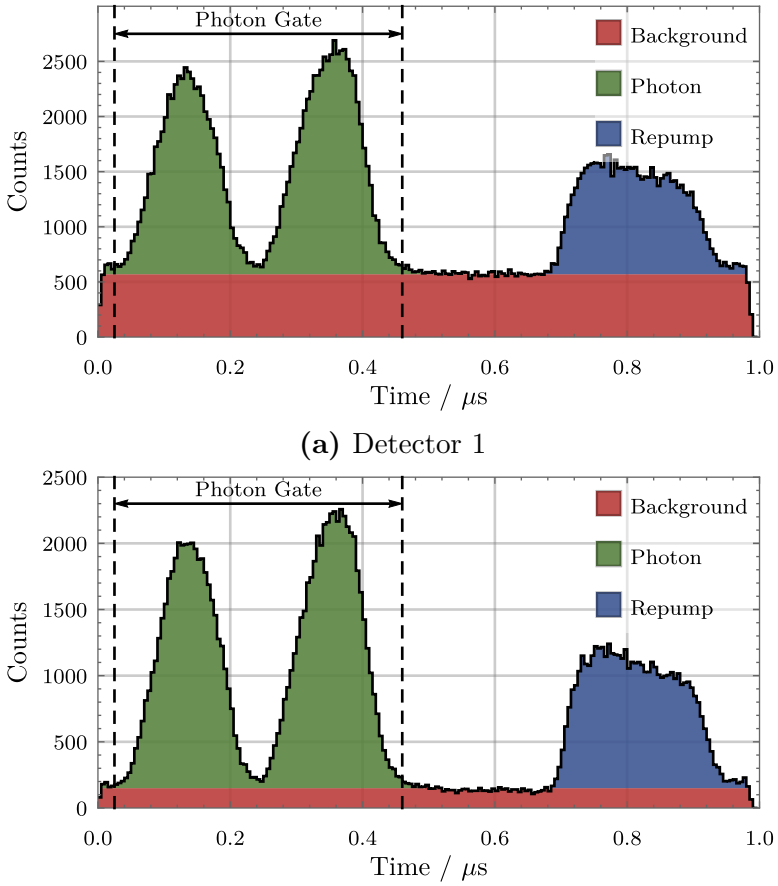
A small percentage ($\sim 0.5\%$) of the recorded data comprise values which describe physically impossible detection events, for example detections on TDC channels which are not connected to an active SPCM or detections at times exceeding the maximum possible for t_{STIRAP} or t_{MOT}. These records are simply discarded at the outset of any data analysis.

A simple histogram of t_{STIRAP} for a given Ch_{TDC} as shown in Figure 2.18 immediately reveals a wealth of information. Firstly the intensity envelope of the generated photons is apparent and takes the desired symmetric sinusoidal form. Any asymmetry remaining in the photon envelope informs the experimentalist as to whether the STIRAP power needs to be increased (if the envelope is negatively skewed) or decreased (positive skew). Furthermore the window of possible arrival times of the photons of interest is obvious, for further data processing we 'gate out' this region and only consider detections within this region when looking for correlations. As well as the counts prescribing the shape of the generated photon, we also observe a number of detections towards the end of the $1\,\mu$s STIRAP period, these are photons

incoherently scattered during the repump stage of the STIRAP process. Between these two periods there are no lasers acting on the atom or cavity and thus no photons should be detected, however we see there are a number of detections registered in this interval which appear to form an elevated background upon which our light-derived detections sit. These are background detections which result from both stray light in the room and the inherent dark counts of the SPCMs. Thus we usefully have an accurate measure of the background detection rate at the exact time the data is collected; using this information we can account for the effect of the background in our experimental results, the details of this process are given in the next chapter.

A histogram of t_{MOT}, shown in Figure 2.19, illustrates the transit of the diffuse atom cloud through the cavity. The profile of this histogram, along with the absorption images of the atomic fountain, aid the optimisation of the atomic fountain. We aim to keep the atom flux delivered to the cavity as constant as possible over the 25 ms window — a more peaked profile would merely increase the likelihood of two atom events for a given total atom flux.

As a final demonstration of the utility of recording all the photon detections we may consider the differences in arrival time t_{MOT} for all of our detections (within our gated window of interest), which constitutes a measure of the second order correlation function, $g^{(2)}(\tau)$. This is shown in Figure 2.20 for data collected with just a single stream of photons incident on a beam splitter with two detectors in a HBT setup. The missing central peak indicates single photon emission. The unusual envelope is due to the intermittent nature of the source — photons are only emitted as an atom transits the cavity. The width of the envelope shows the time for which atoms interact with the cavity, in this instance up to around 70 μs, again this figure may be referenced when optimising the atomic fountain. The background level is mainly



(a) Detector 1

(b) Detector 2

Figure 2.18: Histograms of t_{STIRAP}: Reveal the photon envelope and temporal location, and the embedded dark count rate for each detector, as well as the rate of scattering during atom repump.

due to correlations with detector dark counts and is discussed in more detail in the next chapter.

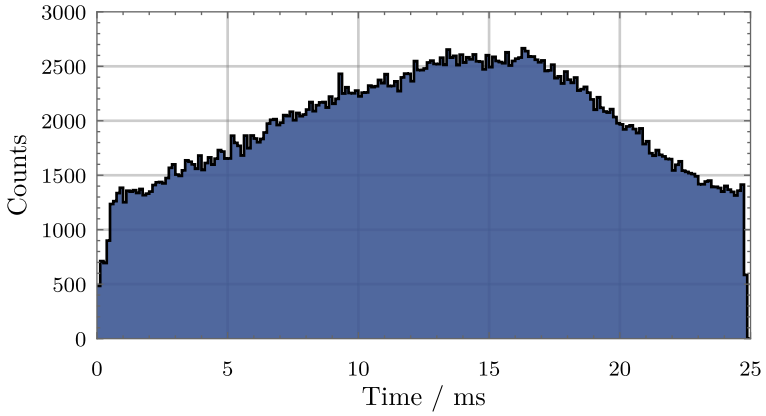


Figure 2.19: Histogram of t_{MOT}: Reveals the passage of the diffuse atom cloud through the cavity. This is both diagnostically useful for optimising the atomic fountain, and for compensating for background correlations, described in detail in Section 3.5.

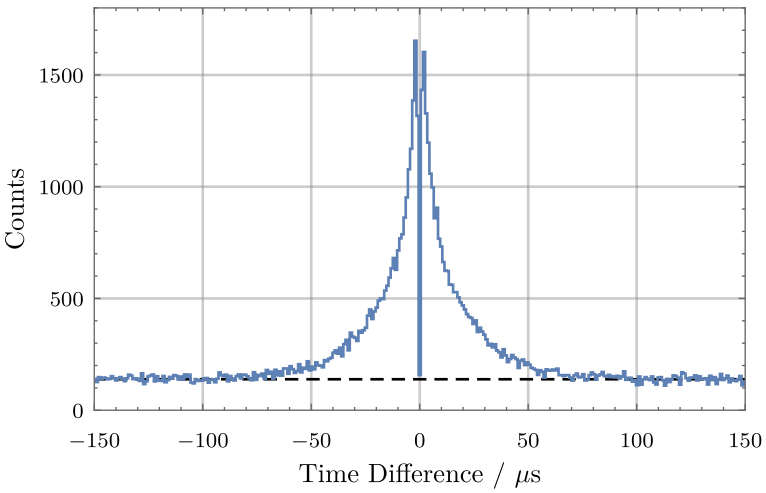


Figure 2.20: Hanbury Brown – Twiss $g^{(2)}$: The detection time differences for all detections is plotted as a histogram between $\pm 150\,\mu$s. The missing central peak indicates single-photon emission. The envelope is a feature of the intermittent nature of the source, it indicates the atom-cavity interaction time, here around $70\,\mu$s.

Chapter 3

Temporally Encoded Qudits

3.1 Introduction

A deterministic source of photons has appeal for many quantum information processing applications including linear optical quantum computing (LOQC). Such applications routinely demand substantial control over the properties of the photons, including their temporal envelope, frequency, bandwidth, spatial mode, and polarisation. This chapter demonstrates the unparalleled degree of control the atom-cavity source provides over the properties of the photons, and in the process prescribes photons with properties that may be desirable for QIP applications.

The power of a quantum information carrier is realised by ascribing information to two (or more) orthogonal modes of the chosen quantum system. For photons a common choice is "dual-rail" encoding, where the photon is

'split' on a $\eta : (1-\eta)$ beam splitter thus leaving it in a superposition of two spatial modes, here labelled A and B, with a state described by

$$\begin{aligned} |\Psi\rangle &= \alpha|0_{\mathrm{A}}, 1_{\mathrm{B}}\rangle + \beta \mathrm{e}^{\mathrm{i}\phi}|1_{\mathrm{A}}, 0_{\mathrm{B}}\rangle \\ &= \alpha|0\rangle + \beta \mathrm{e}^{\mathrm{i}\phi}|1\rangle \end{aligned} \tag{3.1}$$

where the amplitudes $\alpha = \sqrt{\eta}$ and $\beta = \sqrt{1-\eta}$ and ϕ is the phase delay in the transmitted mode. Such a two level quantum system is termed a qubit and for photons there exist many possibilities including occupation number ("single-rail" encoding), polarisation, orbital angular momentum and others; each encoding method offers both benefits and drawbacks. Another possibility is to encode in the temporal domain [106], which has the potential to make more efficient use of limited physical resources. With spontaneous sources this encoding has been performed probabilistically with the aid of an unbalanced Mach-Zehnder [107], however as is demonstrated in this chapter we are able to directly generate our photons with qubits encoded in the temporal domain. The state, now described by the superposition of two temporal modes or 'time bins' labelled 1 and 2, is trivially described by the same wavefunction as for spatial superpositions above:

$$\begin{aligned} |\Psi\rangle &= \alpha|0_1, 1_2\rangle + \beta \mathrm{e}^{\mathrm{i}\phi}|1_1, 0_2\rangle \\ &= \alpha|0\rangle + \beta \mathrm{e}^{\mathrm{i}\phi}|1\rangle \,. \end{aligned} \tag{3.2}$$

Not only does our system allow direct encoding into time bins but also full control over the amplitudes α and β and the relative phase ϕ between them. Furthermore it is trivial with this system to extend this temporal encoding to more than two modes, a provision which holds great promise in many applications. Additional modes unlock higher dimensional Hilbert spaces

and can significantly reduce the number of gates required for many quantum circuits [108], as well as improve data throughput and security in many quantum cryptography applications [109]. For example in time-frequency encoded QKD, one could obtain $\log_2 d$ bits per photon subdivided into d temporal modes. The preparation of the system into three modes is termed a qutrit and can be described by the equation below; the general term for a d-levelled system is a qudit.

$$\begin{aligned} |\Psi\rangle &= \alpha|0_1, 0_2, 1_3\rangle + \beta e^{i\phi_1}|0_1, 1_2, 0_3\rangle + \gamma e^{i\phi_2}|1_1, 0_2, 0_3\rangle \\ &= \alpha|0\rangle + \beta e^{i\phi_1}|1\rangle + \gamma e^{i\phi_2}|2\rangle \,. \end{aligned} \tag{3.3}$$

The chapter begins with a brief extension to the theory of HOM presented in Section 3.2 which provides a more compact, more understandable, view of the interference of time-bin encoded photons. Then the method of encoding the qudits is detailed in Section 3.3 before confirmation that the desired properties are indeed obtained is given in Section 3.4. The data presented in this chapter also provided the basis of the paper [110]. Section 3.5 gives a comprehensive look at how the data are analysed. Following in Section 3.6 is the extension beyond the binary system before the limits and fidelity of the preparation are discussed in Section 3.7.

3.2 Time-Resolved Two-Photon Interference

Inspection of the generated photon states is performed via time-resolved two-photon interference measurements in a quantum homodyne setup. Although the theory of two-photon HOM interference is set out comprehensively in Section 2.2, it is somewhat involved and is computationally taxing for sinusoidal envelopes. Instead a more intuitive understanding of the interference

of time-binned qudits and the effect of relative phases within, can be garnered by a simple extension to the corpuscular presentation from the beginning of Section 2.2.

We consider our photons to be equally split into two independent time-bins, 1 and 2, as in Figure 3.1, and define distinct modes for each of the time bins. Allowing a free phase ϕ between the two time bins of one of the photons, our creation operators are therefore:

$$\hat{a}_A^\dagger = \frac{1}{\sqrt{2}}(\hat{a}_{A1}^\dagger + \hat{a}_{A2}^\dagger) \qquad \hat{a}_B^\dagger = \frac{1}{\sqrt{2}}(\hat{a}_{B1}^\dagger + \mathrm{e}^{\mathrm{i}\phi}\hat{a}_{B2}^\dagger)$$

and we can use the standard beam splitter relations for each time bin individually:

$$\begin{aligned} \hat{a}_{Ai}^\dagger &= \frac{1}{\sqrt{2}}(\hat{a}_{Ci}^\dagger + \hat{a}_{Di}^\dagger) & \hat{a}_{Ci}^\dagger &= \frac{1}{\sqrt{2}}(\hat{a}_{Ai}^\dagger + \hat{a}_{Bi}^\dagger) \\ \hat{a}_{Bi}^\dagger &= \frac{1}{\sqrt{2}}(\hat{a}_{Ci}^\dagger - \hat{a}_{Di}^\dagger) & \hat{a}_{Di}^\dagger &= \frac{1}{\sqrt{2}}(\hat{a}_{Ai}^\dagger - \hat{a}_{Bi}^\dagger)\,. \end{aligned}$$

Note that we allow for a relative phase of ϕ between the two time bins of mode B.

Following the method from Section 2.2 we now use the relations above to generate the output state from our input of one double hump photon in each

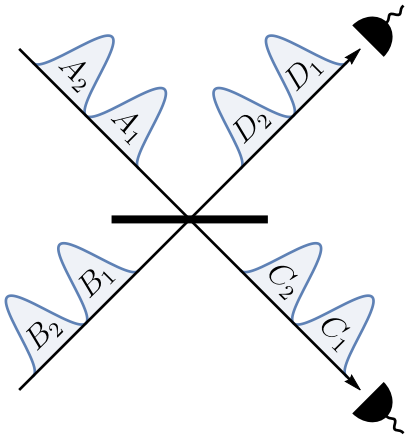


Figure 3.1: Time-binned HOM: The theory of Hong-Ou-Mandel interference, described using a beam splitter to mix inputs and output modes, can be extended to apply to photons subdivided into multiple time-bins.

of modes A and B:

$$\begin{aligned}
|1_A 1_B\rangle &= \hat{a}_A^\dagger \hat{a}_B^\dagger |0\rangle = \frac{1}{2}(\hat{a}_{A1}^\dagger + \hat{a}_{A2}^\dagger)(\hat{a}_{B1}^\dagger + \mathrm{e}^{\mathrm{i}\phi}\hat{a}_{B2}^\dagger)|0\rangle \\
&= \frac{1}{2\sqrt{2}}((\hat{a}_{C1}^\dagger + \hat{a}_{D1}^\dagger) + (\hat{a}_{C2}^\dagger + \hat{a}_{D2}^\dagger))((\hat{a}_{C1}^\dagger - \hat{a}_{D1}^\dagger) + \mathrm{e}^{\mathrm{i}\phi}(\hat{a}_{C2}^\dagger - \hat{a}_{D2}^\dagger))|0\rangle \\
&= \frac{1}{2\sqrt{2}}\Big((\hat{a}_{C1}^\dagger \hat{a}_{C1}^\dagger + \mathrm{e}^{\mathrm{i}\phi}\hat{a}_{C2}^\dagger \hat{a}_{C2}^\dagger - \hat{a}_{D1}^\dagger \hat{a}_{D1}^\dagger - \mathrm{e}^{\mathrm{i}\phi}\hat{a}_{D2}^\dagger \hat{a}_{D2}^\dagger) \\
&+ (\mathrm{e}^{\mathrm{i}\phi} + 1)(\hat{a}_{C1}^\dagger \hat{a}_{C2}^\dagger - \hat{a}_{D1}^\dagger \hat{a}_{D2}^\dagger) + (\mathrm{e}^{\mathrm{i}\phi} - 1)(\hat{a}_{C2}^\dagger \hat{a}_{D1}^\dagger - \hat{a}_{C1}^\dagger \hat{a}_{D2}^\dagger)\Big)|0\rangle\,.
\end{aligned} \tag{3.4}$$

The first four terms in the expression are unaffected by the relative phase and describe standard bosonic bunching with the photons coalescing and leaving the beam splitter through the same output port. The contribution of the remaining four terms however is modulated by the phase ϕ and describes correlations between different time bins. For some particular value of ϕ, these are either forced to the same or to opposite detectors. With no relative phase, $\phi = 0$, there is no deviation from standard behaviour as both photons leave via the same port. However with $\phi = \pi$ the photons no longer coalesce

and are instead forced into opposite output ports, they exhibit fermionic behaviour. This result can be understood with reference to Figure 3.1 if we remember that the phase relation between the photons is only initialised upon the first detection. More strictly, the first photon detection projects the one remaining excitation into a mode superposition of well-defined mutual phase, which changes by $\phi = \pi$ if the until the second photon is not detected until the second time bin. Therefore when both detections occur in the same time bin the phase change of ϕ never manifests, it is only when the two detections occur in separate time bins that the change of the phase at the halfway point enters.

Experimentally it is only possible to monitor correlations between different output modes (rather than those occurring within the same output mode) due to the limitations of our detectors as discussed in Section 2.3.5. We therefore expect to observe a phase-dependent number of correlations at detection time differences corresponding to one time bin. The exact form of the correlations can be found using the full time-resolved theory presented in Section 2.2 and is shown below in Figure 3.2.

In the above analysis it is apparent that the picture of two photons as point particles is not sufficient to fully understand their interference, as correlated behaviour still exists even for detections well separated in time, provided the wavefunctions overlap. In fact further care must be taken with our mental picture of interference as the key requirement of two-photon interference is that the photon amplitudes are indistinguishable at the detectors and not at the beam splitter. If this condition is met interference will occur even if the photons never overlapped at the beam splitter [111].

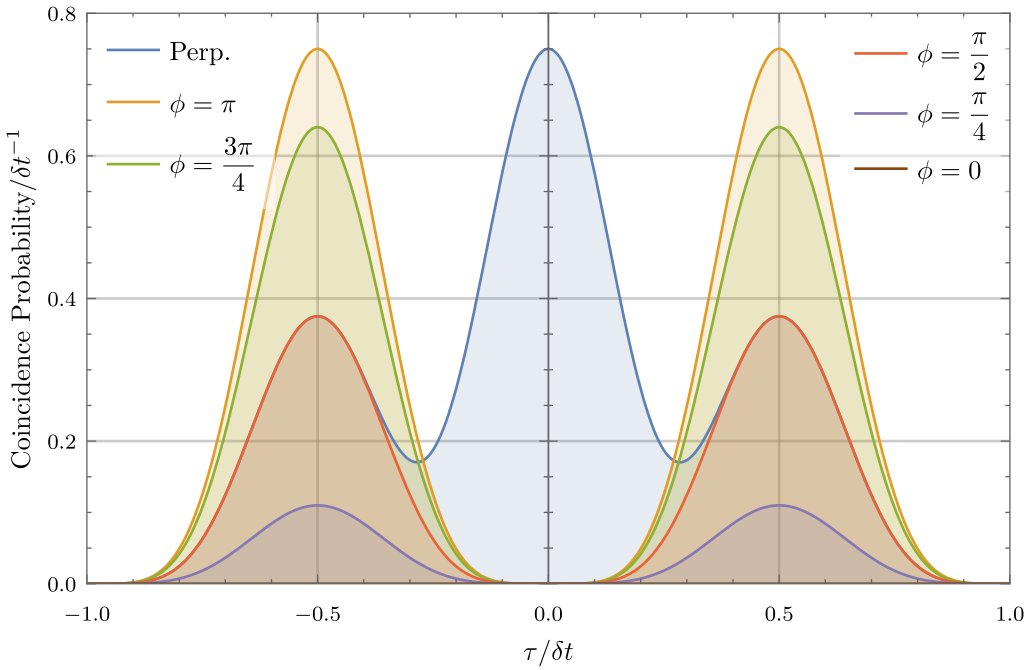


Figure 3.2: Theoretical HOM interference patterns for double-hump photons with a phase shift: The theoretical distributions of time-resolved correlations for double hump photons with various relative phases between the humps are shown along with a reference signal of non-interfering orthogonally polarised photons. The relative phase only enters between time bins and thus only affects the satellite peaks as shown.

3.3 Qudit Preparation

Our photons are generated on the D_2 line of a ^{87}Rb atom strongly coupled to our high-finesse optical cavity by means of a controlled Raman process. The subdivision of the intensity envelope into time bins, thus producing our temporally encoded qudits, occurs at the point of generation by careful control of the Raman process. The details of this process, which allows the exact amplitude and phase evolution of the photon to be prescribed, are presented in Section 2.1.2.

Modulation of the control laser is achieved by a double-passed AOM which allows arbitrary control over the intensity and phase and control over the

frequency in an approximately 40 MHz range, though care must be taken to normalise for the approximately cubic response of the intensity transmitted through the AOM with voltage. The RF for the AOM is supplied by an AWG providing 1.25 Gs/s, Figure 3.3 shows two example waveforms to generate qubits with and without a phase flip, along with the probability density of the corresponding photons. The asymmetry of the driving waveforms is a requirement of the Raman process; the waveform for the qubit is the same as that obtained by joining two single-hump waveforms, the first calculated for 50% (of η_{cav}) efficiency and the second for 100%. The qubits are roughly 430 ns long, the qutrits are longer by around one time bin at 640 ns which is towards the upper end of achievable coherence, the ququads are therefore also squeezed into an overall time interval of 640 ns. The bandwidth of the AOM limits pulse shapes to modulations slower than 3 MHz which is of no concern for encoding qudits which have in this chapter a smooth $\sin^2$ intensity profile requiring far slower modulation. Its effect can be seen rounding out some of the sharper features in the more whimsical shapes demonstrating the full versatility of the algorithm and source presented in [112].

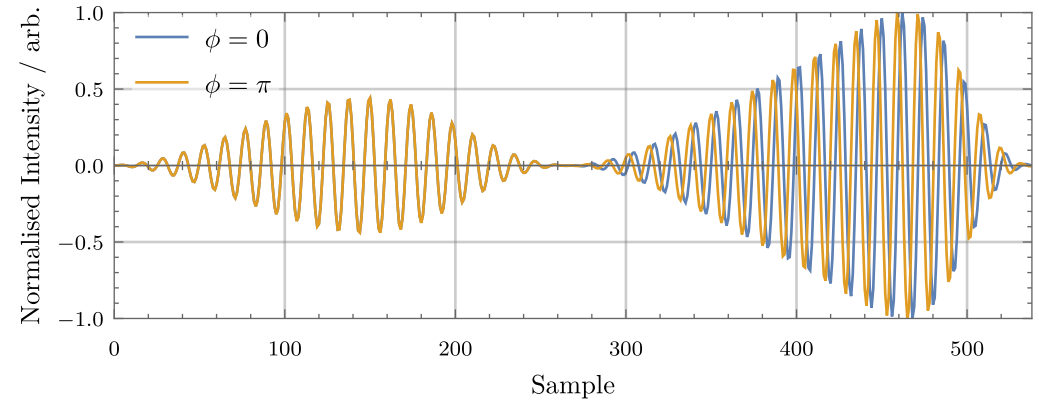
Slight variations in the envelopes of the photons are to be expected as the balance of probability between the two bins is sensitive to the power of the STIRAP beam. A corollary of this is that the different atom-cavity coupling strengths will also result in similarly varied photon envelopes. In practice small differences in the exact profile of the driving pulse have minimal impact on the photon generation process, the generated photons are symmeterised by adjusting the power in the STIRAP beam; a suboptimal driving pulse then only results in a small reduction in efficiency. Interestingly although the STIRAP process technically mandates a smooth switch on of the electric field, and therefore a $\sin^2$ profile of the *amplitude* of the pulse, no reduction in

generation efficiency is observed when using a $\sin^2$ *intensity* profile — which has a sinusoidal switch on, discontinuous in the gradient at $t = 0$.

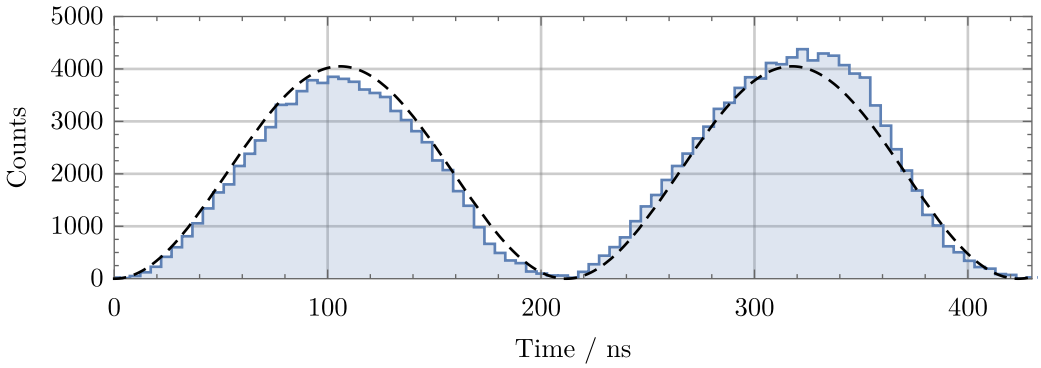
The phase change is only imposed when the cavity mode is empty, the Hamiltonian of the coupled system therefore remains unitary throughout the whole process, ensuring the adiabatic evolution necessary to construct the emitted photon in a coherent superposition of temporal modes. In addition to arbitrary control over the amplitude profile of the photons, and the relative phase between time bins, the STIRAP process allows control over the frequency of the generated photons, even within the same photon, and in principle the polarisation of the emitted photons by coupling to different Zeeman levels [113]— although this is not possible with the current cavity as the linewidth is too great.

Photon emissions are triggered with a repetition rate of 1 MHz as is standard for our source and we alternate between our target signal photon and local oscillator photons which have no phase changes. This alternating stream is split by a polarising beam splitter into one of two paths, one presenting a delay of 1 μs relative to the other, which results probabilistically in pairs arriving simultaneously at a non-polarising 50:50 beam splitter.

In addition to the photon interference measurements we must also make reference measurements with non-interfering photons of orthogonal polarisation. The degree of distinguishability between the interfering photons is adjusted by rotating the relative polarisation by means of $\lambda/2$ waveplates upfront each input to the HOM beam splitter.



(a) RF Waveform



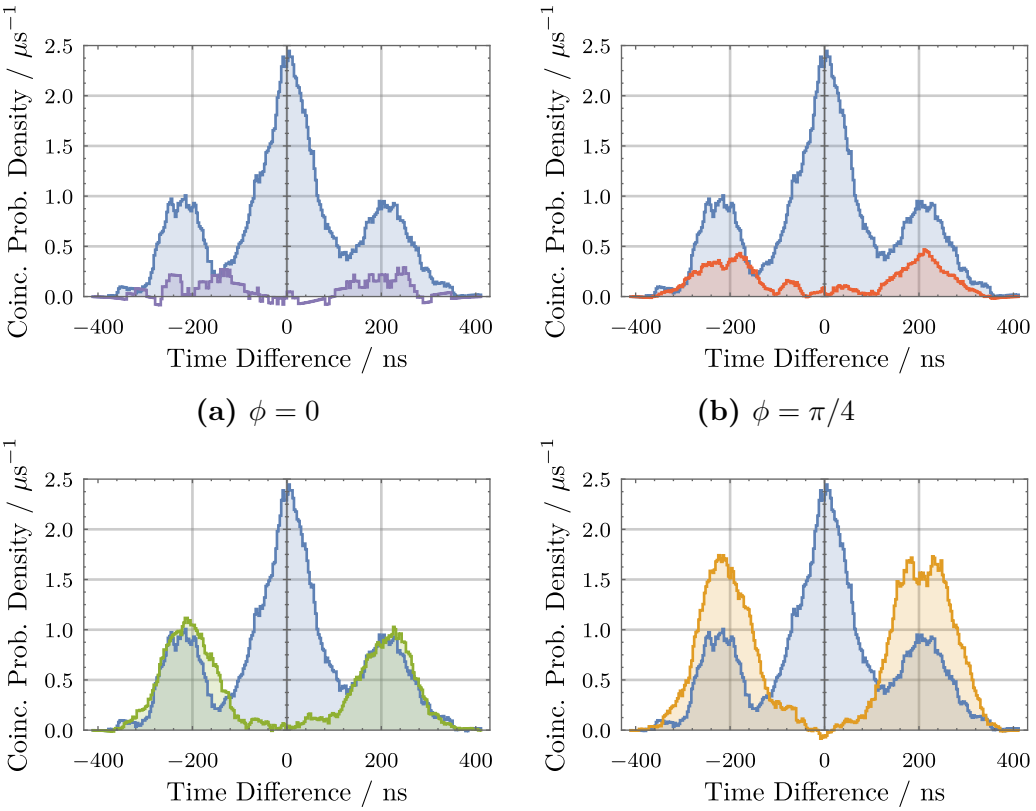
(b) Generated Photon Shape

Figure 3.3: Qubit photon generation waveform: The RF waveforms in (a) are those used to generate the photons contributing to the histogram below. The step phase change of $\phi/2$ can be seen in the second half of the waveform, the laser is double-passed through the AOM and will thus acquire the required ϕ phase. The double passing also doubles the frequency shift acquired by the beam which in this case will be $2 \times 103\,\mathrm{MHz}$. The waveform comprises 538 samples which at $1.25\,\mathrm{Gs/s}$ directly corresponds to the 430 ns photon below. The photon shape shows very little deviation from the desired $\sin^2$ profile shown as a dashed overlay.

3.4 Results - Qubits

The generated photon states are analysed via time-resolved two-photon interference, which can be interpreted as a "quantum homodyne" setup. In standard homodyne detection a modulated optical signal is interfered with a copy of the bright laser from which it was initially derived, which is termed the local oscillator (LO). In our quantum homodyne scheme both the signal and the local oscillator are single photons with identical envelopes, the only difference being possible phase changes within the signal photon. This measurement scheme provides not only a measure of the indistinguishability of the photons but also provides verification that the desired phase change is present in the qubit state. An experimental run of about 30 mins comprising ∼3000 MOT throws is sufficient to retrieve an accurate picture of the state under consideration. The time-resolved interference patterns for four different values of ϕ are shown in Figure 3.4 along with a reference signal recorded using photons of orthogonal polarisation. A direct comparison of these traces to the theory can be found in the following section at Figure 3.10, where the degree of uncertainty in the data is also discussed and presented. The following Section 3.5 also explains in detail the methods used to analyse and present the data.

Immediately obvious is the triple peak structure from the orthogonal photons, which is simply the autocorrelation of their double-peaked intensity envelopes. Also we note the absence of the central peak for all values of ϕ for parallel polarised photons as expected from the discussion in Section 3.2. Furthermore the height of the satellite peaks, populated by correlations of the form $\hat{a}^\dagger_{C2}\hat{a}^\dagger_{D1}$ and $\hat{a}^\dagger_{C1}\hat{a}^\dagger_{D2}$, is strongly dependent on the value of ϕ. On closer inspection a couple of deviations from our expectations are obvious. Notably



(a) $\phi = 0$ **(b)** $\phi = \pi/4$

(c) $\phi = \pi/2$ **(d)** $\phi = \pi$

Figure 3.4: Measured HOM interference patterns for double-hump photons with a phase shift: The measured time-resolved interference patterns for double-humped photons with a relative phase shift of ϕ between the two humps are shown for four different values of ϕ alongside a reference distribution measured using non-interfering orthogonally polarised photons (blue). The data are plotted as sliding histograms using a bin width of 41 ns and pitch of 3 ns. The satellite peaks show the expected phase dependence with evidence of only slight decoherence appearing in the $\phi = 0$ case.

that the central peak for the orthogonal case is more than twice the height of the satellites — theory predicts it should be equal to twice the height — and that there appear correlations in the satellites even for $\phi = 0$, where theory predicts no correlations should present. The first issue can be understood with reference to Figure 3.3b above in which it can be seen that the envelope of the ensemble of photons is not perfectly symmetric but has slightly more detections in the second time bin. Any asymmetry between the two time bins will lead to an excess of correlations in the central peak of the HOM and a deficit in the satellites - this is the case regardless of the direction of the asymmetry. The balance of probability between the two time bins depends on the exact values of g and Ω experienced by the atom as discussed in Section 2.1.2. Given the random trajectories of atoms through the cavity it is reasonable to assume that many photons are emitted with marginally asymmetric profiles whilst resulting in an approximately symmetric overall profile. This contributes to an imbalance between the central and satellite peaks in the HOM profile. However this is likely counterbalanced by the fact that the probability of emission also changes with the exact values of g and Ω experienced by the atom and therefore designing a control pulse shape for the best coupled atoms minimises the contribution of asymmetric qubits.

The second anomaly is more simply explained, the correlations present in the satellites in Figure 3.4a are due to imperfect coherence between the two interfering photons. As demonstrated in Section 2.2 decoherence serves to introduce correlations (by limiting interference) towards longer detection time differences. Effects limiting the coherence in our apparatus include the limited laser linewidth, drift in the cavity resonance frequency (the cavity is not locked during the transit of the atom cloud) and uncontrolled fluctuations in the magnetic environment.

The HOM traces allow us to derive a great deal of information about the quantum states under consideration. If the signal and LO photons are not fully indistinguishable by means of non-parallel polarisation then the parallel traces would show an admixture of the orthogonal reference signal which would be most apparent at time differences around zero. All the traces in Figure 3.4 show good extinction at $\Delta\tau = 0$ thus suggesting accurate collinear polarisation.

Using the normal definition for the visibility, V, of quantum interference:

$$V = 1 - \frac{N_{\parallel}}{N_{\perp}}\,, \tag{3.5}$$

where $N_{\parallel}$ is the total number of correlations observed with parallel polarised photons (and in this case $\phi = 0$) and $N_{\perp}$ the total number of orthogonally polarised reference correlations, we measure a visibility of $91 \pm 3\%$.

Two double-humped temporal modes, one with a π phase shift and one without, are field-orthogonal. Therefore if the detection timing information is dropped, the statistics show no interference and are identical to those obtained for orthogonal polarisations. This can be seen both in Figure 3.4d, where the total areas of the two traces are equal, and also in Figure 3.13d, where the total area $2 \times 1/4 = 1/2$ is the same as for the orthogonal case $4 \times 1/8 = 1/2$, shown in Figure 3.12b.

The effect of the phase is encapsulated in the areas of the satellite peaks. In the following section a method to distinguish between correlations contributing to the central peak and those contributing to the satellites is presented. Regardless, the overall lack of correlation in the centre allows us to summarise the effect of the phase shift by simply considering the total number of correlations observed, this is done in Figure 3.5. The limited visibility

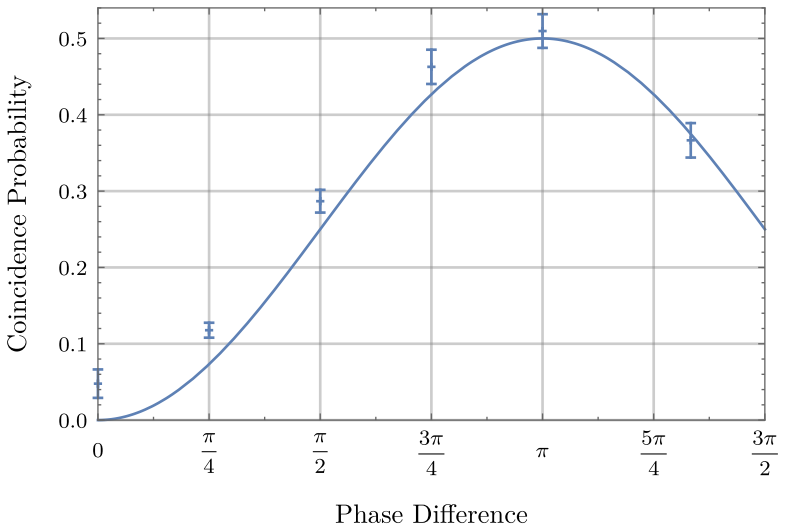


Figure 3.5: Phase dependence of coincidence probability: The overall measured coincidence probability for different phase shifts is shown for six different values of ϕ. It follows the expected $\sin^2$ behaviour given by the solid line, with a slight deviation near $\phi = 0$ due to imperfect coherence.

can be seen most clearly at $\phi = 0$ where the coincidence probability does not drop to zero.

The use of a temporal superposition allows for scaling up of the effective circuit without physical resource scaling. This can be seen clearly in Figure 3.6 which details the equivalent physical circuit which would be required to replicate the experiment in dual rail encoding.

3.5 Data Analysis

In the section above a series of HOM traces were presented showing the effect of relative phase between time bins on the two-photon interference signal. It has only been briefly mentioned that we record all detection events and there are several processing steps to convert these time stamps to the traces presented above. This data processing is the subject of this section. Our

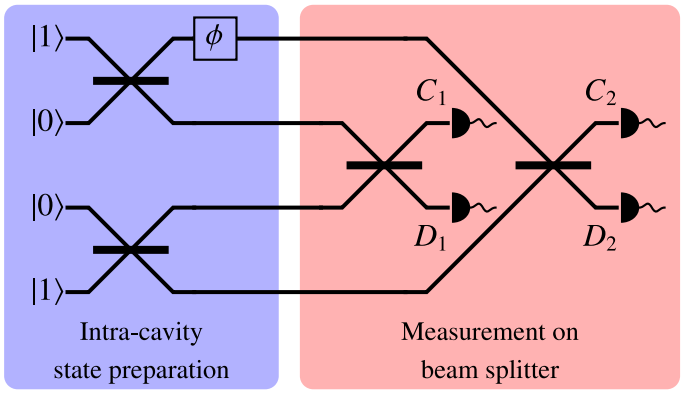


Figure 3.6: Dual-rail equivalent circuit for qubits: The results of the interference of time bin encoded qubits could also be reproduced by the above dual-rail encoded qubits in the spatial domain. However this requires additional resources to replicate the intra-cavity temporal superposition and phase shift and, an additional beam splitter and pairs of detectors to perform the measurements.

ultimate goal is to reconstruct from our data the function $P_{\text{joint}}(\tau)$ derived in Section 2.2 which details the probability of recording a correlation between different beam splitter outputs with a time difference τ per input photon pair. This section first describes how correlations are identified within the data, how these are then normalised (essential for being able to compare between experimental runs), how the effect of detector dark counts is quantified and compensated, and concludes by presenting a more robust way of displaying the data for time-bin photons. It is commonplace to be dealing with millions of lines of data from the photon pistol and therefore care was taken to develop both efficient algorithms and code for the processing.

3.5.1 Identifying Correlations

Filtering well coupled atoms

We know that the atom-cavity coupling strength, g, varies as a function of the atoms position in the cavity, rapidly along the axial direction as a standing

wave and more slowly in the radial direction as the envelope of the cavity mode. The atoms traverse the cavity along random trajectories and therefore experience different and varying coupling strengths. This variation results in a changing probability of emission and furthermore a different photon envelope (equivalent to varying the power of the stimulating STIRAP beam). We might therefore consider some method of discriminating those intervals in the data stream where we believe we have an atom well coupled to the cavity; for instance it has been shown that the shape of the overall photon ensemble varies slightly with such filters [94]. However, correlations are essentially self filtering — we only get correlations when an atom emits sequential photons for which it must almost certainly have been well-coupled. Therefore no such filtering for well-coupled atoms is performed.

HOM Algorithm

As has already been explained, given the length of our photons we expect correlated behaviour between detections that occur at different times given the resolution of our detectors. Thus the question arises of when two detections constitute a 'correlation'. Quite simply a correlation is a pair of detections whose associated photon wavefunctions should have simultaneously coexisted within the linear optical network under investigation (be that a beam splitter of a more complicated photonic chip). That is to say the two detections will occur within the same 1 μs STIRAP interval, and will have been labelled in the data with the same pulse number, n_{pulse} (see Section 2.3.5 for the origin of these labels). Correlations fulfilling this criterion are identified and the time (t_{STIRAP}) difference between the two detections is returned. A histogram of these time differences results in the plots such as those in Figure 3.8. This histogram is not yet a representation of function $P_{\text{joint}}(\tau)$ as it plots the num-

bers of correlations, not the probability of a correlation. To resolve this, and thus allow us to compare results from different experimental runs, we need to normalise the histogram by the number of 'experiments' performed, that is the number of input photon pairs, which turns out to be a difficult number to determine. Before discussing normalisation we examine the contribution of background correlations to the results.

3.5.2 Sliding Histogram

The histograms of the results presented in Figure 3.4 and the majority of the histograms presenting HOM data to follow are not typical in that there is overlap between the histogram bins. Bins of constant width are used, however their centre spacing is not equal to the bin width but is instead significantly shorter; for the data shown in this section the width is 41 ns with a pitch (centre spacing) of 3 ns. The effect is to produce a much smoother looking histogram which facilitates qualitative comparison between traces — the reason the data is plotted in the first place. In order to form such a smooth time-resolved plot without overlapping bins one would need orders of magnitude more data which is superfluous for any quantitative statements. The area under such a 'sliding histogram' could be found by integrating the trace provided one accounts for the degree of bin overlap (to within a small discrepancy). However this is not necessary here because the total number of counts in the histogram is already known.

3.5.3 Background Correction

As was shown in Figure 2.18 there are a significant number of background detections arriving alongside our real (cavity-sourced) photons. These back-

ground detections are a combination of inherent detector dark counts and other stray photons. There is a chance that one of these randomly distributed background events will occur alongside the detection of a 'real' photon, or indeed another background detection, thus leading to a background correlation. These background correlations will be present in both our HOM and our $g^{(2)}$ data and we would like to be able to correct for these. Our $g^{(2)}$ is a series of peaks at times dictated by the repetition rate (1 MHz) and our HOM is simply the central peak (or dip) with the finer time resolution of t_{STIRAP} taken into account. Let us therefore first consider how to find the number of background correlations present at each tooth in the $g^{(2)}$ comb and later work out the time resolved contribution to the HOM. Recall from Section 2.3.5 that a histogram of the STIRAP times of the detections for a channel gave us the rate of background detections and therefore the total number of background detections and real photon detections in our gated window of interest, this can also be seen in Figure 3.9a. Thus we have the distributions

$$n_B^{(X)}(t) \qquad\qquad n_P^{(X)}(t) \tag{3.6}$$

$$\int_0^{T_{\mathrm{MOT}}} n_B^{(X)}(t)\mathrm{d}t = N_B^{(X)} \qquad \int_0^{T_{\mathrm{MOT}}} n_P^{(X)}(t)\mathrm{d}t = N_P^{(X)} \tag{3.7}$$

respectively describing the number of background (B) or legitimate photon detections (P) on detector X at time $0 < t < T_{\mathrm{MOT}}$ where $T_{\mathrm{MOT}} = 25\,\mathrm{ms}$, the total time for which the observations are made as the diffuse MOT transits the cavity. The number of background correlations introduced into the $g^{(2)}$ between detectors A and B at time difference τ by a background detection

on each detector is given by:

$$N_{BB}^{(A)(B)}(\tau) = \int_0^{T_{\mathrm{MOT}}} n_B^{(A)}(t) n_B^{(B)}(t+\tau)\mathrm{d}t \tag{3.8}$$

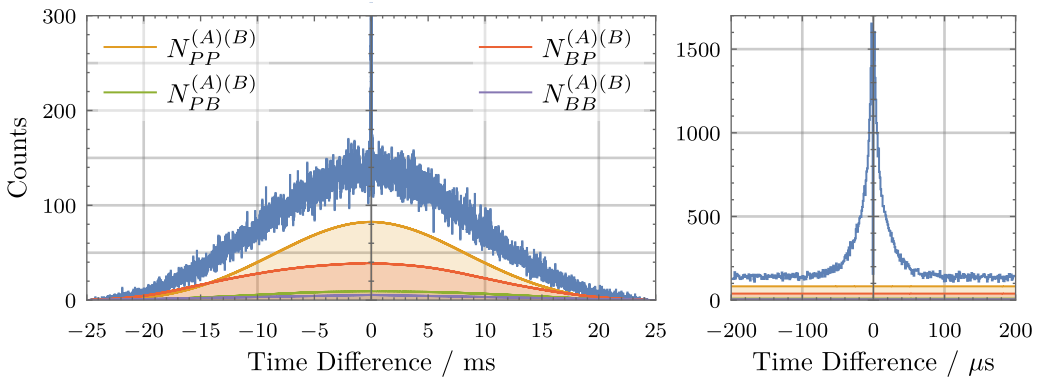
$$= \left(n_B^{(A)} * n_B^{(B)}\right)(\tau)\,. \tag{3.9}$$

The total contribution to the correlation background is the sum of the four pairwise combinations of background, B, and photon, P, detections:

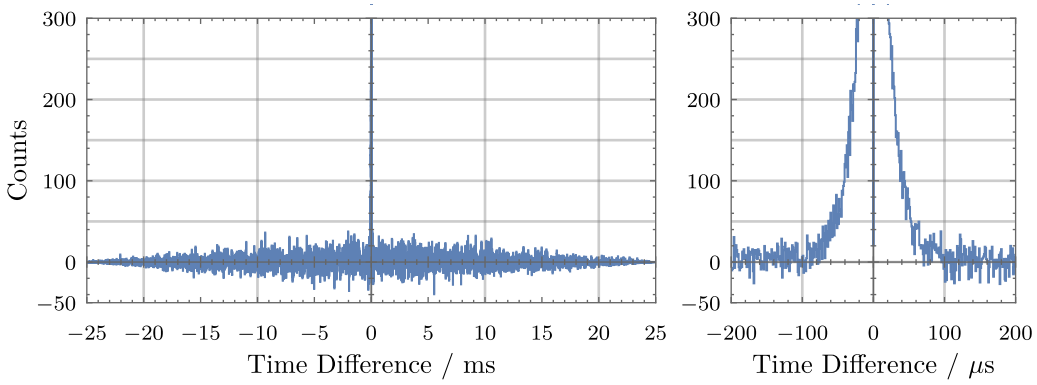
$$N_{\mathrm{total}}^{(A)(B)}(\tau) = N_{BB}^{(A)(B)}(\tau) + N_{BP}^{(A)(B)}(\tau) + N_{PB}^{(A)(B)}(\tau) + N_{PP}^{(A)(B)}(\tau)\,. \tag{3.10}$$

The term $N_{PP}^{(A)(B)}$ requires a brief explanation; are correlations between two photons not the signal of interest? As laid out above, $N_{PP}^{(A)(B)}$ assumes photon arrivals distributed according to $n_P^{(X)}$, a smooth continuous distribution from 0 to 25 ms. However, we know that photon arrivals are strongly bunched within this because of atom transits, $n_P^{(X)}$ is only the overall average of many many atom transits. It is correlations within these bunches that are of interest and these are seen as the sharp peak in Figure 3.7a and further resolved in Figure 3.7b. The contribution of $N_{PP}^{(A)(B)}$ to the large plateau of background correlations on which those of interest sit is therefore due to photons emitted from different atoms, traversing the cavity at random and thus represents the two-atom event background. When these four background contributions are taken together, the three pertaining to detector dark counts and the forth due to the random loading of atoms into the cavity, they account fully for all those correlations in the $g^{(2)}$ at times greater than the atom-cavity interaction time (Figures 3.7c and 3.7d).

The total number background of background correlations that have been included in our previously identified HOM correlations is therefore $N_{\mathrm{total}}^{(A)(B)}(0)$.



(a) All Correlations **(b)** Centre Zoom



(c) All Correlations Minus Background **(d)** Centre Zoom

Figure 3.7: HOM background estimation: (a) shows all the correlations between two detectors, stretching out to the 25 ms time limit for which the detectors are gated on. Only the central spike, shown in (b), is attributed to correlations between photons from the same atom, the approximately 100 μs interaction time is obvious. Also shown are the estimated contributions of the four background sources which should fully account for all not-same-atom photon correlations. When the subtraction is performed, (c) and (d), the correlations drop to zero everywhere apart from the remaining central spike, thus instilling confidence in the estimations. The correlations contributing to the HOM interference patterns, and the corresponding background estimates, are contained fully within the single central bin at zero time difference.

In order to correct for their presence in the HOM histogram we need to time resolve their contribution. As with the background contributions to the $g^{(2)}$ each of the four terms has its own time dependence which can be found using an analogous approach to above. We obtain from Figure 3.9a the time distribution of the the real photons and background within the 1 μs STIRAP interval, denoted $m_P^{(X)}$ and $m_B^{(X)}$ (note that because we are using the gated data, $m = 0$ for times outside of the gated interval). The areas of these individual distributions are not meaningful, we therefore normalise them to one. It is the area of their convolutions with one another that is important and these are the values we determined above. The number of background correlations in our HOM at time difference τ is therefore given by:

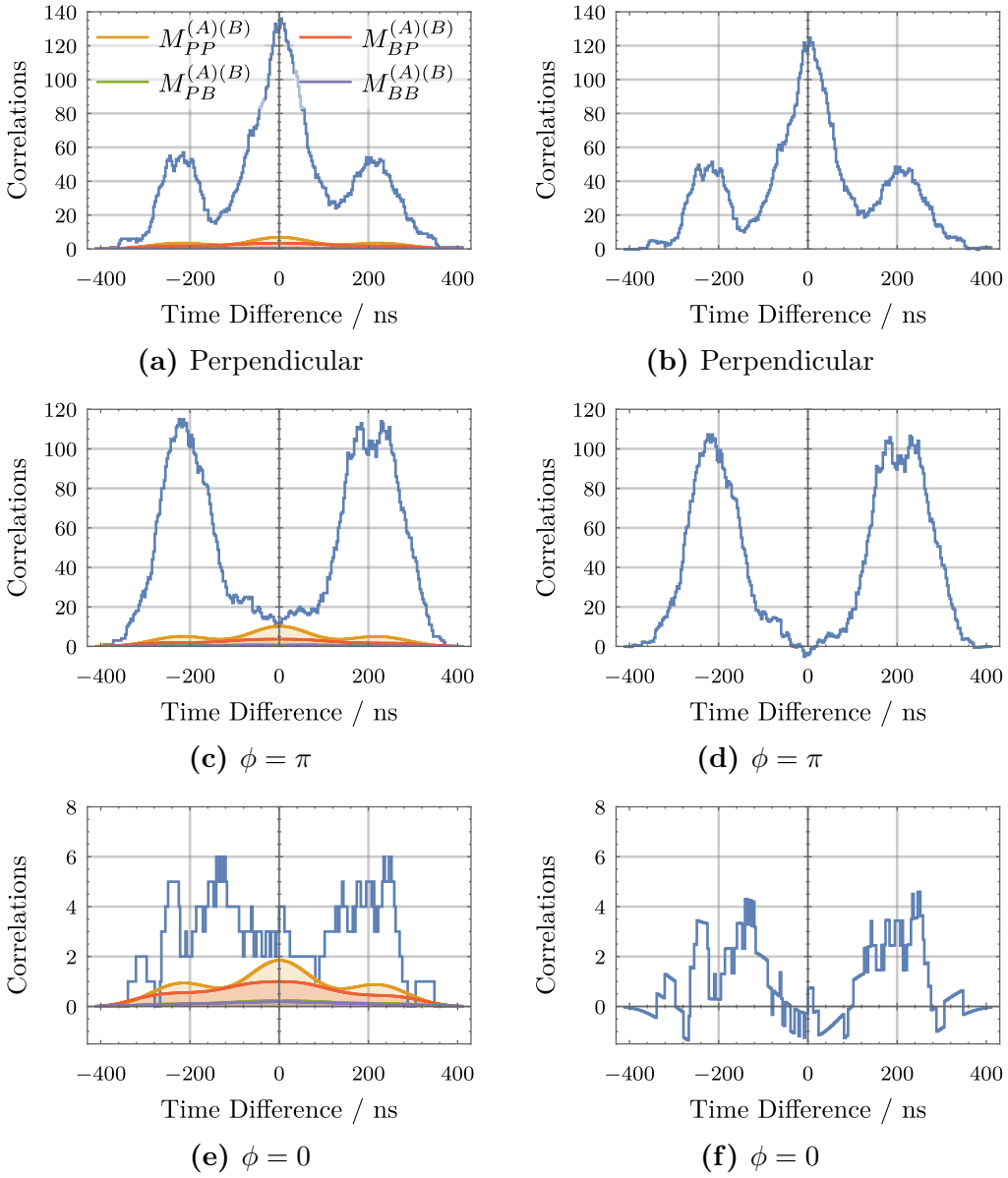
$$M_{BB}^{(A)(B)}(\tau) = \left(m_B^{(A)} * m_B^{(B)}\right)(\tau)\,, \tag{3.11}$$

normalised such that:

$$\int_{-T_{\mathrm{STIRAP}}}^{T_{\mathrm{STIRAP}}} M_{BB}^{(A)(B)}(\tau)\mathrm{d}\tau = N_{BB}^{(A)(B)}(0)\,. \tag{3.12}$$

The time-resolved background contribution to the HOM is then obtained by sampling these distributions with the same histogram parameters as that being used for the data. As one would expect, the majority of the correction occurs for times differences τ around zero, which has a marked impact for all those parallel HOMs; Figure 3.8 shows several examples.

A potentially disconcerting feature of our corrected HOMs (Figures 3.8b, 3.8d and 3.8f) is the deviation of the trace below the x-axis, seemingly suggesting a negative probability for correlations, which is obviously unphysical. However there are uncertainties associated with our data and it is shown in the next section that such deviations are within our expected error of

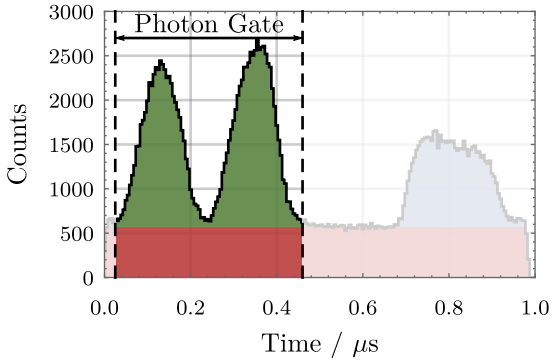


(a) Perpendicular **(b)** Perpendicular

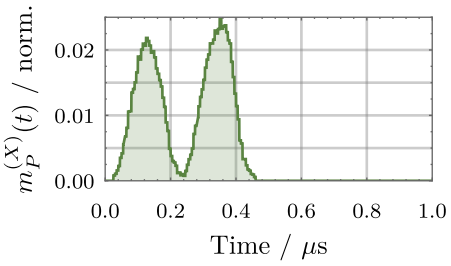
(c) $\phi = \pi$ **(d)** $\phi = \pi$

(e) $\phi = 0$ **(f)** $\phi = 0$

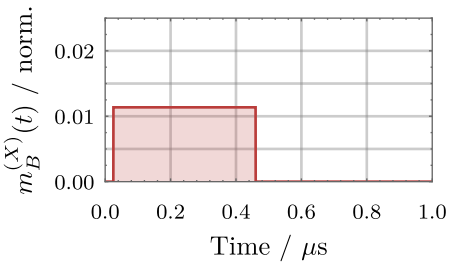
Figure 3.8: HOM background correction: The magnitude and relative contributions of the four background correlation sources are shown for three different cases. Notably the largest overall and relative contribution of the background is around time difference zero, indeed it appears to fully account for the otherwise unexpected correlations in the centre of the traces for both $\phi = \pi$ and $\phi = 0$. After accounting for the background the visibility increases from $V = 79 \pm 3\%$ to $V = 91 \pm 3\%$.



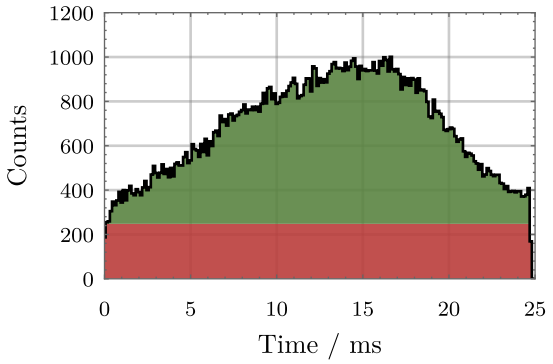
(a) STIRAP Histogram



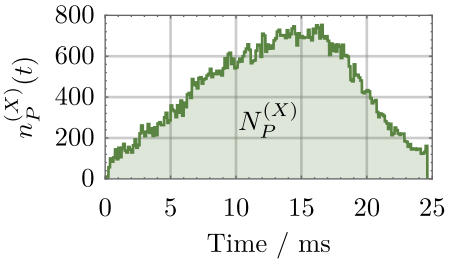
(c) Photon Distribution



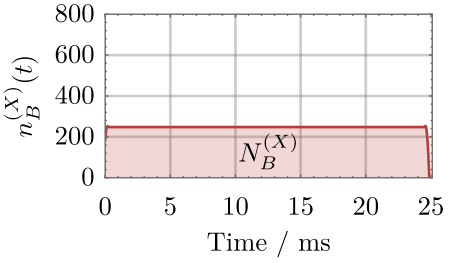
(d) Background Distribution



(b) MOT Histogram



(e) Photon Distribution



(f) Background Distribution

Figure 3.9: Overview of background estimation and correction: Initially all detections on a given detector are histogrammed according to their arrival time relative to the repeating 1 μs long STIRAP generation time (a). From this the window of times potentially corresponding to legitimate photons is identified along with the background level of dark counts. The distribution of photon and background arrival times within this window are then extracted, (c) and (d), for use in calculating the temporal dependence of the background within the HOM. Those detections within the gated window are also histogrammed according the their arrival time in the 25 ms MOT throw window (b), again split into distributions for real photons an dark counts, (e) and (f), which are then used to calculate the total magnitudes of the background contributions in the HOM.

measurement.

3.5.4 Normalisation

The final step necessary to recreate $P_{\text{joint}}(\tau)$, and to allow comparison between different experimental runs is to normalise the data - the plots in Figure 3.8 still display numbers of correlations per bin, not probabilities yet. We therefore need to know how many individual photon-pair experiments were performed, i.e. how many photon pairs were actually input to our beam splitter, N_0. With ideal detectors, capable of number resolving and with no dead time, the situation would be simple, we would count not only the number of correlations between detectors but also the correlations on one and the same detector, the total would give us our normalisation constant. Unfortunately as has been discussed before, we are unable to do this. With heralded sources the detection of the herald(s) signals that a photon (pair of photons) has entered the optical network of interest, the total number of heralded events is the normalisation constant (provided one also considers the heralding efficiency).

If we wanted to trust that the rate of photon generation, and sequential-photon-pair generation from the apparatus remained constant then we could simply normalise by the total number of MOT throws contributing to an experimental run. This would however only allow for comparison of results between experimental runs and would not provide an absolute normalisation permitting quantitative comparison to the theory. The performance of the apparatus however is far from constant, varying due to many slowly changing parameters.

Our solution is to look at the $g^{(2)}$ (Figure 3.7d). We observe a great

number of 'correlations' at time differences with $|\Delta\tau| > 1\,\mu$s, where our photons cannot have interacted - they were not concurrent within the apparatus. These 'correlations' occur so separated in time that we are not limited by any of our detector imperfections, therefore we are able to count the total number of these events, including those where both photons went to the same detector. The total number of 'correlations' separated by two STIRAP intervals form the basis for our normalisation constant, $N_2 = g^{(2)}(-2) + g^{(2)}(2)$. We must consider though that for an atom with a finite interaction time there are more opportunities to emit two sequential photons than there are for two photons separated by $n > 0$ STIRAP intervals. For large interaction time and small n the difference is minimal and fortunately this is the regime we are in, our interaction time is 50–100 μs and as can be seen in Table 3.1 the correlations observed at $g^{(2)}(\pm 2)$ are predominantly due to emissions separated by $n = 1$ STIRAP intervals. Therefore we are happy that the total number of 'correlations' observed separated by two STIRAP intervals is a good approximation of the total number of input photon pairs, with one modification as follows. Recall from Section 2.3.4 that between the cavity and the HOM

Emission	$\mathcal{LS}$	$\mathcal{SS}$	$\mathcal{LL}$	$\mathcal{SL}$
● ●	0	1	1	2
● ○ ●	1	2	2	3
● ○ ○ ●	2	3	3	4
⋮	⋮	⋮	⋮	⋮

Table 3.1: Photon emission delay arm branching: The table shows, for different emission patterns (● - photon emission, ○ - no emission), the $\Delta\tau$ value of the peak in the $g^{(2)}$ in which the correlations will be recorded depending on how the photons branch at the beam splitter before the delay arm. A coincident detection (red), can only occur for a sequential emission of two photons with the first photon entering the delay arm, $\mathcal{L}$ and the second entering the short arm $\mathcal{S}$. The normalisation constant is based on the number of correlations at ± 2 in the g2 (blue), for which there are four times as many pathways.

beam splitter there is a random routing of photons into one of two paths of

different lengths, one short, $\mathcal{S}$, and the other 200 m of optical fibre longer, $\mathcal{L}$, thus delaying one photon with respect to the other and providing concurrent pairs. Table 3.1 shows that for an interfering correlation there is only one possible route (highlighted red): two photons emitted sequentially with the first entering the long path and the second the short. However for those 'correlations' at $\Delta\tau = \pm 2$ we see there are four routes (highlighted blue) and therefore we expect four times as many correlations at ± 2 in total, N_2, than at 0. Our final normalisation constant N_0, representing the total number of input pairs, is therefore the total number of pairs observed at ± 2 divided by four. Note however that the prefactor 1/4 assumes that both paths $\mathcal{S}$ and $\mathcal{L}$ incur identical losses, an assumption we know to be not true as the long path incurs additional losses both within the fibre and more prominently due to the additional coupling required. More reasonable then would be to assume path $\mathcal{L}$ is only $\eta_{\mathcal{L}}$ as efficient as path $\mathcal{S}$ giving a prefactor of

$$\frac{\eta_{\mathcal{L}}}{1 + 2\eta_{\mathcal{L}} + \eta_{\mathcal{L}}^2} \tag{3.13}$$

which is only 1/4 in the limit $\eta_{\mathcal{L}} = 1$. Investigation of this expression shows that for reasonable values of $\eta_{\mathcal{L}}$ the approximation of 1/4 is very good. Experimentally $\eta_{\mathcal{L}}$ is measured as 0.72 ± 0.03 giving a prefactor of 0.243 ± 0.001 and therefore normalisation is calculated as $N_0 = 0.243 N_2$.

The final step to generate the histograms as shown in Figure 3.4 is to not only divide by N_0 but also by the histogram bin width (as is standard for histograms), thus producing the units correlation probability density. If we multiply the ordinate coincidence probability density values (which have dimensions of inverse time) by the photon length, and divide the abscissae by the same, then we obtain our results in the same dimensionless format as

the theory presented in Section 2.2 and we may thus compare our results to the theory with no free parameters. The agreement is very good, shown in Figure 3.10.

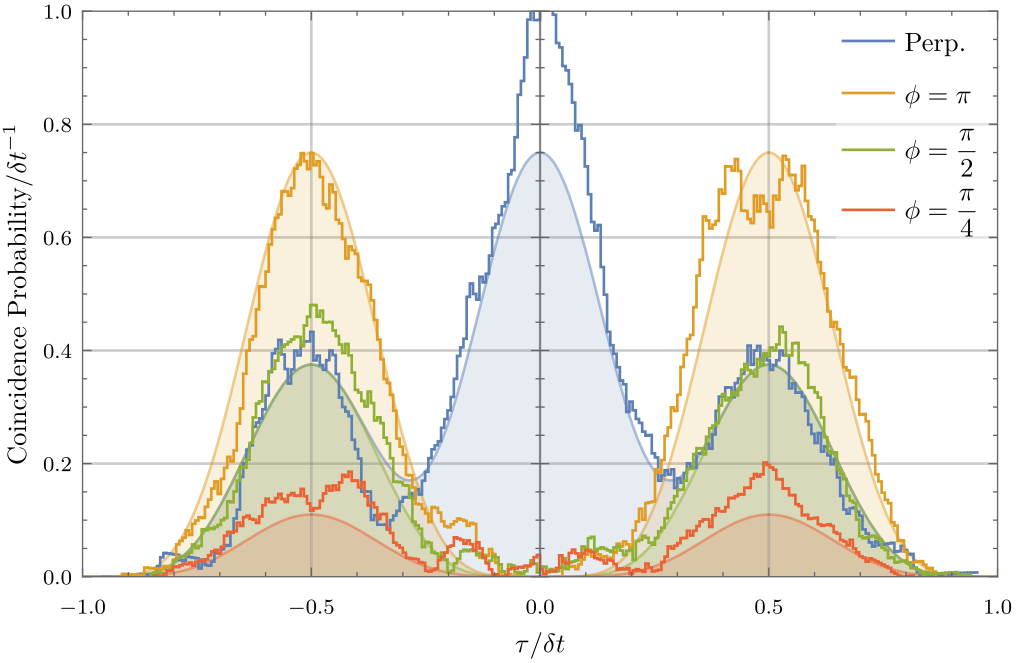


Figure 3.10: HOM zero parameter theory comparison: The same coincidence probability data from Figure 3.4 is here further normalised by the photon length (430 ns) thus allowing a dimensionless comparison to the theory (shown in isolation in Figure 3.2). The smooth theory curves are shown with shading behind the data. There are no free parameters in the theory curves, they are simply the expected distributions for $\sin^2$ photons. The agreement is excellent.

3.5.5 Errors

Thus far the HOM traces presented have been shown without any indication of the degree of uncertainty in the data, in this section we consider the sources of uncertainties and examine their effect. The predominant uncertainty is the standard $\sqrt{N}$ Poissonian error from the number of elements in

a histogram bin. The additional manipulations performed above to account for the background and normalise the data do not alter the uncertainty. The background correction is based on the averages of hundreds of thousands of detection events, and therefore has no appreciable error. Also, the normalisation constant is calculated from several thousand detections, roughly four-fold more than the HOM data itself, and consequently its impact on the total error is negligible when the data is subdivided into histogram time bins. The only situation in which the uncertainty on the normalisation might be considered is when the HOM data is taken as a whole, as in Figure 3.5, however even then here it only accounts for less than 10% of the total error.

The magnitude of the uncertainties in the histograms is indicated in Figure 3.11 and it can be seen that any probability excursions below zero are within error of zero which puts us at ease. Furthermore the overlap with the theory is excellent, demonstrating clearly the high degree of control we are able to exert over the photons' properties, this is quantified in Section 3.7 using the fidelity. The only reasonable deviation from the expected trace is for $\pi/4$ where the slight decoherence towards the limits of the photons has more of an impact.

A final note about $\sqrt{N}$ errors. The use of symmetric $\pm\sqrt{N}$ error bars on the number of events, N, in a histogram time bin is commonplace and well justified because the number of events is a random variable drawn from a Poisson distribution and therefore has a variance equal to the mean. However such error bars rarely cover the 68% of the distribution of the true value of the variable as they should, especially for small N when the distribution becomes increasingly asymmetric. The inadequacies of $\pm\sqrt{N}$ error bars have been well documented and better solutions proposed [114]. Although they are deemed (just) satisfactory for presenting the data in this chapter, in Chapter 4 a

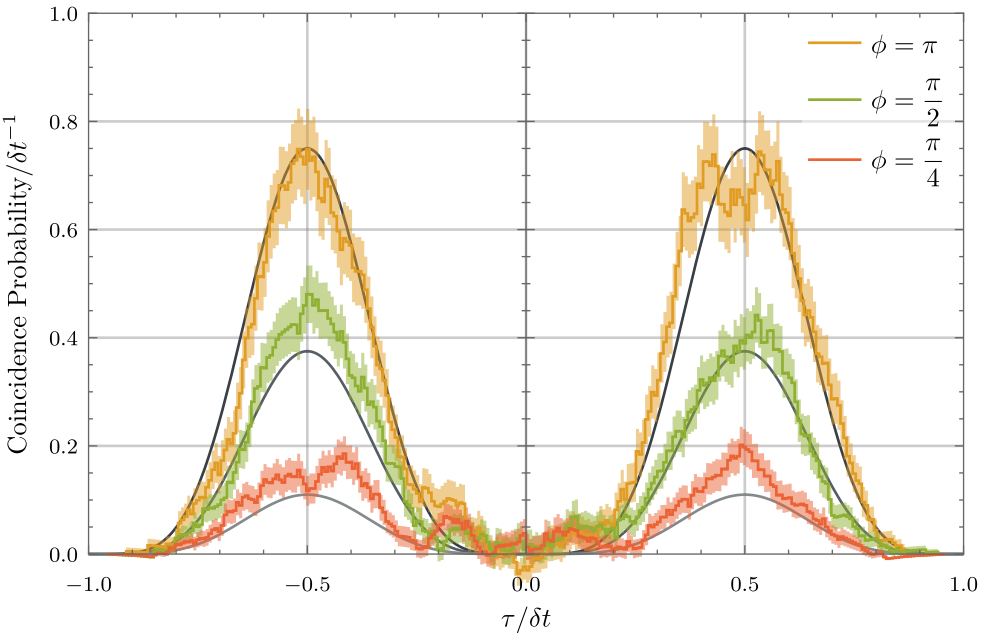


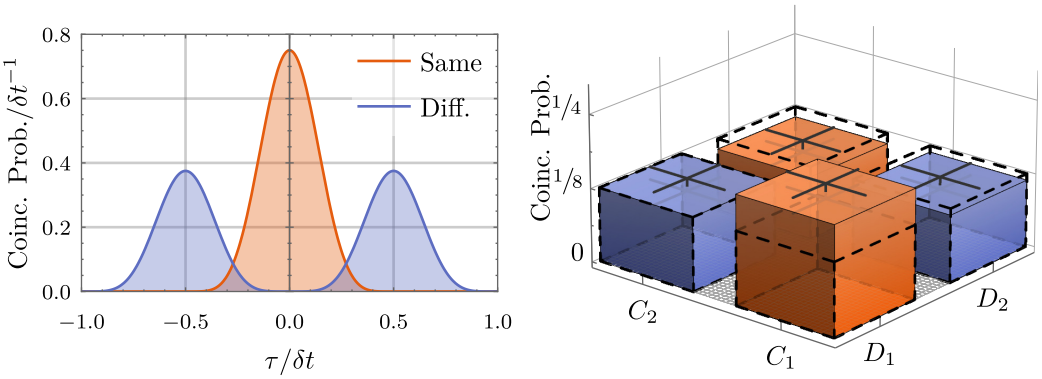
Figure 3.11: HOM error bounds: The same time-resolved coincidence probabilities as before are shown (solid coloured lines) along with the corresponding one standard deviation uncertainty at each data point (shaded). The errors are calculated by propagating the $\sqrt{N}$ uncertainly for the total number of correlation in a histogram bin. Also shown are the theory curves (solid grey) for the three traces.

more nuanced treatment is necessary. Maximum likelihood estimation is used to preclude unphysical probabilities whilst Monte Carlo methods are used to propagate the uncertainties, the final strongly asymmetric error bars are then found as the limits of the highest posterior density interval.

3.5.6 Discretised Time Bins

The histograms presented so far demonstrate the two different behaviours very well: no correlations for same time bin detections and a phase dependent number of correlations for sequential time bin detections. However the two regions are not well separated and technically overlap for the central half of

the histogram. Within a small region the overlap is not negligible as can be seen in Figure 3.12a. However this overlap is merely an artefact of the method of displaying the data and is unnecessary given we know exactly during which time bin photons were detected and therefore which behaviour bin they should be in. We can actually consider the correlations between virtual detectors, corresponding to each detector in each time bin (as shown in the equivalent physical circuit Figure 3.6). The equivalence of the continuous time and discretised pictures can be seen clearly in Figure 3.12 and the phase dependence of the satellite peaks is even more pronounced in this picture as shown in Figure 3.13

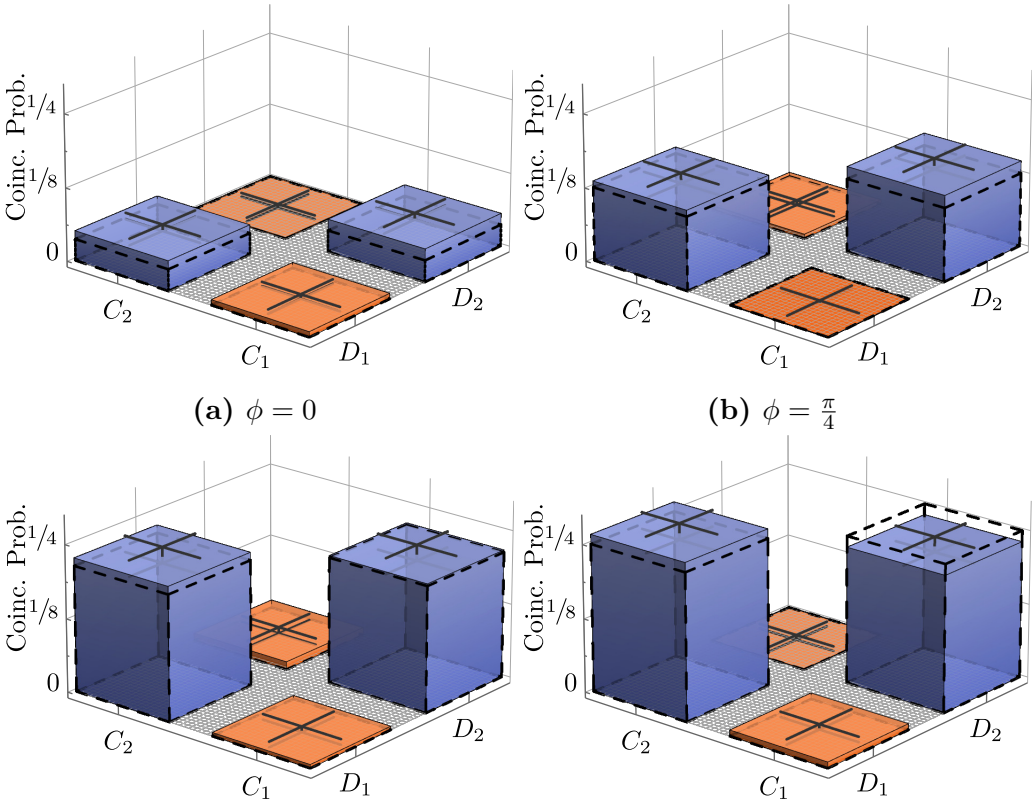


(a) Time-Resolved HOM **(b)** Time-Binned HOM

Figure 3.12: Time-binned HOM: The time-resolved correlations can be split explicitly into four bins described by which detector fired in which time bin. The correspondence between the continuous and discretised signal can be seen where the red correlations correspond to same time bin detections and the blue to successive time bin detections. The discretise data is shown along with the theoretically expected values, delineated by dashed cages, and the associated error, extended crosses.

3.6 Results - Qutrits & Ququads

Extending the scheme to generate temporally encoded qutrits is trivial. A triple peaked STIRAP pulse, designed either by repeating the algorithm



(a) $\phi = 0$ **(b)** $\phi = \frac{\pi}{4}$

(c) $\phi = \frac{\pi}{2}$ **(d)** $\phi = \pi$

Figure 3.13: Time-Binned HOM results: A selection of the previous continuous time-resolved HOMs are shown binned according to exactly which detector fired during which time bin. Detections in the same time bin are coloured red, successive time bin detections in blue. The dashed cages represent the theoretically expected values and the crosses show the one standard deviation error in each detection bin.

for a 3-peak structure, or by prepending a 1/3 efficient single pulse to the qubit waveform, results in the qutrit photon shown in Figure 3.14. The relative height of the three peaks suggests the driving shape used was not quite accurate as a lower central peak is not explained by a simple driving pulse power imbalance which could only skew the distribution as a whole. This state has two free phase differences which we are able to control in the same manner as within the qubit. The corresponding HOM trace shows a reference five-peak structure with perpendicular photons, as expected from the autocorrelation of the intensity envelope (for n peaks there will be $2n-1$ in the autocorrelation). The central peak is again missing in the HOM signal with parallel polarisation and the satellite peaks reveal relative phase changes within the signal photon (Figure 3.15).

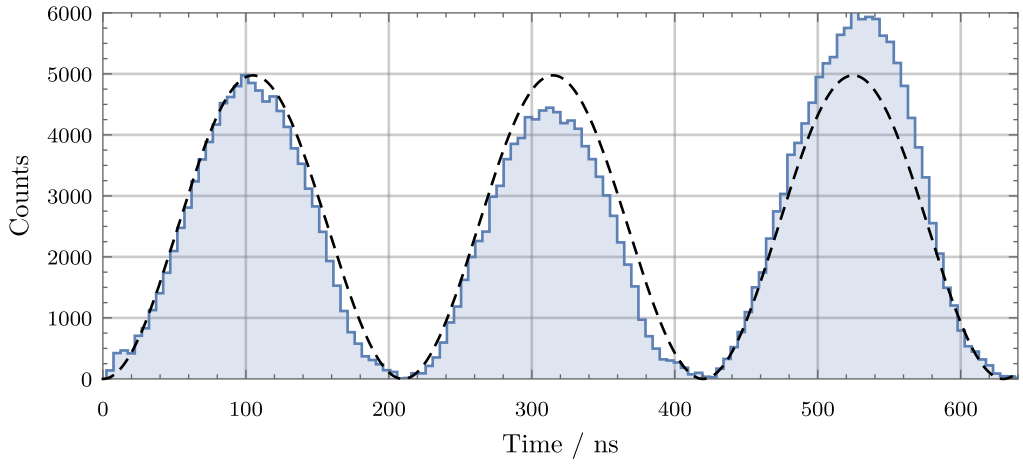
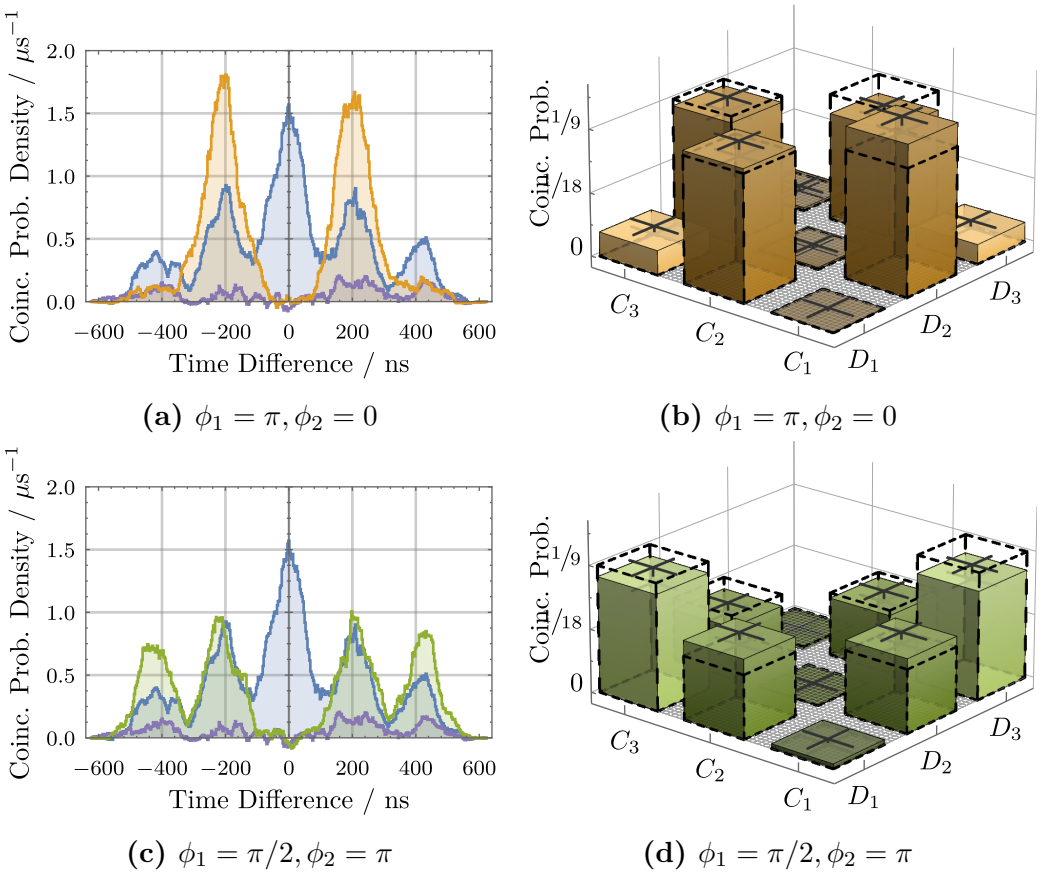


Figure 3.14: Qutrit photon shape: A histogram of qutrit photon detections showing the triple humped intensity envelope. There is slight deviation from the desired $\sin^2$ profile shown dashed.

The equivalent virtual circuit, shown in Figure 3.16 is now even more complex requiring seven beam splitters to achieve what is actually done with just one. Furthermore we are now simulating six virtual detectors with just two real ones. Although the resource savings on the right hand side of the circuit



(a) $\phi_1 = \pi, \phi_2 = 0$ **(b)** $\phi_1 = \pi, \phi_2 = 0$

(c) $\phi_1 = \pi/2, \phi_2 = \pi$ **(d)** $\phi_1 = \pi/2, \phi_2 = \pi$

Figure 3.15: Qutrit HOM interference: The time-resolved interference patterns measured for qutrits with phase shifts of $\phi_1 = \pi$, $\phi_2 = 0$ (yellow) and $\phi_1 = \pi/2$, $\phi_2 = \pi$ (green) are shown alongside reference patterns measured with orthogonally polarised photons (blue) and parallel polarised photons with no phase shifts (purple). Also shown are the time-binned patterns with theory cages and error markers.

for measurement are present in any temporal encoding, the additional savings of those resources on the left necessary for state preparation are unique to our source which generates states in de facto temporal superpositions.

The correlations for the qutrit states are shown both as a time-resolved HOM and as the matrix of correlations between virtual detectors in Figure 3.15.

A final demonstration of the technique is given in Figure 3.17 which shows

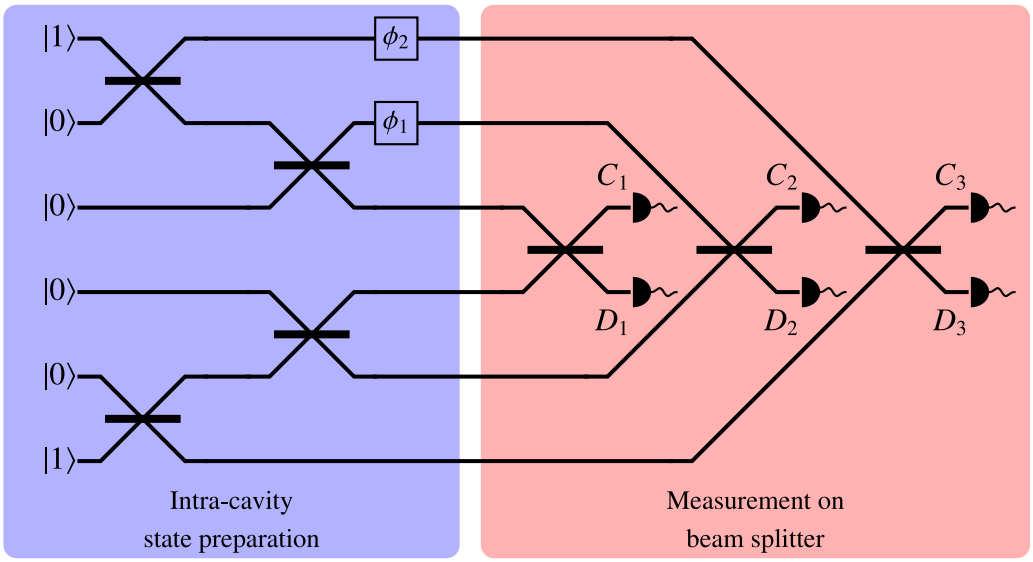
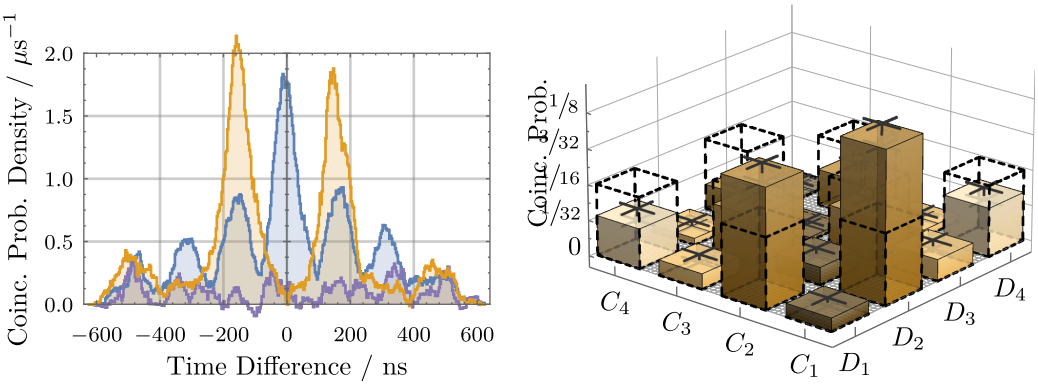


Figure 3.16: Dual-rail equivalent circuit for qutrits: The equivalent dual-rail encoded circuit necessary to replicate the operations performed by the time-bin encoded qutrits from the cavity requires even more resources than that for the qubits in Figure 3.6. Four beam splitters and two phase shifts are required to produce the qutrits which are generated in cavity without any resource overhead, and six detectors would be required to do the job of just two in the time domain.

the correlations of a ququad state for which there are three free phases. The results are shown for the state

$$|\Psi\rangle = \alpha|0\rangle + \beta e^{i\pi}|1\rangle + \gamma e^{i0}|2\rangle + \delta e^{i\pi}|3\rangle\,. \tag{3.14}$$

The driving waveform was not balanced as carefully as those for the qubits and qutrits and consequently the coefficients α, β, γ, and δ were not equal, leading to the excess in correlations between time bins 1 and 2. However the results do show the ability to generate and control the phase over four time bins.



(a) $\phi_1 = \pi, \phi_2 = 0, \phi_3 = \pi$ **(b)** $\phi_1 = \pi, \phi_2 = 0, \phi_3 = \pi$

Figure 3.17: Ququad HOM interference: The time-resolved interference pattern measured for ququads with phase shifts of $\phi_1 = \pi$, $\phi_2 = 0$, $\phi_3 = \pi$ (yellow) is shown alongside reference patterns measured with orthogonally polarised photons (blue) and parallel polarised photons with no phase shifts (purple). The time-binned pattern is shown with theory cages and error markers.

3.7 Conclusions

This chapter has demonstrated the deterministic generation of temporally encoded qudits in photons up to 640 ns long. That the time-bin encoding takes place upon photon generation provides significant advantages in terms of reconfigurability (see Chapter 6) and loss when compared to systems which rely on variable amplitude attenuation [115], phase modulation [116], or interferometric techniques for photon shaping [106]. The availability of time bins as an additional degree of freedom to LOQC is another step towards large-scale quantum computing in photonic networks [117]. The utility of time-bin encoded qudits is likely to be further enhanced by single-qubit operations, implemented with phase-coherent optical delay lines and active optical routing to either switch between temporal and spatial modes, or to swap the two time bins.

We have shown the extensibility of the time-bin encoding method by creating up to four discrete time bins within a single photon. Technologically

the bandwidth of the AOM limits the rate at which we can shape the STIRAP driving beam and consequently the number or density of time bins within any single photon; this limit is easily lifted by using an EOM. Fundamentally the encoding density is limited by the requirement for adiabaticity and the linewidth of the cavity. The observed upper limit of around 600 ns for the coherence length of the photons (limited by sources such as stray magnetic fields, cavity length drift, and laser stability), and the cavity linewidth of around 24 MHz suggest that currently we could achieve a maximum of 10-15 time bins.

3.7.1 Fidelity of the Qudit Preparation

To determine the fidelity of the state preparation, we must first reconstruct the density matrix $\hat{\rho}$, for which a couple of assumptions must be made. Firstly the values on the diagonal are proportional to the square root of the number of correlations detected in time bin 1 and 2, normalised to one, for the two-photon coincidence measurement of perpendicular photons. Secondly, we assume that signal and LO photons only differ in phase, such that their off-diagonal elements only differ in sign. Their magnitude is given by the ratio of the square root of the maximum observed to the maximum possible side peak visibility. Thus for the qubit with $\phi = \pi$ we obtain

$$\hat{\rho} = \frac{1}{2}\begin{pmatrix} 1.01 & -0.85 \\ -0.85 & 0.99 \end{pmatrix} . \tag{3.15}$$

The fidelity is then found using the standard formula $F\left(|\psi\rangle, \hat{\rho}\right) = \sqrt{\langle\psi|\hat{\rho}|\psi\rangle}$ [21] which gives 0.96 ± 0.01 for the above case, where our reference state is $|\psi\rangle = (|10\rangle - |01\rangle/\sqrt{2}$. An equivalent procedure yields fidelities of 0.94 ± 0.01

and 0.89 ± 0.02 for qutrits and ququads, respectively.

In addition to decoherence from uncontrolled sources (predominantly stray magnetic fields), the other factor likely limiting the fidelity is the variation in the exact photon envelope due to the random position of the atom in the cavity. This could be significantly mitigated by trapping the atom in the cavity, thus limiting the variance of the atom-cavity coupling strength and Rabi frequency experienced by the atom.

Chapter 4

Operation of a Linear-optical CNOT Gate

4.1 Introduction

The paradigm of linear optical quantum computing [58], whereby photons are used as information carries and linear optical elements are used to process the quantum information, has enabled new application of quantum technologies [118] and phenomena [119]. Typically such processing is implemented with bulk optics and spontaneous sources. However more advanced processing requires more complex optical circuits as well as greater numbers of photons, for which spontaneous sources require increasing overheads. The availability of integrated photonics has solved one half of this scalability problem, providing low loss, interferometrically stable optical circuitry in centimetre scale packages. Artificial atoms, such as quantum dots and diamond colour centres can yield photons deterministically thus offering a solution to the photon

side of the scaling problem [74, 120, 121]. Our real atom, in a high finesse optical cavity is also an excellent deterministic source of narrowband single photons, which, it has already been shown, provides unparalleled control over most properties of the photon (Chapter 3). An additional attractive feature of atom-cavity sources for quantum information processing is that they are naturally isomorphic to the stationary-node – flying-qubit picture of quantum networking [34, 37] and have already demonstrated mapping of the atomic states to photons [84, 102, 112] and generating photon-atom and distant atom-atom entanglement [40, 41].

In this chapter we demonstrate the operation of the quantum-controlled not (CNOT) gate within an integrated photonic chip with photons from the atom-cavity source, interfacing two hitherto separate systems; the work can be found in [122]. The CNOT operation is an excellent choice for demonstrating quantum photonic logic as it requires both quantum and classical interference [123]. The two-qubit gate negates the state of the Target qubit, conditional on the state of the Control and operates in the post selected coincidence basis with a 1/9th success probability. The CNOT is also important as it can generate maximally entangled states from separable inputs and can with the addition of linear optical quantum non-demolition measurements and single qubit gates, be used to build a quantum computer [60].

Details of the photon chip used follow in Section 4.1.1 along with initial characterisation measurements in Section 4.1.2. The theory of its operation is described in Section 4.2. The results of the operation of the CNOT gate along with details of the analysis performed are presented in Section 4.3. Finally in Section 4.4 we verify the generation of entanglement on the chip.

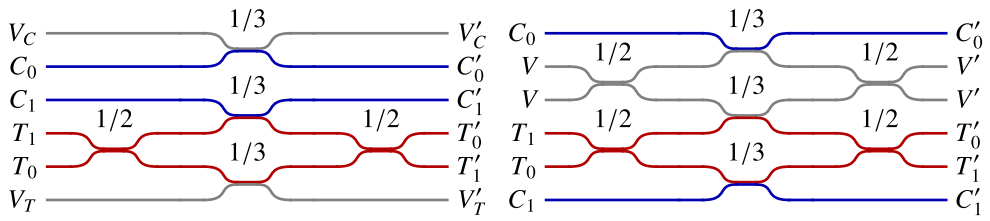
4.1.1 Photonic Circuit

The integrated photonic circuit is a simple network of single-mode waveguide directional couplers, shown in Figure 4.1b, and was provided by our collaborators in Bristol. It was fabricated lithographically using germanium and boron doped silica on a silicon substrate. The waveguides have a square 3.5 μm $\times$3.5 μm core which is comparable to the 4-5 μm core of single mode fibres at 780 nm. A refractive index contrast $\Delta = ({n_{\text{core}}}^2 - {n_{\text{cladding}}}^2)/2{n_{\text{core}}}^2 = 0.5\%$ is chosen such that the waveguides only support the fundamental mode at 780 nm. The full quantum process for this exact chip has already ben performed using nm bandwidth NIR photons generated via spontaneous parametric down conversion, with a coherence length in the 100 μm range [62].

Coupling to the chip is by way of polarisation maintaining fibre arrays. For preliminary chip experiments these arrays were buttcoupled to the chip with index matching fluid used to facilitate the coupling. This however results in time varying coupling efficiencies as the fluid evaporates and the alignment itself drifts. For the experiments presented in this chapter the fibre arrays were glued to the chip with an optical adhesive which left us with an average loss across the chip from input fibre to output fibre of $\sim$ 3.3 dB (this was measured with a CW laser at 780 nm).

Inscribed in the chip are three 1/3 and four 1/2 directional couplers, laid out as shown in Figure 4.1b, such a configuration is known colloquially as a CNOT4. It can be seen that this is very similar to a standard CNOT photonic circuit (shown alongside) but with two additional 1/2 couplers. To perform an analogous CNOT operation we therefore use a modified waveguide labelling as indicated in Figure 4.1.

The splitting ratios of the directional couplers are controlled by litho-



(a) CNOT Photonic Circuit **(b)** CNOT4 Photonic Circuit

Figure 4.1: CNOT and CNOT4 photonic circuit diagrams: (a) shows the layout and labelling of the waveguides and directional couplers typically used to implement the CNOT gate using dual rail encoding. (b) shows the layout of the CNOT4 chip used in this chapter which has two additional 1/2 couplers. The colouring illustrates how the CNOT4 can be labelled to behave equivalently to the CNOT chip — mixing the vacuum modes is inconsequential.

graphically tuning the separation between the waveguides and the length of the couplers. However, due to slight variations in the manufacturing the 1/2 couplers do not have a 'reflectivity'[1] of 1/2 but instead are in the range 0.49-0.54; measured using 780 nm CW input into waveguides A, F, A', F'. Unfortunately it is not possible to measure the reflectivities of the 1/3 couplers. However in the construction process the 1/2 couplers are most sensitive to errors in coupler length, and therefore deviations in the splitting ratios of the 1/3 couplers from ideal are expected to be minimal. As mentioned in the introduction one huge advantage of integrated photonic circuits is that they provide phase stable interferometers. However, again due to slight imperfections in construction, the two interferometers in the interior of the chip contain non-zero phases, instead they measure $\phi = 0.24\pi$ and $\phi = 0.09\pi$. These experimental imperfections are all shown in Figure 4.2.

[1]Strictly speaking a directional coupler does not reflect light in the same manner as a beam splitter however using the same terminology can be useful. Light will either cross from one waveguide to the other - the equivalent of transmission, or not - the equivalent of reflection.

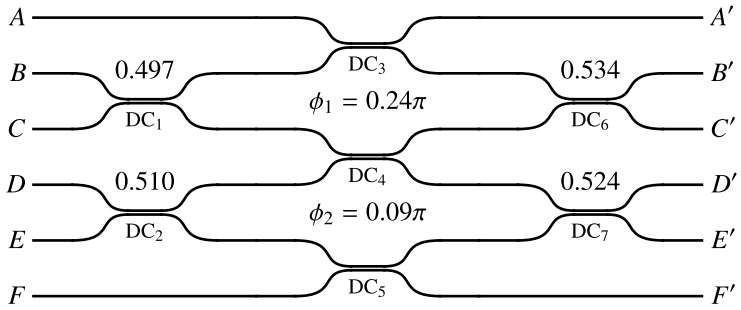


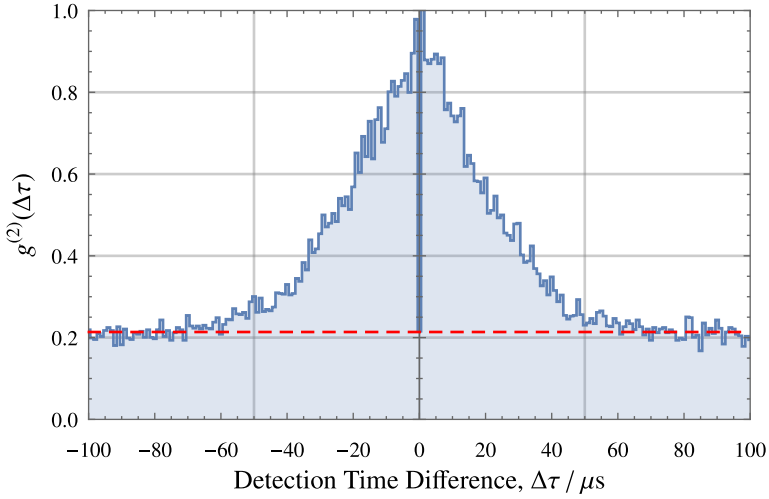
Figure 4.2: Photonic chip imperfections: The values of the reflectivities of the directional couplers and the phases in the two interferometers on the chip differ from the ideal due to imperfect control in the manufacturing process. The exact reflectivities of the 1/2 couplers, and the phases in the two interferometers are shown. A sequential labelling of the waveguides is occasionally useful, particularly when performing measurements not pertaining to the CNOT operation, the convention above is adopted in such situations.

4.1.2 Circuit Based Source Characterisation

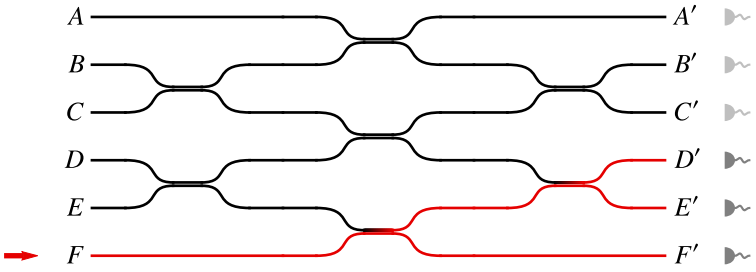
As mentioned previously, the CNOT gate operation requires both quantum and classical interference. We therefore first perform a simple two-photon HOM, which not only shows the indistinguishability of the source but also the degree of quantum interference realised on chip. In addition we demonstrate the ability to fully characterise our source on-chip by also measuring a $g^{(2)}$.

A stream of single photons were input into waveguide F as shown in Figure 4.3b. Following the action of the 1/3 and then 1/2 directional couplers photons should arrive randomly at one of the three outputs $D'-F'$ with equal probability. By inspecting the correlations between the three detector pairs ($D'E'$, $D'F'$, and $E'F'$) we measure the second-order correlation function shown in Figure 4.3a. The atypical envelope of the correlation function is due to the intermittent operation of the source as explained in Section 2.3.5. The value $g^{(2)}(0) = 0.15$ is at the background level caused by detector dark counts, the shot noise imposes an upper limit of $g^{(2)}(0) < 0.02$ to the photon

stream at the one-sigma confidence level.



(a) HBT

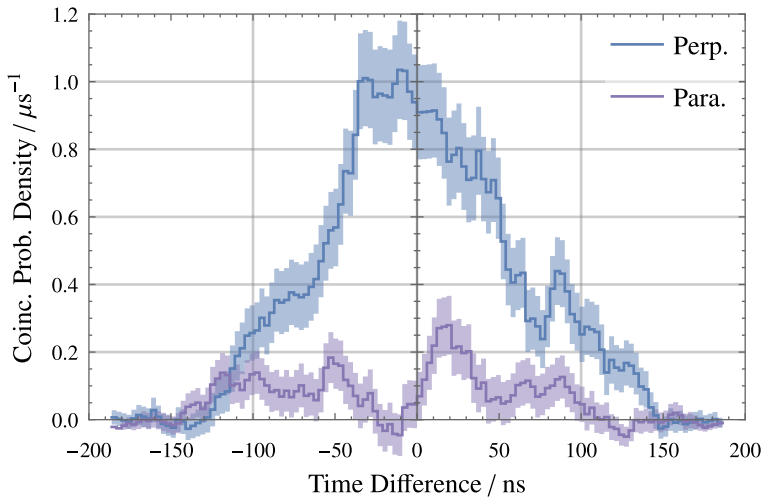


(b) Chip Configuration

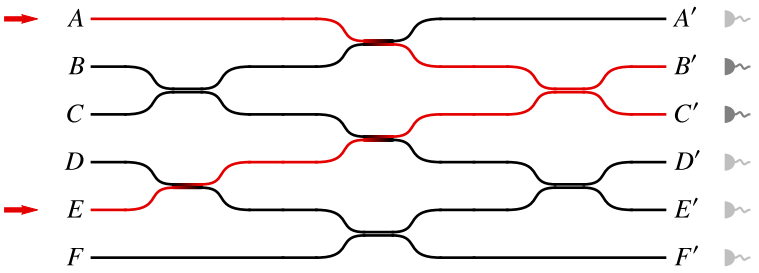
Figure 4.3: On-chip $g^{(2)}$: The second-order correlation function is measured as shown in (b) by inputting photons into a single waveguide (F) and observing correlations between all pairs of the three possible output detectors D', E', and F'. The central value $g^{(2)}(0) = 0.15$ is at the background level due to detector dark counts (dashed line); the restricted temporal envelope shows the 60 μs atom cavity interaction time.

The degree of quantum interference, and thus the mutual indistinguishability of two photons, is verified by time-resolved HOM interference. Photons are launched into waveguides A and D, after which they interfere on a single 1/2 coupler in front of detectors monitoring chip outputs B' and C'. The probability of coincidences between the two detectors is recorded as a function of detection time difference as shown in Figure 4.4a. Upon transitioning

from non-interfering photons of orthogonal (perpendicular) polarisation to interfering photons of identical (parallel) polarisation, the likelihood for coincidences drops by $85 \pm 5\%$. This is consistent with the visibility measured using photons from the source off-chip on a standard fibre beam splitter thus suggesting very good quantum behaviour of the photons in the integrated environment. The chip itself has been shown to achieve $V = 95 \pm 5\%$ at similar wavelengths.



(a) HOM



(b) Chip Configuration

Figure 4.4: On-chip HOM: Photons input into waveguides A and E interfere at the 1/2 directional coupler in front of detectors at outputs B' and C'. The coincidence probability drops by $V = 85 \pm 5\%$ when switching from non-interfering perpendicularly polarised photons to interfering parallel polarised photons.

4.2 LOQC Model

The operation of the CNOT gate as implemented by the photonic networks presented above (Figure 4.1) can be understood purely heuristically: A sign change in the interferometer formed by the splitting and remixing of the target modes occurs conditional on the presence of a photon in the C_1 mode - thus changing the output waveguide of the target photon. However in order to make predictions about the operation of the chip in more complicated cases and assess the implications of the imperfections of the chip it is necessary to formally model the behaviour of photons through the chip.

I adopted an approach similar to that presented in [124] where the behaviour of a photonic network for the many particle (photon) input is derived by summing the multiple amplitudes for the single particle time evolution. This method gives us the probabilities of all possible output configurations for a given input but not the phases between the particles at the output. However given we cannot measure such properties this does not limit the utility of the method. We could also calculate the expected behaviour of the circuit in the Schrödinger picture using the Heisenburg equations relating the input modes to output modes as done in [123] which would give us the full output state. However this becomes increasingly tedious as the circuit size or particle number increase. The model is not limited to bosons, it is also able to predict the behaviour of fermions and distinguishable particles under a unitary, by taking into account the relevant exchange symmetries. This is used in the following section to validate the observed behaviour of the circuit with orthogonally polarised photons, and in the following chapter where phases between photons produce fermionic behaviours.

We must first describe the action of the circuit on one particle. A 50-50

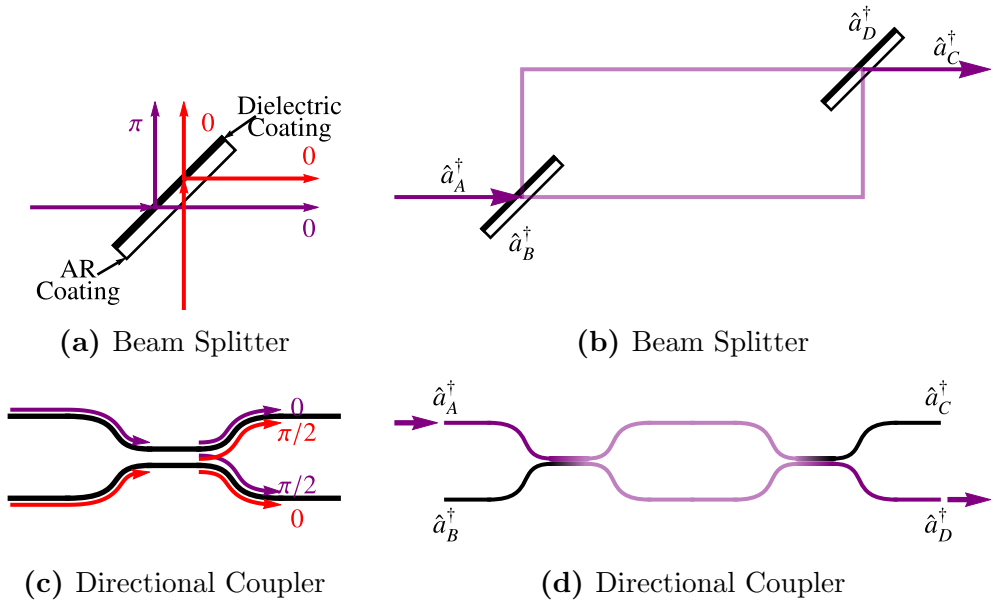
beam splitter is often described by the following matrix where the entries detail how the splitter divides the amplitudes present in each of the inputs:

$$H = \frac{1}{\sqrt{2}} \begin{pmatrix} 1 & 1 \\ 1 & -1 \end{pmatrix} . \tag{4.1}$$

This however is merely one version of the general unitary matrix which describes a two-port lossless beam splitter [125]:

$$BS(\theta, \phi_\tau, \phi_\rho) = \begin{pmatrix} \mathrm{e}^{\mathrm{i}\phi_\tau} \cos(\theta) & \mathrm{e}^{\mathrm{i}\phi_\rho} \sin(\theta) \\ -\mathrm{e}^{-\mathrm{i}\phi_\rho} \sin(\theta) & \mathrm{e}^{-\mathrm{i}\phi_\tau} \cos(\theta) \end{pmatrix} , \tag{4.2}$$

which can be found under the constraints of energy conservation and the commutation relations of the fields. Here θ parameterises the reflectivity of the beam splitter and ϕ_τ and ϕ_ρ detail the phases acquired by the transmitted and reflected beams. The values of ϕ_τ and ϕ_ρ depends upon the exact physical implementation of the beam splitter. When only considering a single beam splitter the choice is rarely important as the phase difference is not measured. However when multiple beam splitters are involved the choices of ϕ_τ and ϕ_ρ, or more specifically the difference between them, can change not the fundamental behaviour of the optical network but the positions / labels of the outcomes. This is illustrated in Figure 4.5 where two Mach-Zehnder interferometers are considered, one utilising glass plates with a dielectric coating and the other constructed with directional couplers. In free space such considerations can be easily ignored as in practice one would never achieve perfectly balanced interferometer path lengths and instead balances the interferometer by varying the length of one of the paths, which can therefore absorb the differences in phase arising form the physical splitters used.



(a) Beam Splitter **(b)** Beam Splitter

(c) Directional Coupler **(d)** Directional Coupler

Figure 4.5: Beam splitters vs directional couplers: The phase shifts associated with the two different physical implementations of a 50-50 splitter differ as shown in (a) and (c). This swaps the behaviour of the output ports in a Mach-Zehnder interferometer: a balanced MZ composed of BS will send $\hat{a}_A^\dagger \to \hat{a}_C^\dagger$ whilst DC results in $\hat{a}_A^\dagger \to \hat{a}_D^\dagger$.

A dielectric glass plate will impart a π phase shift only to photons reflecting from one side of the splitter — the interface which changes from low to high refractive index — and thus the unitary (for a balanced splitter) is the one above in Equation (4.1) (this is the convention adopted in [123]). However, for a directional coupler both 'reflected' beams acquire a phase of $\pi/2$ and therefore the unitary for a directional coupler with reflectivity η is:

$$DC(\eta) = \begin{pmatrix} \sqrt{\eta} & \mathrm{i}\sqrt{1-\eta} \\ \mathrm{i}\sqrt{1-\eta} & \sqrt{\eta} \end{pmatrix} . \tag{4.3}$$

The overall single particle time evolution operator for a network of such splitters is then simply the product of matrices describing the action of each

splitter. The unitary describing the complete process of our circuit is not in itself instructive, its form is more transparently written as the product of the four matrices

$$U_{\mathrm{CNOT4}} = A_1.A_2.F.A_3\,, \tag{4.4}$$

where $A_{1,2,3}$ detail the action of the directional couplers as labelled in Figure 4.2 and F the phases in the two interferometers; explicitly:

$$A_1 = \begin{pmatrix} 1 & 0 & 0 & 0 & 0 & 0 \\ 0 & \sqrt{\eta_1} & \mathrm{i}\sqrt{1-\eta_1} & 0 & 0 & 0 \\ 0 & \mathrm{i}\sqrt{1-\eta_1} & \sqrt{\eta_1} & 0 & 0 & 0 \\ 0 & 0 & 0 & \sqrt{\eta_2} & \mathrm{i}\sqrt{1-\eta_2} & 0 \\ 0 & 0 & 0 & \mathrm{i}\sqrt{1-\eta_2} & \sqrt{\eta_2} & 0 \\ 0 & 0 & 0 & 0 & 0 & 1 \end{pmatrix}, \tag{4.5}$$

$$A_2 = \begin{pmatrix} \sqrt{\eta_3} & \mathrm{i}\sqrt{1-\eta_3} & 0 & 0 & 0 & 0 \\ \mathrm{i}\sqrt{1-\eta_3} & \sqrt{\eta_3} & 0 & 0 & 0 & 0 \\ 0 & 0 & \sqrt{\eta_4} & \mathrm{i}\sqrt{1-\eta_4} & 0 & 0 \\ 0 & 0 & \mathrm{i}\sqrt{1-\eta_4} & \sqrt{\eta_4} & 0 & 0 \\ 0 & 0 & 0 & 0 & \sqrt{\eta_5} & \mathrm{i}\sqrt{1-\eta_5} \\ 0 & 0 & 0 & 0 & \mathrm{i}\sqrt{1-\eta_5} & \sqrt{\eta_5} \end{pmatrix}, \tag{4.6}$$

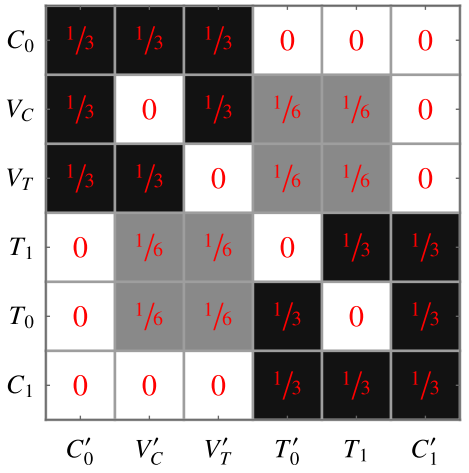
$$A_3 = \begin{pmatrix} 1 & 0 & 0 & 0 & 0 & 0 \\ 0 & \sqrt{\eta_6} & \mathrm{i}\sqrt{1-\eta_6} & 0 & 0 & 0 \\ 0 & \mathrm{i}\sqrt{1-\eta_6} & \sqrt{\eta_6} & 0 & 0 & 0 \\ 0 & 0 & 0 & \sqrt{\eta_7} & \mathrm{i}\sqrt{1-\eta_7} & 0 \\ 0 & 0 & 0 & \mathrm{i}\sqrt{1-\eta_7} & \sqrt{\eta_7} & 0 \\ 0 & 0 & 0 & 0 & 0 & 1 \end{pmatrix}, \tag{4.7}$$

and

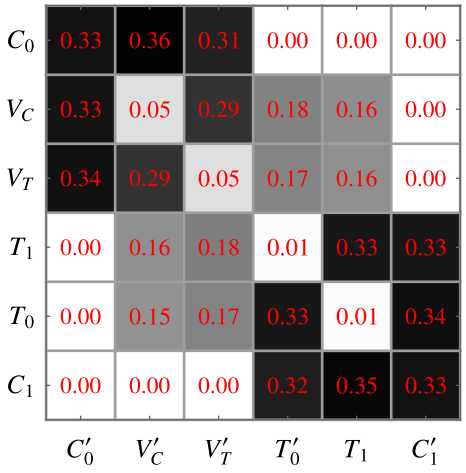
$$F = \begin{pmatrix} 1 & 0 & 0 & 0 & 0 & 0 \\ 0 & 1 & 0 & 0 & 0 & 0 \\ 0 & 0 & e^{i\phi_1} & 0 & 0 & 0 \\ 0 & 0 & 0 & 1 & 0 & 0 \\ 0 & 0 & 0 & 0 & e^{i\phi_2} & 0 \\ 0 & 0 & 0 & 0 & 0 & 1 \end{pmatrix} . \tag{4.8}$$

Using this unitary we are now able to make predictions about the behaviour of the circuit and probe the effects of the deviations of the chip characteristics from the ideal. Figure 4.6 shows first the single photon behaviour of the chip, then the operation of the CNOT logical inputs with pairs of photons. The calculation is repeated for both the ideal and measured imperfect values of the couplers and it can be seen that the deviations are small. The single photon operation elucidates why the target waveguides must be relabelled to produce correct logical operation; a photon input into the 4th waveguide, labelled T_1, will in the absence of a C_1 photon, exit the chip via the 5th waveguide and vice versa, therefore the 4th and 5th waveguides are relabelled at the chip output. It is also possible to see the origin of the 1/9th probability of operation of the gate with both the control and target qubits only remaining in a control or target waveguide respectively 1/3 of the time.

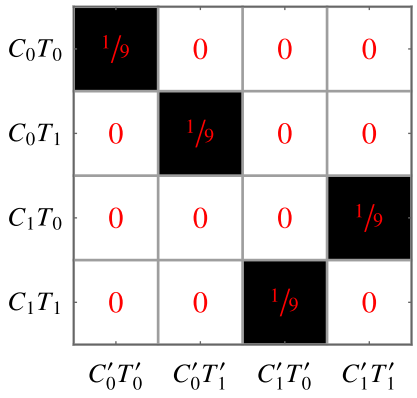
In Section 4.4 two of the outputs of the chip are connected to one another and photons are re-routed back through the chip in the opposite direction. The corresponding unitary for this configuration can be found by duplicating and unwrapping the circuit as shown in Figure 4.7, then noting that there are now ten unique waveguides and building a 10×10 unitary in the same manner as for the 6×6 U_{CNOT4} above.



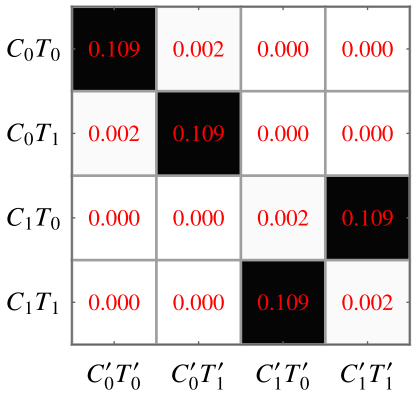
(a) Ideal single photon operation



(b) Expected single photon operation

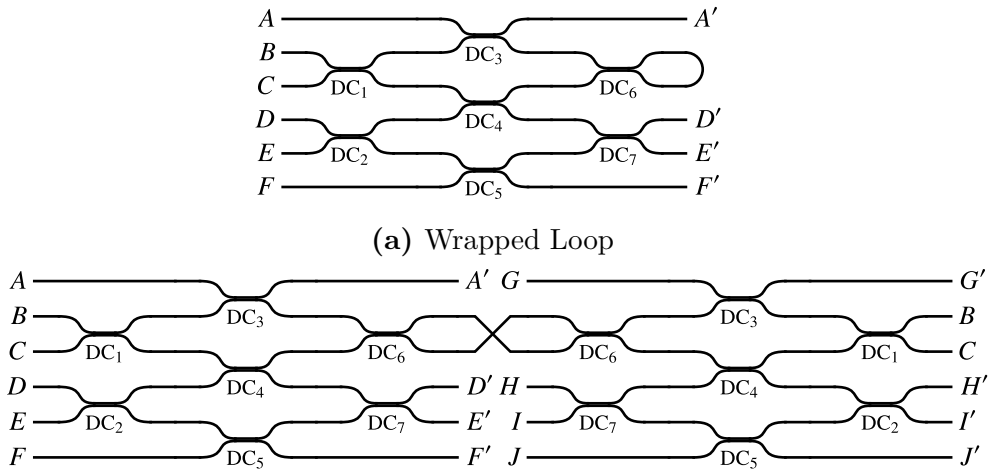


(c) Ideal photon pair operation



(d) Expected photon pair operation

Figure 4.6: CNOT4 chip operation: The predicted behaviour of the CNOT4 chip as labelled in Figure 4.1b for single photon inputs (upper) and pairwise inputs for the CNOT operation (lower). The predicted operation accounting for the imperfections (right) differs only slightly from that for the ideal chip (left).



(a) Wrapped Loop

(b) Unwrapped Loop

Figure 4.7: Equivalent looped chip layout: The operation of the chip with two outputs connected to one another (a) can be studied by adding a theoretical second set of waveguides such that time move continuously from left to right (b). With 10 unique waveguides the operation will be represented by a 10×10 unitary.

4.3 Results

Measuring the complete CNOT truth table requires four separate experimental runs with photons input into the waveguide pairs C_0T_0, C_0T_1, C_1T_0, and C_1T_1 in turn. All six of the output ports are monitored which gives us the possibility of normalising the data via a choice of methods as all photons entering the chip should be recorded (notwithstanding losses). Furthermore monitoring all six outputs allows correlations to be measured in all 15 unique pairwise combinations of the outputs which can be used to further quantify the performance of hybrid chip-source, this is done towards the end of this section.

The truth table represents the probability of obtaining certain outputs for a given input. We therefore count the number of events observed on the output correlation channels of interest and normalise — a raw correlation

number is useless as the brightness of the source is not constant and furthermore the measuring time is not constant between the inputs. We could normalise the number of correlations observed by our best guess of the number of input pairs as done in Chapter 3. Or, given that we know the gate operates in the post-selected basis for one photon in a control and one in a target waveguide we can simply normalise each row to 1, known as the logical basis. This is the most common approach and is the convention adopted throughout this chapter.

We measured 1110 coincidences across the four output channels of interest in approximately 20 hours of experimental runtime. This is not however a true measure of the brightness of our source as the majority of that time is spent loading the MOT; the 20 hours experimental time corresponds to only around 1 hour of observation time, during which the cavity is still mostly empty. The total time for which an atom was in the cavity and photons could have been generated is approximately 30 s, the appeal of trapping an atom in the cavity is evident and discussed further in Chapter 7.

The truth table formed by these 1110 correlations is shown in Figure 4.8 and deviates from both the ideal CNOT truth table and that taking into account the chip imperfections, Figures 4.6c and 4.6d, in some areas significantly. We note that there are not insignificant contributions in regions which are simply unphysical, for example it should not be possible to observe a correlation in output C_0T_0 given input C_1T_1. These are of course due to detector dark counts which have impacted the measurement to a significant extent. This truth table also doesn't account for the heterogeneous detector efficiencies.

As explained in detail in Section 3.5 we are able to make a very good estimate of the contribution of the detector dark counts to our correlation data

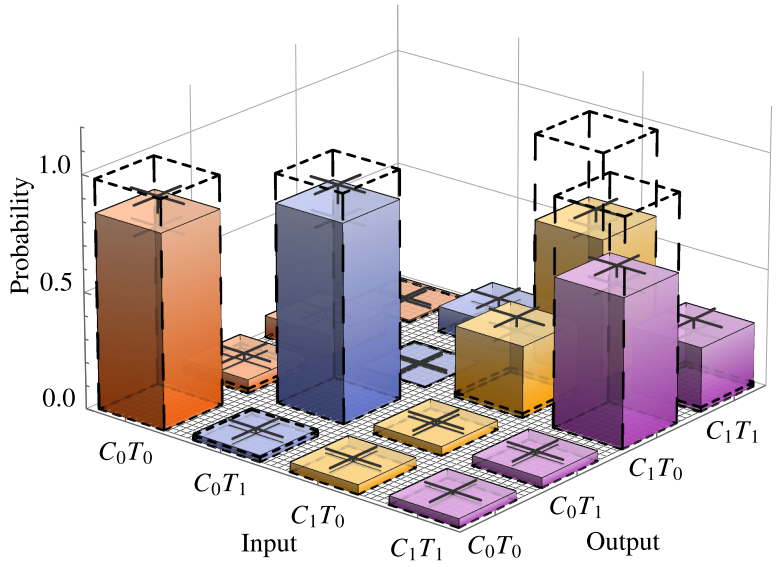


Figure 4.8: Measured CNOT truth table - raw counts: The measured truth table normalised in the logical basis without any removal of background correlations from detector dark counts. Bars are also shown with associated error markers (crosses) and the theoretically predicted values (dashed cages). The truth table shows a similarity (see Equation (4.9)) $S = 0.850^{+0.015}_{-0.015}$ to the ideal.

and account for it. Subtracting the background estimate produces Figure 4.9 which at first glance appears greatly improved with almost all unphysical correlations no longer present. However some of the entries are now (slightly) negative, this isn't surprising as we have subtracted an estimate of the average background but it does pose its own problem. Normalising the sum of each row to one is somewhat questionable in the presence of negative entries and furthermore the table can no longer be considered to represent a probability distribution. This produces further problems ahead when attempting to quantify the classical fidelity of the truth table to some reference distribution. The solution is to perform a more intelligent subtraction of background contribution using maximum likelihood estimation to restrict the truth table entries to the positive domain. We essentially ask the question "Given our observations (number of correlations and background estimates), what is the

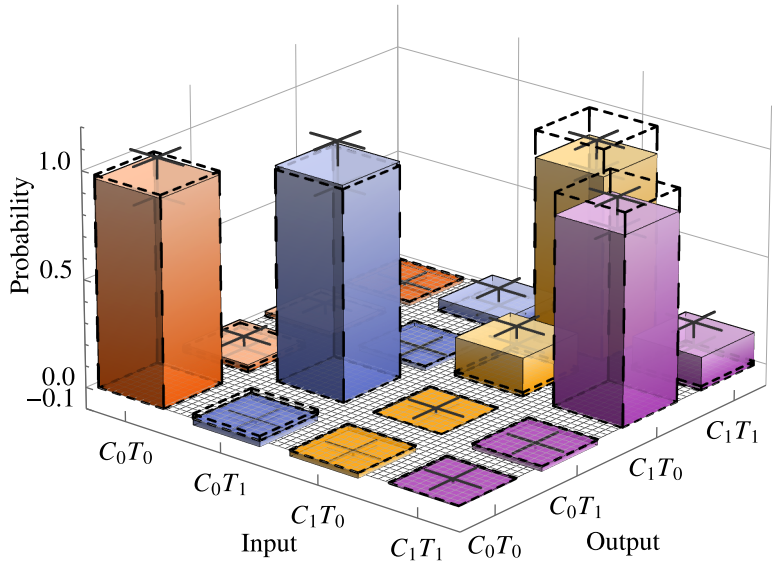


Figure 4.9: Measured CNOT truth table - simple background subtraction: The truth tables found in the logical basis after subtracting the background estimates. The negative values render this no longer a probability distribution and preclude calculation of the similarity.

most likely distribution describing the action of the chip?". This process is described in detail in Section 4.3.2 further below and the resultant truth table is displayed in Figure 4.10.

In this reconstructed background-subtracted truth table the only significant deviations from expected behaviour occur when the input is of the form C_1T_x for which two photon quantum interference is necessary to reach the correct output. We know from our preliminary work that we only achieve approximately 85% visibility which would explain the deviations here. Further proof that these deviations are due to imperfect quantum interference is provided by measuring the truth table again but using photons of orthogonal polarisation, Figure 4.11, where the C_1T_x rows no longer deviate from the expected.

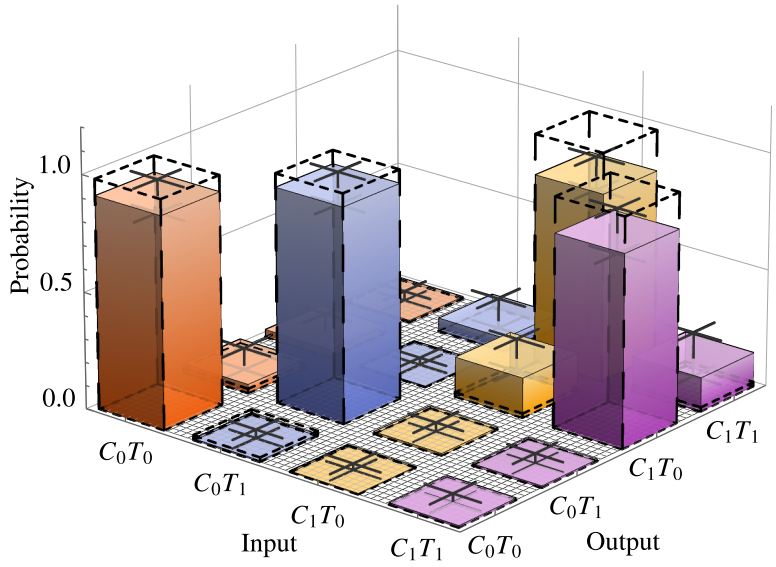


Figure 4.10: Measured CNOT truth table - MLE: The measured truth table as reconstructed using maximum likelihood estimation to compensate for the background in a physically restrained manner. Similarity, $S = 0.93^{+0.02}_{-0.02}$ to the ideal CNOT truth table.

Similarity

Finally we wish to quantify the overlap between our measured truth tables and the ideal CNOT operation (or the result predicted by the model taking into account the chip imperfections). To this end we use the classical fidelity $F(\boldsymbol{p}, \boldsymbol{q}) = \sum_i \sqrt{\boldsymbol{p}_i \boldsymbol{q}_i}$ [21], also known as the Bhattacharyya coefficient [126], with the addition of a denominator to account for the fact that our distributions $\boldsymbol{p}$ and $\boldsymbol{q}$ are not necessarily normalised to 1 (with the rows normalised to 1 the matrices will sum to 4). Thus we define the similarity

$$S(\boldsymbol{p}, \boldsymbol{q}) = \frac{\sum_i \sqrt{\boldsymbol{p}_i \boldsymbol{q}_i}}{\sqrt{\sum_i \boldsymbol{p}_i \sum_i \boldsymbol{q}_i}}, \tag{4.9}$$

where $\boldsymbol{p}_i$ and $\boldsymbol{q}_i$ are elements of the two discrete probability distributions under comparison. This measure produces values between 0 and 1 and is commonly used elsewhere therefore allowing comparison of the results pre-

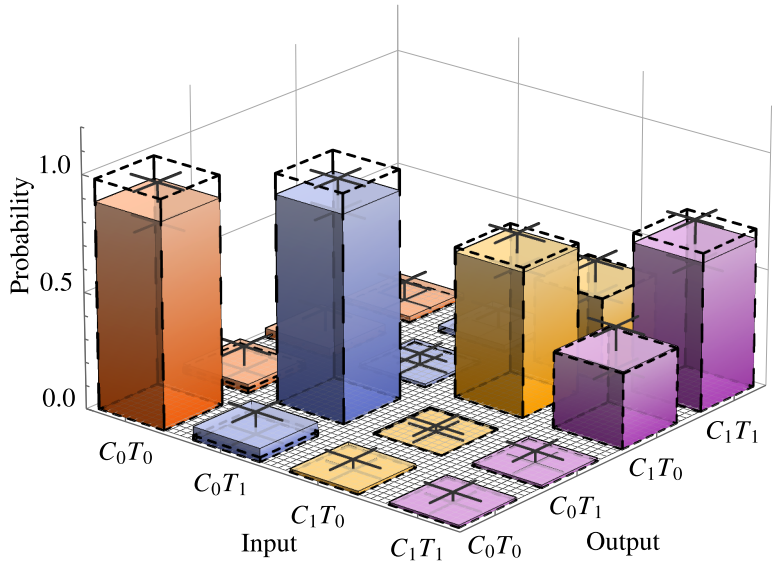


Figure 4.11: Measured perpendicular CNOT truth table - MLE: The truth table as found measuring with non-interfering orthogonally polarised photons, again reconstructed using MLE. The similarity to the predicted behaviour (dashed cages) is $S = 0.975^{+0.011}_{-0.016}$.

sented here with the wider field (e.g. [62]); sometimes the square of the above definition is used (e.g. [127]). The reconstructed truth table (Figure 4.10) shows a similarity of $S = 93^{+2}_{-2}\%$ with the ideal CNOT truth table, which sits in good agreement with the value of 94% measured by Politi with an SPDC source on the same chip. If the non-ideal directional coupler reflectivities and interferometer phase shifts are taken into account, S increases to $S = 95.8^{+1.5}_{-1.7}\%$. Table 4.1 lists the similarities for both the raw and processed truth tables displayed above. The similarity displays some perhaps unintuitive properties in that seemingly very different distributions can yield unexpectedly high values, for example two completely random truth tables show on average $S = 84\%$ (although with large variance). A selection of examples are provided in Table 4.2.

We can use this similarity measure to also quantify the overlap of the full correlation matrix obtained for a given input with that expected for the

	Raw	MLE
Ideal	$0.850^{+0.015}_{-0.015}$	$0.93^{+0.02}_{-0.02}$
Model	$0.895^{+0.012}_{-0.014}$	$0.959^{+0.014}_{-0.018}$

Table 4.1: Similarities: The similarities (as defined in Equation (4.9)) for both the truth table formed of the raw counts and that derived via MLE accounting for the background correlations when compared to both the ideal CNOT truth table and that predicted accounting for the chip imperfections (denoted "Model"). The error bounds indicate the limits of the 95% confidence interval.

$\boldsymbol{p}$	$\boldsymbol{q}$	Description	$S(\boldsymbol{p}, \boldsymbol{q})$
Ideal	No Op.	No operation as implemented by the identity	0.5
Ideal	Max Mix	Both control and target qubits are sent randomly to their 0 or 1 output	0.707
Ideal	No Quantum	As the chip would perform without quantum interference (i.e. orthogonally polarised photons)	0.789
Ideal	Random	A randomly generated truth table — four samples of a 4-d unit simplex.	$0.46^{+0.20}_{-0.20}$
Random	Random	A randomly generated truth table	$0.84^{+0.10}_{-0.13}$

Table 4.2: Reference similarities: The similarities between various pertinent distributions to aid in contextualising the similarities presented in this chapter. Ideal is the ideal CNOT truth table. Note that the Random truth table is is not a sample from a 16 dimensional space but four random 4-d variables compared simultaneously.

unitary supposedly implemented by our CNOT4 circuit. With six outputs there are obviously a total of 36 different ways two detections could present, the truth tables only show four of these. Of these 36, only 21 are unique as we are not concerned with the order of detection, thus correlations on $B'A'$ are counted in the same channel as $A'B'$. Finally six of these 21 have both photons reaching the same detector which unfortunately is not a situation we can resolve - our detectors are not number resolving and have a dead time on the order of 50 ns. Therefore we are able to measure correlations in 15 unique channels, producing a correlation matrix as shown in Figure 4.12. It does not make sense to normalise such a correlation matrix to the logical

basis (setting the sum of the matrix elements to 1) as we know we do not observe all the input pairs. The matrices are therefore normalised using the best estimate of the number of input pairs as detailed in Section 3.5, which as can be seen in the figure appears to work well. The average similarity of the measured correlation matrices for the four different inputs is 98%, Table 4.3 lists the values for each input. Note the value of the similarity is unchanged by the inclusion of the 21 strictly zero entries in the correlation matrices.

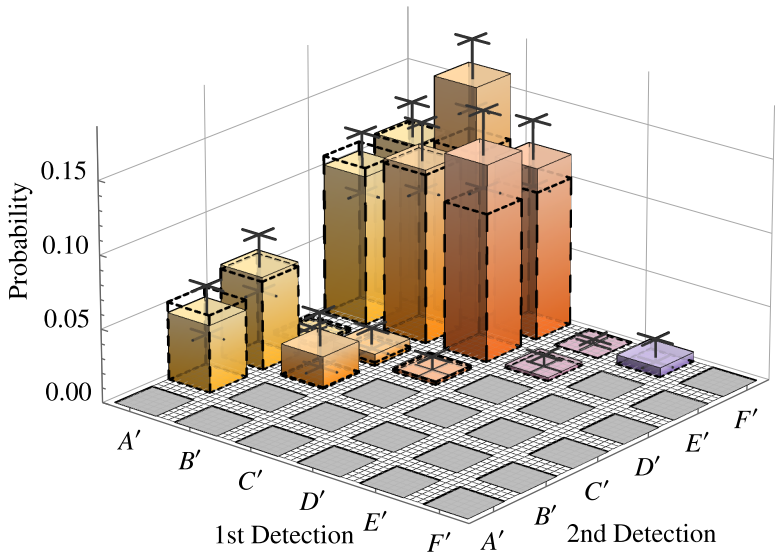


Figure 4.12: Full correlation matrix: The probabilities of observing a correlation in the 15 unique correlation channels when photon pairs are input waveguides A and D. These values are normalised by the best guess of the number of input pairs.

Although above we choose to ignore the time order of the correlations, grouping $B'A'$ with $A'B'$, the photons we are using are approximately 200 ns long, considerably longer than the timing resolution of the SPCMs which is around 300 ps, and therefore we have the information to resolve the time order of the correlations. Each of the 15 entries in the matrix shown in Figure 4.12 are actually just the total area of a time-resolved HOM plot like that shown in Figure 4.4a. The decision to group the data is simply to

Input	Correlation Matrix	
	Raw	MLE
DA	$0.942^{+0.008}_{-0.008}$	$0.981^{+0.009}_{-0.011}$
EA	$0.959^{+0.007}_{-0.007}$	$0.988^{+0.007}_{-0.008}$
DF	$0.925^{+0.010}_{-0.010}$	$0.972^{+0.013}_{-0.014}$
EF	$0.914^{+0.011}_{-0.011}$	$0.966^{+0.011}_{-0.013}$

Table 4.3: Correlation matrix similarities: The correlation matrices represent the probability of measuring a correlation in each of the 15 unique correlation channels given a pairwise input, as shown in Figure 4.12. They are normalised by the best guess of the number of input pairs. The similarities are when compared to predicted values given the imperfection in the chip.

reduce the noise on each of the matrix elements (additionally the truth table is not concerned with the order of detection), the next subsection uses the time resolution to investigate the function of the CNOT gate for correlations notably separated in time.

4.3.1 Time Resolved Similarity

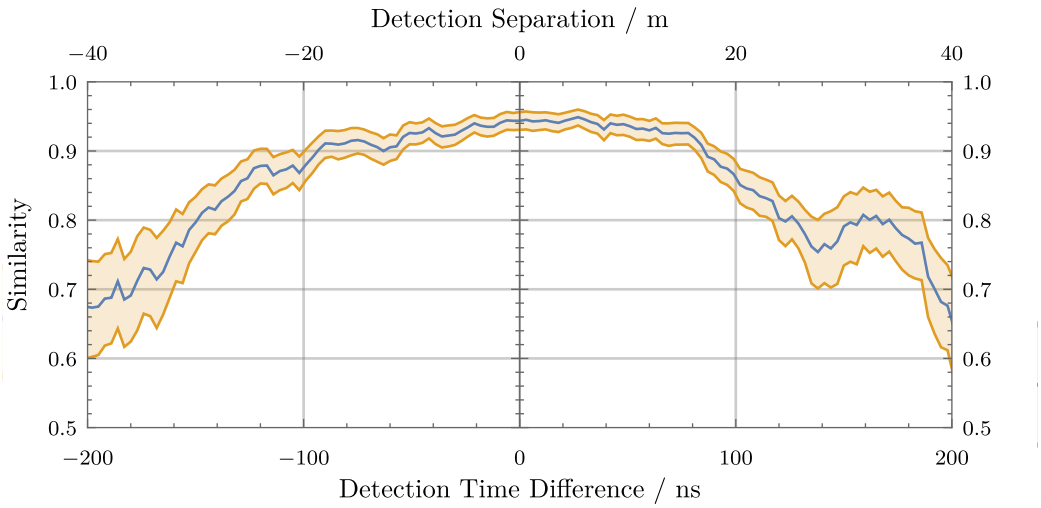
As explained above, the truth tables so far have ignored the time difference between the two detections constituting a correlation. Using the time resolution of the correlations we can determine the similarity with the expected truth table as a function of the detection-time difference, Figure 4.13a. We calculate the similarity to the ideal truth table of subsets of the data with detections separated by a time t with $\Delta\tau - w/2 < t < \Delta\tau + w/2$ where w parameterises the width of our observation window centred at a time difference of $\Delta\tau$. A compromise between time-resolution and signal to noise must be made when selecting a value for w as shorter observation windows reduce the number of correlations included in each bin; a window of 60 ns ($\pm$30 ns) is used below. The shape of the photon envelope further reduces the number of correlations in those bins towards the limit of the plot (al-

though the background contribution from dark counts will remain constant) and thus the similarity falls away rapidly, this is further evident in the subset truth tables, Figures 4.13b to 4.13d. This gate itself is only around 10 mm long with a corresponding crossing time of around 50 ps, thus we see from Figure 4.13a that the gate operates as expected even for detections occurring orders of magnitude further apart in time that the chip dimensions. This is another interesting demonstration that the effects of classical and quantum interference operate beyond the point particle picture.

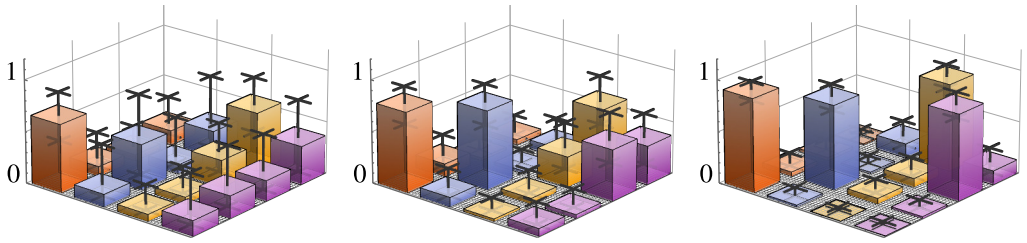
One might be concerned that at no point does the trace in Figure 4.13a exceed the value of $S = 95.8^{+1.5}_{-1.7}\%$ calculated when taking the dataset as a whole. However, each point on the trace only contains a small subset of the data and therefore suffers correspondingly higher statistical noise than the dataset taken as a whole. There are many more ways that statistical noise can affect the probability distribution unfavourably than favourably, and therefore even in the centre of the trace where the signal to random noise of the experiment is higher, the statistical noise due to the paucity of events still suppresses the calculated value of S.

4.3.2 Maximum Likelihood Estimation

There are a not insignificant number of background correlations entering the truth table, predominantly due to detector dark counts, which must be accounted for to make a fair analysis of the performance of the source and the gate operation. The average value of this background for each correlation channel is well known but simply subtracting its value from the number of observed correlations is inadequate as it leaves some negative entries in the truth tables, as well as error bars extending below zero. The solution is to use



(a) Time-resolved Similarity



(b) -168 ns **(c)** -129 ns **(d)** 0 ns

Figure 4.13: Time-resolved similarity: Similarity of the measured truth table to the ideal as a function of the detection time difference of the contributing correlations; the shading represents a one-sigma confidence interval. Events are considered within $\Delta\tau \pm 30\,\text{ns}$. Insets (b)-(d) shown the degradation of the truth table as both the mutual coherence of the photons decreases towards larger $\Delta\tau$ and more importunely the table becomes dominated by noise.

the principles of maximum-likelihood estimation to construct a distribution describing the most likely number of signal correlations per channel. Given these distributions we can then use Monte Carlo methods to find normalised truth tables and similarities with error bounds constrained to the interval $[0, 1]$.

Maximum-likelihood estimation is a way of estimating the parameters of a statistical model given data. In our case the data are the number of correlations observed and the model must relate the number of observed correlations, background correlations, and signal correlations. We expect both the number of signal correlations and background correlations to follow Poisson distributions. The number of observed correlations will be the sum of these, which is therefore also a Poisson variable. Therefore the probability of observing n total correlations, given a mean number of background correlations λ and signal correlations κ is

$$\begin{aligned} \Pr(X = n) &= \mathrm{Pois}(\kappa) + \mathrm{Pois}(\lambda) \\ &= \mathrm{Pois}(\kappa + \lambda) \\ &= \frac{\mathrm{e}^{-(\kappa+\lambda)}(\kappa + \lambda)^n}{n!}\,. \end{aligned} \tag{4.10}$$

We would like to find the value of κ which maximises the likelihood of getting the data we observed. For multiple observations $x_1, x_2, \ldots, x_n$, this is done by maximising a likelihood function, generally written as

$$\mathcal{L}(\theta\,;\, x_1, \ldots, x_n) = \prod_{i=1}^{n} f(x_i \mid \theta)\,, \tag{4.11}$$

where $f(x_i \mid \theta)$ is the probability density function of variable X_i with a parameter vector θ.

We have a very good estimate of the mean number of background correlations, λ, and therefore the only parameter in our model is the number of signal correlations, κ. For each correlation channel we only have the one observation, namely n observed correlations, therefore the RHS of Equation (4.10) is in fact our likelihood function for κ real correlations:

$$\mathcal{L}(\kappa; n, \lambda) = \frac{\mathrm{e}^{-(\kappa+\lambda)}(\kappa+\lambda)^n}{n!} \,. \tag{4.12}$$

Maximising this for $\kappa \geq 0$ is straightforward and gives the trivial and perhaps obvious result

$$\kappa_{\mathrm{mle}} = \max\left[0, n-\lambda\right] \,. \tag{4.13}$$

The most likely number of signal correlations in a correlation channel is the total number observed minus the background, constrained to be positive.

The truth tables are presented in the logical basis by normalising the sum of each row to one; if accounting for the heterogenous detector efficiencies each element is scaled according the efficiencies of the two detectors on that correlation channel prior to normalising the row. It is not the case that the most likely truth table is simply the normalised table of most likely values. This is because the normalisation process is a non-trivial mapping relating previously independent values. Therefore to recover the most likely normalised truth table given our data we use Monte Carlo methods to draw samples from the likelihood functions (Equation (4.12)), thus generating many sample unnormalised truth tables which are then normalised to give a distribution of truth tables. From these we can recover not only the mean but also error bounds of every element.

To draw samples from the likelihood function it must first be normalised such that it represents the PDF of κ, doing so yields

$$f(\kappa) = \frac{\mathrm{e}^{-(\kappa+\lambda)}(\kappa+\lambda)^n}{\Gamma(1+n,\lambda)}\,, \tag{4.14}$$

where Γ is the upper incomplete gamma function. From this we integrate to obtain the CDF, $F(\kappa)$, which we can then invert allowing us to use inverse transform sampling to draw random samples:

$$\begin{aligned} F(\kappa) &= \int_0^{\kappa} f(x)\mathrm{d}x \\ &= \frac{\Gamma(1+n,\lambda) - \Gamma(1+n,\kappa+\lambda)}{\Gamma(1+n,\lambda)} \\ &= \frac{Q(1+n,\lambda) - Q(1+n,\kappa+\lambda)}{Q(1+n,\lambda)} \end{aligned} \tag{4.15}$$

$$\Rightarrow F^{-1}(u) = Q^{-1}\left(1+n, (1-u)\,Q\left(1+n,\lambda\right)\right) - \lambda\,. \tag{4.16}$$

Where Q is the regularised upper incomplete gamma function, which is also the CDF for Poisson random variables. Using Equation (4.16) we can transform random samples on the interval $u \in [0,1]$ to a sample from the PDF (Equation (4.14)).

The magnitude of the background subtraction and the effect it has on the likelihood distribution for κ is evident in Figure 4.14 which also demonstrates that sampling using Equation (4.16) does indeed approach the PDF. The corresponding distributions after normalisation are shown in Figure 4.15 which clearly demonstrates that simply normalising the most likely values of κ (red lines) does not correspond to the most likely entries for the normalised truth table (blue lines). It is from these distributions we get the error bounds for the elements in the truth table, as indicated in Figure 4.15, and similarity, as

indicated in Figure 4.16. The plots clearly show that underlying some of the data are highly asymmetric distributions for which the approximation that the variance of a Poisson distributed random variable is equal to the mean is not good [114]. Instead we opt to demarcate the uncertainties using shortest confidence intervals.

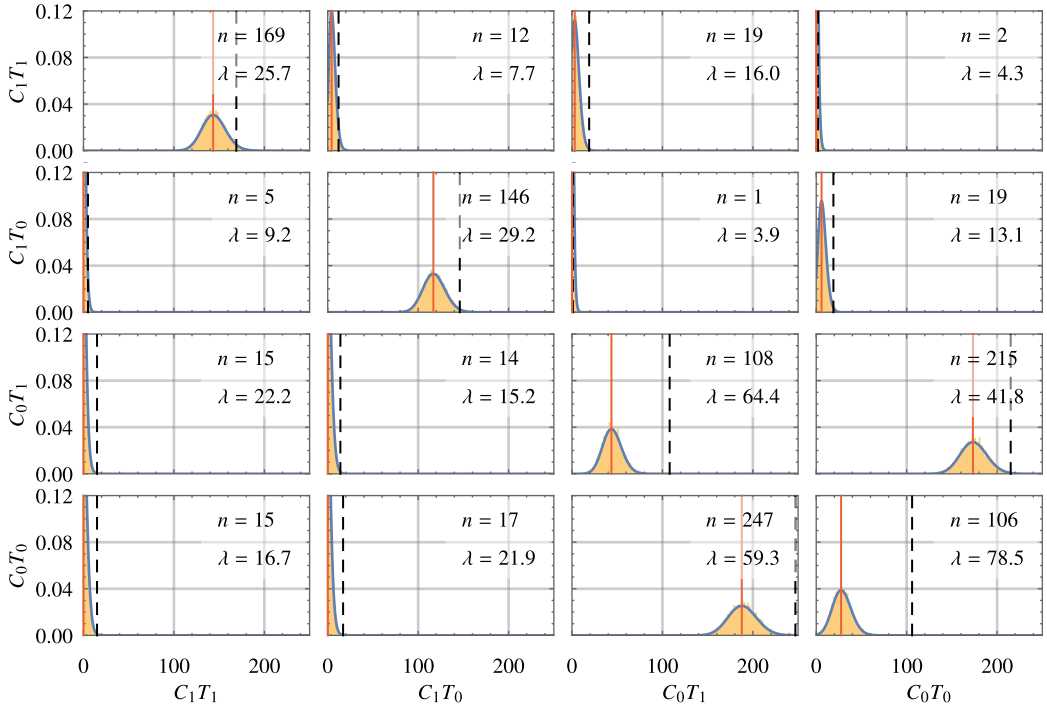


Figure 4.14: Likelihood distributions: From the raw number of correlations n (dashed line), subtracting the background estimate λ produces a likelihood distribution (blue) for the number of true correlations κ. The peak of this distribution is at κ_{mle} and marked with a red line. The distributions in yellow are histograms of samples drawn using the inverse CDF (Equation (4.16)) which it can be seen successfully approach the PDF (Equation (4.14)).

The final process we wish to perform with our normalised truth tables is to calculate their similarity (as defined in Equation (4.9)) to the expected values. This is now a simple matter of evaluating the similarity for each of the sample truth tables we have generated to thus generate a distribution for the value of the similarity, Figure 4.16. Once again it can be seen firstly

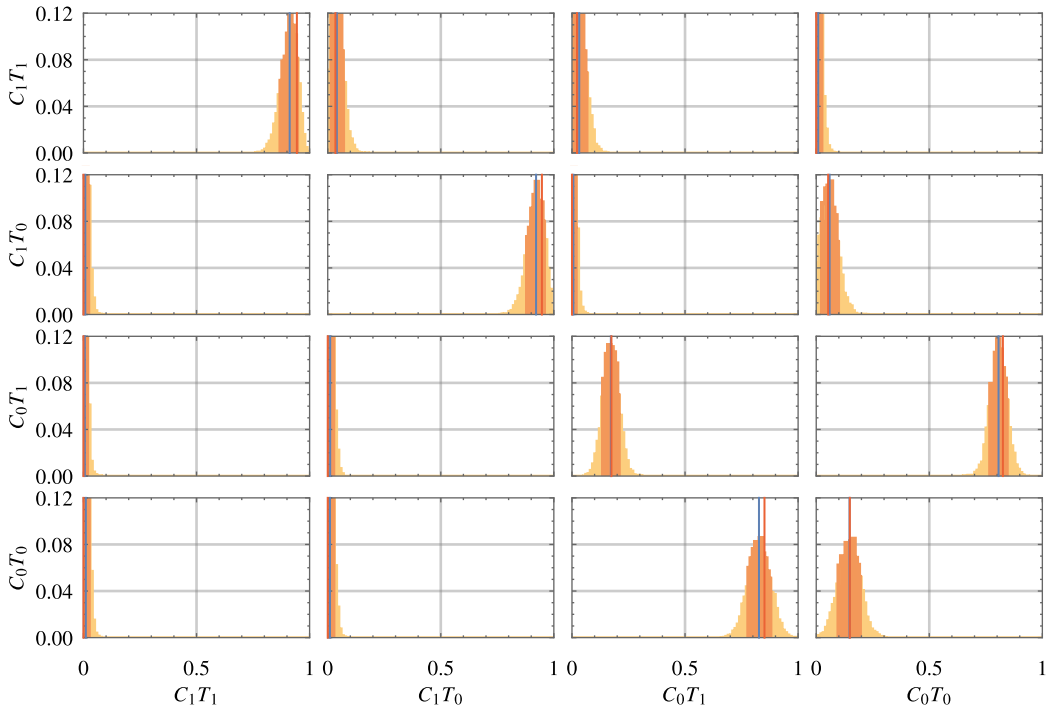


Figure 4.15: Normalised likelihood distributions: Taking 5000 samples from the likelihood distributions for the number of true correlations and normalising each row to 1 (logical basis) results in the above distributions. The blue lines denote the peaks of these distributions and are the most likely values for the truth table entries given our data. These differ from the normalised κ_{mle}'s shown in red. The 68% confidence intervals are shaded in red.

how inadequate it is to simply use the most likely values without propagating the entire distribution and secondly how the Monte Carlo method provides a straightforward means of obtaining the error bounds on S, even when the distribution is asymmetric.

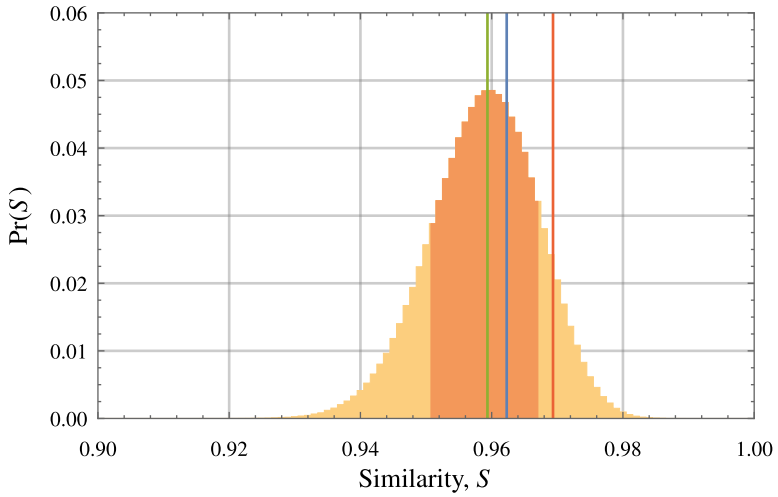


Figure 4.16: Similarity distribution: The distribution of similarities produced following a Monte Carlo propagation. The red line shows the similarity given by the normalised values of the most likely number of true correlations (κ_{mle}). The blue line is the similarity given by most likely entries in the normalised truth table. The green line is the peak of the fully propagated distribution and represents the most likely similarity given our data. The red shading highlights the 68% confidence interval.

4.4 Entanglement Verification

A defining feature of two-qubit logic is the ability to generate entanglement from separable input states. The CNOT gate is particularly suited for this as it can generate the four maximally entangled Bell states with the addition of just one single-qubit gate. Typically verification of the generation of an entangled state would be performed by using quantum state tomography to reconstruct the density matrix of the state [128]. We are unable to perform

Axis	$\|\psi_+\rangle$	$\|\psi_-\rangle$	Name
x	$\|+\rangle = \frac{1}{\sqrt{2}}(\|0\rangle + \|1\rangle)$	$\|-\rangle = \frac{1}{\sqrt{2}}(\|0\rangle - \|1\rangle)$	Diagonal
y	$\|+\mathrm{i}\rangle = \frac{1}{\sqrt{2}}(\|0\rangle + \mathrm{i}\|1\rangle)$	$\|-\mathrm{i}\rangle = \frac{1}{\sqrt{2}}(\|0\rangle - \mathrm{i}\|1\rangle)$	Circular
z	$\|0\rangle$	$\|1\rangle$	Computational

Table 4.4: Basis vectors: The notation of the eigenvectors for the orthonormal measurement bases given by the cartesian axes of the Bloch sphere.

full quantum state tomography as it requires measurements in more bases than we can easily access (see Section 4.4.2). However we are able to lower-bound the quantum state fidelity to a maximally entangled Bell state by making measurements of our generated quantum state in more than one measurement basis - a defining feature of entangled systems is that they show correlated behaviour across multiple measurement bases.

Measurement Bases

The state space of a quantum two level system, such as that spanned by photons in dual rail logic circuits, is often represented using a Bloch sphere. Any pair of antipodal points on the sphere represent a pair of state vectors which form a measurement basis. Three such oft-used orthonormal measurement bases are given by the Cartesian axes of the sphere and have eigenvectors as listed in Table 4.4. The matrix form of the operators whose eigenstates form the measurement basis are the three Pauli matrices:

$$\sigma_{\mathrm{x}} = \begin{pmatrix} 0 & 1 \\ 1 & 0 \end{pmatrix} \qquad \sigma_{\mathrm{y}} = \begin{pmatrix} 0 & -\mathrm{i} \\ \mathrm{i} & 0 \end{pmatrix} \qquad \sigma_{\mathrm{z}} = \begin{pmatrix} 1 & 0 \\ 0 & -1 \end{pmatrix}. \tag{4.17}$$

Up until now all measurements using the CNOT4 chip have been made in the computational basis — we labelled our waveguides such that a detection of a photon in the C_0' channel corresponded to measurement of the control

qubit in the $|0\rangle$ computational basis state (C_1' to $|1\rangle$). How then to perform a measurement in one of these others bases? Recall from Section 4.2 the action of a single 1/2 directional coupler is $|0\rangle \rightarrow \frac{1}{\sqrt{2}}(|0\rangle + \mathrm{i}|1\rangle) = |+\mathrm{i}\rangle$ and $|1\rangle \rightarrow \frac{\mathrm{i}}{\sqrt{2}}(|0\rangle - \mathrm{i}|1\rangle) = \mathrm{i}|-\mathrm{i}\rangle$, thus transforming the dual rails from the z-basis to the y-basis, Figure 4.17 further illuminates this.

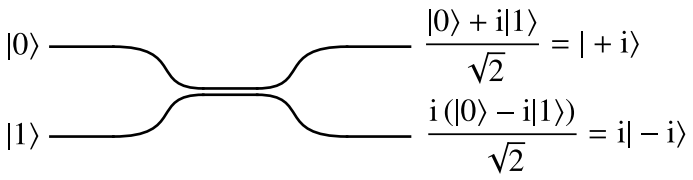
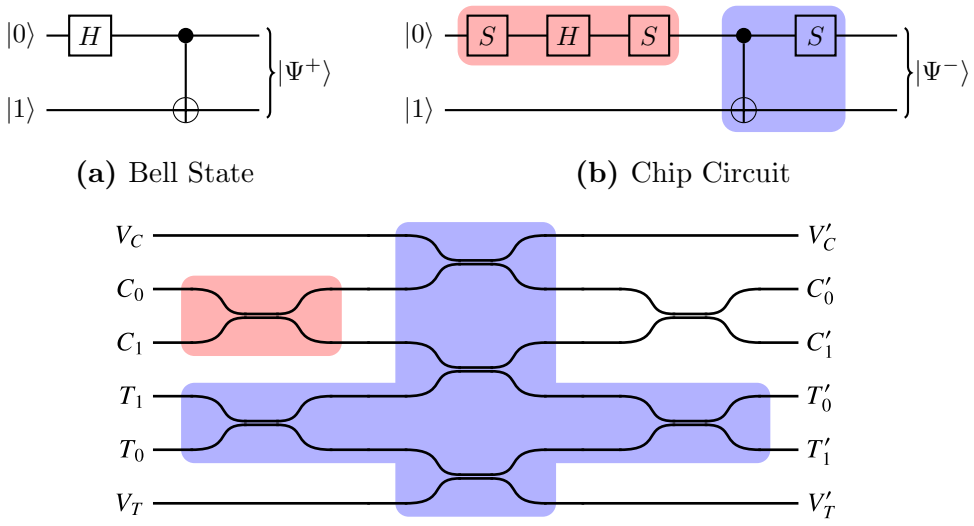


Figure 4.17: Operation of directional coupler: Before the DC the dual rails represent a qubit encoded in the computational (z) basis. After the DC the rails now encode the qubit in the y-basis and therefore a detection of a photon in the upper rail represents a measurement of +1 in the y-basis

4.4.1 Generating entanglement

The only addition to a CNOT gate required to generate any of the maximally entangled Bell states is a single Hadamard gate. The action of a Hadamard is to map the state $|0\rangle$ to $\frac{1}{\sqrt{2}}(|0\rangle + |1\rangle)$ and $|1\rangle$ to $\frac{1}{\sqrt{2}}(|0\rangle + |1\rangle)$ which is simply the transformation performed by a simple beam splitter as expressed in matrix form in Equation (4.1). Consider the circuit in Figure 4.18a where the top rail represents the control qubit and the bottom the target. Given the input $|0\rangle_{\mathrm{C}}|1\rangle_{\mathrm{T}}$, the Hadamard will first put the control qubit into the superposition $\frac{1}{\sqrt{2}}(|0\rangle_{\mathrm{C}} + |1\rangle_{\mathrm{C}})$, the total state is therefore $\frac{1}{\sqrt{2}}(|01\rangle + |11\rangle)$, where we have dropped the subscripts and simply let the first (second) entry refer to the control (target) qubit. The action of the CNOT then produces $\frac{1}{\sqrt{2}}(|01\rangle + |10\rangle)$, the $|\Psi^+\rangle$ Bell state.

Usefully we have additional 1/2 directional couplers already present on



(a) Bell State **(b)** Chip Circuit

(c) Corresponding Couplers on Chip

Figure 4.18: Generating entanglement: (a) A single Hadamard gate in combination with a CNOT gate generates a maximally entangled state. (b) The couplers on our chip implementing the Hadamard (red) and the CNOT (blue) are highlighted. (c) The directional couplers additional implement phase shifts, resulting in the operation described by the circuit shown; the S phase gate implements a phase shift of $\pi/2$ [129].

the chip, however we recall that the action of a directional coupler (Equation (4.3)) is not quite the same as that of a beam splitter and therefore does not represent a true Hadamard operation: the Hadamard matrix is real and antisymmetric whereas that for the directional coupler is complex and symmetric. The difference is the addition of $\pi/2$ phase shift gates before and after a Hadamard, thus the combination of the directional coupler and CNOT highlighted in Figure 4.18c can be represented by the quantum circuit in Figure 4.18b. Given the input C_0T_1 as shown, we therefore produce the $|\Psi^-\rangle$ state. We can verify this with a step-by-step analysis of the action of each coupler in turn (and in doing so appreciate why the matrix formulation

is favoured):

$$\begin{aligned}
|01\rangle &\xrightarrow{\mathrm{DC}_1} \frac{1}{\sqrt{2}}(|01\rangle + \mathrm{i}|11\rangle) \\
&\xrightarrow{\mathrm{DC}_2} \frac{1}{2}(\mathrm{i}|00\rangle + |01\rangle - |10\rangle + \mathrm{i}|11\rangle) \\
&\xrightarrow{\mathrm{DC}_3} \frac{1}{2}(\frac{\mathrm{i}}{\sqrt{3}}|00\rangle + \frac{1}{\sqrt{3}}|01\rangle - |10\rangle + \mathrm{i}|11\rangle) \\
&\xrightarrow{\mathrm{DC}_4} \frac{1}{2\sqrt{3}}(\mathrm{i}|00\rangle + \frac{1}{\sqrt{3}}|01\rangle - |10\rangle - \frac{\mathrm{i}}{\sqrt{3}}|11\rangle) \\
&\xrightarrow{\mathrm{DC}_5} \frac{1}{6}(\mathrm{i}|00\rangle + |01\rangle - |10\rangle - \mathrm{i}|11\rangle) \\
&\xrightarrow{\mathrm{DC}_7} \frac{\mathrm{i}}{3\sqrt{2}}(|00\rangle - |11\rangle) \\
&\xrightarrow{\mathrm{relabel}} \frac{\mathrm{i}}{3\sqrt{2}}(|01\rangle - |10\rangle) \\
&= \frac{\mathrm{i}}{3}|\Psi^-\rangle\,.
\end{aligned} \tag{4.18}$$

4.4.2 Verifying entanglement

We verify that we do indeed produce the $|\Psi^-\rangle$ state, and place a lower bound on the degree of entanglement generated by measuring the expectation values of both the Pauli z and y operators. The fidelity bound, $F_{\min}$, is constructed by first considering the fidelity of an arbitrary two qubit state ρ to the $|\Psi^-\rangle = \frac{1}{\sqrt{2}}(|01\rangle - |10\rangle)$ Bell state, which is given by the overlap:

$$F_{\Psi^-} = \langle\Psi^-|\rho|\Psi^-\rangle = \frac{1}{2}(\langle 01|\rho|01\rangle + \langle 10|\rho|10\rangle - \langle 01|\rho|10\rangle - \langle 10|\rho|01\rangle)\,. \tag{4.19}$$

Similarly the fidelity to the $|\Phi^-\rangle = \frac{1}{\sqrt{2}}(|00\rangle - |11\rangle)$ Bell state is given by:

$$F_{\Phi^-} = \langle\Phi^-|\rho|\Phi^-\rangle = \frac{1}{2}(\langle 00|\rho|00\rangle + \langle 11|\rho|11\rangle - \langle 00|\rho|11\rangle - \langle 11|\rho|00\rangle)\,. \tag{4.20}$$

Measuring the expectation value of the z Pauli operator, $\langle Z\rangle$, with eigen-

values z_n and eigenvectors $|z_n\rangle$, for the state $\rho = |\psi\rangle\langle\psi|$ can be written as

$$\begin{aligned}\langle Z\rangle &= \langle\psi|Z|\psi\rangle \\ &= \langle\psi|\left(\sum z_n|z_n\rangle\langle z_n|\right)|\psi\rangle \\ &= \sum z_n\langle\psi||z_n\rangle\langle z_n||\psi\rangle \\ &= \sum z_n\langle z_n||\psi\rangle\langle\psi||z_n\rangle \\ &= \sum z_n\langle z_n|\rho|z_n\rangle \\ &= 1\langle 0|\rho|0\rangle - 1\langle 1|\rho|1\rangle\,.\end{aligned}$$

Which when measuring the expectation values for both qubits in the two qubit state generalises using the tensor product of the Hilbert spaces to

$$\langle Z\otimes Z\rangle = \langle 00|\rho|00\rangle + \langle 11|\rho|11\rangle - \langle 01|\rho|01\rangle - \langle 10|\rho|10\rangle\,. \tag{4.21}$$

This is simply the fraction of C_0T_0 or C_1T_1 correlations minus the fraction of C_0T_1 or C_0T_1 correlations.

Similarly in the y-direction we have

$$\begin{aligned}\langle Y\otimes Y\rangle = &\langle +\mathrm{i}+\mathrm{i}|\rho|+\mathrm{i}+\mathrm{i}\rangle + \langle -\mathrm{i}-\mathrm{i}|\rho|-\mathrm{i}-\mathrm{i}\rangle \\ &- \langle +\mathrm{i}-\mathrm{i}|\rho|+\mathrm{i}-\mathrm{i}\rangle - \langle -\mathrm{i}+\mathrm{i}|\rho|-\mathrm{i}+\mathrm{i}\rangle \\ = &-\langle 11|\rho|00\rangle - \langle 00|\rho|11\rangle + \langle 10|\rho|01\rangle + \langle 01|\rho|10\rangle\,.\end{aligned} \tag{4.22}$$

If we now construct the quantity $F_{\min} = F_{\Psi^-} - F_{\Phi^-}$ we can see by com-

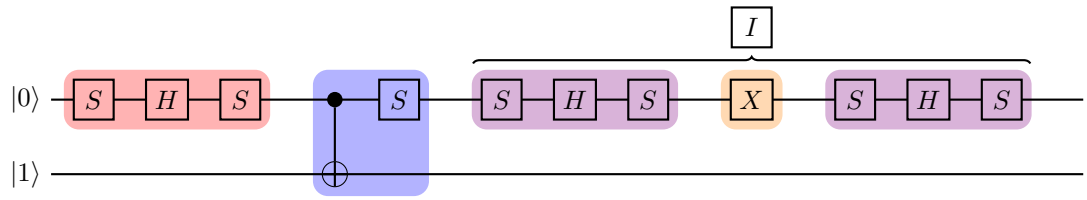
bining Equations (4.19) to (4.22) that

$$\begin{aligned} F_{\text{min}} &= F_{\Psi^-} - F_{\Phi^-} \\ &= -\frac{1}{2}(\langle Z \otimes Z \rangle + \langle Y \otimes Y \rangle) \\ &\leq F_{\Psi^-} \,. \end{aligned} \tag{4.23}$$

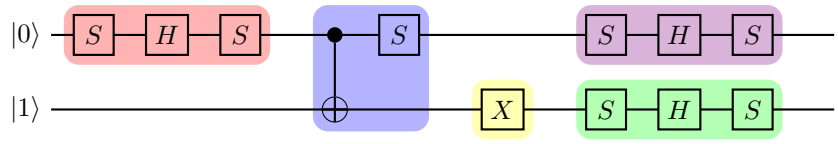
Thus by counting the number of events in different correlation channels we can place a lower bound on the fidelity of our generated state to $|\Psi^-\rangle$. Our F_{min} measure is equivalent to an entanglement witness [130] where a value of $F_{\text{min}} > \frac{1}{2}$ witnesses entanglement.

Unfortunately, because we now use waveguides B and C to encode the control qubit as shown in Figure 4.18b, we have a problem where DC_6 rotates the control qubit into the y-basis whilst the target qubit remains in the z-basis. At the chip outputs we would therefore measure $\langle Y \otimes Z \rangle$. Our solution is to exploit the interferometric stability provided by the chip and connect the two control outputs together, as shown in Figure 4.19b, thus routing the control photons back through the same coupler, after which they branch outwards and can be measured with detectors placed on the input side of the chip. The combination of the repeated coupler and the loop results in the identity operation as shown in Figure 4.19a thus returning the control qubit to the z-basis. For the $\langle Y \otimes Y \rangle$ measurement the same trick is used, now on the target qubit with detectors positioned as shown in Figure 4.19d.

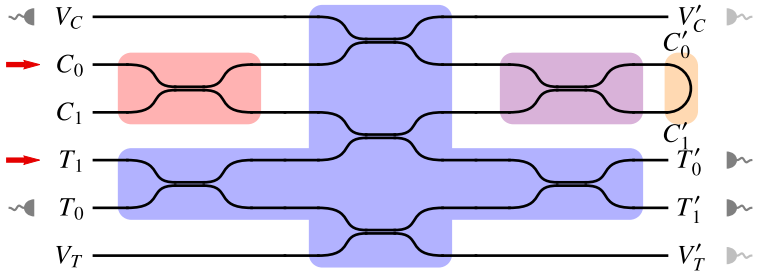
For full quantum state tomography we would also need to perform measurements on the qubits in the x-basis. This would require additional phase shifts within the chip, which we are unable to implement.



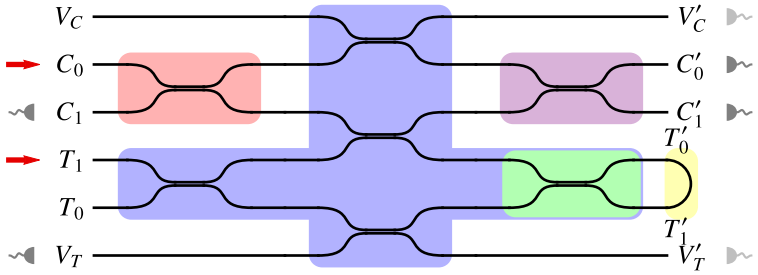
(a) $\langle Z \otimes Z \rangle$ Quantum Circuit



(b) $\langle Y \otimes Y \rangle$ Quantum Circuit



(c) $\langle Z \otimes Z \rangle$ Chip Layout

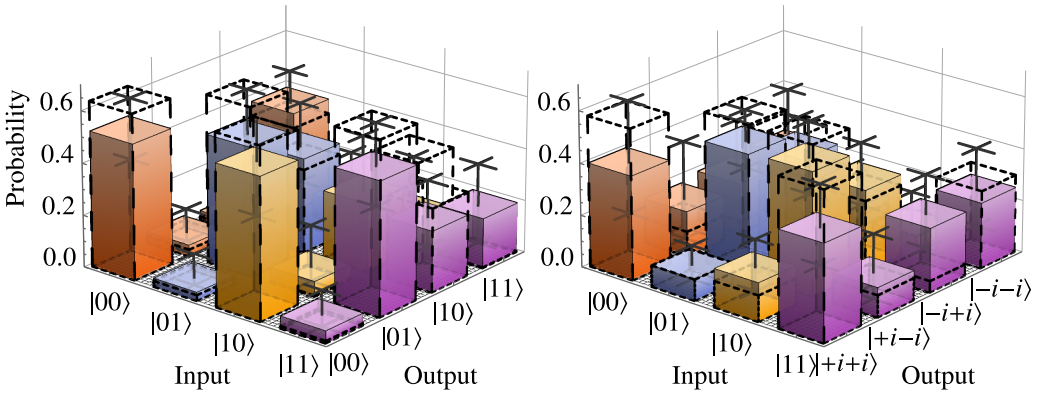


(d) $\langle Y \otimes Y \rangle$ Chip Layout

Figure 4.19: Pauli observables circuit diagrams: The quantum circuits used to perform the $\langle Z \otimes Z \rangle$ and $\langle Y \otimes Y \rangle$ measurements (top) along with the corresponding photonic chip configuration (below). The X-gate is the Pauli-X gate which corresponds to the classical NOT gate and is the action performed by the loop. Detections in channels V_C, T_0, T'_0, T'_1 correspond to measurements of the states $|0\rangle_C$, $|1\rangle_C$, $|0\rangle_T$, $|1\rangle_T$ in (c) and C_1, V_T, C'_0, C'_1 to $|-\mathrm{i}\rangle_T$, $|+\mathrm{i}\rangle_T$, $|+\mathrm{i}\rangle_C$, $|-\mathrm{i}\rangle_C$ in (d).

4.4.3 Results

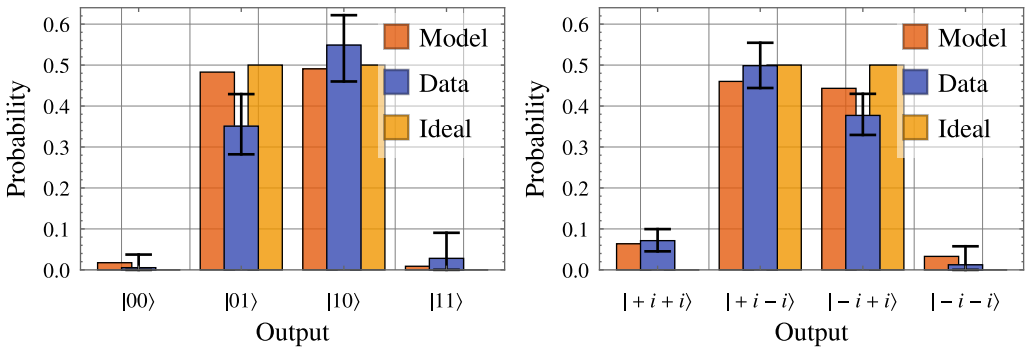
The addition of the loop introduces a significant amount of loss. Not only does one of the two qubits incur an additional coupling and propagation loss (totalling around $\sim 6\,\mathrm{dB}$) but furthermore the branching of the looped qubit to the detectors on the input side means the success probability is further reduced from 1/9 by a factor of 2/3. The results are therefore considerably more noisy than those presented in Section 4.3 as can be seen in the two 'truth tables' in Figure 4.20. These tables no longer strictly correspond to a logical operation and therefore the term truth table is a little unmerited. However in the sense that they represent the probability of measuring certain outputs, given certain inputs, normalised in the logic basis as performed previously, the term is here retained. The overlap with the predicted truth tables is good with a similarity of $S = 0.92^{+0.04}_{-0.04}$ for those measurements performed with the loop on the control qubit and $S = 0.96^{+0.02}_{-0.03}$ for the target qubit loop.



(a) Control Loop **(b)** Target Loop

Figure 4.20: Control and target loop truth tables: Although no longer representing a logical operation, these tables, which are normalised in the logical basis, show the full span of measurements performed in the Z (a) and Y (b) bases. The inputs $|01\rangle$, $|10\rangle$, $|11\rangle$, $|00\rangle$ produce on-chip the $|\Phi^-\rangle$, $|\Psi^-\rangle$, $|\Phi^+\rangle$, $|\Psi^+\rangle$ Bell states. The data are very noisy due to the many additional loss factors introduced by the loops, however they do show the correct trends.

The $|\Psi^-\rangle$ state discussed above should be generated by the input C_0T_1, the second row of the truth tables. The other three inputs produce the three other Bell states, however in response to the exaggerated losses, sufficient data for meaningfully bounding the fidelity was only taken for one input — C_0T_1. The distributions of the measurement outcomes for the two expectation values are shown in Figure 4.21 which includes an additional correction for the reduced detection efficiency of one of the four detector channels due to a 1/2 coupler. The individual rows show good overlap with expectation, $S = 0.98^{+0.01}_{-0.03}$ and $S = 0.996^{+0.004}_{-0.008}$, and yield $\langle Z \otimes Z \rangle = -0.82^{+0.24}_{-0.16}$ and $\langle Y \otimes Y \rangle = -0.78^{+0.18}_{-0.13}$. Thus, from Equation (4.23) we measure $F_{\min} = 0.79^{+0.11}_{-0.15}$. From Figure 4.21 it can be seen that the model values do not reach the ideal values of 0 and 1/2, this is again due to the deviations of the components of the chip from their ideal values. We therefore note that the maximum value of $F_{\min}$ we would expect to measure is $F_{\min} = 0.87$.



(a) $\langle Z \otimes Z \rangle = -0.82^{+0.24}_{-0.16}$ **(b)** $\langle Y \otimes Y \rangle = -0.78^{+0.18}_{-0.13}$

Figure 4.21: Bell state correlation measurements: The measured outcomes for the expectation values of $Z \otimes Z$ and $Y \otimes Y$ for the $|\Psi^-\rangle$ Bell state. The values predicted by the model do not reach the full span of 0-0.5 due to the chip imperfections, suggesting at best we would measure $F_{\min} = 0.87$. The data show $F_{\min} = 0.79^{+0.11}_{-0.15}$ which is an unambiguous witness of entanglement.

Time Resolved F_{min}

Finally we can again use the time resolution present within our correlation data to probe a time-resolved picture of the fidelity of our entangled state. The process is the same as that presented in Section 4.3.1 where we consider only subsets of our data — those correlations separated by a given time difference — however here we must use a slightly wider window of ±50 ns as we have fewer correlations overall. It can be seen from Figure 4.22 that the degree of entanglement is largely insensitive to the detection time difference and we unambiguously witness entanglement in detections up to 100 ns apart. Recall again that due to the subdivision of the dataset the trace in Figure 4.22 is likely to remain below the value $F_{\text{min}} = 0.78$ calculated using the whole dataset, this quirk of statistics is discussed at the end of Section 4.3.1.

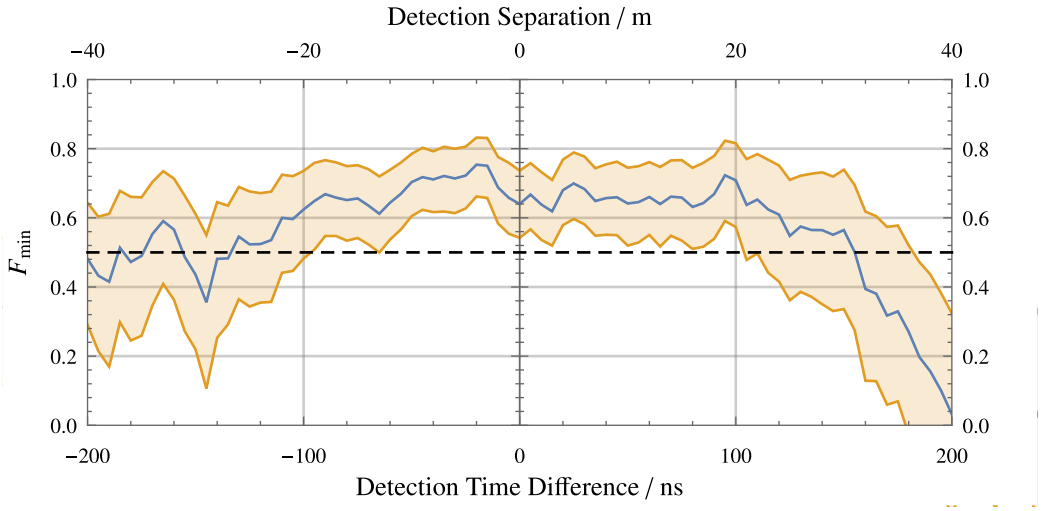


Figure 4.22: Time-resolved fidelity of entanglement: As in Figure 4.13a, we calculate the fidelity F_{min} when considering only a subset of the correlations, separated by $\Delta\tau \pm 50$ ns. The dashed line at $F_{\text{min}} = 0.5$ represents the threshold for an entanglement witness. The yellow shading covers the standard one-sigma confidence interval.

4.4.4 Backfiring

The data presented above are actually beset by yet another loss not present in the normal CNOT configuration, introduced by having SPCMs positioned on opposing sides of the chip. The nature of operation of SPADs results in a finite chance of photon *emission* from the detector, characteristically most likely following a detection. In typical applications this doesn't present a problem as the emission has a broad spectrum which is unlikely to interact with the apparatus or make its way back to the SPCM within an observation window or indeed be then detected by the module. However with detectors facing one another across the short fibre-coupled chip as is the case shown in Figures 4.19c and 4.19d we observe a significant number of these detector backfirings.

They initially present as an unusually high incidence of correlations in just a handful of the 15 possible correlation channels. A time resolved look at the distribution of the correlations shows the error is confined to a small region in time around 0 detection time difference. Increasing the time resolution further to a histogram with 1 ns wide bins reveals the temporal distribution of these backfiring events, Figure 4.23. With such a fine resolution we would expect only one or two correlations per histogram bin, however it can be seen that in those channels comprising opposing detectors there are narrow distributions of significantly more correlations. Backfiring events are disproportionally more likely to be correlated with another detection (than 'normal' detections) as they are most likely to be generated following a detection. It can be seen that they are recorded roughly 20 ns after an initial detection, the exact timing will be a combination of the internal properties of the individual SPCMs and the length of chip waveguide separating them. Most of the channels show correlations due to backfirings at both a positive and negative

detection time difference with an asymmetry in the number of correlations related to the raw number of detections on the respective detectors — e.g. there are more backfiring-correlations at positive time difference on the T_0T_1' channel as T_1' receives more detections in general than T_0.

It might have been possible to prevent backfirings from entering the correlation data with optical bandpass filters in front of the detectors to only permit detections at the desired 780 nm wavelength, however doing so would undoubtedly have lead to further losses as well as experimental complexity and expense. Instead we opted to simply ignore all correlations occurring in a manually set temporal window(s). The same window was used for all correlation channels for a given experimental input; the background correction was also compensated accordingly. Typically the exclusion accounted for roughly 5% of the total ±300 ns correlation span which corresponds to roughly 12% of the total number of correlations because it is centred near the peak correlation density at a detection time difference of 0 ns.

4.5 Conclusions

This chapter has demonstrated the reliable operation of two-qubit linear optical quantum gates with narrow linewidth photons from an atom cavity source. The CNOT operation was performed with a classical fidelity of $S = 93^{+2}_{-2}\%$, which increases to $S = 95.9^{+1.4}_{-1.7}\%$ when accounting for the imperfections of the photonic chip used. In addition we were able to verify the generation of entanglement from separable input states and place a lower bound on the quantum fidelity of the entangled state of $F_{\min} = 79^{+11}_{-15}\%$. The coherence length of the photons exceeds the very short dimensions of the linear optical setup by several orders of magnitude. Nonetheless neither the pho-

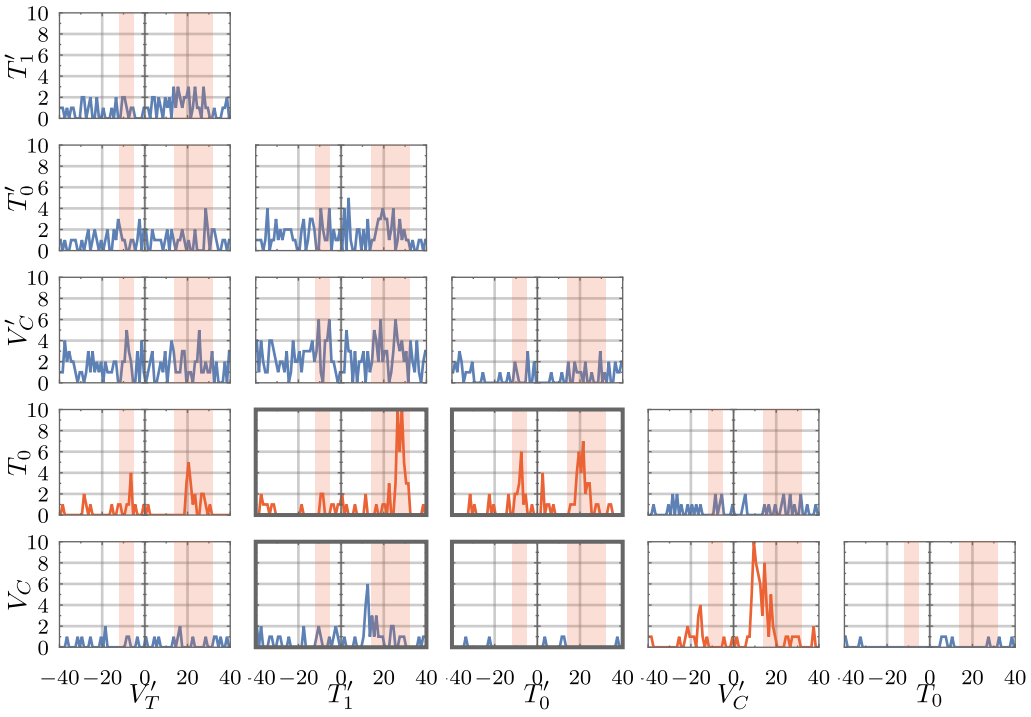


Figure 4.23: SPCM photo-emission: The 15 histograms show the time dependence of the correlations across the 6 detectors of interest in Figure 4.19c used for the $\langle Z \otimes Z \rangle$ measurements on the $|\Psi^-\rangle$ Bell state. Specifically only those correlations up to 40 ns away from exactly coincident are shown, which given the number of overall correlations should result in only a few correlations per bin at most. The four red traces highlight detector pairs where it is possible for photo-emision from one detector to be registered by the other, indeed on these channels an excess of correlations is observed within a narrow distribution. Therefore two windows are manually set during which all detections on all channels are ignored, shaded in pink.

tonic chip's ability to operate as quantum logic circuit nor the measurement of non-classical correlations due to entanglement are significantly affected. The deterministic nature of an atom-cavity source removes the fundamental scaling limits that plague spontaneous sources. Although in practice the current source is limited to two-photon experiments there are a number of improvements (Chapter 7) which should easily allow four or more photon experiments. The successful operation of integrated photonic logic presented in this chapter hopefully shows how powerful an atom-cavity source could be

for processing quantum information, which will only increase with increasing photon number.

Chapter 5

CNOT with Temporal Qubits

5.1 Introduction

This chapter combines approaches from the previous two. Specifically we investigate the operation of the CNOT gate on an integrated photonic chip with time-bin encoded photons, and observed how the behaviour changes as a function of the phase shift between the time bins. This allows us to measure the action of the CNOT gate on not only bosons, but also fermions and intermediate quantum particles.

The two fundamental classes of quantum particles, bosons and fermions, are characterised by their opposing behaviour under pairwise exchange. The behaviour is quantified by exchange statistics, which describes the phase acquired by the N particle wavefunction after interchanging two indistinguishable particles. Bose-Einstein statistics describes the bunching of bosons, for which $\hat{a}_j^\dagger \hat{a}_k^\dagger = +\hat{a}_k^\dagger \hat{a}_j^\dagger$ when swapping particles in modes j and k [95]. Whilst

Fermi-Dirac statistics leads to the Pauli-exculision principle for fermions, $\hat{a}_j^\dagger \hat{a}_k^\dagger = -\hat{a}_k^\dagger \hat{a}_j^\dagger$ [131]. Particles confined to two-dimensions are able to exhibit intermediate behaviour, where the exchange statistics are given by $\hat{a}_j^\dagger \hat{a}_k^\dagger = \mathrm{e}^{\mathrm{i}\phi} \hat{a}_k^\dagger \hat{a}_j^\dagger$ with $0 < \phi < \pi$; bosons and fermions therefore correspond to the limiting cases with $\phi = 0$ and $\phi = \pi$. Such intermediate particles are known as anyons [132] and appear in superconductivity [133] and the fractional quantum Hall effect [134].

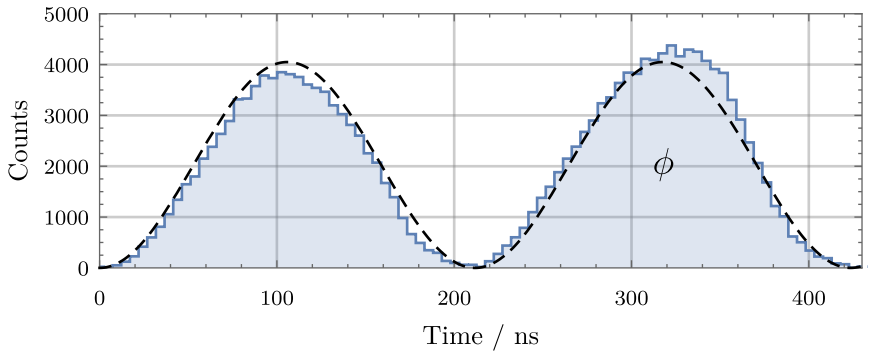


Figure 5.1: Qubit photon envelope: A histogram of many detections reveals the envelope of the double-hump photons used in this chapter. A relative phase shift of ϕ is imparted between the two time bins, resulting in the state $|\Psi\rangle = \frac{1}{\sqrt{2}}\left(|0\rangle + \mathrm{e}^{\mathrm{i}\phi}|1\rangle\right)$.

In Chapter 3 photons were prepared in temporal superpositions of two time bins with a phase shift between the bins, thus described by the state

$$|\Psi\rangle = \frac{1}{\sqrt{2}}\left(|0\rangle + \mathrm{e}^{\mathrm{i}\phi}|1\rangle\right) . \tag{5.1}$$

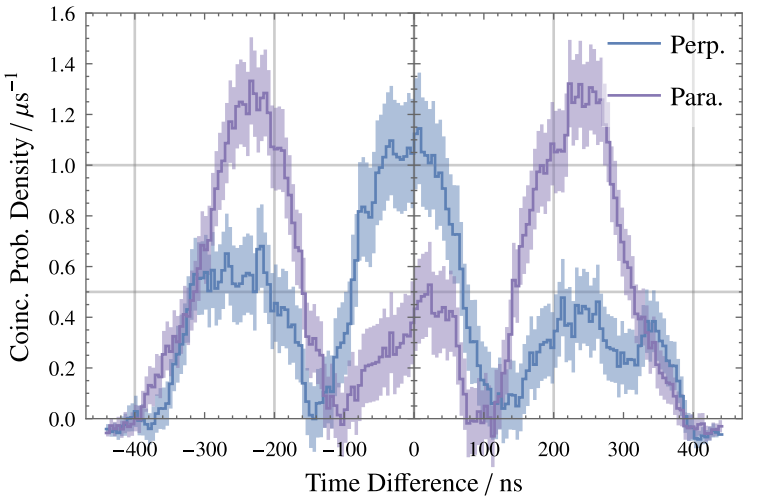
These 'signal' photons were interfered with 'local oscillator' photons without a phase shift and it was observed that the phase shift ϕ lead to an increase in correlations between the two time bins as ϕ varied from 0 to π. The envelope of the double-hump photons can be seen in Figure 5.1. The effect of the phase shift is such that the correlations observed between the photon time bins mimic the statistics of particles with an exchange parameter ϕ [127].

Therefore with our control over ϕ we are able to mimic the full range of particle behaviours from bosons to fermions. The effect is not limited to just a single beam splitter but also applies to any arbitrary unitary we can implement. The unitary considered in this chapter is that implemented by the CNOT4 photonic chip which is described in detail in Chapter 4.

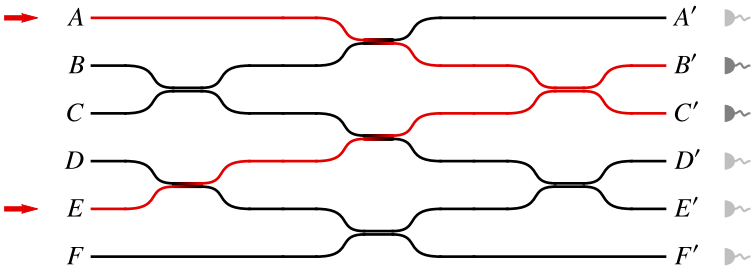
By the same process, measuring the correlations between different time-bins at the output of the CNOT photonic chip as a function of phase, we are also able to investigate the phase sensitivity of the gate. That is to say we can find out at what level of phase noise on the input photons the logical operation of the chip is compromised.

We first once again probe the quality of the quantum interference achieved with our photons in the integrated environment with a simple time-resolved HOM measurement, carried out as shown in Figure 5.2. The effect of the $\phi = \pi$ phase is clearly seen in the increased coincidence probability for parallel photons in the two satellite peaks when compared to the reference case of non-interfering, perpendicularly polarised photons. The remaining correlations around zero detection time difference suggest that (for this data set at least) the parallel polarised photons were not completely colinearly polarised. This is reflected in the value of visibility (Equation (3.5)), $V = -29 \pm 7\%$, which would ideally be 0. We know better contrast is attainable from the measured value of 85% (ideally 100%) in the previous chapter.

The next section briefly details how we can extend our existing methods of modelling the correlations expected for photons in our photonic network, outlined in Section 4.2, to the current case where the photons are subdivided into time bins. This allows us to predict the behaviour of both the CNOT gate and the general chip unitary as a function of phase. In Section 5.3 we first measure the full behaviour of the CNOT gate for the maximally different



(a) HOM



(b) Chip Configuration

Figure 5.2: On-chip double-hump HOM: Photons input into waveguides A and E interfere at the 1/2 directional coupler in front of detectors at outputs B' and C'. The presence of a non-zero contribution at zero detection time difference suggests the polarisation was not completely parallel between the interfering photons. The overall coincidence probability should remain unchanged when switching from non-interfering perpendicularly polarised photons to interfering parallel polarised photons for this case where there is a $\phi = \pi$ phase shift between the time bins of the photons — the increase in correlation probability in the satellite peak should compensate for the reduction in the centre. However the presence of correlations remaining around zero detection time difference suggest imperfect polarisation alignment, reflected in the measured visibility of $V = -29 \pm 7\%$.

case of $\phi = \pi$, before focusing on the more interesting areas with additional phases; the section concludes with an attempt to reach a continuous spectrum of phase. Section 5.4 summarises the content of the chapter.

5.2 Time-Bin LOQC Model

To model the statistics of time-bin encoded photons propagating through the CNOT4 chip we use the concept of *equivalent physical circuits* presented when first dealing with qudits in Chapter 3. We envisage duplicated physical networks, one for each time-bin, and then examine the correlations both within and between these networks. This construct allows us to straightforwardly reuse the modelling theory already developed in Chapter 4, where the operation of the CNOT4 photonic chip is discussed at length. The corresponding equivalent physical circuit for time-bin qubits propagating through the CNOT4 chip looks as shown in Figure 5.3.

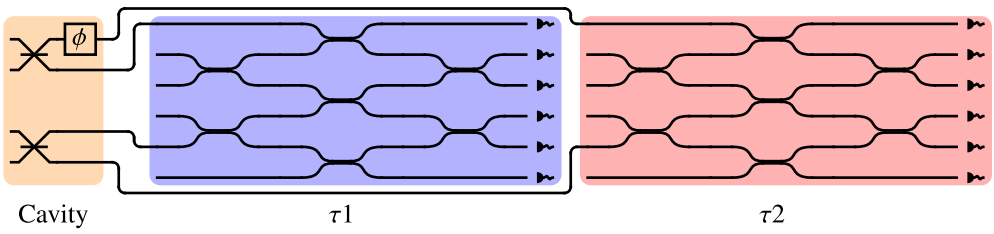


Figure 5.3: Equivalent virtual circuit: The form of the equivalent virtual circuit for two temporal qubits in the CNOT4 photonic network is shown. The circuit can be broken into three components, the intra-cavity state preparation, and then the propagation of each of the two time bins through the photonic network.

We therefore consider 12 independent modes with the unitary given by

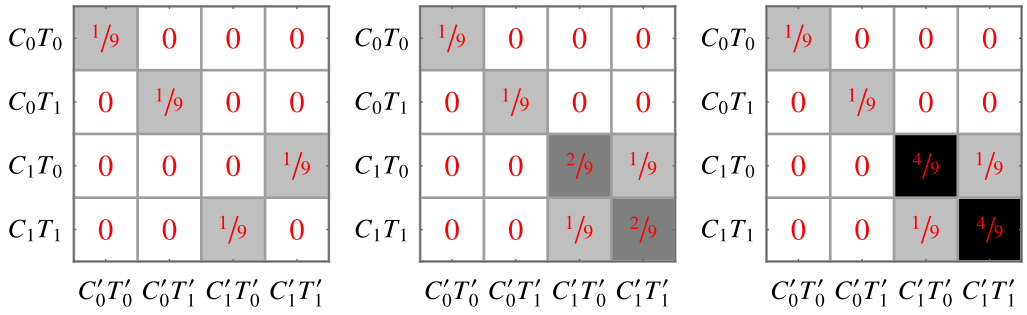
$$U = \begin{pmatrix} U_{\text{CNOT4}} & 0_{6,6} \\ 0_{6,6} & U_{\text{CNOT4}} \end{pmatrix}, \tag{5.2}$$

where the explicit form of U_{CNOT4} can be found in Section 4.2. In addition to this one must also mix the relevant input modes and include a phase shift (if required) as outlined in Figure 5.3. For correlations between the same time bins one simply looks at correlations between the modes $\{1..6\}$ or $\{7..12\}$ and for cross time bin effects one looks at the correlations between one mode from $\{1..6\}$ and one from $\{7..12\}$.

The relative phase between the two photons is only initialised upon the first detection (see Section 3.2). Therefore as the phase shift on the signal photon only occurs between the two time-bins, the phase only effects those correlations between time bins. For the same-time-bins statistics, the action of the CNOT4 unitary and the outcome of the CNOT gate will therefore be unchanged from that presented in Chapter 4. We do however expect new phase dependent effects in the cross-time-bin correlations, at least in those regions of the truth table and correlation matrix that rely on two-photon interference — specifically the C_1T_x rows. This can be seen in Figure 5.4 where the diagonal C_1T_x elements of the truth table show a phase dependence, increasing from their original zero value up to four times the value of the typical outcome. This has implications for the logical operation of the CNOT gate in noisy phase environments.

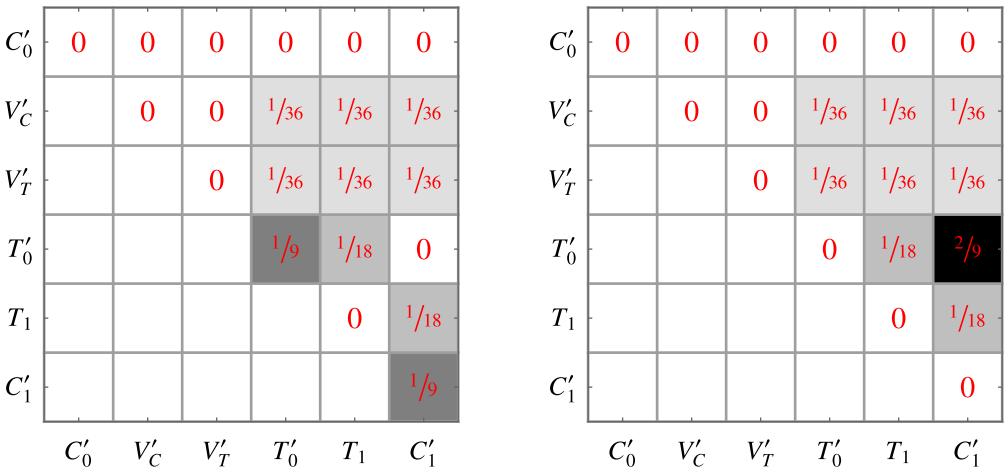
A sense of why a number of additional correlations are introduced into the truth table can be found from considering the correlation matrix as a whole. Of the 21 possible unique pairwise combinations of the 6 chip outputs, the 6 diagonal pairs, $A'A'$ etc, are not available to those (cross time bin correlations of) photons with a $\phi = \pi$ phase shift, which we know exhibit fermionic anti-bunching and therefore cannot leave via the same exit port. This can be seen for the EF input in Figure 5.5.

The antibunching behaviour exhibited by sequential time bins of pho-



(a) $\phi = 0$ **(b)** $\phi = \frac{\pi}{2}$ **(c)** $\phi = \pi$

Figure 5.4: CNOT truth table as a function of particle class: The phases of 0, $\pi/2$, and π correspond to the statistics of bosons, distinguishable quantum particles, and fermions respectively. It can be sen that the only effect of phase is to introduce correlations along the diagonal in the C_1T_x entries. Note that because the phase only enters into correlations between time bins, it is only manifest for half the input photon pairs. The normalisation in these tables therefore is not "per input photon pair" but rather double this, so that the boson case corresponds to the truth tables presented in Chapter 4. See Figure 5.5 for further explanation.



(a) Same Time Bin **(b)** Diff. Time Bin

Figure 5.5: CNOT4 chip operation with phase difference: The matrices show the full distribution of the unique expected correlations for a pair of photons, with a $\phi = \pi$ phase shift, input into waveguides EF. Each table sums to 1/2, corresponding to the fact that half the time two photons will produce a correlation in the same time bin, and half the time a correlation between different time bins.

tons with a π relative phase shift has been described as fermionic. It does however exactly reproduce the statistics of fermions under the same unitary operations. In fact, the statistics of cross time bin correlations for photons with a phase shift of ϕ are exactly those for indistinguishable particles with exchange statistics ϕ, where the limiting cases of $\phi = 0$ and $\phi = \pi$ correspond to bosons and fermions respectively. In between, there is a continuous transition from simulation of Bose-Einstein to Fermi-Dirac quantum interference. This can be verified with a model which explicitly includes the particle exchange statistics, such as that presented in [127]. Those particles with fractional exchange statistics, $0 < \phi < \pi$, are termed anyons. There is one other slightly special case at $\phi = \frac{\pi}{2}$ where the statistics are also equivalent to distinguishable, yet still quantum and therefore self-interfering, particles.

The values presented in Figures 5.4 and 5.5 have been calculated assuming the ideal CNOT4 photonic network where the couplers have the exact reflectivities of 1/2 and 1/3. We know that due to imperfections in the manufacturing process there are slight deviations in the behaviour of the actual chip from these ideal values, however as discussed in Section 4.2 they are small.

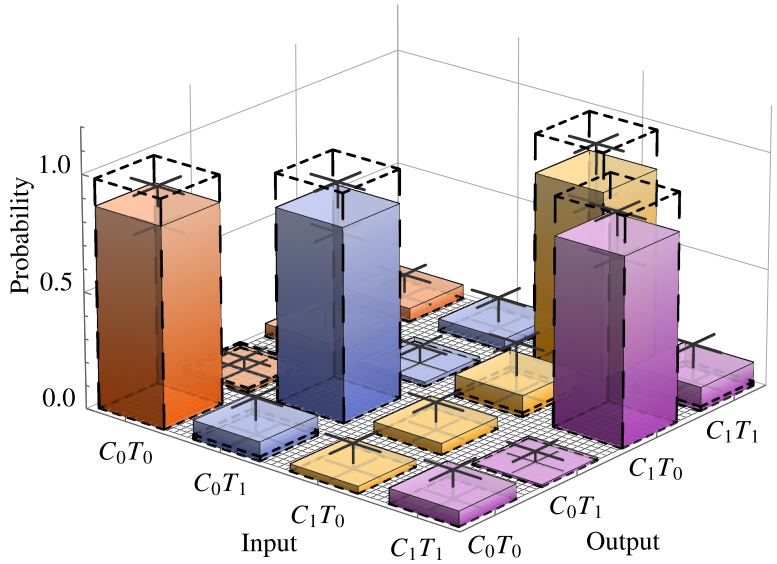
5.3 Results

The results presented in this section were measured and analysed using the same methods as those previously presented in Chapter 4. The key process involved is accounting for the presence of 'background correlations' which are introduced primarily due to the dark counts of the SPCMs. Their contribution is (well) estimated by the methods described in Section 3.5 and then removed from the correlation matrices by maximum likelihood estimation

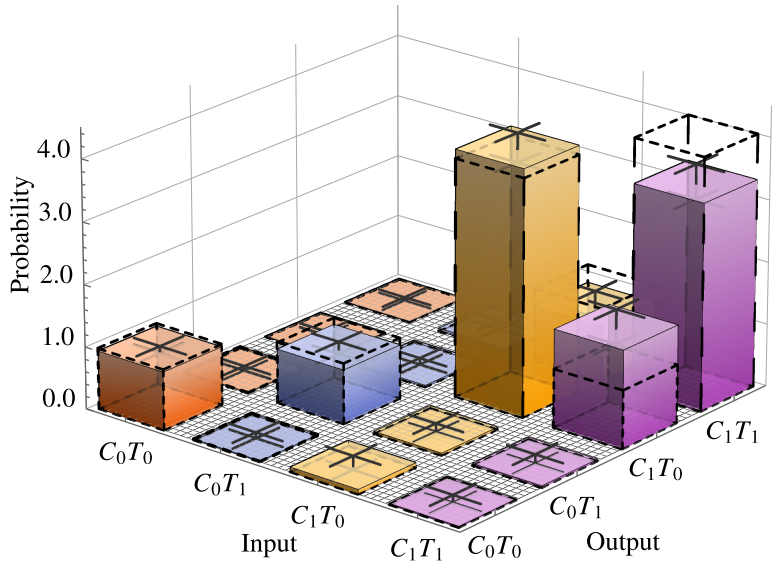
methods which ensure no negative values, as described in Section 4.3.2.

As discussed already, the effect of the phase shift only enters into those correlations between the two time bins and furthermore it only enters into the truth table in those rows relying on two-photon interference, namely the C_1T_x rows. This is obvious in Figure 5.6 which show the corresponding truth tables for both same and sequential time bin correlations when there is a relative phase shift of π between the two time bins of the signal photon. These truth tables are presented, as those previously, in the so called logical basis, where each row of the table is normalised to sum to one. This is justified as this CNOT gate is operated in the post-selected basis where we require one detection in both a control and target waveguide; this occurs with 1/9 probability per input pair. However, when departing from bosonic statistics the CNOT gate no longer operates with a balanced probability — the success probability depends upon the input — with the C_1T_x rows achieving a 5/9 success probability whilst the C_0T_x rows are unchanged. We therefore extend our concept of the logical basis to normalise the sum of a row to its theoretical success probability in units of 1/9. Consequently the C_1T_x rows of the truth table in Figure 5.6b are normalised to 5 and reach a maximum 'probability' of 4. Although a probability in excess of 1 is uncomfortable, this convention does allow simple comparison between truth tables derived from 'particles' following different exchange statistics, for example the two tables in Figure 5.6.

The degree of overlap between the measured truth tables and the expected distributions can be quantified by the similarity (Equation (4.9)). For double hump photons with a relative phase shift of $\phi = \pi$ we measure for the similarity of the CNOT truth table formed of same time bin correlations to the ideal bosonic CNOT truth table (Figure 5.4a) $S = 91^{+3}_{-3}\%$ and for the



(a) Same Time Bin Correlations



(b) Diff. Time Bin Correlations

Figure 5.6: Measured $\phi = \pi$ truth table: The complete CNOT truth tables measured with double-hump photons with a $\phi = \pi$ phase shift, resolved into the two different behaviours for correlations between the same time bins and those between different time bins. The dashed cages represent the expected values, the error bars are indicated with the crosses. The normalisation is discussed in the main body text. The similarities of truth tables (a) and (b) to their expected distributions are $S = 91^{+3}_{-3}\%$ and $S = 98^{+1}_{-1}\%$ respectively.

table formed of sequential time bin correlations $S = 98^{+1}_{-1}\%$ when compared to the fermionic truth table (Figure 5.4c). These values sit in agreement with that of $S = 93^{+2}_{-2}\%$ measured with simple single hump photons in Chapter 4. However to achieve a similar scale of uncertainty the measurement time had to be doubled as obviously each input pair can only register as a correlation in one of the two tables. In total 2615 correlations contribute to the two truth tables in Figure 5.6.

We know from symmetry that the state of the input target qubit doesn't fundamentally change the outcome, just the labelling. Therefore when investigating the effect of the phase on the truth table it is superfluous to measure all four input pairs, the effect of the phase is fully characterised in just one of the two C_1T_x rows. In Figure 5.7 below we therefore just measure the C_1T_0 row for a series of different values of relative phase shift ϕ. The phase dependence of the 'incorrect' C_1T_0 output is obvious whilst the 'normal' C_1T_1 output is unaffected. The similarities for the individual rows to their respective expected distributions vary from 96-99%; when taken as a whole the data show $S = 98.1^{+0.6}_{-0.7}\%$.

Once again because we are monitoring all six output ports of the chip we are also able to reconstruct the full correlation matrix, notwithstanding the diagonal which cannot be observed due to the limitations of our detectors (they are not number resolving and the dead time precludes measuring twice within a time bin). We can therefore perform a full simulation of the action of the unitary implemented by our chip on particles with any exchange statistics. Figure 5.8 shows the results for the EF inputs (now using sequential alphabetical labels as we are no longer concerned with the logical CNOT operation) for both bosonic ($\phi = 0$) and fermionic ($\phi = \pi$) particles.

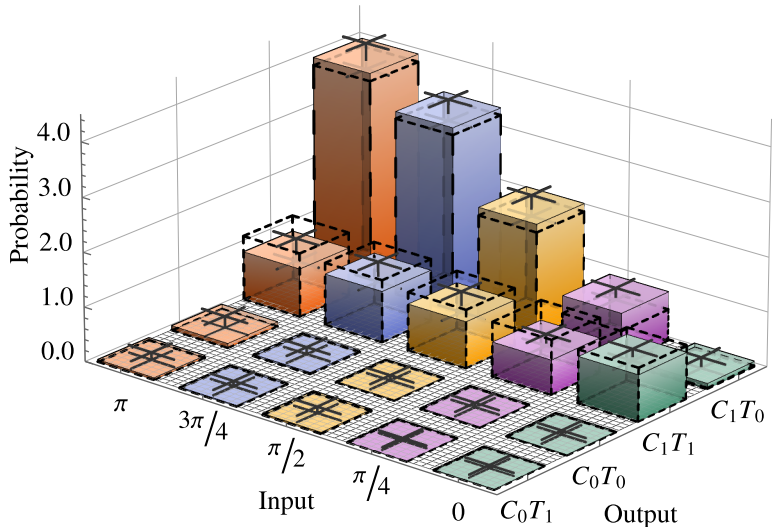
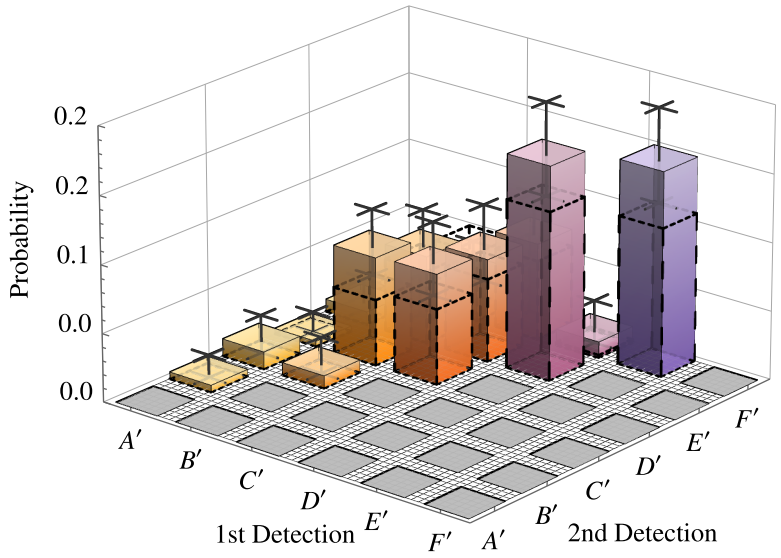


Figure 5.7: CNOT C_1T_0 row as a function of phase: The effect of the phase is measured for five different values for just a single row of the truth table (we know it only affects the C_1T_x inputs in a symmetric fashion). Note the outputs have been reordered to more clearly show the behaviour.

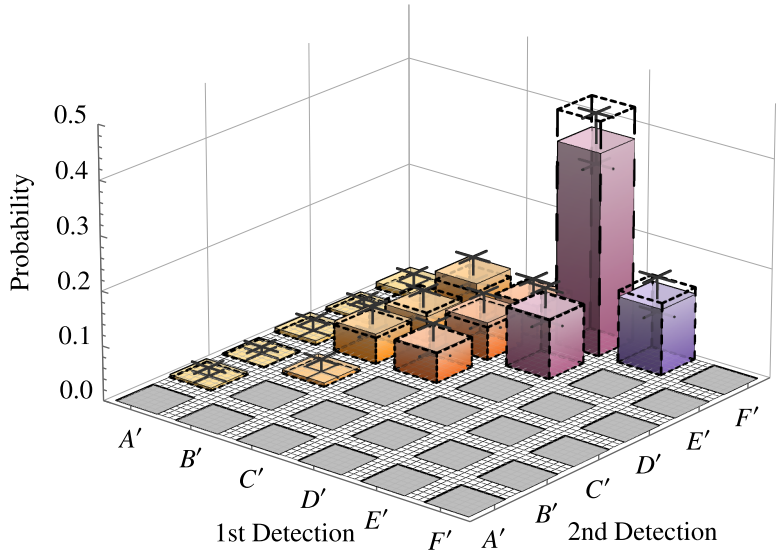
5.3.1 Finer Phase Resolution

In Figure 5.7 the operation of one row of the CNOT gate was measured for a handful of different phases. We would like to extend this and perform measurements for a continuous spectrum of phases from 0 to π. This is not possible with the current configuration whereby we generate alternating signal and idler double hump photons, with and without a phase shift respectively, as we would have to rerun the experiment for a theoretically infinite number of signal photon waveforms. Figure 5.7 shows everything but as a demonstration of the versatility we would like to do better.

If we do away with the signal and local oscillator picture and instead impart a random (but known) phase shift to every photon, we will acquire data across the full range of values of ϕ, furthermore the acquisition only requires one (admittedly long) data run. There is a slight increase in computational complexity associated with recording the assumed relative phase shift differ-



(a) Same Time Bin Correlations



(b) Diff. Time Bin Correlations

Figure 5.8: Experimental quantum simulation: The full correlation matrices for same time bin (a) and different time bin (b) correlations for photons with a $\phi = \pi$ phase shift compared to the predicted bosonic (Figure 5.5a) and fermionic (Figure 5.5b) distributions for the CNOT4 photonic network unitary. The waveguides are labelled using the sequential alphabetical labels shown in Figure 5.2b as we are no longer considering a logical operation. The probabilities are normalised to our estimate of the input number of photon pairs. The similarities are $S = 95^{+2}_{-2}\%$ and $S = 97^{+1}_{-1}\%$ for (a) and (b) respectively.

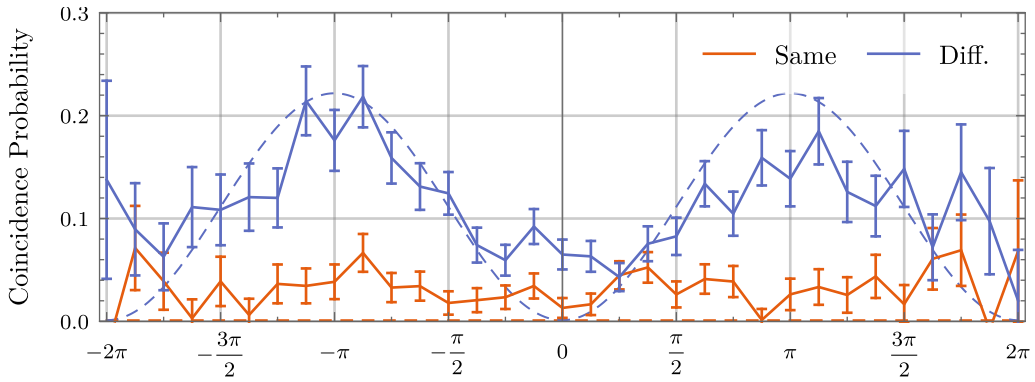
ence for every photon detection. If the ith STIRAP driving waveform has a phase shift ϕ_i between it's two time bins, then a photon detected during the ith interval is recorded as potentially having undergone interference within the chip with a phase shift of $\Delta\phi = \phi_{i-1} - \phi_i$ between the two interfering photons [1]. We know this to be the case as a correlation requires one photon to pass through the delay line and the other to take the short path; because we have two paths it is therefore impossible to know the phase shift ϕ_i for a detection, only the difference $\Delta\phi$ associated with that detection's potential correlation. There are however also experimental advantages to this method as any fluctuations in source performance will be spread across all phases.

Unfortunately accessing a fully continuous spectrum of phases is still beyond us due to the limitations of the AWG, which cannot generate waveforms on-the-fly and can only store a limited number of unique waveforms. Such a spectrum would also require a great deal of data, and would require binning of similar phases thus potentially reducing the visibility. We therefore use a sequence of waveforms with phases randomly chosen between 0 and 2π in steps of $\pi/8$. Admittedly this is only twice the resolution of that in Figure 5.7, however the method is extensible and finer resolution simply requires longer experimental runtimes.

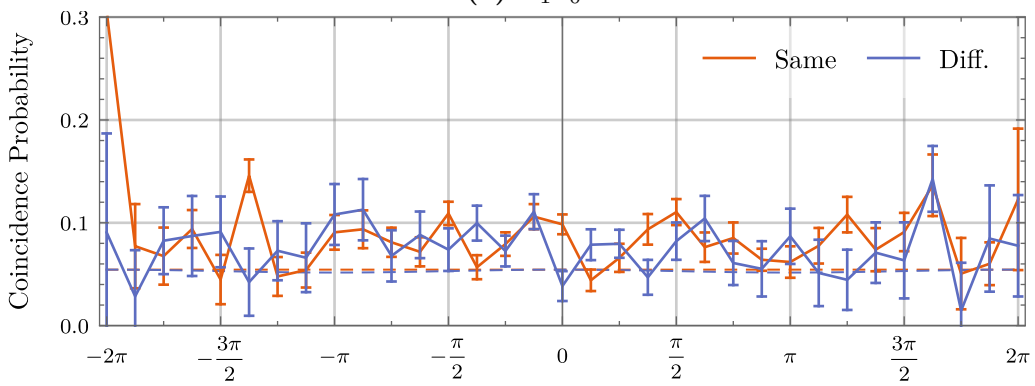
In total this setup produces measurements across 33 unique phases as shown in Figure 5.9, which is built from around 8 hours of data, totalling around 60 000 MOT throws. It shows the interesting C_1T_x outputs for the C_1T_0 input, with the data normalised to the best guess of the number of input pairs with that phase difference.

A result of sampling the phases from the finite uniform distribution 0

[1] Up to this point $\Delta\phi = \phi$ as the signal photons had identical phase shifts ϕ and for the local oscillator photons $\phi = 0$.



(a) C_1T_0



(b) C_1T_1

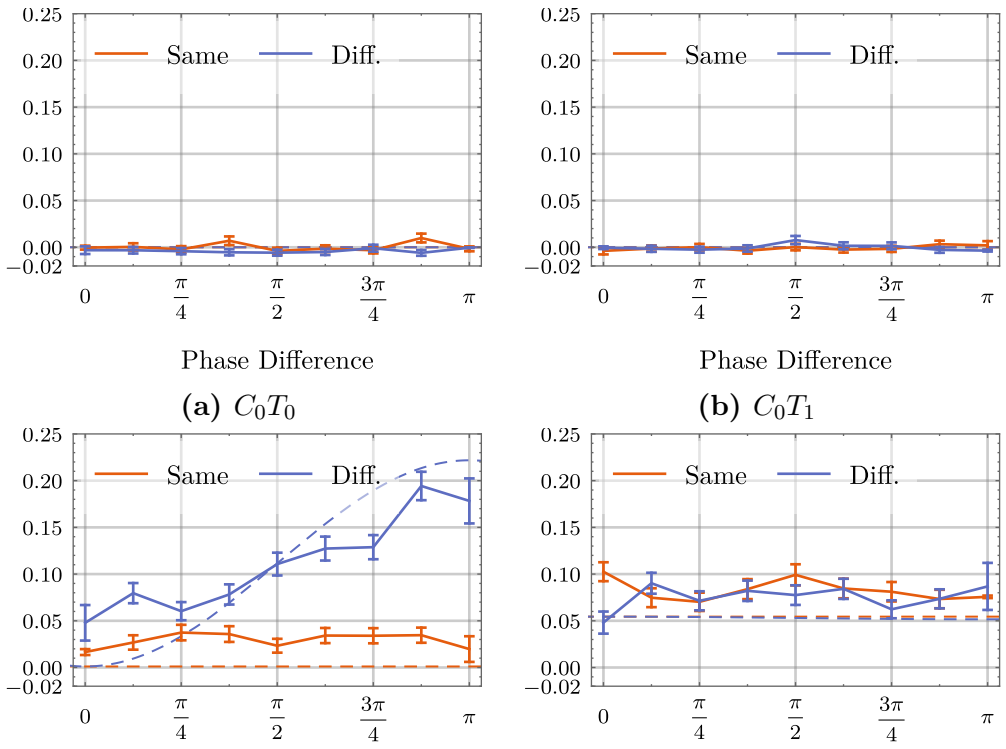
Figure 5.9: Complete phase behaviour of CNOT gate: The plots show the variation in probability for correlations at the C_1T_0 and C_1T_1 outputs, resolved into correlations within the same time-bin, and correlations between different time-bins, for temporal qubits with a phase difference ϕ launched into C_1T_0. The phase effects only manifest for correlations between different time bins; the effect is periodic and unique on the interval $[0, \pi]$. The dashed lines show the theoretically predicted values.

to 2π is a triangular distribution of phase differences. There are therefore more photon pairs with a phase difference near 0 than the limits of $\pm 2\pi$, this is reflected in the size of the error bars. This could be avoided by instead randomly choosing phase differences on the interval $[-2\pi, 2\pi]$ and setting the ϕ_i to the running total.

As expected the behaviour is only unique on the interval $[0, \pi]$, we can therefore wrap the data back onto that interval and reduce the errors somewhat, as shown in Figure 5.10, which also includes the C_0T_x outputs. Not only does this data correspond to a simulation of particles with variable exchange statistics, but also it allows us to probe the stability of this CNOT gate to phase variation. The logical performance of the CNOT gate is randomised when the target qubit leaves via either output port with equal probability. For the control C_1T_x inputs this occurs before the halfway point. The output will be randomised when

$$\begin{aligned} \frac{4}{9}\sin^2\left(\frac{\phi}{2}\right) &= \frac{1}{9}\,, \\ \Rightarrow \phi &= \frac{\pi}{3}\,. \end{aligned} \tag{5.3}$$

If we take into account the deviations of the chip parameters from the ideal CNOT circuit, the phase at which the outputs are randomised actually increases fractionally to $\phi = 1.078$ ($\pi/3 \approx 1.047$). In reality the noise present on the data makes it hard to say exactly at what phase the outputs are randomised, furthermore the reduced interference contrast achieved limits the data from reaching the full span of the expected values.



(a) C_0T_0 **(b)** C_0T_1

(c) C_1T_0 **(d)** C_1T_1

Figure 5.10: Complete unique phase behaviour of CNOT gate: Photons are inputs into C_1T_0. The data is the same as that behind Figure 5.9 but is now wrapped onto the interval of unique behaviour between 0 and 2π which reduces the error bars somewhat. The two uninteresting C_0T_x outputs channels are also shown for completeness.

5.4 Conclusions

This chapter has looked at the operation of a CNOT gate, integrated into a photonic chip, with temporally encoded qubits. It was shown that by varying the free phase parameter between the two time bins of the qubits, the correlation statistics of particles described by a range of exchange statistics can be simulated. Consequently we found that for fermions the CNOT operation no longer succeeds 1/9 of the time but that the success probability depends upon the inputs. The equivalence between the statistics of bosons / fermions and pairs of photons with a phase parameter ϕ arises simply from the identical (anti-)symmetries of the multi-particle wavefunctions in either case; for more than two photons the corresponding symmetries are harder to produce. Aside from the aspect of quantum simulation the results also show the phase sensitivity of the CNOT gate. With an ideal gate the operation is randomised at $\phi = \pi/3$ however the imperfections present in the chip actually make it fractionally more robust to phase errors.

The ability to simulate multiple classes of particles with such a simple setup is an attractive feature of the photon source. It could have wider uses in simulating classes of particles with intermediate exchange statistics, anyons, which only occur in exotic two-dimensional systems, and may have uses in QIP [29]. The simplicity of the approach is lost somewhat when scaling up to more than two particles as additional local and controlled swap operations are required to maintain the required (anti)symmetry between all pairs of particles (see the supplementary information provided in [127]). There are also proposals to use photonic simulation of particle statistics to perform quantum chemistry simulations [135].

Chapter 6

Quantum Feedback

6.1 Introduction

Feedback control is the name given to the technique by which a control system, or "controller", obtains information about the trajectory of a system[1], and uses the information to control the system in real time. Typically this is done to steer the output of the system towards some reference. Other control technique exist, however feedback is an essential component to allow systems, both classical and quantum, to operate as desired in the presence of noise.

Feedback control was first introduced into quantum dynamics in the 1980's [136], and the earliest implementations used measurement-based feedback control in quantum optical systems [137]. Measurement-based control is not the only paradigm of quantum feedback control; it has been shown that

[1] In control theory the system being controlled is called the "plant".

it is possible to implement feedback control on quantum systems without performing measurements, in so called coherent feedback control. This can be achieved by using a "cascade connection" to feed the output of a system back into the same system [138, 139], for example mirrors and an optical isolator can be used to return the output of an optical cavity [140]. Alternatively measurement-free feedback control can be achieved with suitable chosen unitary interactions between the controlled system and a quantum controller [141].

Coherent feedback control, in which both the dynamical system and the controller are quantum systems, coupled through a unitary interaction, is also known as *directly* coupled quantum feedback [142]. Whilst measurement-based feedback control, where the quantum dynamical system can be viewed as also having a classical input (from a classical controller) is termed *indirectly* coupled quantum feedback. In both it is a quantum system which is under control, thus both constitute quantum feedback control. Typically the quantum system is controlled toward some desired steady state; this is not the case in this chapter where the quantum system is a spatially entangled pair of photons whose spatial modes are controlled.

Although measurement-based feedback is typically easier to implement (than coherent feedback) it suffers a few disadvantages. Measurements made on quantum systems typically require significant amplification before they can be used by a classical controller, and such amplification is rarely without noise. In addition, the amplification and consequent processing of the information require time and therefore measurement-based feedback has an associated bandwidth. However a classical controller can perform noise-free processing of the measurement information, whereas a quantum controller will likely be vulnerable to noise from the environment. Finally, the fidelity

of the control is often strongly linked to the measurement efficiency.

Measurement-based quantum feedback control has been leveraged in quantum metrology to improve the performance of single-shot phase measurements [143]. In atom optics, it has been used to stabilise the combined quantum state of an atom-cavity system [144], and with weak measurements to prepare and stabilise Fock states [145, 146] in a high-Q microwave cavity. Repeated weak measurements are often used in order to minimally disturb the system according to the information-disturbance trade-off heuristic [147]. However strong measurements may also be used as required in some proposed quantum Zeno schemes [148]. A recent review of both the theory and experimental results can be found at [149]

This chapter demonstrates active control over the routing of temporally encoded qubits in long photons. Two double-hump photons are interfered on a beam splitter and, in the case of one detection in each time bin, the second detection is steered to a chosen detector via on-the-fly processing of the first detection outcome. This is measurement-based quantum feedback control, where SPCMs provide a strong measurement of the spatial mode of the photons and the information gained is used to control the following quantum state reduction.

Recall from Chapter 3 that when demonstrating the versatility of the source a stream of temporally encoded qubits was produced where every other qubit had a phase difference between its time bins, therefore described by the wavefunction

$$|\Psi\rangle = \alpha|0_1, 1_2\rangle + \beta e^{i\phi}|1_1, 0_2\rangle\,. \tag{6.1}$$

These photons are generated by the coherent STIRAP process outlined in

Section 2.1.2, where the waveform is pre-calculated and the contained phase flip is imparted to the driving laser by an AOM. If we consider the relative time- and length-scales involved in the experiment it becomes apparent that a photon under generation spends the majority of its lifetime simultaneously present at the detectors, the beam splitter, the cavity, and the AOM; the light transit time from AOM to detector is under 50 ns and the photon length around 430 ns. By simultaneously present we understand that the wavefunction of the photon has non-zero amplitude concurrently at these different places.

It should therefore be possible to only set the phase shift ϕ on the second time bin, at the time of detection of the first time bin. With just a single photon, changing anything about its generation process cannot have an effect after it has been detected, additionally we have no way to measure the relative phase of just a single photon. However, if two photons are present, one in the delay arm, one in the short, we have no way of knowing which of the two was detected and following the first detection we have an entangled state such that the phase change will influence the result of the second detection. The details of this quantum state reduction follow below.

6.1.1 Feedback Plan

Let us examine carefully the feedback plan by performing a step by step analysis of the different possible outcomes for our two detection events. Recall from Section 3.2 that when two double-hump photons interfere on a beam

splitter (see Figure 3.1) the full output state can be described by

$$\frac{1}{2\sqrt{2}}\Big((\hat{a}^\dagger_{C1}\hat{a}^\dagger_{C1} + \mathrm{e}^{\mathrm{i}\phi}\hat{a}^\dagger_{C2}\hat{a}^\dagger_{C2} - \hat{a}^\dagger_{D1}\hat{a}^\dagger_{D1} - \mathrm{e}^{\mathrm{i}\phi}\hat{a}^\dagger_{D2}\hat{a}^\dagger_{D2}) \\ +(\mathrm{e}^{\mathrm{i}\phi}+1)(\hat{a}^\dagger_{C1}\hat{a}^\dagger_{C2} - \hat{a}^\dagger_{D1}\hat{a}^\dagger_{D2}) + (\mathrm{e}^{\mathrm{i}\phi}-1)(\hat{a}^\dagger_{C2}\hat{a}^\dagger_{D1} - \hat{a}^\dagger_{C1}\hat{a}^\dagger_{D2})\Big)|0\rangle \quad (6.2)$$

with subscripts C and D referring to the two spatial output modes and subscripts 1, 2 indexing the time bins. We can ignore the first four terms where the detections occur in the same spatio-temporal mode as they are unobservable (with our non-number resolving detectors). Rearranging the remaining terms leave us with

$$\hat{a}^\dagger_{C1}\left((\mathrm{e}^{\mathrm{i}\phi}+1)\hat{a}^\dagger_{C2} - (\mathrm{e}^{\mathrm{i}\phi}-1)\hat{a}^\dagger_{D2}\right) + \hat{a}^\dagger_{D1}\left((\mathrm{e}^{\mathrm{i}\phi}-1)\hat{a}^\dagger_{C2} - (\mathrm{e}^{\mathrm{i}\phi}+1)\hat{a}^\dagger_{D2}\right). \quad (6.3)$$

From this it can be seen that after the first detection, the following quantum state reduction will leave us in one of two states in which the phase ϕ, which is still not necessarily defined yet, has opposite effects. With judicious choice of ϕ in the two cases, we can therefore control the outcome of the second detection. If the first detection is in channel C, we may choose $\phi = \pi$, thus steering the second detection to

$$(\mathrm{e}^{\mathrm{i}\pi}+1)\hat{a}^\dagger_{C2} - (\mathrm{e}^{\mathrm{i}\pi}-1)\hat{a}^\dagger_{D2} = 2\hat{a}^\dagger_{D2}\,. \quad (6.4)$$

Conversely if the first detection was in channel D, we could reverse our choice of ϕ and set $\phi = 0$ to achieve the same outcome

$$(\mathrm{e}^{\mathrm{i}0}-1)\hat{a}^\dagger_{C2} - (\mathrm{e}^{\mathrm{i}0}+1)\hat{a}^\dagger_{D2} = 2\hat{a}^\dagger_{D2}\,. \quad (6.5)$$

Thus far it has only been shown that it is theoretically possible to im-

plement such a scheme, the implicit assumption has been that feedback can be instigated instantaneously which obviously cannot be the case. The next section presents a detailed look at the timings involved and describes how the decision making and phase generation are carried out within just 13 ns, consequently allowing feedback to be performed with an error rate under 0.5%.

6.2 Implementation

As with many feedback systems, three general elements are required: some form of measurement of the system, a controller to decide what needs to be done, and an effector to perform any required action on the system. Measurement is taken care of by the SPCMs which are already in place for measuring the interference of the photons, we therefore need a controller to decide whether or not a phase should be applied (or perhaps what value of phase) and an effector to impart the phase to the driving STIRAP waveform — the AOM already in place for pulse shaping might seem like an obvious choice but it will be shown shortly that it is prohibitively slow. These two additional operations (control and effecting) must be carried out as quickly as possible as there is no artificial separation between the two time bins of the 430 ns $\sin^4$ intensity envelope photons used. Consider a first detection after 150 ns on detector C, thus necessitating a phase change of π on the STIRAP driving pulse for the second time bin to achieve our goal of always routing the second detection to detector D. If the control and effect take 200 ns, then already 135 ns, over half, the second time bin will have been generated before the phase comes into effect. Not only does this constitute a significant probability of lack of control but also a phase change in the driving laser away

from the zero intensity midpoint is likely to be unadiabatic and destroy the photon generation process. The time delay problem is actually worse still, as the light transit time of 45 ns from effector to detector means even if the feedback control was instantaneous, there is still a small chance of an error (Figure 6.2). It is technically possible to separate the photon time bins to alleviate the latency problem, however increasing the overall photon length in undesirable given the roughly 500 ns long coherence length achieved; it will be shown shortly that even without any artificial separation, the expected error rate is under 1%.

This section first analyses the time budget before presenting the solutions used for the control and effector — some home-built electronics and a fiberised EOM.

6.2.1 Time Budget

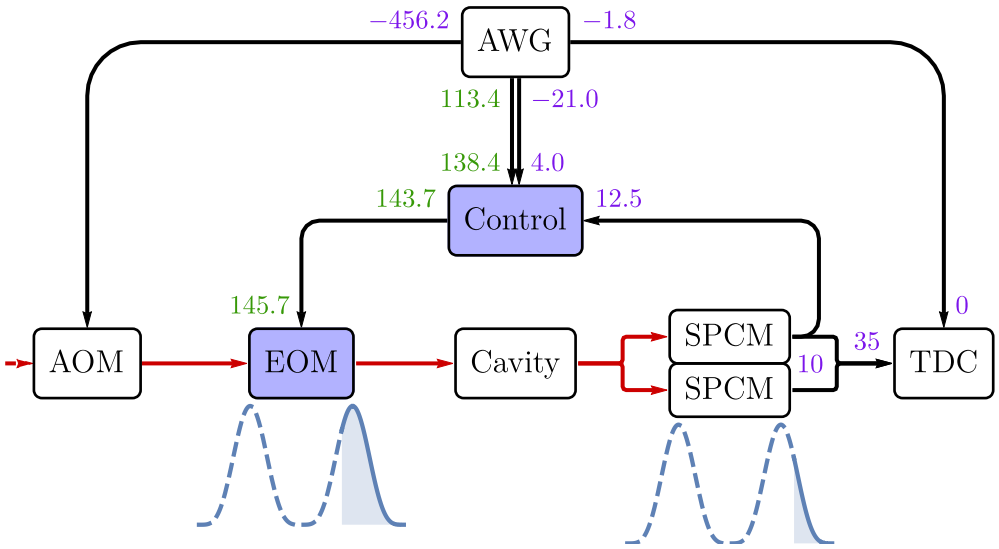
Given that we need to be able to change the phase only for the second time bin, conditional on detections only in the first time bin it is obviously crucial that we know the exact spatio-temporal position of the photon excitation — not only whilst it is an actual photon but also before, whilst the signal is still imprinted in the STIRAP driving pulse, and after, when it is a TTL signal from an SPCM. To that end a complete map of signal timings was created using a fast oscilloscope to record the arrival time of various signals with reference to a common zero, Figure 6.1. The choice of time zero is arbitrary, here it is defined as the time at which the trigger signal from the AWG arrives at the TDC. An overview of the normal pulse generation – photon detection sequence and the hardware involved was given in Section 2.3.4, however a refresh here detailing the incorporation of the additional hardware should be

useful.

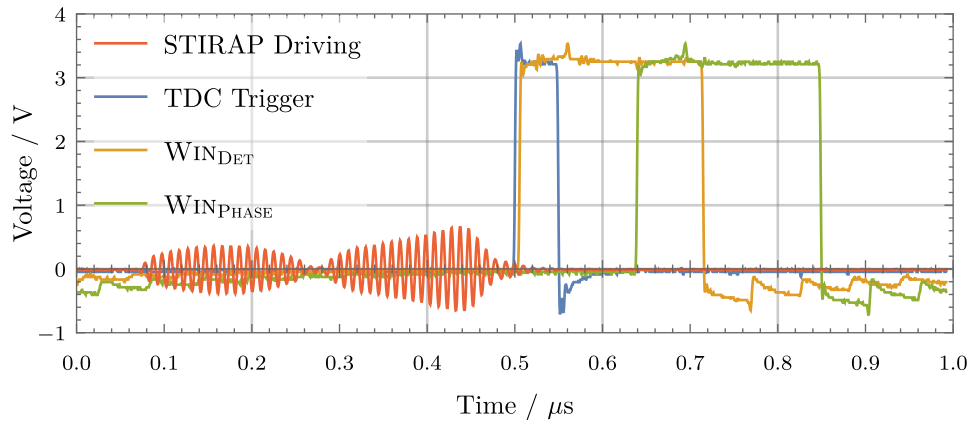
The AWG can be considered to be the clock for everything. It generates the pump and repump RF waveforms (precomputed for the desired pulse shape) and distributes them to relevant AOMs, sets the time zero for the TDC (which then records the times of all SPCM detection events) by means of a short trigger pulse, and now additionally provides windows (square voltage pulses) to the feedback control hardware to relay timing information (these waveforms can be seen in Figure 6.1b). From Figure 6.1a it can be seen that the total signal propagation time, from AWG to AOM, through the cavity, to SPCM and finally to TDC is such that the start of the photon pulse waveform is emitted from the AWG around 450 ns before the trigger pulse to the TDC. Around 300 ns of this total propagation time is in the AOM which is why it is too slow to be used as our effector. The speed of signal propagation down the RG58 coaxial cabling used was measured consistently to 5 ns per metre (in agreement with the literature value) which is slow enough that cable lengths must be taken into consideration for the feedback side of the experiment. However a useful consequence of this 'slow' transmission speed is that it also provides a convenient means of compensating timings on a timescale shorter than that possible on the digital channels of the AWG, whose resolution is limited to units of 8 samples, which at 1.25 Gs/s corresponds to 6.4 ns — over a meter of cable.

A concerning issue is highlighted by Figure 6.1: the photon signal takes just under 80 ns to reach the output of the SPCMs from the EOM[2]. This means that for detections within 80 ns of each other there is no possibility of

[2]Unfortunately we have no means of measuring the delay between photon impact and TTL pulse out of the SPCM and the value is not stated in the data sheets. From correspondence with the manufacturer we believe it to be around 35 ns which would leave a credible light transit time from EOM to SPCM.



(a) Setup, all times in nanoseconds



(b) Waveforms

Figure 6.1: Feedback control setup: The addition of a Controller and an EOM (both in blue) to the standard apparatus allow feedback control to be implemented. The red arrows indicate the path taken by the laser / photons, the black arrows are electrical signals. The numbers detail the emission and arrival times of the leading edge of various signals, designed to either coincide with the start of the first time bin (purple) or the second (green). The arrival of the trigger at the TDC is chosen as time zero. The timings of the various waveforms emitted from the AWG are also shown in (b) (the STIRAP repump is not shown). A visual illustration of the propagation time from EOM to SPCM is shown, where the shading of the photon corresponds to how much of the photon wavefunction has reached / passed that point.

achieving feedback control. This 'dead time' will be extended by the latency of the controller. Considering the shape of the qubits used we note that the amplitude of the photon is very small for the majority of the central 80 ns and therefore the probability of a correlation occurring during the dead time is low. The probability of a correlation (with one detection in each time bin) occurring during the dead time is given by

$$P(\tau) = \int_{\max\left[\frac{1}{2}-\tau,0\right]}^{\frac{1}{2}} f(t_1) \int_{\frac{1}{2}}^{\min[t_1+\tau,1]} f(t_2)\,\mathrm{d}t_2\,\mathrm{d}t_1\,, \tag{6.6}$$

where τ is the dead time given as a fraction of the total photon length, t_1 and t_2 are also dimensionless, expressed as fractions of the photon length, specifically $t_1 \in (0, \frac{1}{2})$ and $t_2 \in (\frac{1}{2}, 1)$, and f is the intensity envelope of the photons; in this case

$$f(t) = \frac{16}{3}\sin^4(2\pi t)\,. \tag{6.7}$$

The result, shown in Figure 6.2, is that the error rate remains negligibly small for dead times of up to around a fifth of the total photon length before increasing quite rapidly. A dead time of 27.2% keeps the error rate below 1% and 20.8% below 0.1%; for the 430 ns photons used these correspond to 117 ns and 90 ns respectively. The following two subsections detail how the control and effecting stages are implemented in just 13 ns, which when combined with the other unavoidable time lags results in a total latency for the feedback of 97 ns, corresponding to an expected error rate of 0.2%; Table 6.1 details the breakdown. Such a latency is typical for measurement-based feedback in the field of quantum optics, the implementations in [144, 145] exhibit delays of 45 ns and 83 ns respectively.

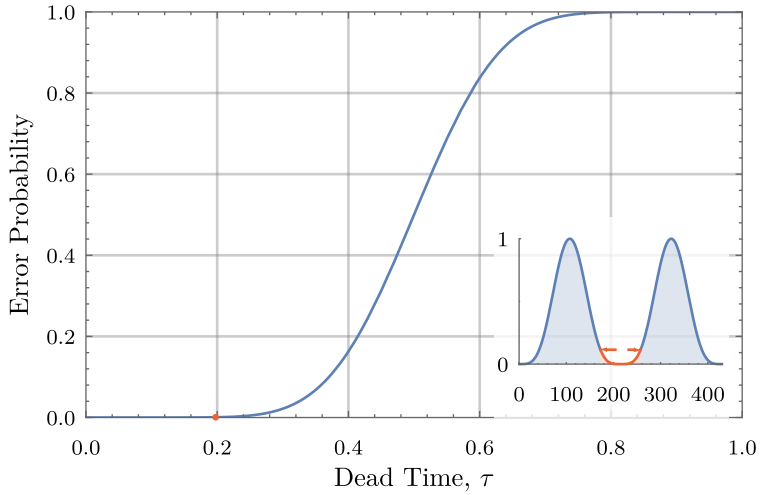


Figure 6.2: Feedback error analysis: The dead time, τ, as a fraction of the photon length, is feedback delay of the system, here as a fraction of the photon length. Specifically it is the round trip time for a signal to pass from the EOM, via the cavity to the SPCMs, be processed by the controller and return to the EOM. It represents a period of time during which feedback control cannot be achieved, therefore introducing an error rate (Equation (6.6)). The profile of the considered photon is shown in the inset along with the measured 97 ns feedback delay of the setup marked in red, the corresponding error rate of 0.2% is coincident with the horizontal axis on this scale.

6.2.2 EOM

As mentioned briefly above, the AOM used for shaping the STIRAP driving pulse, and typically responsible for setting the phase shifts within time-binned photons (Chapter 3) is simply too slow to be used in a reactive manner. The acoustic velocity in the crystal is 4.2 mm/μs and it is not practically possible to position the laser closer than around 1 mm to the edge of the crystal, which constitutes an unavoidable 250 ns delay, on top of which there is also a 50 ns rise time.

We therefore turn to an EOM to modulate the phase[3]. An EOM functions based on the Pockels effect, an electro-optic effect where the refractive index of a medium is linearly proportional to an applied electric field [150]. A

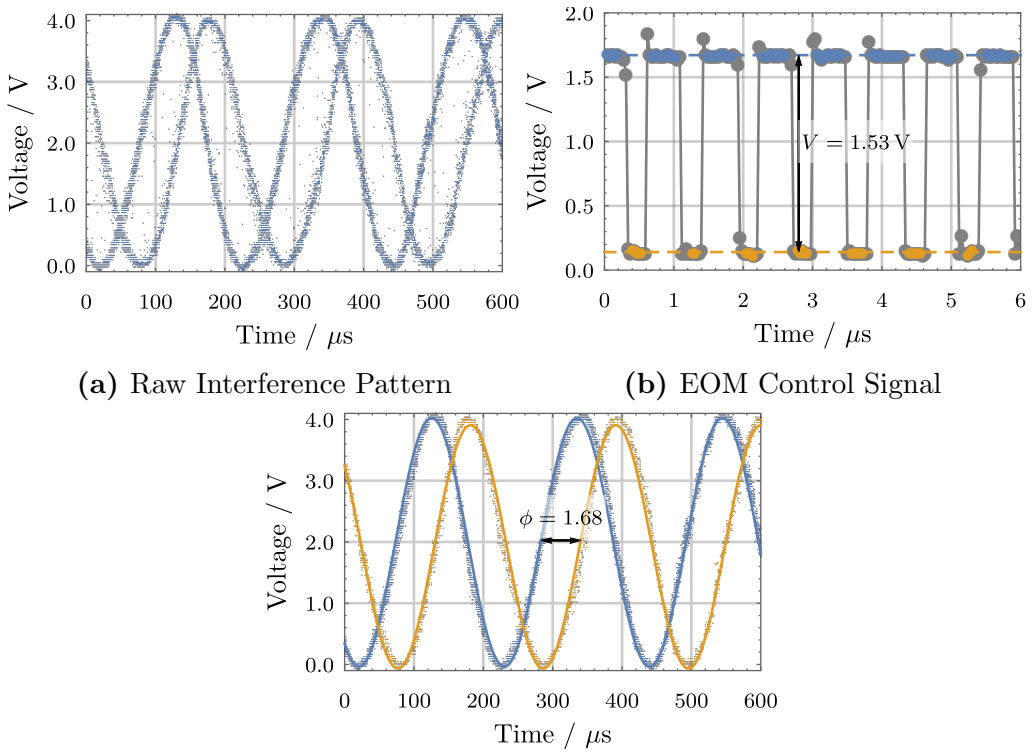
[3]Photline NIR-MPX800-LN-05, now iXBlue Photonics

Element	Time / ns
Optical Transit Time EOM → Cavity → SPCM	45
SPCM Response	35
Circuit Response	7.0
Signal Rise Time	5.5
Total Cable Delay SPCM → Control → EOM	4.5
Total	97.0

Table 6.1: Feedback latency breakdown: A breakdown of the contributing elements to the feedback delay. The first two rows are not known absolutely, only their sum was measured. However from discussions with the manufacturer it is believed that the SPCM response (time delay between photon impact and TTL output) is around 35 ns.

linear change in refractive index gives a linear change in optical length and correspondingly in (relative) phase. The change in the refractive index is small, typically requiring thousands of volts to achieve a π phase change in free space EOMs. Switching such large voltages quickly poses its own set of experimental difficulties, we therefore opt for a fibre-coupled EOM which uses long travelling wave electrodes to achieve deep phase modulation at low voltage, $V_\pi \approx 3\,\mathrm{V}$.

The phase-voltage relationship of the EOM varies with modulation frequency, it was therefore necessary to characterise the relationship at the operational frequency. This was done by inserting the EOM into one arm of an otherwise free space Mach-Zehnder interferometer with fast photodiodes at the outputs. The interferometer is not stabilised and therefore oscillating interference fringes are observed even in the absence of modulation by the EOM. These have three sources with different timescales. The fastest are due to the 20 MHz modulation of the laser for the PDH locking (Section 2.3.3), the slowest, on the one second timescale, are due to thermal fluctuations and air currents. Between these two extremes are fringes arising due to the



(a) Raw Interference Pattern **(b)** EOM Control Signal

(c) Deinterleaved Interference Pattern

Figure 6.3: Unstable interferometric phase voltage characterisation of EOM: The EOM is placed in one arm of an otherwise free-space, unstable interferometer, whilst the laser is scanned to produce 7 kHz sinusoidal interference fringes. The EOM is then modulated at around 1 MHz as shown in (b) which splits the the fringes into two (a). Recording at 40 Ms/s, the interference pattern is deinterleaved using the control signal, and two identical sinusoids are fitted with a free phase shift (c). Thus a data point of the phase-voltage relationship of the EOM is obtained.

scanning of the laser frequency at the 50-5000 Hz range (to aid relocking of the laser). It is not possible to measure the effect of the EOM directly in this unstable setup. However, by removing the 20 MHz modulation we can use the EOM to rapidly modulate the kHz fringes at 10-1000 kHz and measure the phase difference between the two shifted sinusoids. The process is outline in Figure 6.3. By repeating this process for many different voltages we obtain a measure of the linear phase-voltage relationship and can thus calculate the voltage required for a π (or any other value) phase shift. This is shown in

Figure 6.4 as measured using the control circuit described in the following subsection. The behaviour of the EOM was also probed using a function generator and the value of V_π was found to vary by around 0.2V across the range 10-1000 kHz.

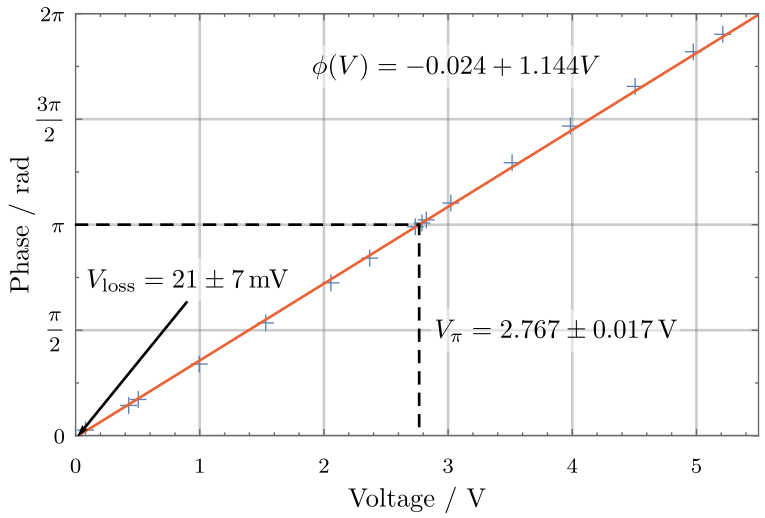


Figure 6.4: EOM phase voltage relationship: The uncertainties in both the voltage and phase measurements are smaller than the plot markers, but are still taken into consideration. The line of best fit is obtained by weighted orthogonal regression, yielding $\phi(V) = -0.024 \pm 0.006 + (1.144 \pm 0.008)V$.

The measured phase-voltage relationship

$$\phi(V) = -0.024 \pm 0.006 + (1.144 \pm 0.008)V \tag{6.8}$$

implies there is a non-zero phase shift with no applied voltage. Conversely it suggests that a voltage of 21 mV produces no phase shift. It is certainly conceivable that there is a voltage loss of that magnitude at some interface in the system, comprising a systematic error not accounted for. The measured relationship as it stands is certainly accurate enough for our use, especially when considering that the interference visibility (what we are ultimately going to be measuring) varies slowly as a function of phase around the point

of maximum contrast at $\phi = \pi$.

A second, in-situ verification of the V_π voltage was obtained when the EOM was inserted into a fiberised Mach-Zehnder interferometer on the STIRAP arm for the purpose of checking the timing (Figure 6.5). The STIRAP pump and repump pulses are overlapped using a fibre beam splitter, the EOM is attached to one of these outputs to enable it to quickly shift the phase on the second time bin of the driving pulse. By connecting a second fibre beam splitter as shown in Figure 6.5a the timing and magnitude of the phase shift can be probed by observing the changes at the interferometer outputs. We can for example generate a simple triangle pulse (using the AOM), then attempt to swap the intensities at the two outputs exactly at the halfway point (Figure 6.5b). Again, this interferometer is neither balanced nor stabilised, therefore the intensities and contrast at the outputs vary, albeit on a timescale far slower than a single pulse. Finally to check the phase we use a double hump pulse similar in profile to the generated photons, wait for the contrast exhibited to be maximal, and attempt to maximally switch the output intensities at the the halfway point (Figure 6.5d). Note that this is not the driving shape used for photon generation, which must be asymmetric as outlined in Section 2.1.2.

6.2.3 Fast Electronics

The task of the controller is to decide whether or not a phase should be applied to the second time bin and, if so, expeditiously supply sufficient voltage to the EOM to enact that phase change. To that end, a circuit was built using off-the-shelf TTL IC logic chips and a custom in-house designed PCB to implement this. The circuit toggles between two modes of operation,

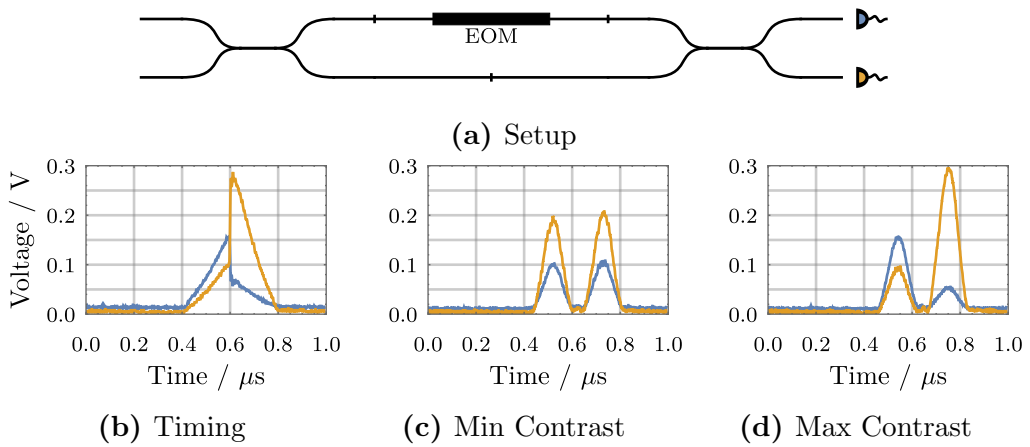


Figure 6.5: EOM timing calibration: The EOM is placed in one arm of an all-fibre, unstable interferometer, as shown in (a). Initially a single triangular light pulse is sent through the interferometer, and the timing of a voltage pulse applied to the EOM set to swap the outputs of the interferometer at the halfway point (b). Then a sinusoidal pulse is used (this has the form of the photon after generation, which is not the form of the required driving pulse) and the timing and amplitude of a voltage pulse applied to the EOM again set to swap the outputs at the halfway point (b) and (c). The interferometer is unbalanced and unstable; the behaviour at the outputs therefore varies.

one in which it does nothing, the other in which it outputs a voltage pulse (the level of which is controllable by a potentiometer) to the EOM during the second time bin. Toggling between the modes is triggered by a detection on a chosen detector during the first time bin. The control circuit therefore receives as inputs a copy of the TTL output from the detector of interest, DET, and two 215 ns TTL pulses from the AWG — one, WIN_{DET}, to outline the first time bin for the registering of detections, the other, $\text{WIN}_{\text{PHASE}}$, to outline the second time bin for the output phase voltage, PHASE. These four connections along with their timings can be seen in Figure 6.1. An abbreviated circuit logic diagram outlining the functioning of the circuit is shown in Figure 6.6 along with a short explanation.

There were a number of considerations to be made in the design and construction of the circuit to overcome difficulties such as: the output stage

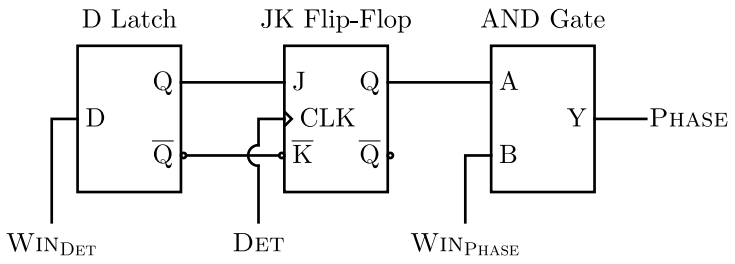


Figure 6.6: Control logical circuit: The JK flip-flop controls the state of operation of the circuit, when its output, Q, is 0, no Phase signal will be output, when Q is high, 1, Phase follows $\text{Win}_{\text{Phase}}$. Toggling between these two states is triggered by a signal on the JK flip-flop CLK input from a detector, Det, but only whilst the JK is in 'Toggle Mode'. With Q ($\overline{Q}$) high (low) the JK is in toggle mode, with Q ($\overline{Q}$) low (high) the JK is in Hold mode. The D latch just buffers the input Win_{Det} to provide a duplicate and negated copy necessary for the JK.

of the SPCMs is not a true TTL signal but rather is designed to drive a 50 Ω load, a fine balance had to be struck in the circuit design to provide sufficient impedance matching that the TTL pulse was not reflected, thus causing double counting at the TDC, whilst keeping sufficient voltage to trigger the JK flip-flop. Another challenge is that the EOM is a 50 Ω load and therefore requires significantly more current than a typical TTL component can source, the solution chosen was to use open collector gates. Additionally, although the experiment runs at a repetition rate of 1 MHz, the necessity of fast feedback demands short rise-times, which requires designing for signals up to 1 GHz. A complete circuit diagram and a full discussion of the design and implementation of the control circuit can be found in Appendix A.

Table 6.2 lists the figures or merit for the control circuit. With the knowledge of these values many of them can be compensated, for example if we know it takes 5.3 ns for the output to react to a Phase input, we simply send Phase from the AWG 5.3 ns earlier. Only the first two rows cannot be compensated and the control therefore adds a total of only 12.5 ns to the overall feedback latency.

Element	Time / ns
PHASE Rise Time 10-90, 0-100	3.0, 5.5
Response Time, $\text{WIN}_{\text{DET}} \rightarrow$ PHASE	7.0
Response Time, $\text{WIN}_{\text{PHASE}} \rightarrow$ PHASE, Rising	5.3
Response Time, $\text{WIN}_{\text{PHASE}} \rightarrow$ PHASE, Falling	15.7
Lag Time, $\text{WIN}_{\text{DET}} \rightarrow$ JK Active, Rising (Opening)	$10.3 < t < 11.0$
Lag Time, $\text{WIN}_{\text{DET}} \rightarrow$ JK Active, Falling (Closing)	$8.9 < t < 9.7$

Table 6.2: Control circuit latency breakdown: The combination of the first two rows constitute the contribution of the control circuit to the overall feedback delay. The remaining entries can have their control signals sent earlier to compensate for their lags. As there is no change in the outputs of the JK flip-flop when it is switched into toggle mode, we can only place bounds on the respective lag times for the process.

A visualisation of some of the data in Table 6.2 is given in Figure 6.7 which shows the lag and rise time of the output reacting to a detection. Also important here is that the output voltage rises not only quickly but with no overshoot, this voltage directly corresponds to the phase being imparted to the photons.

The correct triggering of the circuit was checked by using detector dark counts to trigger the circuit whilst monitoring all inputs and outputs on a fast oscilloscope. Unfortunately the DET input cannot be simultaneously monitored on the oscilloscope as there is a careful interplay between the TDC and the control circuit to avoid back reflections of the signal to the TDC which results in double counting. Therefore the detection data was extracted from the TDC and superimposed back onto the oscilloscope data. The resulting traces, Figure 6.8, show clearly the desired behaviour, with detections occurring close enough to the edges of control windows that we are confident in the triggering behaviour.

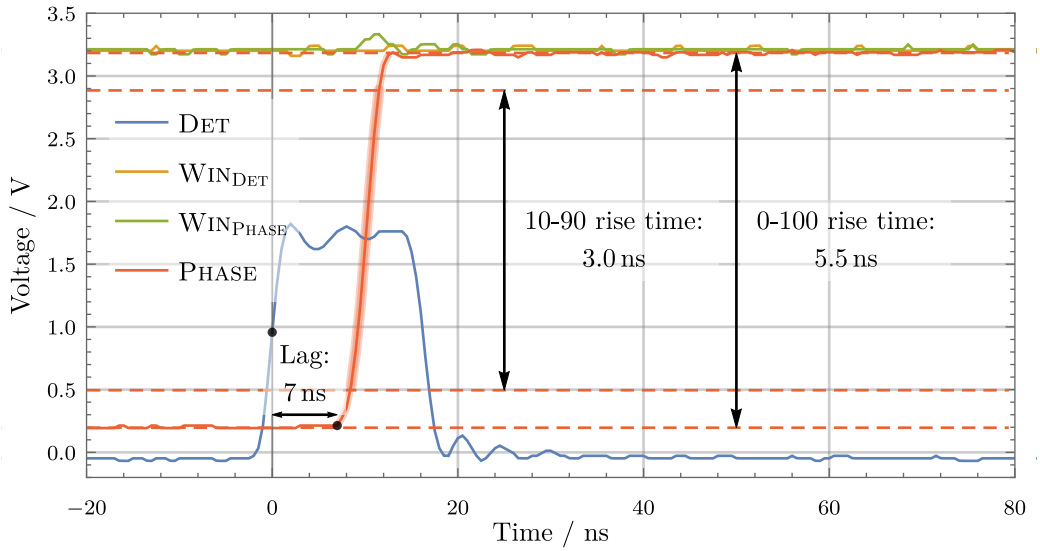
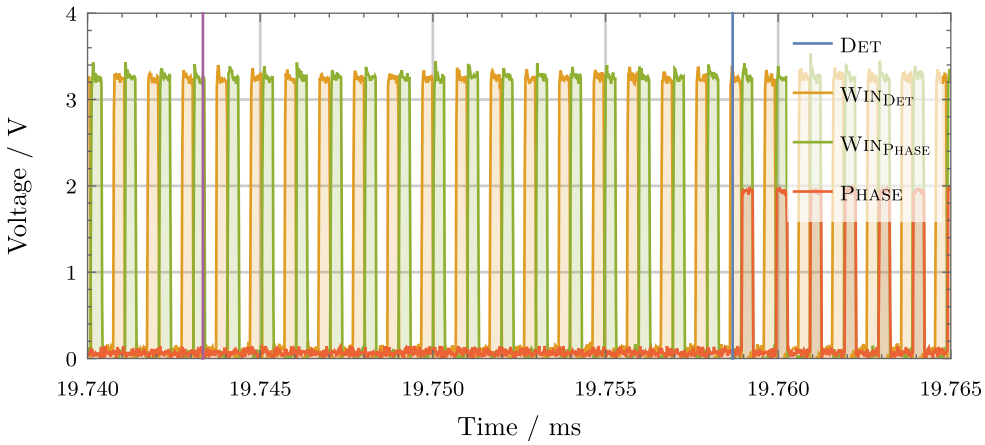


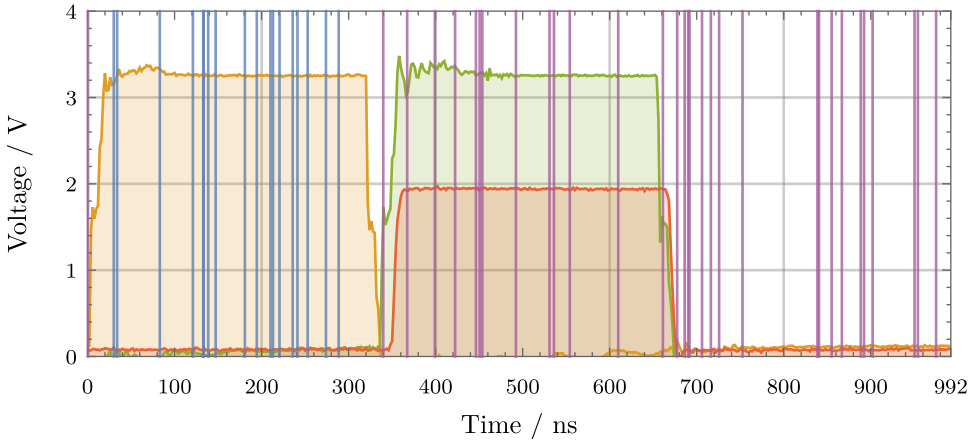
Figure 6.7: Control circuit response: With both the detection (WIN_{DET}) and phase output ($\text{WIN}_{\text{PHASE}}$) windows high, a detection signal, DET, should immediately trigger the output voltage, PHASE. However it can be seen that there is a 7 ns lag, and a measurable rise time.

6.3 Results

Characterisation of the feedback control is performed using the time-resolved quantum homodyne techniques presented in Section 2.2 and utilised in Chapter 3 (see Section 3.4 for an explanation of the term "quantum homodyne"). In brief: the time-resolved correlation spectrum of non-interfering double hump photons (orthogonally polarised) exhibits a triple-peaked structure, simply corresponding to the convolution of the two photon intensity envelopes. Identical photons always bunch, as predicted by Hong-Ou-Mandel interference, and present no correlations for all detection time differences. Two (otherwise identical) double hump photons, with different relative phase shifts between their time bins, exhibit a phase-dependent number of correlations between the two time bins, manifesting in the time-resolved spectrum as phase-dependent satellite peaks. We would therefore expect the correla-



(a) Real time view



(b) Overlay

Figure 6.8: Verification of control circuit functionality: The behaviour of the control circuit was checked using detector dark counts to trigger the circuit. (a) shows two detections, the first of which lies outside the detection window (WIN_{DET}) and correctly doesn't trigger a shift to PHASE output, the second is within a detection window and does trigger the circuit. (b) shows an overlay of 50 detections, coloured blue if they triggered the circuit or purple if they did not; correctly all, and only, blue detections lie within the detection window. A total of over 200 detections were examined and none violated the triggering criteria.

tion spectrum measured under active feedback control to be asymmetric, as we hope to always route the second detection to the same chosen detector (Equations (6.3) to (6.5)). We should thus prevent the incidence of D_1C_2 correlations — which manifest at positive detection time differences τ, where τ is the time of detection on C, less the time of detection on D — whilst enhancing C_1D_2 correlations, which appear at negative detection time differences.

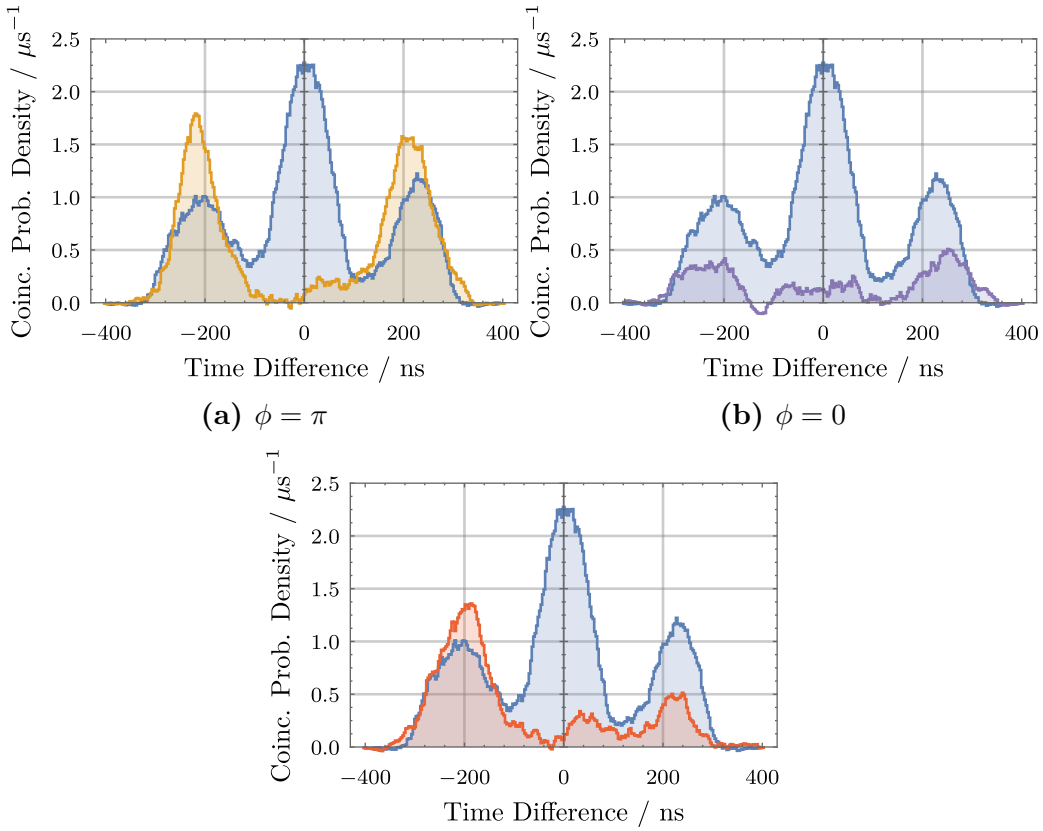
To provide reference signals we not only take data with the feedback active but also three other standard configurations without the feedback: identical photons with no relative phase, identical photons with a π relative phase between their second time bins, and orthogonally polarised photons. These additional reference experiments should allow us to quantify the precision of the feedback. All four results can be seen in Figure 6.9.

Although pronounced, we note that the asymmetry under feedback (Figure 6.9c) is not perfect. This is not surprising as we know there sometimes exists imperfect coherence between photons in the experiment leading to residual correlations where there should be none. The action of the feedback should be to switch the behaviour of the HOM at $\tau = 0$ between the behaviour of $\phi = \pi$ one side (Figure 6.9a) and $\phi = 0$ the other (Figure 6.9b), which indeed corresponds to what we see.

We can quantify the quality of the interference by the visibility,

$$V = 1 - \frac{N_{\parallel}}{N_{\perp}} \tag{6.9}$$

where $N_{\parallel}$ and $N_{\perp}$ are the total numbers of correlations observed for interfering and non-interfering photons respectively. Strictly speaking we do not use the total numbers of correlations but rather the total probability of a



(a) $\phi = \pi$ **(b)** $\phi = 0$

(c) Feedback

Figure 6.9: Time-resolved HOM interference under feedback control: (c) shows the asymmetric pattern observed under feedback control, where the feedback has prevented (most) correlations in the right satellite peak. (a) and (b) show the traces obtained for photons with phase shifts of π and 0 without feedback. All traces have the same orthogonal-photons reference case in blue.

correlation per input photon pair. Using the results obtained with $\phi = 0$ for $N_{\|}$ we find $V = 0.79 \pm 0.04$.

We might extend this concept of visibility to attempt to quantify the fidelity of the feedback control. The feedback attempts to switch between the two behaviours, $\phi = \pi$ and $\phi = 0$, let us therefore define a phase visibility, V_ϕ, as

$$V_\phi = 1 - \frac{N_0}{N_\pi} \tag{6.10}$$

where N_0 and N_π are now the total coincidence probabilities between pairs of photons with relative phase shifts of $\phi = 0$ and $\phi = \pi$ respectively. We need only consider the contributions in the satellite peaks as we know the phase does not manifest in the central region. Figure 6.10 provides a clearer view of the different behaviours by binning the correlations according their respective detection time bin differences.

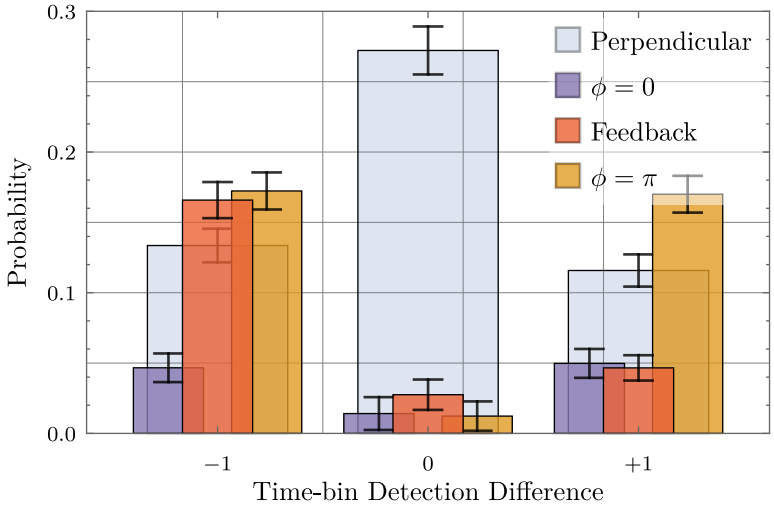


Figure 6.10: Time-binned HOM interference under feedback control: The data from Figure 6.9 is now binned according to the time-bin detection difference, clearly separating the regions where difference behaviour is expected. The relative phase shifts only effect the ± 1 bins, the 0 sin should be zero for all the non-perpendicular cases. The feedback matches the $\phi = \pi$ and $\phi = 0$ behaviours well.

The data is somewhat noisy as attested to by the difference in the values of the ± 1 bars for the reference perpendicular photons which we would expect to be equal (they are however just within error of each another). It is obvious that there is some uncontrolled decoherence leading to the visibility of $V = 0.79$ as we see more correlations in each of the ± 1 bins than the 0 bin for identical, $\phi = 0$, photons. One can also calculate the visibility between the orthogonal reference and the $\phi = \pi$ case, which would ideally reach 0, however given observed decoherence we might expect a value closer to 0.2. What we

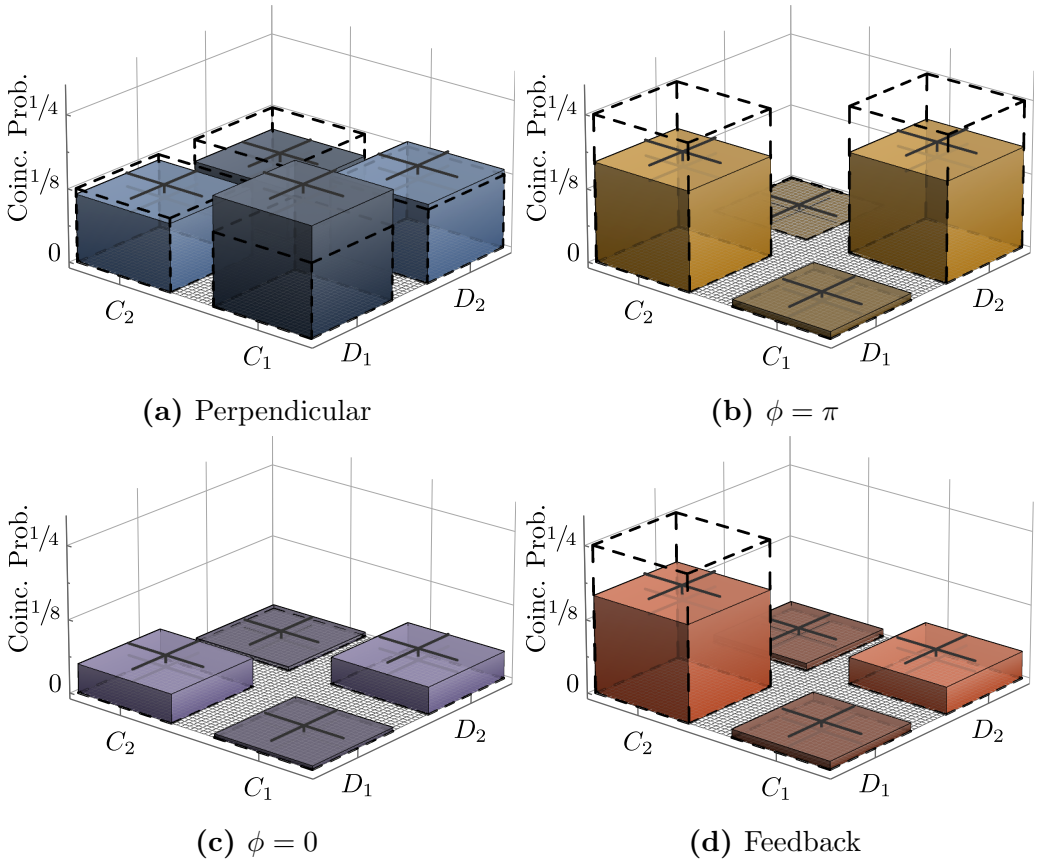
measure is $V = 0.32 \pm 0.05$ which suggests we are better at suppressing correlations than increasing them. This might indicate that the phase shift applied by the AOM is interrupting the adiabaticity, potentially because the AOM is not reducing the amplitude to zero when applying the non-adiabatic phase shift.

Returning now to V_ϕ, taking the values N_0 and N_π from the $+1$ and -1 peaks for the feedback trace in Figure 6.10, we find $V_{\phi,\mathrm{FC}} = 0.72 \pm 0.06$. This could suggest that our feedback control is only functioning 72% of the time, however we know even without the feedback active we are not achieving perfect interference. As a reference for the maximum possible value of $V_{\phi,\mathrm{FC}}$ we could expect to measure, given our limited interference visibility, we can consider the value obtained in the absence of feedback, that is using the values of the ± 1 peaks for both the $\phi = 0$ and $\phi = \pi$ traces. These produce $V_{\phi,\mathrm{ref}} = 0.72 \pm 0.04$, indiscernibly different from the value measured under feedback. Defining the feedback fidelity as the ratio of the phase visibility achieved under feedback control to the maximum possible, obtained from the reference measurements we find:

$$F = \frac{V_{\phi,\mathrm{FC}}}{V_{\phi,\mathrm{ref}}} = 1.00 \pm 0.10\,. \tag{6.11}$$

6.4 Discussion

This chapter has demonstrated the implementation of measurement-based quantum feedback control to actively route the second time bin of a spatially entangled two-photon state. This constitutes an elementary step towards introducing active control into processes such as quantum random walks and



(a) Perpendicular **(b)** $\phi = \pi$

(c) $\phi = 0$ **(d)** Feedback

Figure 6.11: Time-binned HOM: For completeness, and to allow comparison to the qubit data presented in Chapter 3, the correlations are resolved according to the exact detector-time-bin detections. The limited visibility is obvious when comparing the data to their theoretical values, shown dashed.

optical networks [151].

The total feedback delay was minimised to 97.0 ns by the careful design of the controller electronics, used in tandem with a fibre-coupled EOM. With this latency, there is no discernible failure rate of the control, which is theoretically predicted to remain below 0.2%. We measure a feedback fidelity, defined as the ratio of the interference phase contrast achieved with a single measurement with active feedback to that from two separates measurements without, of $F = 1.00 \pm 0.10$. However, we concede that the overall interference visibility during the experiment was limited to $V = 0.79 \pm 0.04$, which

reduces the sensitivity of the feedback fidelity measure to errors.

A classical interpretation of the experiment fails. Classically one might expect the feedback control to only succeed when the first detection corresponds to the photon in the delay arm, and that the other half of the time when the first detection corresponds to the photon in the short arm the change in the phase of the driving laser would have no effect — as the photon under generation has already been detected. One would therefore classically expect to measure at best $F = 0.5$.

In contrast to some other measurement-based feedback control systems, the measurement efficiency doesn't limit feedback fidelity. This is a convenience of correlation measurements, as we only 'look' for the effects of feedback control if we have already detected both photons (and therefore achieved 100% detection efficiency post-selected).

Should more complicated control logic need to be implemented, for example if scaling the approach up for more than two photons or with multiple detectors contributing to the phase logic, then moving to an FPGA-based controller would likely simplify the apparatus. Furthermore moving away from SPCMs to faster detectors, such as superconducting nanowire sensors [68], could immediately reduce the feedback delay by around 30%.

Chapter 7

Outlook

This thesis has demonstrated the versatile operation of an atom-cavity system, predominantly as a single photon source for quantum information processing, though the system itself is well suited to wider applications in the field of quantum networking. The high level of control in the photon generation process was proven with the production of photons in temporal superpositions of up to four time bins, with controllable arbitrary phases between. The narrowband nature of the emitted photons was then utilised to perform high fidelity quantum logic in an integrated photonic chip. This showed non-classical correlations between detection events separated by periods exceeding the travel time across the chip by several orders of magnitude. The ability to generate temporal qubits, with controllable phase shifts, was exploited to model the statistics of classes of particles other than bosons in the photonic chip. Finally the temporal length of photons allowed the implementation of measurement-based quantum feedback to modify the properties of a photon

midway through its generation, in order to achieve active control over the routing of temporally encoded qubits.

7.1 Source Improvements

As a source of photons for LOQC, the pair-brightness, the rate of production of photon pairs is of great importance. Furthermore the ability to generate simultaneous configurations of more than two photons is highly desirable [72, 152, 153]. Let us therefore consider the performance of the current source in this context and ask what limits might be reached with improvements.

The overall efficiency of the source can be considered as the product of all the generation, transmission, and detection efficiencies. Strictly the transmission and detection efficiencies are not properties of the source itself, however they are intrinsic in the usefulness of the source for LOQC and therefore are included. For n simultaneous photons, each efficiency will be scaled to the power of n, apart from the routing efficiency, which for the random routing in the current source is $\eta_{\text{route}}(n) = n^{-n}$. The overall efficiency for an n state is therefore

$$\eta_{\text{total}}(n) = (\eta_{\text{cav}} \cdot \eta_{\text{extract}} \cdot \eta_{\text{coupling}} \cdot \eta_{\text{det}})^n \cdot \eta_{\text{route}}(n)\,. \tag{7.1}$$

The values of the different efficiencies for the current source are summarised in Table 7.1 which shows we achieve an overall two-photon efficiency of just under 1%. The random routing of photons precludes the use of higher n states as $\eta_{\text{total}}(n)$ drops off rapidly.

The coupling and detection efficiencies are merely technological limits with the current apparatus. With greater experimental care, coupling effi-

	η_{cav}	η_{extract}	η_{coupling}	η_{det}	$\eta_{\text{route}}(n)$	$\eta_{\text{total}}(2)$	$\eta_{\text{total}}(3)$
Current	0.86	0.52	0.70	0.62	$(n)^{-n}$	0.009	3×10^{-4}
Projected	0.95	0.93	0.85	0.90	$(0.85)^{n}$	0.31	0.17

Table 7.1: Photon source efficiency breakdown: The breakdown of the contributions to the overall efficiency of the current photon source is shown alongside a projection of what is feasible with current technology. Not only is the photon-pair efficiency, $\eta_{\text{total}}(2)$, substantially increased, but also the efficiency falls off far more slowly towards higher photon numbers.

ciencies of 80-85% are reachable, and moving away from silicon-based SPCMs to superconducting nanowire photon detectors would provide detection efficiencies in excess of 90%. With an improved cavity design, outlined below, both photon generation and extraction efficiencies can be considerably improved, with predicted values shown in Table 7.1. Furthermore with a suitably designed cavity one can utilise a slightly different STIRAP scheme which provides photons of known polarisation, consequently allowing deterministic routing, discussed below. The combination of these gains is that one could expect a roughly 30 fold increase in two-photon efficiency. Additionally, the removal of the random routing improves the scaling of the efficiency with n; a value comparable to the current 1% would not be reached until generating $n = 8$ photon states.

This section now looks in more detail at the design parameters of such an improved cavity, followed by the impact of polarisation controlled photon generation on deterministic routing.

An Improved Cavity

The theory behind the operation of optical cavities was outlined in detail in Section 2.1.1. The key properties of an atom-cavity system, notably g, κ, γ, C, η_{cav} η_{extract}, $g_1 g_2$, and potentially others, depend upon a multitude of

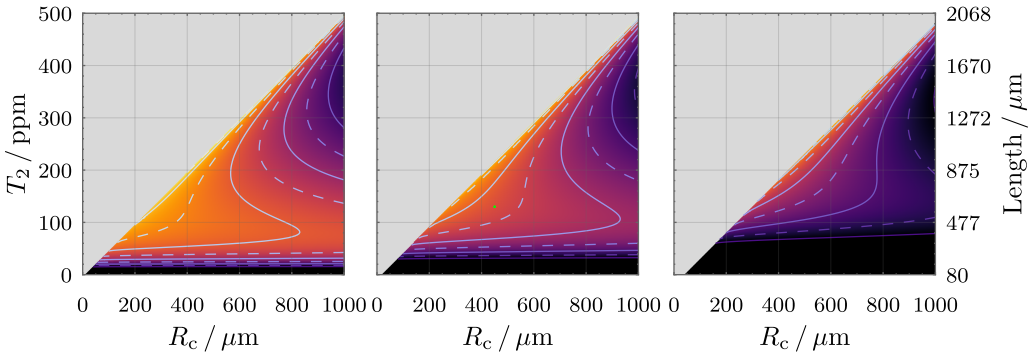
free parameters, thus making design a nuanced topic. In general one is free to specify the transmissions, T_1 and T_2, losses, L_1 and L_2, and the radius of curvature, R_c, of both mirrors, as well as the length, L, of the cavity. We can reduce these six parameters down to just three, simplifying the parameter space to be explored. Firstly in an ideal cavity $T_1 = L_1 = L_2 = 0$, and as these three terms only appear as their sum we replace them with a single parameter for the total unwanted loss, $\xi = T_1 + L_1 + L_2$ [1]. Secondly, the altered STIRAP process considered below, requires the addressing of individual Zeeman sublevels, which places an upper limit on the cavity linewidth, and therefore κ. Designing for a given value of κ allows us to to constrain T_2 and L via Equation (2.5) giving

$$L = \frac{c(\xi + T_2)}{4\kappa}\,. \tag{7.2}$$

Pursuant to these constraints, we wish to choose values of T_2 and R_c which produce the most efficient ($\eta_{\text{cav}} \times \eta_{\text{extract}}$) cavity for a given value of unwanted loss ξ. Figure 7.1 shows the value of the overall cavity efficiency as a function of both T_2 and R_c for several realistic values of ξ and reveals some interesting behaviours.

The overall efficiency is obviously strongly dependent on the cavity losses. Generally the efficiency is highest along the diagonal, where $L = 2R_c$. This is the concentric cavity limit which produces small mode volumes and therefore high atom-cavity couplings. However this is also the stability limit and in practice one would not want to operate a cavity near this limit. Away from the concentric limit we see that decreasing T_2 generally increases the

[1] The mirror transmissions and losses enter into the equations for cavity finesse (Equation (2.6)), which is well approximated by $\mathcal{F} = 2\pi/T_1 + L_1 + T_2 + L_2$, and η_{extract} (Equation (2.37)).



(a) $\xi = 5\,\text{ppm}$ **(b)** $\xi = 10\,\text{ppm}$ **(c)** $\xi = 20\,\text{ppm}$

Figure 7.1: Cavity efficiencies: The maps show the overall efficiency of a cavity ($\eta_{\text{cav}} \times \eta_{\text{extract}}$) as a function of the radius of curvature of the mirrors, R_c, and the transmission of the out-coupling mirror, T_2, for three different values of cavity losses, ξ. It can be seen that lower T_2 is not always favourable and that the optimal value of T_2 depends strongly on the cavity losses. The contours are plotted from 0.75 to 1 in steps of 0.025, alternating solid and dashed. The green point in (b) is the design point for which values were taken for Table 7.1 and sits at $R_c = 450\,\mu\text{m}$, $T_2 = 130\,\text{ppm}$, where the overall efficiency is 0.885.

efficiency, this is a by-product of the reduction in cavity length required to maintain the prescribed cavity linewidth, which again reduces the cavity volume. However at some point the efficiency drops off sharply as T_2 is further reduced; the point at which this occurs is strongly dependent on the cavity losses, ξ. Ultimately a limit is reached with increasing reflectivity (decreasing T_2) where improved generation efficiency is offset by reduced out-coupling efficiency. The pathway to improved overall efficiency is therefore not to reduce the mode volume with a higher finesse and shorter length, but by reducing the radius of curvature of the mirrors.

The projected values for the cavity in Table 7.1 are for a cavity designed around $\xi = 10\,\text{ppm}$, with $R_c = 450\,\mu\text{m}$ and $T_2 = 130\,\text{ppm}$, as indicated by the green point in Figure 7.1b. Such a cavity would have far lower finesse than that used in the current setup at around 45 000 but the cooperativity would be much higher, in excess of 10.

Such tight mirror curvatures lend themselves to fibre-tip cavities, where the two mirrors are coated onto the ends of optical fibres. Although fibre-tip cavities come with their own set of complexities [154, 155], the generated photon would be extracted from the cavity directly into fibre thus simplifying the remaining experimental apparatus as well as potentially reducing further coupling losses.

Polarisation Control and Deterministic Routing

It was originally the goal of the current cavity to drive a V-STIRAP process between the magnetic substates of the atom, as outlined in [113]. This requires a magnetic field to lift the degeneracy of the substates, splitting them sufficiently far apart that transitions between different substates can be individually addressed by the cavity. Unfortunately the aforementioned reduction in cavity finesse (Section 2.3.1), resulted in a linewidth for which the required magnetic field would be great enough to introduce unwanted excited states. The cavity design outlined above would be able to use the scheme presented in [113], which generates a stream of photons with alternating circular polarisation. Not only does this allow deterministic routing of the photons but it also removes the need for a repump process, thus increasing the repetition rate two-fold.

The probabilistic routing of photons in the current apparatus is really what precludes more then $n = 2$ photon experiments, as the efficiency of routing scales as n^{-n}. If the emitted photons are of known polarisation then one could use a network of electro-optic switches to deterministically route the photons into delay lines, with a routing efficiency which scales as η^n_{switch}. The switches would need to be able to operate at a few MHz, with actual switching times shorter than 100 ns. Electro-optic switches can achieve

this, at efficiencies exceeding $\eta_{\text{switch}} = 0.9$. An all-fibre switch would in many ways be preferable to a free space implementation, potentially allowing greater flexibility, however although devices exist at telecomm wavelengths, the performance available at 780 nm is not yet sufficient.

One sacrifice to be made in deterministic routing is that one failure at any point in the routing of a sequence of n photons upsets the whole stream. Whereas with probabilistic routing a new stream of n can be initiated immediately following any error.

Dipole Trap

The brightness [156] of the current source is greatly limited by the stochastic nature of the atomic loading process. We saw in Section 4.3 that in 20 hours of experimental runtime, corresponding to 1 hour of data capture, an atom was loaded for only around 30 s. Trapping an atom within the cavity would considerably increase the fraction of the time for which the cavity is loaded. A dipole trap can be realised with a tightly focused laser, far detuned from the ^{87}Rb D_2 line, and has already been demonstrated [157]. Additional lasers are required to re-cool the atom and to keep it trapped near the motional ground state to aid localisation within the cavity. Care must also be taken that the trapping lasers do not adversely perturb the energy level structure of the atom.

7.2 Future Work

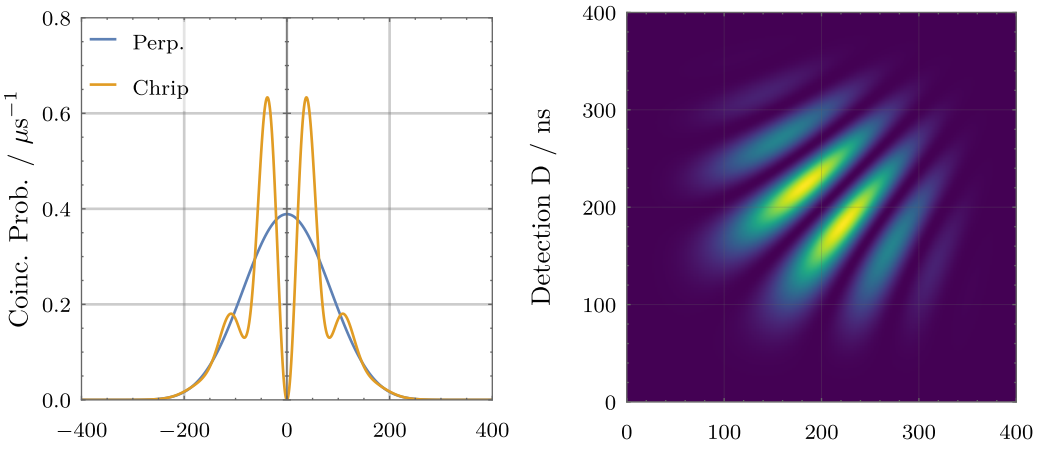
Entanglement Swapping

With polarisation controlled photons and deterministic routing of the photons it would be a relatively small step to include not only delay lines corresponding to the source repetition rate, but also to delay photons by units of one (or more) time-bin(s). This would allow a chain of interleaved photons to be formed, where under certain detections, photons at opposite ends of the chain, which have never 'met', can be entangled [158]. This is analogous to the scheme presented in [159] to scaleably generate multiphoton entangled states through entanglement fusion. Furthermore, time-bin length delay lines would increase the utility of the source for linear optical quantum computations, potentially allowing schemes involving arbitrary qudits to be implemented [108]. Such delay lines would need to be phase stable, however it is envisioned that this can be achieved with a similar approach to that currently used to lock the cavity.

Chirp

One facet of two-photon interference that has not yet been probed with the long photons from our atom-cavity source, is the interference of two photons whose frequency difference varies as a function of time, i.e. relative chirp. The theoretical predictions of the time-resolved interference patterns obtained for two photons with a constant frequency difference, as shown in Figure 2.10, have been measured [98]. However, uniquely for the time-resolved interference of chirped photons, one cannot simply consider the detection time difference, as has been the case throughout this thesis (at best we have been

concerned with the detection time-bins but never the two exact detection times). Instead the correlation probability is strictly dependent on the exact detection times of both the photons. This can be seen in Figure 7.2 which shows the predicted interference pattern for two photons whose relative frequency difference increases from 0 to 12 MHz along their length.



(a) 1D Picture **(b)** 2D Picture

Figure 7.2: Time-resolved chirped HOM: The time resolved interference pattern is shown for two photons whose frequency difference changes as a function of time. Explicitly the phase evolutions of the two photons are given by $\phi_1(t) = \omega t$ and $\phi_2(t) = (\omega + \Delta t/T)t$, such that at the end of their $T = 400\,\text{ns}$ envelope their frequency difference is $\Delta = 12\,\text{MHz}$. It can be seen that the usual procedure of representing the correlation probability purely as a function of detection time difference, (a), does not reveal the full detail of the rich interference pattern formed when considering the exact time of both detection events, (b).

The chirp produces an increasingly oscillatory phase difference between the two photons towards later detection times, on the 2D plot this is evident as the interference fringes start to bunch closer together. The 1D picture integrates over this behaviour, returning to the orthogonal reference case towards larger time differences as it integrates over faster oscillations. Note however that as always, no correlations are predicted at exactly zero detection

time difference.

Final Remarks

That quantum information will play a large role in the future of computation and communication seems assured. The physical systems used to glance into this future today are diverse and what final technologies we come to rely on are still unknown. Atom-cavity systems show great potential, both as efficient sources of photons for LOQC, and as an efficient interface between stationary material qubits and flying optical qubits. Such systems are still experimentally complex, providing a significant barrier to constructing large scale quantum networks. The quantum networks and computers of the future might more closely resemble the classical computers of the modern day, with on-chip photon sources, cavities and detectors. For now though, single atoms coupled to high-finesse optical cavities provide an excellent platform for exploring many aspects of quantum information processing.

Appendix A

Feedback Controller Circuit Design

A.1 Introduction

This appendix details some of the design choices made during the construction of the circuit (Figure A.1) used to perform the controlling logic for the quantum feedback data presented in Chapter 6. The role of the control circuit is to decide whether a phase change should be present in the STIRAP driving pulse and if so supply a voltage pulse to an EOM during an exact time window. The requirement of a phase change is based upon the exact timing of photon detections on one of the SPCMs. To that end the control circuit receives three inputs:

WIN_{DET} A voltage pulse outlining the window during which detections should trigger a change in output behaviour.

DET A copy of the pseudo-TTL voltage pulse output from the SPCM signalling a photon detection.

$\text{WIN}_{\text{PHASE}}$ A voltage pulse outlining the window for which a voltage should be output if required.

and produces one output:

PHASE The output voltage pulse of certain voltage to enact a given phase shift in the EOM.

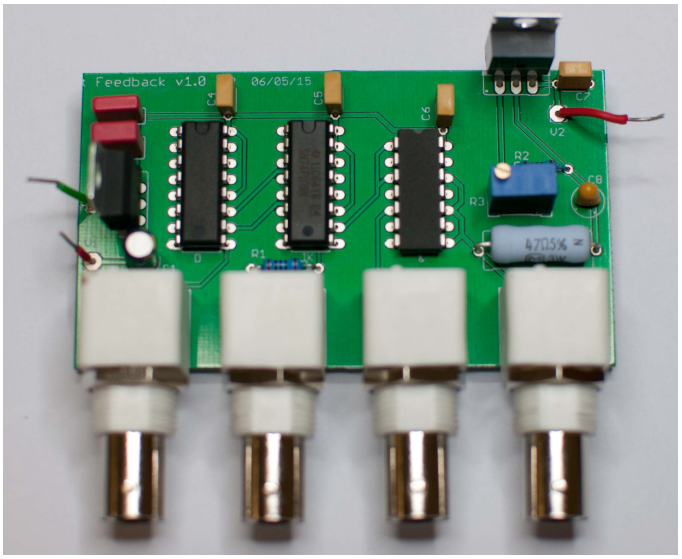


Figure A.1: Photo of controller circuit

It is outlined in detail in Chapter 6 that for the feedback to work the control logic must be performed quickly and, although there is no hard cutoff (the error rate simply increases with latency) a latency of 30 ns would result in approximately 1% error and by 70 ns this rises to nearly 10%. These times are far beyond what can be achieved with a computer and DAQ cards thus the decision was made to perform the logic at the hardware level with a homebuilt circuit.

The requirements on the circuit are unusual in that we require a fast response but a relatively low frequency signal. Many electronics applications require a high frequency ($> 100\,\text{MHz}$) oscillating signal, but do not worry about any initial delay in the generation of the signal. The opposite is the case here, the output will oscillate only once per photon generation cycle — around 1 MHz — but keeping the delays and rise times below 10 ns requires bandwidth up to 100 MHz. A PCB based circuit was therefore chosen to improve high frequency behaviour and reduce transmission delays, along with the 7400 series of TTL integrated circuit components (easy to use, cheap, many options, still fast).

The full circuit diagram is shown in Figure A.2 below. This appendix first looks at the design and choice of components for the logic followed by the modifications that had to be made to the output stage.

A.2 Logical Processing

The logical performance of the circuit is implemented by just three components as outlined in Figure A.3 below.

At its core the control circuit must switch between two modes of operation for which a JK flip-flop is a natural choice. In Toggle mode, $J = K = 1$, the JK flip-flop inverts its two outputs (Q and $\overline{Q}$) on every clock (CLK) pulse. We want the toggling to occur on photon detection, therefore the detector TTL pulse is connected to CLK. Most JK flip-flops trigger on the falling edge of a clock pulse which is no good given that the TTL pulses from the SPCM are 25 ns wide. Fortunately there exists a positive (rising) edge triggered model, the 74109, which is available in the fast F-series of components; the SN74F109N used takes typically 5-6 ns to switch following a CLK pulse.

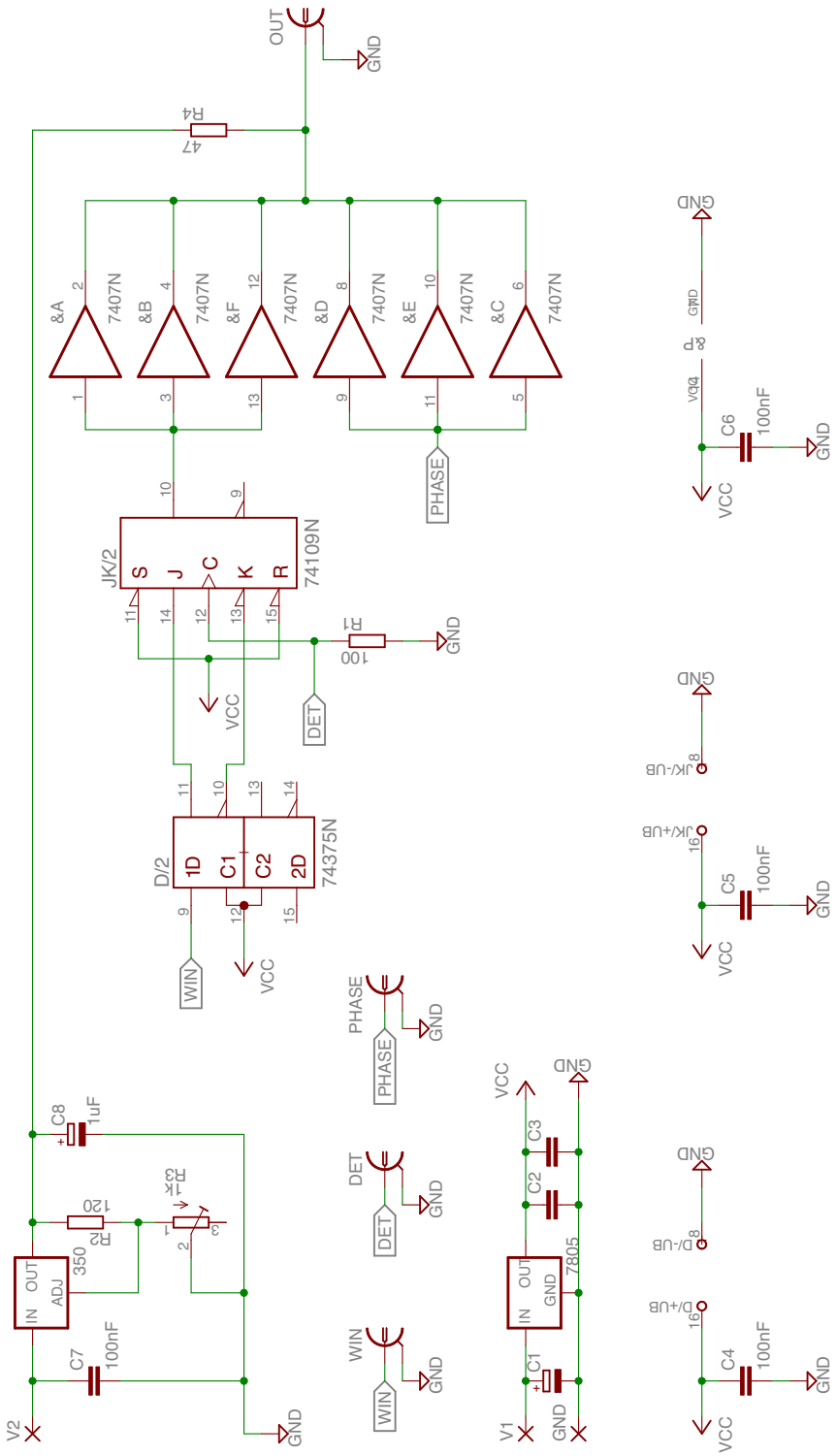


Figure A.2: Complete controller circuit diagram

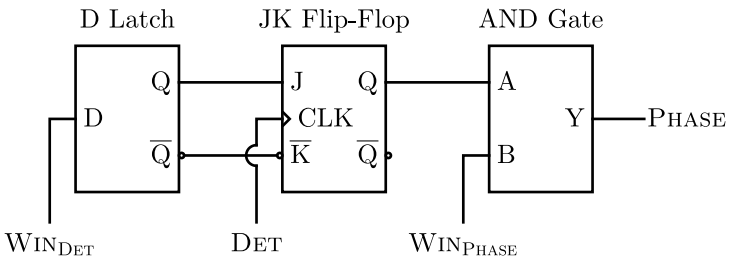


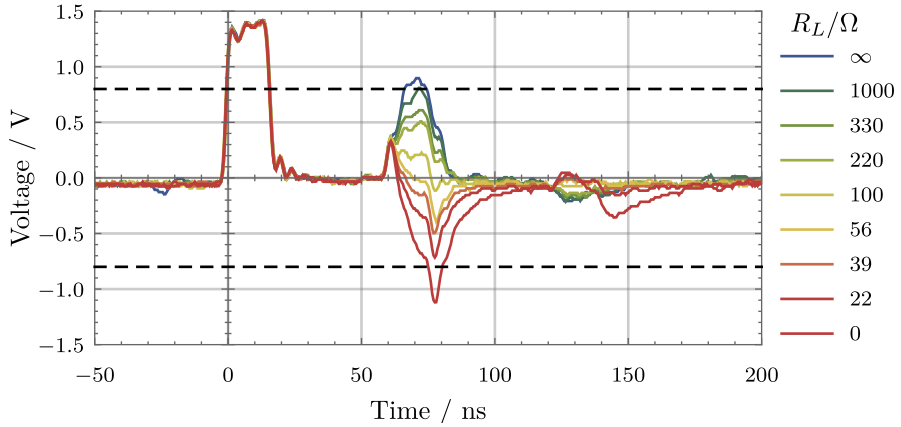
Figure A.3: Logic circuit diagram: The SN74F109N also has additional CLR and PRE inputs for initialising the gate, however the initial state of the gate is inconsequential to us and these two inputs are therefore tied high to the 5 V power supply.

However we do not want the flip-flop to toggle mode for every detection, only those when the detection is during the first time bin which is demarcated by the WIN_{DET} signal. The JK is only in Toggle mode when $J = K = 1$, when $J = K = 0$ the flip-flop is in Hold mode with its outputs remaining unchanging, the WIN_{DET} signal is therefore used to control the state of the JK. However the SN74F109N is actually a J$\overline{K}$ flip-flop and therefore requires a negated copy of WIN_{DET} on the $\overline{K}$ input. This could be achieved with a simple inverting buffer but this would introduce a delay before the $\overline{K}$ input not present on the J input and could result in the gate entering a Set or Reset mode. A D-latch has roughly equal latency to both its outputs and is an elegant way to provide a duplicated and negated version of a signal; the SN74LS375N is used here. Note that the switching time of the D latch is irrelevant as the WIN_{DET} signal can simply be sent earlier to compensate for it.

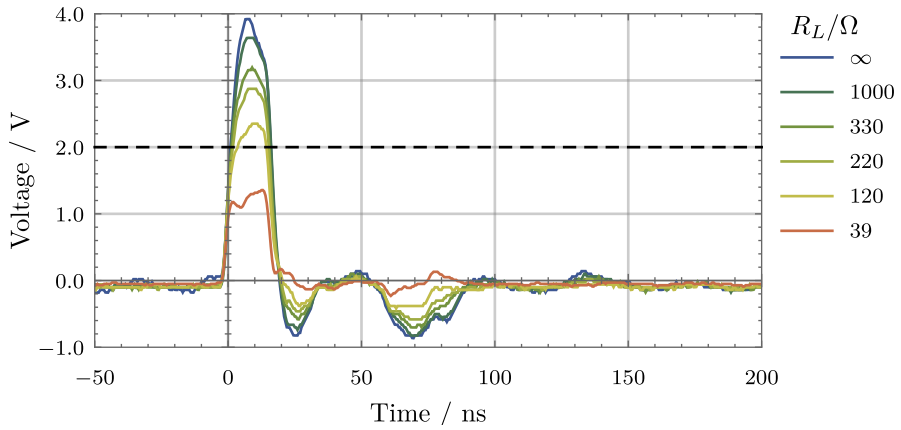
The DET signal from the SPCM, although TTL-levelled, originates at a 50 Ω output and therefore reflects significantly at the high impedance input of the JK IC if not correctly impedance matched. The TDC receives the same signal from the SPCM and will therefore record the reflected signal as a duplicate count. A simple load termination scheme comprising a single resistor,

R_L positioned as shown in Figure A.2 is used to reduce the impedance mismatch; Figure A.4a shows the magnitude of the reflected signal as a function of R_L with the expected minimum around $R_L = 50\,\Omega$. However as shown in Figure A.4b the voltage registered at the CLK input is reduced by the presence of R_L and a compromise must be made between reducing the reflections enough to prevent triggering the TDC whilst maintaining sufficient voltage to trigger the JK. A value of $R_L = 100\,\Omega$ was chosen to minimise reflections, however a slightly higher value around $200\,\Omega$ could potentially trigger the JK one or two nanoseconds quicker whilst still avoiding significant reflections.

The output Q of the JK now inverts every time a detection is recorded within the first time-bin, however we only require a PHASE output signal during the window of the second time bin. Restricting the PHASE output voltage to only that period defined by $\text{WIN}_{\text{PHASE}}$ can be achieved with a simple AND gate as shown in Figure A.3. However the EOM is a $50\,\Omega$ load and to reach voltages around 3 V necessary for a π phase change therefore requires around 60 mA which is far more than a simple AND chip such as the SN74F08N can source (1 mA per gate). A buffer/driver version of the AND gate is available (SN74AS1008AN) which can source 48 mA per gate, connecting several together should provide the required current. Note it is not advisable to connect the outputs of totem-pole TTL gates together as if one gate outputs high and the other low excessive current can flow to thermally damage the transistors. However with identical inputs this situation should never arise for longer than the response time of the gate which at around 6 ns is insufficient for thermal damage to occur. Unfortunately although this setup was able to provide sufficient voltage to the EOM, a voltage divider was required to control the output voltage level which produced a circuit with an RC time constant $\tau \approx 7.5$ ns corresponding to a slow 10-90 rise time



(a) Reflection Voltage



(b) Input Voltage

Figure A.4: Impedance matching at the DET input: The high impedance of the TTL integrated circuits substantially reflects the 50 Ω pulses from the SPCMs, which cause 'double counting' at the TDC if not reduced — the dashed lines in (a) show the TDC trigger level. A load resistor is used to reduce the impedance mismatch and bring the the amplitude of the reflected signal to within acceptable limits (a). However, too small a value of R_L reduces the voltage at the CLK input below its trigger level (shown dashed in (b)). A value of 100 Ω was chosen as a satisfactory compromise.

of around 17 ns and a damning 0-100 rise time around 37 ns. The solution, with a 0-100 rise time around 5.5 ns was to use open collector TTL gates to create a wired AND gate to switch a voltage from a variable regulator.

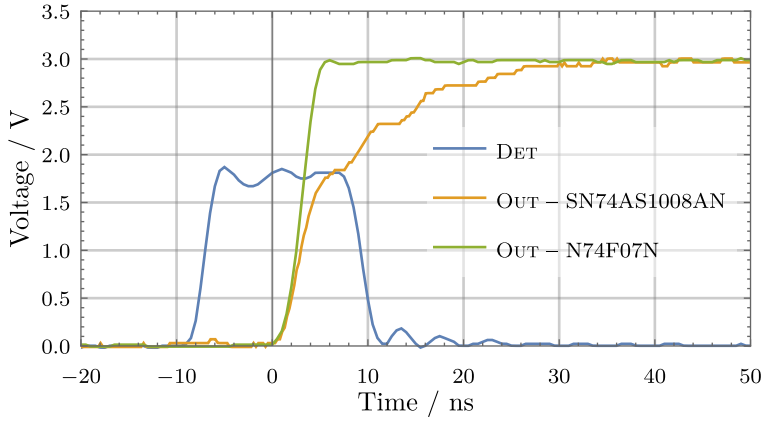


Figure A.5: Phase rise times: Although the buffer/driver version of the AND gate, the SN74AS1008AN, is able to supply sufficient output voltage, the rise time is unacceptably slow. A wired AND gate, created using the N74F07N open collector buffers, provides a substantially faster output voltage rise time.

A.3 Output Stage

The output of an open collector IC doesn't supply a specific voltage but instead provides either an open circuit or a connection to ground. This allows switching of a voltage at the output which need not be the same level as that of the IC logic levels, they are therefore commonly used to interface different families of IC and here we use them to switch the variable voltage supplied to the EOM. Connecting the outputs of multiple open collector gates results in a so called "wired AND gate" whereby if any of the OC gates output logical 0, a path to ground, the voltage being switched will be routed to ground and not the output. This configuration can be seen in Figure A.2 where three open collector buffers are used for each input of the wired AND

gate which switched the voltage V_ϕ. These buffers are the six gates on an N74F07N and are each capable of sinking 64 mA. A key feature of a wired AND is the resistor R_{pull} which acts as a pull up resistor - the open collector gates can drain current but for the voltage at the output to drop to zero the current must be pulled through a resistor.

The final output voltage V_ϕ is given by

$$V_\phi = V_{\text{S}} \frac{R_{\text{load}}}{R_{\text{load}} + R_{\text{pull}}} , \tag{A.1}$$

where V_{S} is the voltage supplied by the variable voltage regulator. An LM350 is used which can supply 3 A at 1.2 V to 33 V. The value of V_{S} is determined by the two resistors R_1 and R_2 in the ratio

$$V_{\text{S}} = V_{\text{REF}} \left(1 + \frac{R_2}{R_1} \right) , \tag{A.2}$$

where V_{REF} for the LM350 is nominally 1.25 V. To ensure correct operation a minimum load current of (in the worst case) 10 mA must be drawn from the regulator which motivates the common choice of 120 Ω for R_1. A trimmer is used for R_2 whose maximum value will determine the maximum value of V_{S}. The buffers on the N74F07N can tolerate a maximum of 12 V and therefore a 1 kΩ trimmer was chosen for R_2 giving a range for V_{S} of 1.25 V to 11.67 V. The value of R_{pull} can now be set to give the desired range for V_ϕ from Equation (A.1). Recall that the buffers on the N74F07N are only capable of draining $I_{\text{OL}} = 64\,\text{mA}$, therefore if $V_{\text{S}} > I_{\text{OL}} R_{\text{pull}}$ they will not be able to drain the full voltage of V_ϕ when required and thus the low level voltage applied to the EOM will not be 0 V. This is not only not good for the EOM but also corresponds to a $\Delta V_\phi < V_\phi$, reducing the useful phase contrast implemented by the EOM. Using only one gate the current limit of 64mA limits ΔV_ϕ to a

maximum of around 2.5 V achieved when $R_{\text{pull}} = 182\,\Omega$, which is insufficient to implement a π phase change which requires $\Delta V_\phi = 2.8\,\text{V}$. Therefore three gates are used for each input of the wired AND thus increasing the current limit allowing us to implement a maximum $\Delta V_\phi = 5.3\,\text{V}$ when $R_{\text{pull}} = 61\,\Omega$. The buffers are actually capable of draining a little more than 64 mA and have a absolute maximum rating of 128 mA, therefore it was decided to use a resistor of $47\,\Omega$ for R_{pull} gives a maximum $\Delta V_\phi = 6.0\,\text{V}$, requiring only 83 mA per drain. The effect of the value of R_{pull} on the achievable ΔV_ϕ is shown in Figure A.6. The final consideration with respect to the choice of R_{pull} is that a significant amount of power is dumped into the resistor, at 11.67 V and $47\,\Omega$, $P = V^2/R = 2.9\,\text{W}$, significantly more than the half watt or so standard resistors can handle.

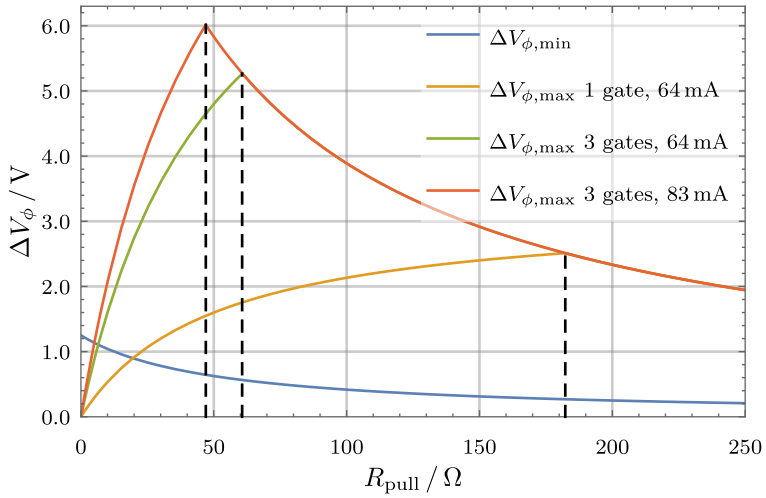


Figure A.6: Pull-up resistor choice: The minimum PHASE output voltage difference accessible, $\Delta V_{\phi,\text{min}}$, produced when $V_\text{S} = 1.25\,\text{V}$ varies slightly with the choice of pull-up resistor. The maximum value, $\Delta V_{\phi,\text{max}}$, at $V_\text{S} = 11.67\,\text{V}$, varies more strongly and considerably higher values are accessible by using multiple gates and flouting the suggested operating current limits.

A.4 Conclusions

The circuit meets and exceeds its design parameters, providing a peak output voltage of up to 6.0 V to the 50 Ω EOM load, with a 0-100 rise time of 5.5 ns and a delay of 7 ns, the timing details are presented in Chapter 6. The smallest peak output voltage accessible is 0.64 V thus the circuit is able to drive the EOM to modulate phase changes of 0.23-2.17 π.

Moving from transistor-transistor logic to emitter coupled logic could improve the response from a few nanoseconds into the sub nanosecond regime at the cost of greater voltage level sensitivity. A simpler modification of increasing R_L to around 300 Ω could also save a couple of nanoseconds. However at this point the signal propagation delay from SPCM to the circuit and to the EOM becomes more significant than the circuit's latency and both are a tiny fraction of the total feedback latency which is dominated by the optical transit time and the SPCM response.

The design principles outlined above could be extended to develop circuits performing more complicated logic perhaps entailing multiple detectors or criteria for phase values. Depending on the complexity it may be more efficient to move to an FPGA, provided speed doesn't have to be compromised, which would allow faster prototyping and reconfigurability.

Bibliography

[1] Planck, M. Über das Gesetz der Energieverteilung im Normalspectrum. *Annalen der Physik* **4,** 553–563 (1901).

[2] Ehrenfest, P. Welche Züge der Lichtquantenhypothese spielen in der Theorie der Wärmestrahlung eine wesentliche Rolle? *Annalen der Physik* **341,** 91–118 (1911).

[3] Einstein, A. Über einen die Erzeugung und Verwandlung des Lichtes betreffenden heuristischen Gesichtspunkt. *Annalen der Physik* **322,** 132–148 (1905).

[4] Lewis, G. N. The Conservation of Photons. *Nature* **118,** 874–875 (1926).

[5] De Broglie, L. *Recherches sur la théorie des quanta* PhD thesis (Paris, 1924).

[6] Heisenberg, W. Über den anschaulichen Inhalt der quantentheoretischen Kinematik und Mechanik. *Zeitschrift für Physik* **43,** 172–198 (1927).

[7] Einstein, A., Podolsky, B. & Rosen, N. Can Quantum-Mechanical Description of Physical Reality Be Considered Complete. *Physical Review* **47,** 2–5 (1935).

[8] Bell, J. S. On the Einstein Podolsky Rosen paradox. *Physics* **1,** 195–200 (1964).

[9] Aspect, A., Dalibard, J. & Roger, G. Experimental test of Bell's inequalities using time-varying analyzers. *Physical Review Letters* **49,** 1804–1807 (1982).

[10] Hensen, B. *et al.* Loophole-free Bell inequality violation using electron spins separated by 1.3 kilometres. *Nature* **526,** 682–686 (2015).

[11] Giustina, M. *et al.* Significant-Loophole-Free Test of Bell's Theorem with Entangled Photons. *Physical Review Letters* **115,** 1–7 (2015).

[12] Bennett, C. H. & Brassard, G. *Quantum cryptography: Public key distribution and coin tossing* in *International Conference on Computer System and Signal Processing* (1984), 175–179.

[13] Ekert, A. K. Quantum cryptography based on Bell's theorem. *Physical Review Letters* **67,** 661–663 (1991).

[14] Gisin, N., Ribordy, G., Tittel, W. & Zbinden, H. Quantum cryptography. *Reviews of Modern Physics* **74,** 145–195 (2002).

[15] Feynman, R. P. Simulating Physics with Quantum Computers. *International Journal of Theoretical Physics* **21,** 467–488 (1982).

[16] Deutsch, D. Quantum theory, the Church-Turing principle and the universal quantum computer. *Proc. R. Soc. Lond. A* **400,** 97–117 (1985).

[17] Deutsch, D. & Jozsa, R. Rapid solution of problems by quantum computation. *Proc. R. Soc. Lond. A* **439,** 553–558 (1992).

[18] Shor, P. W. Polynomial-Time Algorithms for Prime Factorization and Discrete Logarithms on a Quantum Computer. *SIAM Journal on Computing* **26,** 1484–1509 (1997).

[19] Grover, L. K. A fast quantum mechanical algorithm for database search. *Proceedings, 28th Annual ACM Symposium on the Theory of Computing (STOC),* 212–219 (1996).

[20] Grover, L. K. Quantum Computers Can Search Arbitrarily Large Databases by a Single Query. *Physical Review Letters* **79,** 4709–4712 (1997).

[21] Nielsen, M. A. & Chuang, I. L. *Quantum computation and quantum information* 708 (Cambridge University Press, 2010).

[22] DiVincenzo, D. P. The Physical Implementation of Quantum Computation. *Fortschritte der Physik* **48,** 771–783 (2000).

[23] DiVincenzo, D. P. Two-bit gates are universal for quantum computation. *Physical Review A* **51,** 1015–1022 (1995).

[24] Loss, D. & DiVincenzo, D. P. Quantum Computation with Quantum Dots. *Physical Review A* **57,** 12 (1998).

[25] Wrachtrup, J. & Jelezko, F. Processing quantum information in diamond. *Journal of Physics: Condensed Matter* **18,** S807 (2006).

[26] Saffman, M., Walker, T. G. & Mølmer, K. Quantum information with Rydberg atoms. *Reviews of Modern Physics* **82,** 2313–2363 (2010).

[27] Devoret, M. H. & Schoelkopf, R. J. Superconducting Circuits for Quantum Information: An Outlook. *Science* **339,** 1169–1174 (2013).

[28] Awschalom, D. D., Bassett, L. C., Dzurak, A. S., Hu, E. L. & Petta, J. R. Quantum Spintronics : Engineering. *Science* **339,** 1174–1179 (2013).

[29] Stern, A. & Lindner, N. H. Topological Quantum ComputationFrom Basic Concepts to First Experiments. *Science* **339,** 1179–1184 (2013).

[30] O'Brien, J. L. Optical quantum computing. *Science* **318,** 1567–1570 (2007).

[31] Reiserer, A. & Rempe, G. Cavity-based quantum networks with single atoms and optical photons. *Reviews of Modern Physics* **87,** 1379 (2015).

[32] Monroe, C. & Kim, J. Scaling the ion trap quantum processor. *Science* **339,** 1164–1169 (2013).

[33] Ladd, T. D. *et al.* Quantum computers. *Nature* **464,** 45–53 (2010).

[34] Kimble, H. J. The quantum internet. *Nature* **453,** 1023–1030 (2008).

[35] Northup, T. E. & Blatt, R. Quantum information transfer using photons. *Nature Photonics* **8,** 356–363 (2014).

[36] Korzh, B. *et al.* Provably Secure and Practical Quantum Key Distribution over 307 km of Optical Fibre. *Nature Photonics* **9,** 7 (2014).

[37] Cirac, J. I., Zoller, P., Kimble, H. J. & Mabuchi, H. Quantum State Transfer and Entanglement Distribution among Distant Nodes in a Quantum Network. *Physical Review Letters* **78,** 3221–3224 (1997).

[38] Duan, L. M. & Monroe, C. Colloquium: Quantum networks with trapped ions. *Reviews of Modern Physics* **82,** 1209–1224 (2010).

[39] Kuhn, A., Hennrich, M. & Rempe, G. Deterministic Single-Photon Source for Distributed Quantum Networking. *Physical Review Letters* **89,** 067901 (2002).

[40] Wilk, T., Webster, S. C., Kuhn, A. & Rempe, G. Single-Atom Single-Photon Quantum Interface. *Science* **317,** 488–490 (2007).

[41] Ritter, S. *et al.* An elementary quantum network of single atoms in optical cavities. *Nature* **484,** 195–200 (2012).

[42] Wootters, W. K. & Zurek, W. H. A single quantum cannot be cloned. *Nature* **299,** 802–803 (1982).

[43] Dieks, D. G. B. J. Communication by EPR devices. *Physics Letters A* **92,** 271–272 (1982).

[44] Sangouard, N., Simon, C., De Riedmatten, H. & Gisin, N. Quantum repeaters based on atomic ensembles and linear optics. *Reviews of Modern Physics* **83,** 33–80 (2011).

[45] Bennett, C. H., Crepeau, C., Jozsa, R., Peres, A. & Wootters, W. K. Teleporting an Unknown Quantum State via Dual Classical and Einstein-Podolsky-Rosen Channels. *Physical Review Letters* **70,** 1895 (1993).

[46] Zukowski, M., Zeilinger, A., Horne, M. A. & Ekert, A. K. "Event-ready-detectors" Bell experiment via entanglement swapping. *Physical Review Letters* **71,** 4287–4290 (1993).

[47] Pan, J. W., Bouwmeester, D., Weinfurter, H. & Zeilinger, A. Experimental entanglement swapping: Entangling photons that never interacted. *Physical Review Letters* **80,** 3891 (1999).

[48] Heshami, K. *et al.* Quantum memories: emerging applications and recent advances. *Journal of Modern Optics* **63,** 2005–2028 (2016).

[49] Chou, C. W. *et al.* Measurement induced entanglement for excitation stored in remote atomic ensembles. *Nature* **438,** 828–832 (2005).

[50] Saglamyurek, E. *et al.* Quantum storage of entangled telecom-wavelength photons in an erbium-doped optical fibre. *Nature Photonics* **9,** 83–87 (2015).

[51] Uphoff, M., Brekenfeld, M., Rempe, G. & Ritter, S. An integrated quantum repeater at telecom wavelength with single atoms in optical fiber cavities. *Applied Physics B* **122,** 1–15 (2016).

[52] Shor, P. W. Scheme for reducing decoherence in quantum computer memory. *Physical Review A* **52,** R2493 (1995).

[53] Steane, A. Multiple Particle Interference and Quantum Error Correction. *Proc. R. Soc. Lond. A* **452,** 2551–2577 (1996).

[54] Hambury Brown, R. & Twiss, R. Q. Correlation between photons in two coherent beams of light. *Nature* **177,** 27–29 (1956).

[55] Glauber, R. J. Coherent and incoherent states of the radiation field. *Physical Review* **131,** 2766–2788 (1963).

[56] Kimble, H. J., Dagenais, M. & Mandel, L. Photon antibunching in resonance fluorescence. *Physical Review Letters* **39,** 691–695 (1977).

[57] Walmsley, I. A. Quantum optics: Science and technology in a new light. *Science* **348,** 525–530 (2015).

[58] Knill, E., Laflamme, R. & Milburn, G. J. A scheme for efficient quantum computation with linear optics. *Nature* **409,** 46–52 (2001).

[59] Pittman, T. B., Jacobs, B. C. & Franson, J. D. Demonstration of nondeterministic quantum logic operations using linear optical elements. *Physical review letters* **88,** 257902 (2002).

[60] O'Brien, J. L., Pryde, G. J., White, A. G., Ralph, T. C. & Branning, D. Demonstration of an all-optical quantum controlled-NOT gate. *Nature* **426,** 264–267 (2003).

[61] Kok, P. *et al.* Linear optical quantum computing with photonic qubits. *Reviews of Modern Physics* **79,** 135–174 (2007).

[62] Politi, A., Cryan, M. J., Rarity, J. G., Yu, S. & O'Brien, J. L. Silica-on-silicon waveguide quantum circuits. *Science* **320,** 646–649 (2008).

[63] Carolan, J. *et al.* Universal Linear Optics. *Science* **349,** 711–716 (2015).

[64] Politi, A., Matthews, J. C. F. & O'Brien, J. L. Shor's quantum factoring algorithm on a photonic chip. *Science* **325,** 1221 (2009).

[65] Metcalf, B. J. *et al.* Quantum teleportation on a photonic chip. *Nature Photonics* **8,** 770–774 (2014).

[66] Spring, J. B. *et al.* Boson Sampling on a Photonic Chip. *Science* **339,** 798–801 (2013).

[67] Hadfield, R. H. Single-photon detectors for optical quantum information applications. *Nature Photonics* **3,** 696 (2009).

[68] Pernice, W. H. P. *et al.* High-speed and high-efficiency travelling wave single-photon detectors embedded in nanophotonic circuits. *Nature Communications* **3,** 1325 (2012).

[69] Eisaman, M. D., Fan, J., Migdall, A. & Polyakov, S. V. Invited Review Article: Single-photon sources and detectors. *Review of Scientific Instruments* **82,** 071101 (2011).

[70] Broome, M. A., Almeida, M. P., Fedrizzi, A. & White, A. G. Reducing multi-photon rates in pulsed down-conversion by temporal multiplexing. *Optics Express* **19,** 22698–22708 (2011).

[71] Nunn, J. *et al.* Enhancing multiphoton rates with quantum memories. *Physical Review Letters* **110,** 133601 (2013).

[72] Spring, J. B. *et al.* An on-chip array of near-identical, pure, heralded single photon sources. *arXiv:1603.06984v1* (2016).

[73] Somaschi, N. *et al.* Near optimal single photon sources in the solid state. *Nature Photonics,* Advance Online Publication (2016).

[74] Kennard, J. E. *et al.* On-Chip Manipulation of Single Photons from a Diamond Defect. *Physical Review Letters* **111,** 213603 (2013).

[75] Sipahigil, A. *et al.* Indistinguishable photons from separated silicon-vacancy centers in diamond. *Physical Review Letters* **113,** 113602 (2014).

[76] Kuhn, A. & Ljunggren, D. Cavity-based single-photon sources. *Contemporary Physics* **51,** 289–313 (2010).

[77] Laurent, S. *et al.* Indistinguishable single photons from a single-quantum dot in a two-dimensional photonic crystal cavity. *Applied Physics Letters* **87,** 163107 (2005).

[78] Barclay, P. E., Fu, K. M. C., Santori, C. & Beausoleil, R. G. Chip-based microcavities coupled to nitrogen-vacancy centers in single crystal diamond. *Applied Physics Letters* **95,** 93–96 (2009).

[79] Patel, R. B. *et al.* Two-photon interference of the emission from electrically tunable remote quantum dots. *Nature Photonics* **4,** 632–635 (2010).

[80] Monteiro, F, Martin, A, Sanguinetti, B, Zbinden, H & Thew, R. T. Narrowband photon pair source for quantum networks. **22,** 4371–4378 (2014).

[81] Hijlkema, M. *et al.* A single-photon server with just one atom. *Nature Physics* **3,** 253–255 (2007).

[82] Law, C. K. & Kimble, H. J. Deterministic generation of a bit-stream of single-photon pulses. *Journal of Modern Optics* **44,** 2067–2074 (1997).

[83] Fox, M. *Quantum Optics: An Introduction* (Oxford University Press, 2006).

[84] Kuhn, A. In *Engineering the Atom-Photon Interaction* (eds Predojević, A. & Mitchell, M. W.) 3–38 (Springer International Publishing, 2015).

[85] Jaynes, E. T. & Cummings, F. W. Comparison of Quantum and Semiclassical Radiation Theories with Application to the Beam Maser. *Proceedings of the IEEE* **51,** 89–109 (1963).

[86] Shore, B. W. & Knight, P. L. The Jaynes-Cummings Model. *Journal of Modern Optics* **40,** 1195–1238 (1993).

[87] Bandres, M. A. & Gutiérrez-Vega, J. C. Ince-Gaussian modes of the paraxial wave equation and stable resonators. *J. Opt. Soc. Am. A* **21,** 873–880 (2004).

[88] Silfvast, W. T. *Laser Fundamentals* 2nd ed. (Cambridge University Press, 2008).

[89] Kimble, H. J. Strong Interactions of Single Atoms and Photons in Cavity QED. *Physica Scripta* **T76,** 127–137 (1998).

[90] Purcell, E. M. Spontaneous emission probabilities at radio frequencies. *Physical Review* **69,** 681 (1946).

[91] Kuhn, A. & Rempe, G. In *Experimental Quantum Computation and Information* (eds De Martini, F. & Monroe, C.) (IOS- Press, Amsterdam, 2002).

[92] Vasilev, G. S., Kuhn, A. & Vitanov, N. V. Optimum pulse shapes for stimulated Raman adiabatic passage. *Physical Review A* **80,** 013417 (2009).

[93] Vasilev, G. S., Ljunggren, D. & Kuhn, A. Single photons made-to-measure. *New Journal of Physics* **12,** 063024 (2010).

[94] Nisbet-Jones, P. B. R. *Shaping Single Photons* PhD thesis (University of Oxford, 2012).

[95] Hong, C. K., Ou, Z. Y. & Mandel, L. Measurement of subpicosecond time intervals between two photons by interference. *Physical Review Letters* **59,** 2044–2046 (1987).

[96] Legero, T., Wilk, T., Kuhn, A. & Rempe, G. Characterization of Single Photons Using Two-Photon Interference. *Advances in Atomic, Molecular and Optical Physics* **53,** 253–289 (2006).

[97] Legero, T., Wilk, T., Kuhn, A. & Rempe, G. Time-resolved two-photon quantum interference. *Applied Physics B* **77,** 797–802 (2003).

[98] Dilley, J. *A Single-Photon Source for Quantum Networking* PhD thesis (University of Oxford, 2012).

[99] Steck, D. A. Rubidium 87 Line Data, 1–29 (2009).

[100] Drever, R. W. P. *et al.* Laser phase and frequency stabilization using an optical resonator. *Applied Physics B* **31,** 97–105 (1983).

[101] Black, E. D. An introduction to Pound-Drever-Hall laser frequency stabilization. *American Journal of Physics* **69,** 79 (2001).

[102] Dilley, J., Nisbet-Jones, P. B. R., Shore, B. W. & Kuhn, A. Single-photon absorption in coupled atom-cavity systems. *Physical Review A* **85,** 023834 (2012).

[103] Gozzini, A. *et al.* Light-induced ejection of alkali atoms in polysiloxane coated cells. *Il Nuovo Cimento D* **15,** 709–722 (1993).

[104] Atutov, S. *et al.* Fast and efficient loading of a Rb magneto-optical trap using light-induced atomic desorption. *Physical Review A* **67,** 053401 (2003).

[105] Klempt, C. *et al.* Ultraviolet light-induced atom desorption for large rubidium and potassium magneto-optical traps. *Physical Review A* **73,** 013410 (2006).

[106] Marcikic, I. *et al.* Time-bin entangled qubits for quantum communication created by femtosecond pulses. *Physical Review A* **66,** 062308 (2002).

[107] Humphreys, P. C. *et al.* Linear optical quantum computing in a single spatial mode. *Physical Review Letters* **111,** 150501 (2013).

[108] Lanyon, B. P. *et al.* Simplifying quantum logic using higher-dimensional Hilbert spaces. *Nature Physics* **5,** 134–140 (2009).

[109] Gröblacher, S., Jennewein, T., Vaziri, A., Weihs, G. & Zeilinger, A. Experimental quantum cryptography with qutrits. *New Journal of Physics* **8,** 75–75 (2006).

[110] Nisbet-Jones, P. B. R., Dilley, J., Holleczek, A., Barter, O. & Kuhn, A. Photonic qubits, qutrits and ququads accurately prepared and delivered on demand. *New Journal of Physics* **15,** 053007 (2013).

[111] Pittman, T. B. *et al.* Can Two-Photon Interference be Considered the Interference of Two Photons? *Physical Review Letters* **77,** 1917–1920 (1996).

[112] Nisbet-Jones, P. B. R., Dilley, J., Ljunggren, D. & Kuhn, A. Highly efficient source for indistinguishable single photons of controlled shape. *New Journal of Physics* **13,** 103036 (2011).

[113] Wilk, T., Webster, S. C., Specht, H. P., Rempe, G. & Kuhn, A. Polarization-controlled single photons. *Physical Review Letters* **98,** 063601 (2007).

[114] Aggarwal, R. & Caldwell, A. Error bars for distributions of numbers of events. *The European Physical Journal Plus* **127** (2012).

[115] Kolchin, P., Belthangady, C., Du, S., Yin, G. Y. & Harris, S. E. Electro-optic modulation of single photons. *Physical Review Letters* **101,** 103601 (2008).

[116] Specht, H. P. *et al.* Phase shaping of single-photon wave packets. *Nature Photonics* **3,** 469–472 (2009).

[117] Bennett, A. J. *et al.* Experimental position-time entanglement with degenerate single photons. *Physical Review A* **77,** 023803 (2008).

[118] O'Brien, J. L., Furusawa, A. & Vučković, J. Photonic quantum technologies. *Nature Photonics* **3,** 687–695 (2009).

[119] Shadbolt, P., Matthews, J. C. F., Laing, A. & O'Brien, J. L. Testing foundations of quantum mechanics with photons. *Nature Physics* **10,** 278–286 (2014).

[120] Pooley, M. A. *et al.* Controlled-NOT gate operating with single photons. *Applied Physics Letters* **100,** 211103 (2012).

[121] Gazzano, O. *et al.* Entangling Quantum-Logic Gate Operated with an Ultrabright Semiconductor Single-Photon Source. *Physical Review Letters* **110,** 250501 (2013).

[122] Holleczek, A. *et al.* Quantum Logic with Cavity Photons From Single Atoms. *Physical Review Letters* **117,** 023602 (2016).

[123] Rarity, J. G., Langford, N. K., Bell, T. B. & White, A. G. Linear Optical CNOT Gate in the Coincidence Basis. *Physical Review A* **65,** 062324 (2002).

[124] Tichy, M. C., Tiersch, M., Mintert, F. & Buchleitner, A. Many-particle interference beyond many-boson and many-fermion statistics. *New Journal of Physics* **14,** 20–22 (2012).

[125] Campos, R. A., Bahaa, E. A. S. & Teich, M. C. Quantum-mechanical lossless beam splitter: SU(2) symmetry and photon statistics. *Physical Review A* **40,** 1371 (1989).

[126] Bhattacharyya, A. On a measure of divergence between two statistical populations defined by their probability distributions. *Bulletin of the Calcutta Mathematical Society* **35,** 99–109 (1943).

[127] Matthews, J. C. F. *et al.* Observing fermionic statistics with photons in arbitrary processes. *Scientific Reports* **3,** 1539 (2013).

[128] Leonhardt, U. & Paul, H. Measuring the quantum state of light. *Progress in Quantum Electronics* **19,** 89–130 (1995).

[129] Tzvetan, S. M., Arvin, I. F. & Frederic, T. C. *Quantum Computing for Computer Architects* 202 (2011).

[130] Terhal, B. M. & Horodecki, P. A Schmidt number for density matrices. *Physical Review A* **61,** 040301 (2000).

[131] Liu, R. C., Odom, B., Yamamoto, Y. & Tarucha, S. Quantum interference in electron collision. *Nature* **391,** 263–265 (1998).

[132] Wilczek, F. Magnetic Flux, Angular Momentum, and Statistics. *Physical Review Letters* **48,** 1144 (1982).

[133] Wilczek, F. & Rokhsar, D. S. *Fractional Statistics and Anyon Superconductivity* **2,** 101 (1992).

[134] Laughlin, R. B. Anomalous quantum Hall effect: An incompressible quantum fluid with fractionally charged excitations. *Physical Review Letters* **50,** 1395–1398 (1983).

[135] Kassal, I, Perdomo-Ortiz, A., Yung, M. H. & Aspuru-Guzik, A. Simulating Chemistry Using Quantum Computers. *Annual Review of Physical Chemistry* **62,** 185–207 (2011).

[136] Belavkin, V. P. Towards the theory of control in observable quantum systems. *arXiv:quant-ph/0408003* (2004).

[137] Yamamoto, Y., Imoto, N. & MacHida, S. Amplitude squeezing in a semiconductor laser using quantum nondemolition measurement and negative feedback. *Physical Review A* **33,** 3243 (1986).

[138] Carmichael, H. J. Quantum trajectory theory for cascaded open systems. *Physical Review Letters* **70,** 2273–2276 (1993).

[139] Gardiner, C. W. Driving a quantum system with the output field from another driven quantum system. *Physical Review Letters* **70,** 2269–2272 (1993).

[140] Wiseman, H. M. & Milburn, G. J. All-optical versus electro-optical quantum-limited feedback. *Physical Review A* **49,** 4110 (1994).

[141] Lloyd, S. Coherent quantum feedback. *Physical Review A* **62,** 022108 (2000).

[142] Habib, S., Jacobs, K. & Mabuchi, H. Quantum Feedback Control. *Los Alamos Science* **27** (2002).

[143] Armen, M. A., Au, J. K., Stockton, J. K., Doherty, A. C. & Mabuchi, H. Adaptive homodyne measurement of optical phase. *Physical Review Letters* **89,** 133602 (2002).

[144] Smith, W. P., Reiner, J. E., Orozco, L. A., Kuhr, S. & Wiseman, H. M. Capture and release of a conditional state of a cavity QED system by quantum feedback. *Physical Review Letters* **89,** 133601 (2002).

[145] Sayrin, C. *et al.* Real-time quantum feedback prepares and stabilizes photon number states. *Nature* **477,** 73 (2011).

[146] Zhou, X. *et al.* Field locked to a fock state by quantum feedback with single photon corrections. *Physical Review Letters* **108,** 243602 (2012).

[147] Banaszek, K. Fidelity balance in quantum operations. *Physical Review Letters* **86,** 1366–1369 (2001).

[148] Raimond, J.-M. *et al.* Quantum Zeno dynamics of a field in a cavity. *Physical Review A* **86,** 032120 (2012).

[149] Zhang, J., Liu, Y.-x., Wu, R.-B., Jacobs, K. & Nori, F. Quantum feedback: theory, experiments, and applications. *arXiv:1407.8536* (2014).

[150] Pockels, F. C. A. *Lehrbuch der kristalloptik* (BG Teubner, 1906).

[151] Peruzzo, A. Quantum walks of correlated photons. *Science* **329,** 1500–1503 (2010).

[152] Jennewein, T., Barbieri, M. & White, A. G. Single-photon device requirements for operating linear optics quantum computing outside the post-selection basis. *Journal of Modern Optics* **58,** 37–41 (2010).

[153] Crespi, A. *et al.* Integrated multimode interferometers with arbitrary designs for photonic boson sampling. *Nature Photonics* **7,** 545–549 (2013).

[154] Hunger, D. *et al.* A fiber FabryPerot cavity with high finesse. *New Journal of Physics* **12,** 065038 (2010).

[155] Takahashi, H., Morphew, J., Oru, F., Kassa, E. & Keller, M. Novel laser machining of optical fibers for long cavities with low birefringence. **22,** 1202–1205 (2014).

[156] Thompson, J., Simon, J., Loh, H. & Vuletić, V. A high-brightness source of narrowband, identical-photon pairs. *Science* **313,** 74 (2006).

[157] Mücke, M. *et al.* Generation of single photons from an atom-cavity system. *Physical Review A* **87,** 063805 (2013).

[158] Megidish, E. *et al.* Entanglement swapping between photons that have never coexisted. *Physical Review Letters* **110,** 210403 (2013).

[159] Megidish, E., Shacham, T., Halevy, A., Dovrat, L. & Eisenberg, H. S. Resource efficient source of multiphoton polarization entanglement. *Physical Review Letters* **109,** 080504 (2012).